

Institut de Physique du Globe de Paris
Ecole doctorale des Sciences de la Terre

Thèse de Doctorat

pour l'obtention du titre de

Docteur en Science

de l'Institut de Physique du Globe de Paris

Spécialité : GEOPHYSIQUE

Soutenue par

Clément THOREY

Magmatisme intrusif sur les planètes telluriques

Équipe PLANÉTOLOGIE ET SCIENCES SPATIALES,

Défendue le 5 Décembre, 2013.

Jury :

<i>Directeur:</i>	Chloé MICHAUT	- IPGP (Paris)
<i>Co-directeur:</i>	Mark WIECZOREK	- IPGP (Paris)
<i>Rapporteur :</i>	Jerome NEUFELD	- DAMPT (Cambridge)
<i>Rapporteur :</i>	Virginie PINEL	- IRD (Chambéry)
<i>Examinateur :</i>	Oded AHARONSON	- WIS (Rehovot)
<i>Examinateur :</i>	Edouard KAMINKSI	- IPGP (Paris)

Remerciements

Je remercie marion rouault mae sans qui tout ceci n'aurait jamais vu le jour
;)

Contents

0 Résumé de la problématique et résultats principaux	1
I Dynamique des magmas à faible profondeur	3
1 Magmatisme intrusif	5
1.1 Formation, transport et stockage des magmas	5
1.1.1 Formation	5
1.1.2 Transport	6
1.1.3 Stockage	7
1.2 Importance et multiples visages du magmatisme intrusif	9
1.2.1 Magmatisme intrusif sur Terre	9
1.2.2 Magmatisme intrusif sur la Lune	13
1.3 Caractérisation de la mise en place d'une intrusion magmatique à faible profondeur	17
1.3.1 Modèle statique de déformation d'une couche élastique	17
1.3.2 Inférence sur la dynamique à partir de la géométrie	18
1.3.3 Discussion	20
2 Isoviscous elastic-plated gravity current model for shallow magmatic intrusion	21
2.1 Theoretical model	22
2.1.1 Governing equation	22
2.1.2 Dimensionless equations	25
2.1.3 Need for regularization	25
2.2 Results	26
2.2.1 Bending regime	27
2.2.2 Gravity current regime	28
2.3 Application to the spreading of shallow magmatic intrusions	29
2.3.1 Observations versus predictions on Earth	29
2.3.2 Low-slope domes on the Moon	34
2.3.3 What causes the arrest of a shallow magmatic intrusion?	36
2.3.4 Discussion	37
2.4 Toward a more realistic model for shallow magmatic intrusions	38

II Evolution thermique des intrusions magmatiques à faible profondeur	41
3 Elastic-plated gravity current with temperature-dependent viscosity	43
3.1 Introduction	44
3.2 Theory	46
3.2.1 Formulation	46
3.2.2 Pressure	47
3.2.3 Injection rate	47
3.2.4 Heat transport equation	48
3.2.5 Equation of motion	50
3.2.6 Dimensionless equations	51
3.2.7 Further simplifications	53
3.2.8 Summary of the equations	54
3.2.9 Preliminary results for an isothermal flow	55
3.3 Evolution in the bending regime	56
3.3.1 Thermal structure for an isoviscous flow, effect of Pe	56
3.3.2 Thickness and temperature profile, effect of ν	57
3.3.3 Evolution of the thickness and the radius	59
3.3.4 Characterization of the thermal anomaly	61
3.3.5 Effective viscosity of the current	62
3.3.6 Note on the effect of crystallization	64
3.4 Evolution in the gravity current regime	66
3.4.1 Thermal structure for an isoviscous flow, effect of Pe	66
3.4.2 Thickness and temperature profile, effect of ν	66
3.4.3 Evolution of the thickness and radius	69
3.4.4 Characterization of the thermal anomaly	70
3.4.5 Effective viscosity of the current	71
3.4.6 Note on the effect of crystallization	73
3.5 Different evolutions with bending and gravity	74
3.6 Summary and conclusion	78
4 Toward a more realistic model and its application to the spreading of shallow magmatic intrusions	81
4.1 Motivation	82
4.2 Theory	83
4.2.1 Thermal boundary condition	84
4.2.2 Dimensionless equations	85
4.2.3 Rheology	87
4.2.4 Comparison with the isothermal model	88

4.3	Evolution in the bending regime	89
4.3.1	Relaxing the thermal boundary condition, effect of Ω . .	90
4.3.2	Considering a more realistic rheology, effect of $\eta(\theta)$. .	91
4.3.3	Characterization of the thermal anomaly	92
4.4	Evolution in the gravity regime	95
4.4.1	Relaxing the thermal boundary condition, effect of Ω . .	95
4.4.2	Considering a more realistic rheology, effect of $\eta(\theta)$. .	97
4.4.3	Characterization of the thermal anomaly	99
4.5	Evolution with bending and gravity in the more realistic model	101
4.6	Application to the spreading of shallow magmatic intrusions .	102
4.6.1	Elba Island christmas-tree laccolith complex	102
4.6.2	Low-slope lunar domes	108
4.6.3	Large mafic sills	111
4.6.4	Contact aureole	112
4.7	Summary and discussion	114

III Cratères à sol fracturée: Témoins d'un magmatisme intrusif lunaire 117

5	Floor-fractured craters	119
5.1	Introduction	120
5.2	Floor-fractured craters	122
5.3	An axisymmetric model for a magmatic intrusion spreading below a crater-like topography	125
5.3.1	Crater topography and overlying layer characteristics .	125
5.3.2	Equations of Motion	128
5.3.3	Nondimensionalization	130
5.3.4	Range of values for the dimensionless numbers	132
5.4	Results	134
5.4.1	Intrusion below a brecciated zone with no elastic strength (effect of Ξ)	134
5.4.2	Intrusion below an elastic layer of constant thickness .	136
5.4.3	Spreading beneath a complex crater topography	138
5.4.4	Spreading beneath a simple crater	144
5.4.5	Effect of a variable injection rate	144
5.5	Discussion	148
5.5.1	Floor appearance	148
5.5.2	Depth of the intrusion	150
5.5.3	Injection rate and formation time scale	152
5.6	Conclusion	154

6 Gravitationnal signature of lunar floor-fractured craters	157
6.1 Introduction	158
6.2 Theoretical considerations	159
6.2.1 Constitutive equations	160
6.2.2 End-member modes of deformation	163
6.2.3 Gravitational signature of FFCs: two case studies	164
6.2.4 Filtered GRAIL gravity	167
6.3 Gravitational signature of lunar craters	168
6.3.1 Normal and floor-fractured crater populations	169
6.3.2 Crater gravitational signatures	171
6.4 Magmatic intrusion characteristics	174
6.4.1 Intrusion thickness	175
6.4.2 Density contrast $\Delta\rho$ of the intrusion	177
6.5 Discussion	178
6.6 Conclusion	179
IV Summary and perspectives	181
V Appendices and bibliography	193
A Numerical schemes	195
A.1 Numerical scheme for a cooling elastic-plated gravity current	195
A.1.1 General procedure	195
A.1.2 Thickness equation	196
A.1.3 Heat equation	199
A.1.4 Integral expressions	201
A.2 Numerical scheme for crater-centered intrusion	202
A.3 Numerical scheme	202
A.3.1 Discretization	203
A.3.2 Boundary conditions	205
A.3.3 Algorithm	206
B Details on the phase diagram	207
C Effect of the prewetting film	209
C.1 Scaling laws for the thickness and the radius	209
C.2 Two stage growth in the second bending phase	210
C.3 Phase diagram	212

D Floor-fractured craters	215
D.1 Elastic stresses in the upper elastic layer	215
D.2 Central peak	216
E Gravitationnal signature of lunar floor-fractured craters: Supplementary material	219
E.0.1 Synthetic gravity anomaly	219
E.0.2 Effect of the downward continuation filter λ	219
E.0.3 Definition of the gravity anomaly	220
E.0.4 Crater depth	220
Bibliography	225

Résumé de la problématique et résultats principaux

Part I

Dynamique des magmas à faible profondeur

CHAPTER 1

Magmatisme intrusif

Contents

1.1	Formation, transport et stockage des magmas	5
1.1.1	Formation	5
1.1.2	Transport	6
1.1.3	Stockage	7
1.2	Importance et multiples visages du magmatisme intrusif	9
1.2.1	Magmatisme intrusif sur Terre	9
1.2.2	Magmatisme intrusif sur la Lune	13
1.3	Caractérisation de la mise en place d'une intrusion magmatique à faible profondeur	17
1.3.1	Modèle statique de déformation d'une couche élastique	17
1.3.2	Inférence sur la dynamique à partir de la géométrie	18
1.3.3	Discussion	20

1.1 Formation, transport et stockage des magmas

1.1.1 Formation

Sur Terre, la majorité des magmas sont formés par fusion partielle des roches du manteau supérieur. Dans les conditions normales de pression, la température du manteau supérieur n'est pourtant pas suffisante pour provoquer leur fusion (Figure 1.1) et d'autres mécanismes sont nécessaires pour amener les roches du manteau à croiser leur liquidus. Au niveau des dorsales en contexte océanique ou des rifts en contexte continental ou encore au sein des panaches mantelliques, la fusion partielle est ainsi générée par décompression (Figure 1.1 b). Au niveau des zones de subduction, les mécanismes mis en jeu sont

plus complexes et font intervenir la déshydratation par chauffage des roches et la migration des fluides abaissant le liquidus et provoquant ainsi la fusion des roches alentour (Figure 1.1 c).

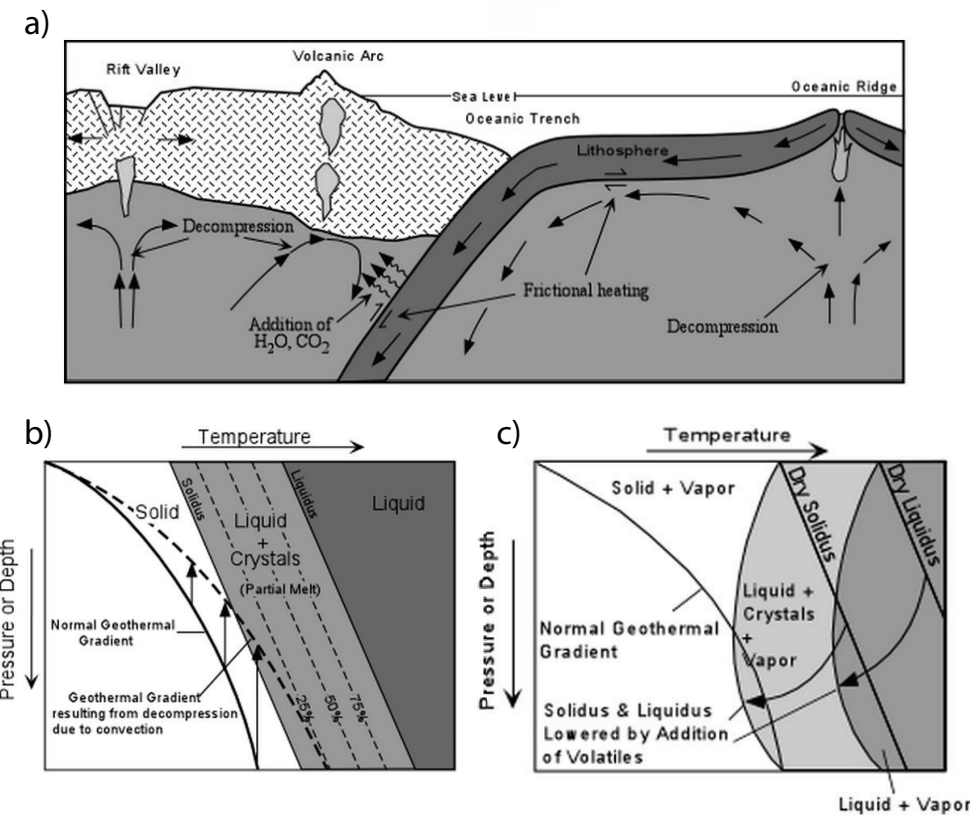


Figure 1.1: a) Lien entre le magmatisme et la tectonique des plaques: production de magma par fusion partielle par décompression au niveau des dorsales océaniques ou des rifts en contexte continental ou par addition de volatiles au niveau des zones de subduction. Schéma du diagramme de phase des roches du manteau supérieur dans deux contextes différents: b) dorsale océanique ou panache mantellique, c) zone de subduction.

1.1.2 Transport

Les liquides de fusions ainsi formés sont moins denses que les roches alentours et s'élèvent donc, par compaction et percolation, au sein de la source (*McKenzie*, 1984, 1985). Le transport du magma depuis la source jusqu'au couches superficielles de la lithosphère a longtemps était l'objet de débat (*Clemens*

and Mawer, 1992; Miller and Paterson, 1999). Cependant, les modèles de gros volumes diapiriques de magma remontant lentement au sein de la lithosphère, invoqués traditionnellement notamment pour expliquer la présence de gros volumes de magma intrudés au sein de la croûte à l'érosion (dans la vallée du Yosemite aux Etats-Unis par exemple), sont maintenant en désaveux. En effet, il est maintenant admis que ces gros volumes se sont mis en place par incrément successif de magmas et que celui-ci est transporté depuis la source rapidement au sein de la croûte au sein de chenaux verticaux, i.e. de dykes ou le long de failles préexistantes (*Clemens and Mawer, 1992; Petford et al., 1993; Rubin, 1995; Glazner et al., 2004*).

1.1.3 Stockage

Les travaux de *Walker (1989)* ont montré que les magmas remontent jusqu'à rencontrer leur zone de flottabilité neutre, une région où la densité de la roche encaissante est proche de celle du magma lui-même. En effet, au-dessus de cette couche, le magma est plus dense que la roche encaissante et sa flottabilité l'entraîne vers le bas. De nombreux travaux, tant théoriques (*Lister and Kerr, 1991; Petford et al., 1993; Rubin, 1995*) qu'expérimentaux (*Taisne and Tait, 2009; Taisne et al., 2011*) ont en effet depuis montré que l'ascension d'un dyke était contrôlée par la différence de densité entre la tête de celui-ci et la roche encaissante. Lorsque le dyke entre dans une région de densité inférieure, la souspression induite peut, sous certaines conditions, conduire à l'étalement du magma au niveau de la base de la région de plus faible densité permettant ainsi la formation de réservoir magmatique sous forme d'intrusion magmatique au sein de la croûte (*Taisne et al., 2011*).

Plus récemment, d'autres études ont montré que les contrastes de rigidité entre les différentes couches crustales pourraient aussi jouer un rôle non négligeable sur l'arrêt de l'ascension des dykes (*Menand, 2011*). En effet, des expériences réalisées par *Kavanagh et al. (2006)* ont montré que la propagation d'un dyke peut être arrêtée quand celui-ci rencontre une interface qui sépare un milieu plus rigide surplombant un milieu moins rigide (Figure 1.2). Le dyke arrête ainsi son ascension verticale et s'étale horizontalement juste en dessous de la couche de rigidité plus élevée. Ce mécanisme serait d'autant plus efficace que le contraste de rigidité est important (*Kavanagh et al., 2006*).

Finalement, les contraintes, locales ou globales, peuvent aussi dévier la trajectoire d'un dyke et influencer les trajets des magmas au sein de la croûte. En effet, de nombreuses études ont montré que les chenaux par lesquels se propage le magma tendent à s'orienter perpendiculairement à la contrainte minimum de compression σ_3 (*Anderson, 1951; Watanabe et al., 2002*). Les dykes ont donc tendance à exister dans des situations dans lesquelles la con-

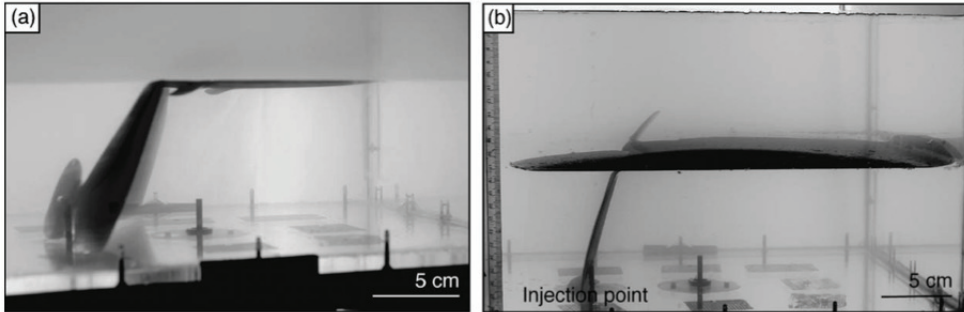


Figure 1.2: a) Photographie de deux des expériences réalisées par *Kavanagh et al. (2006)* sur le comportement d'un dyke à l'interface entre deux milieux de rigidité différente. a) Le contraste de rigidité est très important et le dyke s'étale sous la couche de rigidité importante. b) Le contraste de rigidité est plus faible et, tout en s'étalant en dessous de la couche de rigidité supérieure, le dyke continue sa progression dans le milieu plus rigide.

La contrainte minimum de compression est horizontales et à être dévié, voir même s'étaler horizontalement si la contrainte minimum de compression devient verticale (*Pinel and Jaupart, 2000, 2004; Maccaferri et al., 2014*). Par exemple, un édifice volcanique a donc tendance à dévier les dykes vers sa base (*Watanabe et al., 2002; Dahm, 2000; Maccaferri et al., 2011*). A l'inverse, une dépression, un graben en contexte de rift continental par exemple, tend à dévier les dykes vers l'extérieur de la dépression (*Maccaferri et al., 2014*). *Menand et al. (2010)* ont cependant montré que l'échelle de longueur sur laquelle le dyke répondait à cette évolution du champ de contrainte dépendait de la flotabilité du magma. Notamment, à l'échelle de la croûte, la propension d'un champ de contrainte à dévier un dyke devient importante seulement si la contrainte de compression domine sur la flotabilité du magma (*Menand et al., 2010*).

En conclusion, même si ces différents facteurs jouent un rôle sur le contrôle des trajets des magmas au sein de la croûte, la densité relative du magma et de la roche encaissante et donc l'existence d'une zone de flottabilité neutre est certainement le facteur le plus déterminant dans la mise en place d'intrusions magmatiques. Le magmatisme intrusif et la question du stockage des magmas, est donc de manière générale étroitement lié à la structure en densité de la croûte elle-même.

1.2 Importance et multiples visages du magmatisme intrusif

1.2.1 Magmatisme intrusif sur Terre

Sur Terre, la composition de la croûte, et donc sa densité, est bimodale. Au niveau des océans, la croûte océanique présente une nature essentiellement basaltique avec une densité moyenne proche de 2900 kg m^{-3} . Elle est formée continuellement au niveau des dorsales océaniques et recyclée, environ 200 Ma d'année plus tard au niveau des zones de subduction. Elle est épaisse en moyenne de 6 km et couvre à elle seule 70% de la surface du globe. Au contraire, la croûte continentale, qui occupe les 30% restants, présente une composition plus évoluée et globalement andésitique avec une densité moyenne plus proche de 2700 kg m^{-3} . Elle est beaucoup plus vieille que la croûte océanique et est âgée en moyenne de 2.5 Ga, avec certaines roches d'environ 4 Ga d'années. Elle est aussi beaucoup plus épaisse que la croûte continentale; son épaisseur moyenne est de 35 km et peut excéder les 70 kilomètres sous certaines chaînes de montagnes comme l'Himalaya.

De par sa densité relativement basse, en particulier au niveau des continents, la croûte constitue un filtre efficace à la remontée des magmas en surface qui sont donc préférentiellement stockés en profondeur sous forme d'intrusions magmatiques. *Crisp* (1984) et *White et al.* (2006) estiment en effet que les volumes de lave extrudée à la surface sont relativement faibles en comparaison des volumes mis en place au sein de la croûte terrestre, i.e. 5 fois plus faibles en contexte océanique et jusqu'à 10 fois plus faibles en contexte continental. Le magmatisme intrusif apparaît donc comme un processus essentiel dans la formation de la croûte. Sur Terre, les mouvements tectoniques en son sein ainsi que l'érosion ont permis d'exposer certaines de ces intrusions à la surface. Outre leur taille, qui peut varier de quelques mètres à des centaines de kilomètres, la morphologie de ces intrusions présente une grande variabilité.

Les batholites sont de loin les plus imposants représentants de cette famille d'intrusions magmatiques se mettant en place au sein de la partie fragile de la croûte. Ils peuvent atteindre jusqu'à quelques kilomètres d'épaisseur et s'étendre sur des centaines de kilomètres. Par exemple, le batholite de la Sierra Nevada est une intrusion granitique qui s'étend sur presque la totalité de la Sierra Nevada en Californie. Des données géochronologiques sur certains de ces batholites ont montré que leur mise en place peut s'échelonner sur quelques millions d'années, un temps beaucoup plus grand que les temps raisonnables pour le refroidissement d'une chambre magmatique dans la partie fragile de la croûte (*Glazner et al.*, 2004). En effet, il est maintenant clair que la mise en place de ces gigantesques volumes de magmas se fait par incrément successifs

de petits volumes de magma se solidifiant lors de leur mise en place sur de longues échelles de temps, de 10^5 à 10^6 années (*Petford et al.*, 2000; *Glazner et al.*, 2004). Dans cette thèse, nous nous focalisons sur les mécanismes de formation et de mise en place de volumes intermédiaires de magma dans la partie fragile de la croûte continentale, à des profondeurs inférieures à 10 km.

Des études géologiques de terrain ont montré la présence de quatre grandes familles d'intrusions magmatiques de taille intermédiaire à faible profondeur. Deux de ces familles, les dykes et les bysmalites, sont discordantes, c'est-à-dire qu'elles se mettent en place perpendiculairement à la stratification naturelle de l'encaissant et deux autres, les sills et les laccolites, sont concordantes, i.e. elles se mettent en place parallèlement aux couches géologiques.

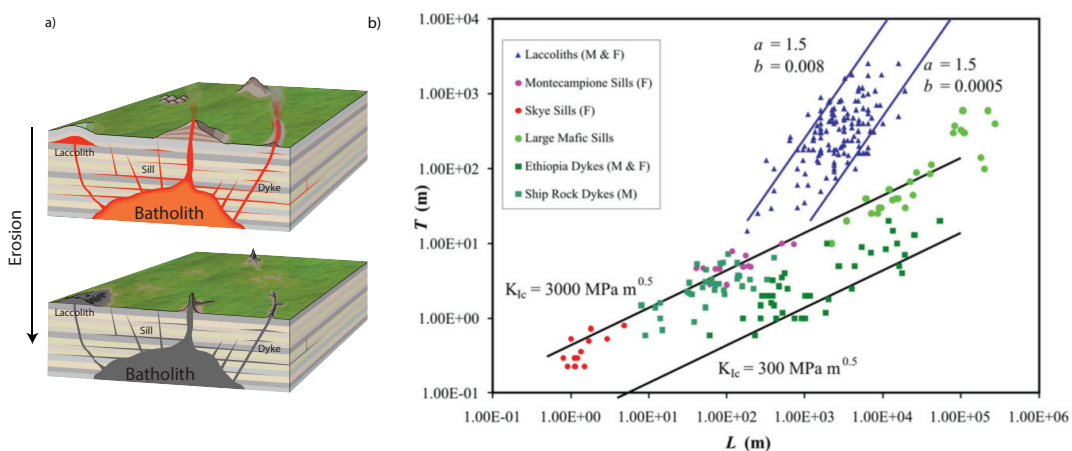


Figure 1.3: a) Différentes formes du magmatisme intrusif: batholite, dyke, sill et laccolite. Dimensions typiques pour des laccolites, dyke et sill de compositions et d'origines différentes d'après de *Cruden et al.* (2012).

- Les dykes, par lesquels remontent le magma à travers la lithosphère sont discordants et caractérisés par de faibles rapports d'aspects, de 0.01 – 0.0001 (Figure 1.3, 1.4 a) (*Rubin*, 1995; *Schultz et al.*, 2008; *Kavanagh and Sparks*, 2011). Leur épaisseur peut varier de quelques mètres à quelques centaines de mètres (*Walker*, 1989; *Krumbholz et al.*, 2014), cependant, l'épaisseur moyenne est de quelques dizaines de mètres. Les dykes de compositions felsiques sont généralement plus épais et moins longs que leurs équivalents mafiques (*Rubin*, 1995).
- Les sills, à la différence des dykes, sont concordants (Figure 1.3, 1.4 b,f). Ils se mettent en place le long de discontinuités ou de failles préexistantes, à la jonction entre deux couches sédimentaires par exemple.

Les sills aux dimensions les plus importantes répertoriés sont mafiques et peuvent attendre jusqu'à 100 km pour des épaisseurs de plusieurs centaines de mètres (*Cruden et al.*, 2012). Leurs homologues felsiques, plus rares, sont souvent de dimensions plus faibles.

- Les laccolites ont été décrits pour la première fois par *Gilbert* (1877) suite à son étude géologique des Henry Mountains, dans l'Utah aux États-Unis (Figure 1.4 c, d, e). Ils se mettent en place principalement par flexion des couches sédimentaires sus-jacentes, ce qui leur donne une forme de dôme caractéristique. Certains d'entre eux peuvent aussi être caractérisés par une forme un peu plus aplatie au centre (*Koch et al.*, 1981). *Corry* (1988) a répertorié à peu près 900 laccolites, principalement dans le nord des États-Unis. Leurs épaisseurs varient de quelques dizaines à quelques centaines de mètres et leurs rayons peuvent atteindre quelques kilomètres pour les plus gros (Figure 1.3 b). Ces laccolites se sont parfois mis en place les uns sur les autres formant une structure en forme de sapin de Noël (*Corry*, 1988). Cette géométrie est aussi observée sur l'île d'Elbe, en Italie, où un complexe de neuf laccolites, exceptionnellement bien conservé, a été étudié en détail par *Rocchi et al.* (2002).
- Les bysmalites sont d'imposants volumes cylindriques, préférentiellement composés de roche granitique, discordants (Figure 1.4 f). Ils sont notamment bordés par d'importantes failles presque verticales et peuvent atteindre quelques centaines de mètres d'épaisseur (*Johnson and Pollard*, 1973). Un exemple typique de ce type d'intrusion est le Black Mesa Bysmalite dans les Henry Mountains (200 m d'épaisseur et 1 km de large (*Morgan et al.*, 2008)).

À l'instar des batholites, de nombreuses observations de terrains proposent que ces intrusions de taille moyenne se forment aussi par incrément successifs de petits volumes de magma (*Habert and De Saint-Blanquat*, 2004; *Horsman et al.*, 2005; *Morgan et al.*, 2008) (Figure 1.5). Cependant, les mêmes études montrent aussi que ces intrusions se forment nécessairement sur de petites échelles de temps, des échelles assez faibles pour pouvoir garder un corps chaud et liquide des premières étapes du processus d'intrusion à la solidification. Au niveau du bysmalite de Black Mesa par exemple (Figure 1.4 f), *Habert and De Saint-Blanquat* (2004) ont montré l'absence de discontinuités entre les différentes couches ainsi que l'absence de métamorphisme important dans l'encaissant indiquant un temps de mise en place de moins de 100 ans. L'absence de discontinuité au sein des différents laccolites sur l'île d'Elbe supporte aussi leur formation rapide, i.e. à la suite d'une seule injection où

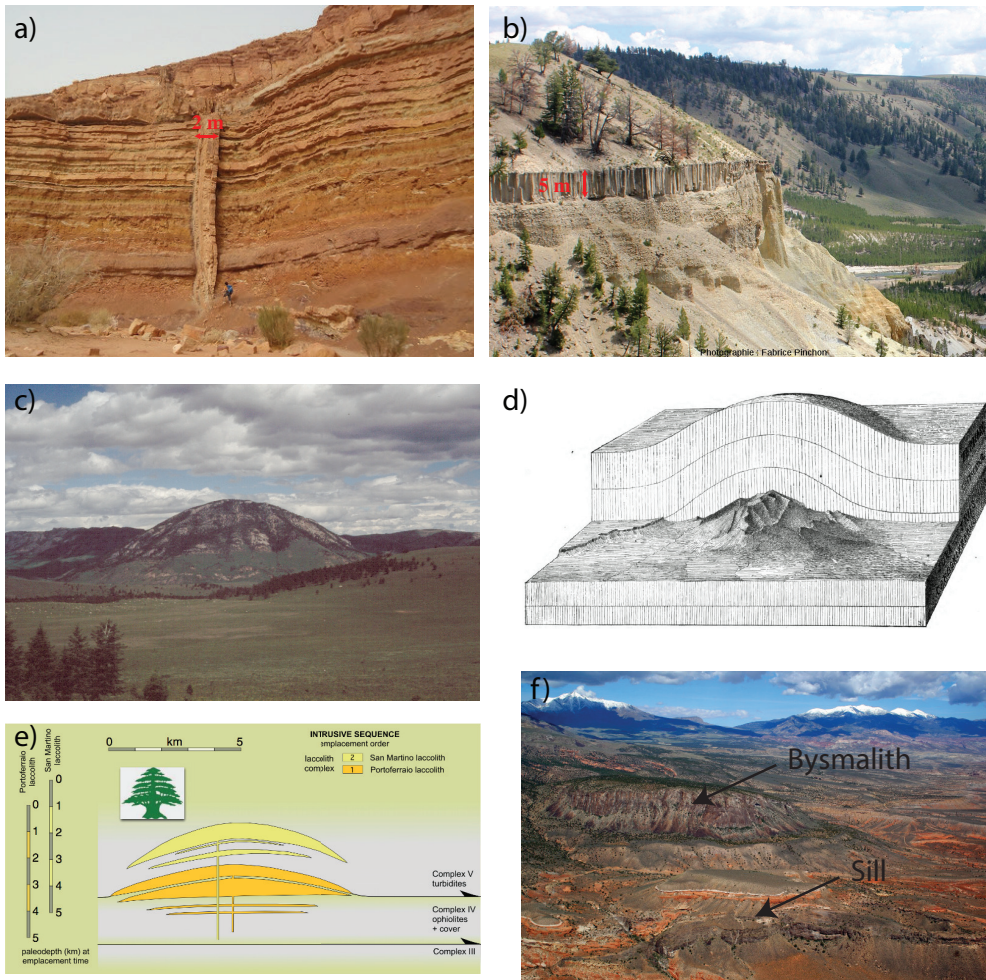


Figure 1.4: a) Dyke traversant des couches sédimentaires dans le Makhtesh Ramon, Israël; b) Sill basaltique au sein de sédiments, vallée de la Yellowstone River, parc National du Yellowstone (USA). Photographie de Fabrice Pinchon. c) Laccolite à l'érosion dans le Montana d) Schéma de l'emplacement d'un laccolite réalisé par [Gilbert \(1877\)](#). e) Schéma simplifié de la structure en arbre de noel d'un complexe de laccolite sur l'île d'Elbe, en Italie, étudiée par [Rocchi et al. \(2010\)](#). f) Intrusions à l'érosion aux alentour de la montagne Hillers, dans les Henry Mountains. On peut distinguer le Black Mesa Bysmalite au centre et le Maiden Creek sill en dessous. Photographie de Jack Share

de plusieurs injections sur un temps assez court pour que les magmas des différentes injections coalescent (*Roni et al.*, 2014).

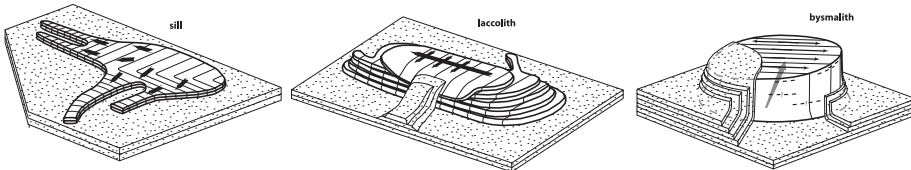


Figure 1.5: Ces diagrammes, réalisés par *Horsman et al.* (2009), montrent la structure verticale en couche de trois intrusions à l'érosion dans les Henry Mountains. De gauche à droite: le Maiden Creek Sill (Figure 1.4 f), le Trachyte Mesa Laccolite et le Black Mesa Bysmalite (Figure 1.4 f).

1.2.2 Magmatisme intrusif sur la Lune

La lune s'est probablement formée suite à l'impact d'un corps de la taille de Mars sur la proto-Terre une centaine de millions d'années après la formation de la Terre, le disque de débris produit se réaccrétant ensuite en moins d'un millier d'années pour former notre satellite (*Mizutani et al.*, 1972; *Cameron and Benz*, 1991; *Canup and Asphaug*, 2001; *Canup*, 2012). Compte tenu des quantités importantes d'énergie libérée durant le processus d'accrétion, on considère aujourd'hui que la Lune était partiellement fondu, sur une épaisseur encore débattue, suite à sa formation (*Elkins-Tanton et al.*, 2011). Le refroidissement et la lente cristallisation fractionnée de l'océan de magma lunaire aurait ensuite conduit à la formation d'une croûte primaire par flottaison des minéraux légers de plagioclase (en particulier du pôle calcique, l'anorthite) à la surface de l'océan de magma. Les éléments les plus incompatibles, en particulier les éléments producteurs de chaleur, se seraient eux concentrés dans les derniers liquides magmatiques résiduels entre la croûte et le manteau, formé, lui, principalement de cumulats d'olivine et de pyroxène (Figure 1.6).

Les échantillons recueillis lors des missions Luna/Appolo ont permis de préciser la suite de l'histoie. Après la cristallisation complète de l'océan magmatique, des instabilités gravitationnelles (les cumulats étant plus dense que la roche sous-jacente) ont conduit à un remaniement du manteau lunaire. Ceci a certainement induit de la convection au sein du manteau lunaire et a engendré sa fusion partielle formant des magmas basaltiques se mettant en place en surface (KREEP) et des roches plutoniques plus en profondeur au sein de la croûte (riche en magnésium) (*Shearer*, 2006). Cette première phase

du magmatisme lunaire est probablement contemporaine au début du grand bombardement tardif.

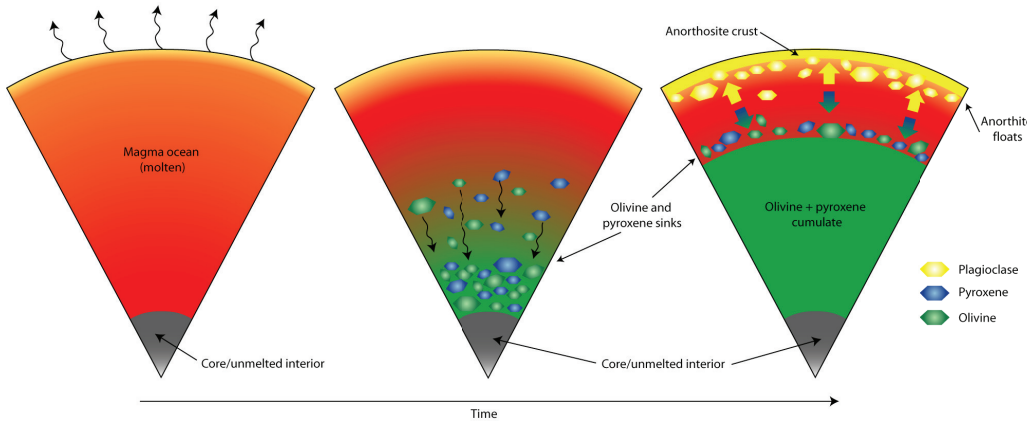


Figure 1.6: Cristallisation fractionnée de l'océan de magma et formation de la croûte primaire composé d'anorthosite. Source: LPI

Etant donné sa composition et la porosité résultante de 4 milliards d'années de bombardement météoritiques, la densité de la croûte lunaire est particulièrement faible (*Huang and Wieczorek, 2012; Han et al., 2014*). D'après les dernières estimations, rendues possibles grâce aux mesures du champ de gravité d'une résolution sans précédent obtenues par la mission GRAIL de la NASA, la densité moyenne au niveau des terres hautes serait de 2550 kg m^{-3} (*Wieczorek et al., 2013*). Ces données ont aussi permis de réévaluer à la baisse l'épaisseur de la crôute à entre 34 et 44 km en moyenne avec une tendance à être moins épaisse au niveau des mers lunaires. Elle est principalement composé d'anorthosites.

L'analyse des échantillons recueillis par les missions Luna/Appolon a aussi permis de mettre en évidence la possible présence de nombreuses

La faible densité de sa crôute et son épaisseur non négligeable ont certainement joué un rôle important sur le volcanisme lunaire. En effet, les magmas formées par fusion du manteau lunaire sont particulièrement dense, de l'ordre de 3000 kg m^{-3} (*Kiefer et al., 2012*) en lien avec leur composition basaltique riche en oxydes métalliques, en particulier en oxyde de Fer FeO et de Titane TiO_2 . Ainsi, la crôute primaire formée par cristallisation de l'océan de magma étant très légère, elle a sans aucun doute aussi été un filtre puissant à l'éruption des magmas sur la lune, leur flottabilité ne leur permettant pas d'être transporté jusqu'à la surface.

Wieczorek et al. (2001) ont ainsi confirmé que le volcanisme à la surface est

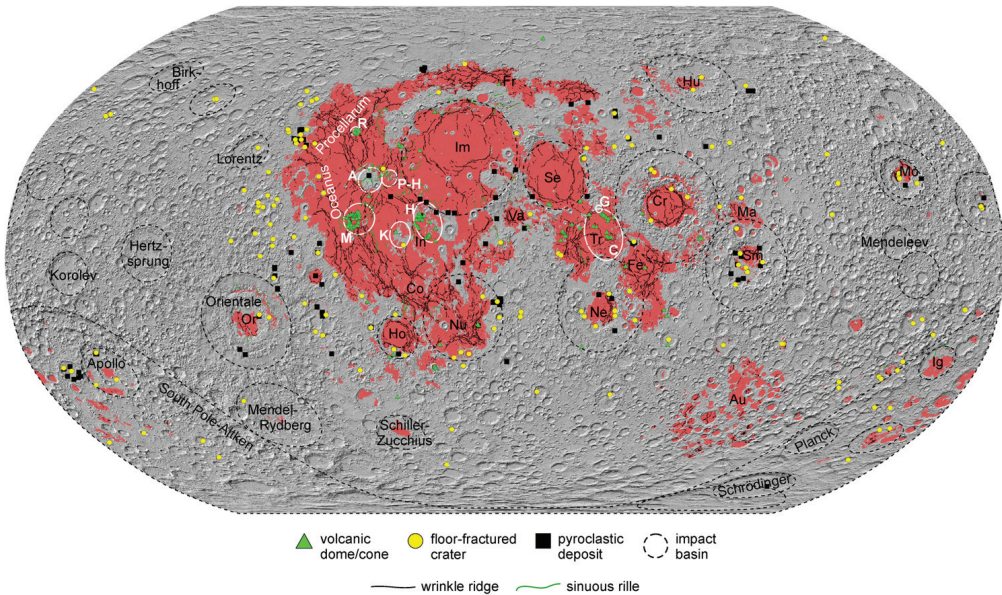


Figure 1.7: Distribution des principales structures d'origines volcaniques à la surface lunaire. Les mers lunaires apparaissent en rouge. Les bassins d'impact supérieurs à 300 km apparaissent en pointillé. Les cratères à sol fracturé sont marqués d'un triangle jaune, les dépôts pyroclastiques d'un carré noir, les dômes et cônes avec un triangle vert et les rilles sinueuses à l'aide d'une ligne verte. Les abréviations utilisées sont: Au, Australe; Co, Cognitum; Cr, Crisium; Fe, Fecundidatis; Fr, Frigoris; Ho, Humorum; Hu, Humboldtianum; Ig, Ingenii; Im, Imbrium; In, Insularum; Ma, Marginis; Mo, Mosoviense; Ne, Nectaris; Nu, Nubium; Or, Orientale; Se, Serenitatis; Sm, Smythii; Tr, Tranquillitatis; Va, Vaporum. Source: [Platz et al. \(2015\)](#)

généralement lié à l'extraction d'une partie de cette croûte de faible densité. C'est le cas par exemple des mers lunaires, qui se sont mises en place au sein de larges bassins d'impacts.

comme c'est le cas par exemple des mers lunaires qui se sont mises en place au sein de larges bassins d'impacts. [Head and Wilson \(1992\)](#) ont estimé à 50 fois plus importants les volumes de magma mis en place en profondeur que les volumes éruptifs en surface. Cependant, bien que ce rapport puisse donner de précieuses indications sur l'évolution thermique et magmatique de la lune elle-même, il est de fait très peu contraint et la part intrusive du magmatisme lunaire est encore mal connue. La détection des déformations de surface induites par la mise en place d'intrusions magmatiques au sein de la croûte apparaît donc comme une première étape visant à la meilleure caractérisation du magmatisme intrusif lunaire.

Deux manifestations principales à la surface de la lune ont été proposées comme potentiellement résultantes de la mise en place d'intrusions magmatiques au sein de la croûte lunaire: les dômes à faible pente et les cratères à sol fracturé.

- Les dômes à faible pente sont localisés en bordure ou dans les mers lunaires, principalement sur la face visible (Figure 1.8 a, b). Une quinzaine de ces dômes, possiblement d'origine intrusive, ont été récemment décrit par *Wöhler et al. (2007)*. Bien que leur morphologie s'apparente à des laccolites terrestres, ils sont de manière générale beaucoup plus étalés que ceux sur Terre; pour une même épaisseur, l'équivalent lunaire peut ainsi être deux fois plus large que son homologue terrestre.
- Les cratères à sol fracturé sont des cratères d'impacts ayant subi des déformations suite à leur formation. À peu près 200 de ces cratères ont été répertorié par *Schultz (1976a)*, principalement autour des mers lunaires (Figure 1.8 c, d, e, f). La principale caractéristique de ces cratères est leur faible profondeur par rapport à celles des cratères non déformés. En effet, certains cratères au sol fracturé peuvent être jusqu'à 2 km moins profonds que leurs homologues non déformés. Leur sol, soit en forme de dôme, soit plat séparé des bords du cratère par un imposant fossé circulaire, est systématiquement caractérisé par d'importants réseaux de fractures radiales, concentriques ou encore pentagonales (Figure 1.8 c, d, e, f). Basé sur leur profondeur, topographie et niveau de déformation, *Schultz (1976a)* a postulé l'existence de six grandes classes de déformation. La proximité de ces cratères avec les mers lunaires, ainsi que la présence de produits volcaniques au sein de certains d'entre eux, suggère qu'ils ont été déformés suite à la mise en place de magma en profondeur sous leur sol.

1.3 Caractérisation de la mise en place d'une intrusion magmatique à faible profondeur

1.3.1 Modèle statique de déformation d'une couche élastique

Bien que la morphologie et les volumes de magma puissent être récupérés, à partir d'observations directes ou de méthodes de prospection géophysique sur Terre ou via les déformations induites à la surface des autres corps telluriques du système solaire, ces informations seules ne donnent que peu d'indications

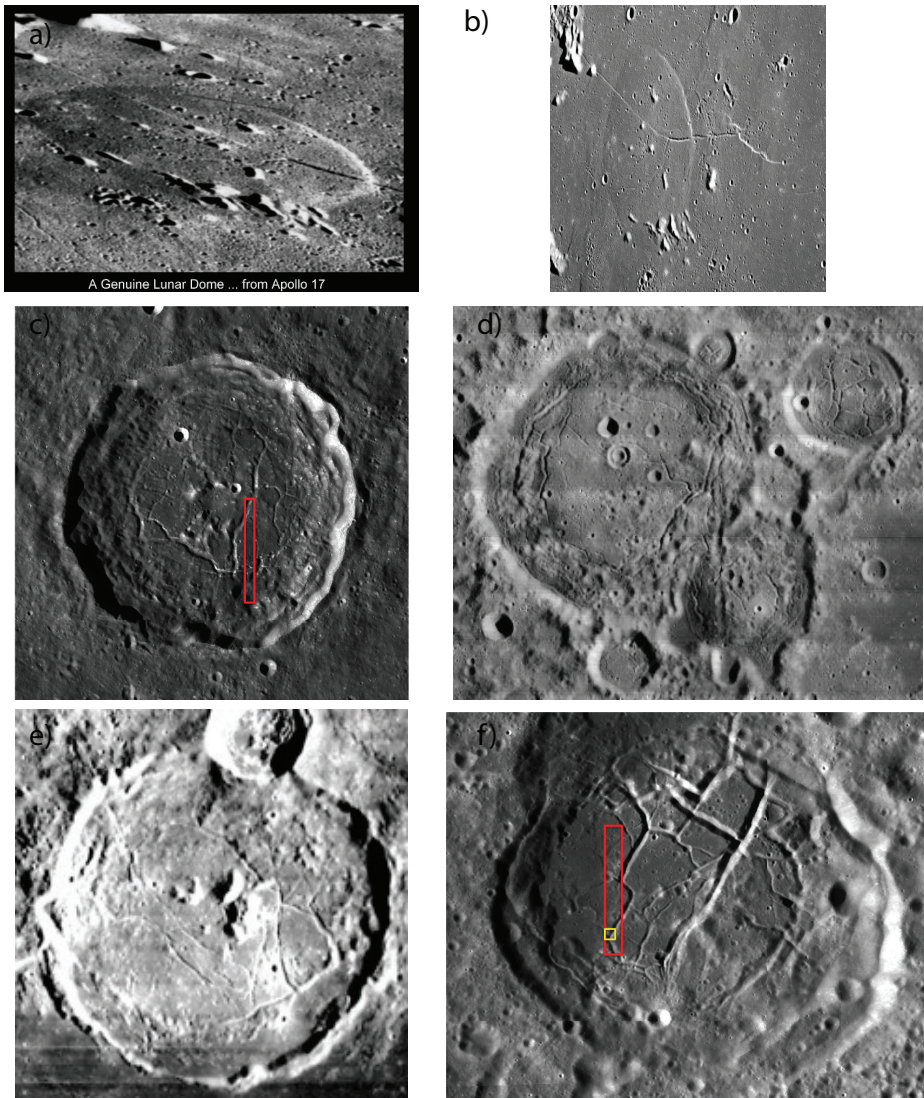


Figure 1.8: a) Dome lunaire, photo par Appolo 17 b) Apollo 15 orbital image AS15-91-12372, vue oblique du dôme Valentine. c) Cratère au sol fracturé Atlas (Classe 1). d) Cratère au sol fracturé Lavoisier (Classe 5). e) Cratère au sol fracturé Gassendi (Classe 3). f) Cratère au sol fracturé Komarov (Classe 5). Photo extraite de *Lunar Orbiter Photographic Atlas of the Moon*, NASA

sur les mécanismes de mise en place de ces intrusions magmatiques. De nombreux travaux ont ainsi été centrés sur la modélisation des processus donnant lieu à ces déformations, dans le but de mieux comprendre le mécanisme d'intrusion d'une part, mais aussi, de déduire des observations des informations sur le magma, les paramètres mécaniques de l'encaissant ou encore la profondeur de l'intrusion au moment de sa mise en place.

La propagation d'un dyke dans un milieu élastique a été beaucoup étudiée (*Lister and Kerr, 1991; Rubin, 1995*). En particulier, ? ont montré que, à l'exception de la tête du dyke où les contraintes élastiques induites par les roches encaissantes jouent un rôle important, la dynamique du magma au sein du dyke est contrôlée par un équilibre entre la flottabilité et les pertes de charge associées aux frottements visqueux sur les parois du conduit. On a vu qu'un dyke peut se transformer en sill si celui-ci rencontre sa zone de flottabilité neutre. Bien que la dynamique des dykes et des sills soit comparable à forte profondeur (*Lister and Kerr, 1991; Cruden et al., 2012*), à faible profondeur, la forme des laccolites suppose que les intrusions magmatiques se mettent en place principalement par flexion des couches sus-jacentes (*Johnson and Pollard, 1973*). Une pratique, courante en science planétaire, consiste à modéliser ces laccolites par la déformation d'une plaque mince élastique, de longueur fixée et égale à la taille de l'intrusion, soumise à une pression donnée (*Pollard and Johnson, 1973*). Dans ces modèles statiques, cette pression, donnant lieu à la déformation, est soit prise constante sur la taille de l'intrusion et égale au poids du magma (*Pollard and Johnson, 1973; Wichman and Schultz, 1996; Jozwiak et al., 2012*), soit imposée suivant un profil décrivant la perte de charge associée à un écoulement visqueux (*Kerr and Pollard, 1998; Wöhler et al., 2009*). Cependant, dans aucun des cas, cette pression n'est reliée aux paramètres de l'écoulement lui-même, i.e. volume ou taux d'injection. De plus, ces modèles ne fournissent pas un cadre théorique suffisant à la compréhension de la dynamique de l'intrusion et sont donc incapables d'expliquer la diversité des formes et des tailles observées. Enfin, ils considèrent la flexion de la couche sus-jacente comme unique pression motrice à l'écoulement, sans considérer le poids du magma lui-même, qui doit pourtant nécessairement jouer un rôle sur la mise en place de l'intrusion.

1.3.2 Inférence sur la dynamique à partir de la géométrie

En l'absence d'un modèle dynamique, la géométrie des intrusions répertoriées a souvent été utilisée pour en déduire des indications sur les processus de mise en place et de croissance de ces intrusions. Ainsi, en utilisant les données répertoriées sur les laccolites par *Corry (1988)*, *McCaffrey and Petford (1997)* proposent une loi de puissance empirique pour l'épaisseur des intrusions h_0 en

fonction de leur longueur R , $h_0 = bR^a$ où a est l'exposant de la loi de puissance et b une constante. Un exposant supérieur à l'unité indique que l'intrusion croît préférentiellement en s'épaississant tandis qu'un exposant inférieur à l'unité indique qu'elle croît plutôt par étalement.

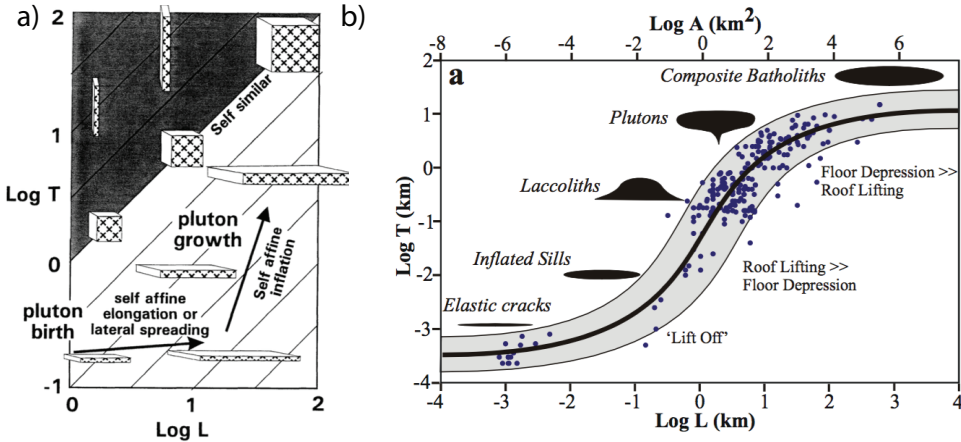


Figure 1.9: a) Schéma de la formation des laccolites en deux étapes par *McCaffrey and Petford* (1997). Épaisseurs en fonction de leur longueur de différents types d'intrusions magmatiques à différentes locations. Figure extraite de *Cruden et al.* (2012).

Les laccolites répertoriées par *Corry* (1988) montrent un exposant $a < 1$ (0.88 ± 0.1), interprété comme reflétant l'étalement de l'intrusion sur une certaine distance sous forme d'un sill avant son épaisseissement (Figure 1.9). Ce modèle est cohérent avec le modèle en deux étapes couramment accepté pour la mise en place des laccolites (*Johnson and Pollard*, 1973; *McCaffrey and Petford*, 1997). Premièrement, le magma s'étale latéralement au niveau de sa zone de flottabilité neutre, i.e. $a < 1$ jusqu'à ce qu'un sill, caractérisé par un rapport d'aspect assez large, soit formé. Ensuite, lorsque le sill est assez large, il s'épaissit par flexion des couches sus-jacentes pour former un laccolite caractérisé par une valeur de $a > 1$ (*Johnson and Pollard*, 1973; *Koch et al.*, 1981). Si la roche sus-jacente est soumise à des contraintes trop importantes, des failles se forment au niveau des bords du sill et celui-ci s'épaissit uniformément sur toute sa surface formant un bysmalite (*Corry*, 1988). Dans la continuité de l'étude de *McCaffrey and Petford* (1997), *Rocchi et al.* (2002) ont réalisé une étude détaillée du complexe intrusif de l'île d'Elbe en Italie et ont trouvé un exposant a supérieur à l'unité, i.e. ~ 1.5 , interprété comme étant la preuve de l'existence d'une phase dominée par l'épaississement de l'intrusion dans la croissance de ces laccolites.

Des modèles plus récents conçoivent plutôt la formation des laccolites par empilements successifs de sills, de grand rapport d'aspect, plutôt que par l'injection d'un seul volume de magma fini à un temps donné (*Menand*, 2011). En effet, ces modèles sont étayés par les expériences de *Kavanagh et al.* (2006) (Section 1.1.3) où il est montré qu'un sill peut se mettre en place à l'interface entre deux couches de rigidité différentes, la rigidité de la couche sus-jacente étant plus importante que celle de la couche sous-jacente. Dès lors, la mise en place d'un sill, en refroidissant, procure un environnement favorable à la mise en place d'un nouveau sill, soit au-dessus si la rigidité du sill solidifié est inférieure à celle de la roche sus-jacente, soit en dessous dans le cas contraire. Ce modèle de croissance a aussi été suggéré par de récentes études structurales et stratigraphiques, notamment au niveau des intrusions de tailles intermédiaires dans les Henry Mountains (*Horsman et al.*, 2005; *Morgan et al.*, 2008; *Horsman et al.*, 2009; *Menand*, 2011). Ce modèle, à la différence des modèles statiques exposés plus haut, a aussi l'avantage de pouvoir expliquer la structure aplatie au niveau du centre de certains laccolites (*Morgan et al.*, 2008). Cependant, ce modèle ne fournit pas de mécanisme ni ne permet d'expliquer l'origine de la loi de puissance caractéristique de la géométrie de ces intrusions. De plus, il ne permet pas de relier la géométrie finale de l'intrusion aux propriétés physiques de l'écoulement (volume, taux d'injection).

Cruden and McCaffrey (2002) ont réuni des données sur une plus grande plage de longueurs, de petits filons de quelques dizaines de mètres à des batholites de quelques centaines de kilomètres (Figure 1.9) et proposent que l'épaisseur en fonction de la longueur des intrusions magmatiques forme une distribution en forme de sigmoïde (dans une échelle logarithmique), avec une pente maximum de 1.5 caractéristique des laccolites. Cependant, aucune théorie sous-jacente ne soutient cette observation. De plus, les données de *Cruden et al.* (2012) sur les larges sills mafiques contredisent cette affirmation (Figure 1.3).

1.3.3 Discussion

Bien que de nombreux modèles ont été proposés pour essayer de rendre compte des observations, peu d'entre eux s'intéressent à la dynamique de l'intrusion qui permettrait cependant de relier la morphologie de ces intrusions aux propriétés physiques de l'écoulement (volume ou taux d'injection). Afin de comprendre la morphologie des intrusions peu profondes, il apparaît donc important de s'intéresser à la dynamique d'un tel écoulement.

Michaut (2011) a ainsi proposé un modèle théorique d'étalement d'un magma visqueux sous une couche élastique d'épaisseur constante continuellement nourrie par un conduit vertical en son centre. Ce modèle diffère des

précédents par sa capacité à traiter la dynamique même de l'intrusion ainsi que le poids du magma comme un moteur de l'écoulement. Les résultats et la capacité de ce modèle à reproduire les observations sont discutés dans le chapitre suivant.

CHAPTER 2

Isoviscous elastic-plated gravity current model for shallow magmatic intrusion

Contents

2.1	Theoretical model	22
2.1.1	Governing equation	22
2.1.2	Dimensionless equations	25
2.1.3	Need for regularization	25
2.2	Results	26
2.2.1	Bending regime	27
2.2.2	Gravity current regime	28
2.3	Application to the spreading of shallow magmatic intrusions	29
2.3.1	Observations versus predictions on Earth	29
2.3.2	Low-slope domes on the Moon	34
2.3.3	What causes the arrest of a shallow magmatic intrusion?	36
2.3.4	Discussion	37
2.4	Toward a more realistic model for shallow magmatic intrusions	38

Michaut (2011) proposed a model for the spreading of a shallow depth intermediate-size intrusion, in which magma is continuously injected at the center and is accommodated by the bending of the overlying strata. In particular, the model differs from previous ones by considering both the dynamics of the emplacement itself, in a sense that the radius is self-consistently determined, and the driving force associated with the magma weight. Both were neglected in previous models. In the original paper from *Michaut* (2011), the model was derived in both cartesian and axisymmetric geometry and the results were presented in 2D. A similar model in 2D with an additional fracture

criterion at the tip of the intrusion has been derived by *Bunger and Cruden* (2011) and *Hewitt et al.* (2014) discussed more precisely the dynamics at the contact line and the case of an elastic-plated gravity current spreading over an inclined plane. In this chapter, we present a summary of the model and the results for the spreading of an isoviscous elastic-plated gravity current over a rigid horizontal surface in an axisymmetrical geometry. Results in this geometry have been thoroughly studied by *Lister et al.* (2013) and this will constitute the reference for more elaborate models in the manuscript.

2.1 Theoretical model

The model considers an isoviscous elastic-plated gravity current, i.e. an isoviscous fluid of viscosity η_h and density ρ_m spreading beneath a thin elastic sheet of thickness d_c and above a semi infinite rigid layer (*Michaut*, 2011; *Bunger and Cruden*, 2011) (Figure 2.1). The fluid is injected continuously at the base and center of the current at a rate Q_0 through a cylindrical conduit of diameter a .

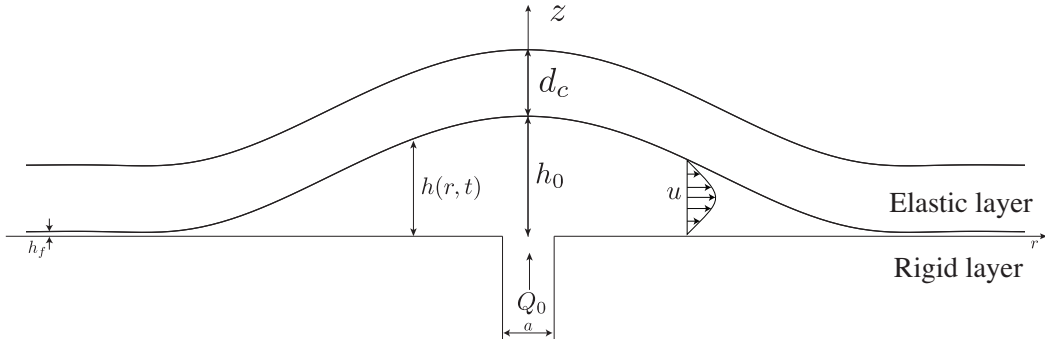


Figure 2.1: Model geometry and parameters.

2.1.1 Governing equation

Driving pressure

The intrusion develops over a length scale Λ that is much larger than its thickness H ($\varepsilon = H/\Lambda \ll 1$). In the laminar regime and in axisymmetrical coordinates (r,z) , the Navier-Stokes equations within the lubrication assumption

tion are

$$-\frac{\partial P}{\partial r} + \frac{\partial}{\partial z} \left(\eta_h \frac{\partial u}{\partial z} \right) = 0 \quad (2.1)$$

$$-\frac{\partial P}{\partial z} - \rho_m g = 0 \quad (2.2)$$

where $u(r, z, t)$ is the radial velocity, g is the standard acceleration due to gravity and $P(r, z, t)$ is the pressure within the fluid. Integration of (2.2) thus gives the total pressure $P(r, z, t)$ within the flow. When the vertical deflection $h(r, t)$ of the upper elastic layer is small compared to its thickness d_c , i.e $h \ll d_c$, we can neglect stretching of the upper layer and only consider bending stresses. Therefore, the total pressure $P(r, z, t)$ at a level z in the intrusion is the sum of four contributions: the weight of the magma and of the upper layer, the bending pressure P_b and the atmospheric pressure P_0

$$P = \rho_m g(h - z) + \rho_r g d_c + P_b + P_0 \quad (2.3)$$

where $h(r, t)$ is the intrusion thickness and ρ_r the density of the surrounding rocks. The bending pressure is given by the force per unit area that is necessary for a vertical displacement h of the thin elastic plate (*Turcotte and Schubert, 1982*)

$$P_d = D \nabla_r^4 h \quad (2.4)$$

where D is the flexural rigidity of the thin elastic layer, that depends on the Young's modulus E , Poisson's ratio ν^* and on the elastic layer thickness d_c as $D = E d_c^3 / (12(1 - \nu^{*2}))$.

Velocity field

At the contact with the elastic sheet $z = h(r, t)$, the no-slip boundary condition hold; the tangential velocity is zero and the normal velocity is the rate of height change ($\partial h / \partial t$). With \vec{n} the normal to the surface and \vec{t} the tangent, we have

$$\vec{n} \cdot \vec{u} = \frac{\partial h}{\partial t} \quad (2.5)$$

$$\vec{t} \cdot \vec{u} = 0 \quad (2.6)$$

The tangent vector is $\vec{t} = (1, \partial h / \partial r)$. However, within the lubrication assumption, the vertical component of the tangent vector scales as ε and thus, is negligible compared to the radial component. Therefore, the boundary condition (2.6) reduces to $u(r, z = h, t) = 0$. At the base of the flow, the same boundary condition holds and $u(r, z = 0, t) = 0$.

Equation (2.1) is integrated twice as a function of z using these boundary conditions and the horizontal velocity is

$$u(r, z, t) = \frac{1}{2\eta_h} \frac{\partial P}{\partial r} (z^2 - hz) \quad (2.7)$$

Injection rate

Assuming a Poiseuille flow within the cylindrical feeding conduit, the vertical injection velocity $w_i(r, t)$ and constant injection rate Q_0 are given by

$$w_i(r, t) = \begin{cases} \frac{\Delta P}{4\eta_h Z_c} \left(\frac{a^2}{4} - r^2 \right) & r \leq \frac{a}{2} \\ 0 & r > \frac{a}{2} \end{cases} \quad (2.8)$$

$$Q_0 = \frac{\pi \Delta P a^4}{128\eta_h Z_c} \quad (2.9)$$

where ΔP is the initial overpressure within the melt at $z = Z_c$.

Mass conservation

The fluid is assumed incompressible and a global statement of mass conservation gives

$$\frac{\partial h}{\partial t} + \frac{1}{r} \frac{\partial}{\partial r} \left(r \int_0^h u dz \right) = w_i. \quad (2.10)$$

Injecting (2.7) into (2.10), we find that the equation for the evolution of the thickness in time and space reads

$$\frac{\partial h}{\partial t} = \frac{\rho_m g}{12\eta_h r} \frac{\partial}{\partial r} \left(r h^3 \frac{\partial h}{\partial r} \right) + \frac{D}{12\eta_h r} \left(r h^3 \frac{\partial}{\partial r} \nabla_r^4 h \right) + w_i. \quad (2.11)$$

It is composed of three different terms on the right hand side. The first term represents gravitational spreading, i.e. spreading of the current under its own weight. The second term represents the squeezing of the flow by the upper elastic layer. Both term are negative and induces spreading. The last term represents fluid injection and is positive.

2.1.2 Dimensionless equations

Equation (2.11) is nondimensionalized using a horizontal scale Λ , a vertical scale H and a time scale τ given by

$$\Lambda = \left(\frac{D}{\rho_m g} \right)^{1/4} \quad (2.12)$$

$$H = \left(\frac{12\eta_h Q_0}{\rho_m g \pi} \right)^{1/4} \quad (2.13)$$

$$\tau = \frac{\pi \Lambda^2 H}{Q_0} \quad (2.14)$$

in which scales are chosen such that $Q_0 = \pi \Lambda^2 H / \tau$. The length scale Λ represents the flexural wavelength of the upper elastic layer, i.e. the length scale at which bending stresses and gravity equally contribute to flow. The height scale H is the thickness of a typical gravity current and the time scale τ is the characteristic time to fill up a cylindrical flow of radius Λ and thickness H at constant rate Q_0 . In addition, we can define a horizontal velocity scale $U = \Lambda / \tau = (\rho_m g H^3) / (12\eta_h \Lambda)$ and a pressure scale $\rho_m g H$.

The dimensionless equation is

$$\begin{aligned} \frac{\partial h}{\partial t} &= \frac{1}{r} \frac{\partial}{\partial r} \left(r h^3 \frac{\partial h}{\partial r} \right) + \frac{1}{r} \left(r h^3 \frac{\partial}{\partial r} \nabla_r^4 h \right) \\ &+ \mathcal{H}\left(\frac{\gamma}{2} - r\right) \frac{32}{\gamma^2} \left(\frac{1}{4} - \frac{r^2}{\gamma^2} \right) \end{aligned} \quad (2.15)$$

where \mathcal{H} is the Heaviside function and $\gamma = a/\Lambda$. γ is the dimensionless radius of the conduit and does not significantly influence the flow; it is set to 0.02 in the following (*Michaut and Bercovici, 2009; Michaut, 2011*).

2.1.3 Need for regularization

One of the main mathematical difficulty in solving equation (2.15) arises at the contact line between the rigid support and the elastic plate. Indeed, the assumption that the thickness of the fluid tends to zero at the contact line leads to divergent viscous stresses, i.e. $\eta_h \partial u / \partial z \rightarrow \infty$ and hence, the theoretical immobility of the blister (*Flitton and King, 2004; Lister et al., 2013; Hewitt et al., 2014*). This problem, known as the contact-line paradox, is a well known problem for surface-tension driven flow such as the spreading of a water droplet (*Bertozzi, 1998; Snoeijer and Andreotti, 2013*).

The formal proof has been given by *Flitton and King* (2004) and can be derived as follows. Suppose that (2.15) has a solution and the solution near

the contact line has the form

$$h \sim A(t)(R(t) - r)^\alpha \quad (2.16)$$

As $r \rightarrow R(t)$, the bending term dominates the gravitational term and (2.15) reduces to

$$\frac{\partial h}{\partial t} = \frac{1}{r} \frac{\partial}{\partial r} \left(rh^3 \frac{\partial}{\partial r} \nabla_r^4 h \right). \quad (2.17)$$

Injecting (2.16) into (2.17) and keeping only the leading powers of $R - r$ gives

$$\begin{aligned} \frac{\partial R}{\partial t} A \alpha (R - r)^{\alpha-1} + \frac{\partial A}{\partial t} (R - r)^\alpha &= A^4 \alpha (\alpha - 1)(\alpha - 2) \\ &\quad (\alpha - 3)(\alpha - 4)(\alpha - 5)(R - r)^{4\alpha-6}. \end{aligned}$$

The time derivative is locally dominated by its convective part at the tip, the second term on the left is small compared to the first and therefore, by equating the exponent of $R - r$, we obtain $\alpha = 5/3$ and then

$$\frac{\partial R}{\partial r} = -\frac{280}{243} A^3. \quad (2.18)$$

Given that $A > 0$, this shows that (2.15) can only have solutions with retreating contact line ($dR/dt < 0$) but not with advancing contact line ($dR/dt > 0$) (*Lister et al.*, 2013; *Flitton and King*, 2004).

To mitigate this problem, one common approach is to add a thin prewetting film, with thickness h_f such that $h \rightarrow h_f$ as $r \rightarrow \infty$ (Figure 2.1). While the solution will depend upon the prewetting film thickness h_f and will not show any convergence properties when $h_f \rightarrow 0$, we will see that the dependence in h_f is weak and the difference between different values for h_f will be relatively small (*Lister et al.*, 2013; *Hewitt et al.*, 2014). Unless otherwise specified, we will often consider $h_f = 5 \cdot 10^{-3}$ in the manuscript which represents the smallest length scale with a physical meaning (Section 2.3.1).

2.2 Results

For a small prewetting film thickness, i.e. $h_f \ll 1$, the numerical resolution of the equation (2.15) shows two or three asymptotic spreading regimes: a bending regime where gravity is negligible, a viscous gravity current regime where bending is negligible or a regime of lateral propagation if the weight of the magma at the center compensates for the initial overpressure (*Michaut*, 2011; *Bunger and Cruden*, 2011; *Lister et al.*, 2013). In the following, we present the shape of the flow as well as scaling laws that predict the evolution of the thickness at the center $h_0(t)$ and the radius $R(t)$ in each regime.

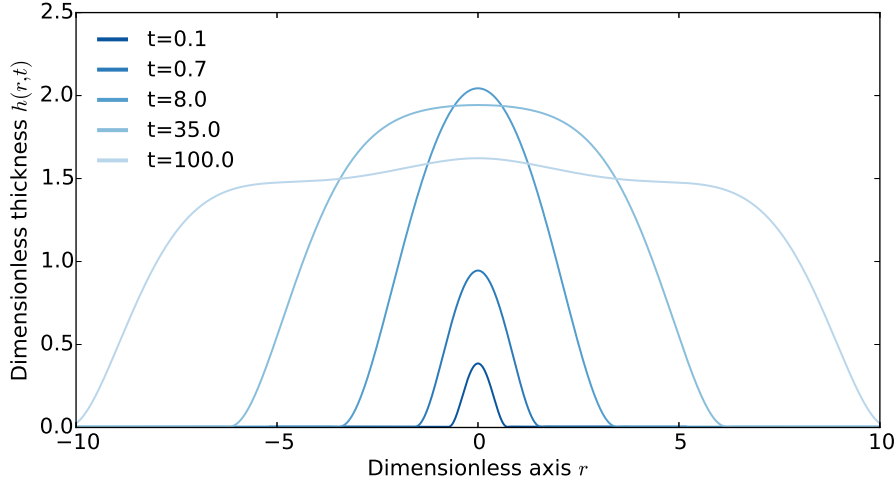


Figure 2.2: Shape of the flow, i.e. thickness $h(r, t)$ as a function of the radial axis r at five different times indicated on the plot. Variables are dimensionless and one needs to multiply by the characteristic scales (thickness, length or time given by (2.13), (2.12) or (2.14)) to obtain dimensional values. For $t < 10$, the intrusion is in the bending regime whereas for $t > 10$ the intrusion is in the gravity current regime.

2.2.1 Bending regime

At early times, when $R \ll \Lambda$, gravity is negligible and the dynamics of the spreading is governed by the bending of the upper layer. In addition, if $h_0 \ll \sigma$, the overpressure ΔP driving the flow is much larger than the weight of the blister at the center and the injection rate can be considered constant.

In that case, the spreading is very slow and the interior has uniform dimensionless pressure $P = \nabla_r^4 h$. The flow is bell-shaped and its thickness is given by

$$h(r, t) = h_0(t) \left(1 - \frac{r^2}{R^2(t)}\right)^2 \quad (2.19)$$

with $h_0(t)$ the thickness of the intrusion at the center (Figure 2.2, $t < 10$) (*Michaut, 2011; Lister et al., 2013*). In this regime, *Lister et al. (2013)* have shown that the spreading is controlled by the propagation of a peeling by bending wave at the intrusion front with dimensionless velocity c

$$c = \frac{\partial R}{\partial t} = h_f^{1/2} \left(\frac{\kappa}{1.35}\right)^{5/2} \quad (2.20)$$

where $\kappa = \partial^2 h / \partial r^2$ is the dimensionless curvature of the interior solution. Using the propagation law (2.20) and the form of the interior solution (2.19),

they find that the radius and the height of the intrusion evolve following

$$R(t) = 2.2h_f^{1/22}t^{7/22} \quad (2.21)$$

$$h_0(t) = 0.7h_f^{-1/11}t^{8/22} \quad (2.22)$$

where the numerical pre-factors match our simulations as well as the results of *Lister et al.* (2013) (Figure 2.3). The bell-shaped morphology of the flow in this regime is very close to the dome-shaped morphology of solidified laccoliths (Figure 1.4 c, d, e) (*Michaut*, 2011).

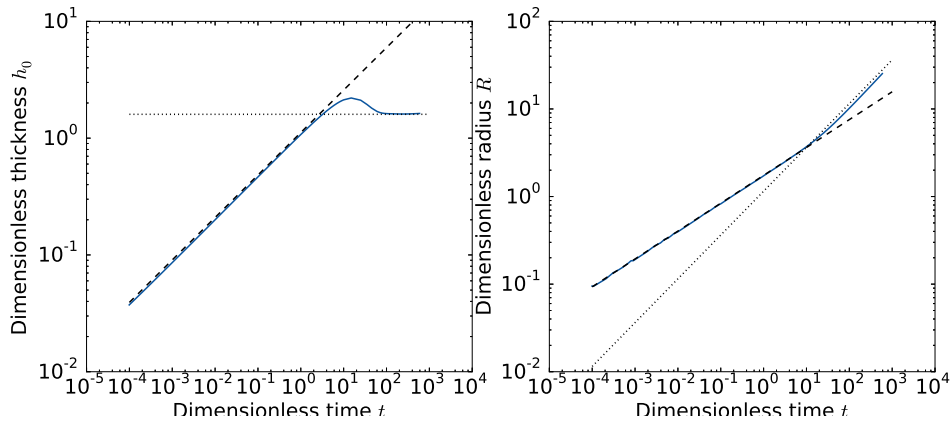


Figure 2.3: Left: Dimensionless thickness at the center h_0 versus dimensionless time t for different dimensionless numbers σ indicated on the plot. The dashed-line represents the scaling law in the bending regime $h_0(t) = 0.7h_f^{-1/11}t^{8/22}$ and the dotted line in the gravity regime $h_0(t) = 1.6$. Right: Dimensionless radius R versus dimensionless time t for the same dimensionless number σ . The dashed-line represents the scaling law in the bending regime $R(t) = 2.2h_f^{1/22}t^{7/22}$ and the dotted line in the gravity regime $R(t) = 1.2t^{1/2}$.

2.2.2 Gravity current regime

In contrast, when the radius R becomes larger than $\sim 4\Lambda$, the weight of the intrusion becomes dominant over the bending terms. The dimensionless pressure is given by the hydrostatic pressure $P = h$ and the intrusion enters a classical viscous gravity current regime where bending terms only affect the solution near the intrusion edge (Figure 2.2, $t > 10$) (*Huppert*, 1982a; *Michaut*, 2011; *Lister et al.*, 2013). In this second regime, while the thickness tends to be a constant, the radius evolves as $t^{1/2}$ (Figure 2.3). The flow is

2.3. Application to the spreading of shallow magmatic intrusion

therefore characterized by a small aspect-ratio h_0/R and a constant thickness disk-like morphology close to the one shown by large mafic sills (Figure 1.4 a).

In between the bending and gravity regime, *Lister et al.* (2013) also describe a short intermediate regime where the peeling by bending continues to control the propagation but where, due to the increasing effect of gravity, the flow shows an interior flat-topped region (Figure 2.2, $t = 38$). This flat-topped morphology is also observed for many laccoliths (*Koch et al.*, 1981; *Bunger and Cruden*, 2011).

Therefore, the model is able to reproduce the variety of shapes of intermediate scale magmatic intrusions: from the dome shape and flat topped morphology of laccolith to the disk-like morphology of large mafic sills. In the following, we quantitatively compare the model predictions to some observations on terrestrial planets.

2.3 Application to the spreading of shallow magmatic intrusions

2.3.1 Observations versus predictions on Earth

Observations

Corry (1988) has made an extensive catalog of 900 laccoliths across the world. In particular, *Corry* (1988) provides the thickness and the radius of 168 laccoliths. For 40 of them, he gives an estimate for the intrusion depth. These laccoliths, who are mainly felsic in composition, show thicknesses that range from 100 meters to 1 km with radii in between 1 and 10 km (Figure 2.5 a). While most of the data are located in the United State ($\sim 90\%$), the different laccoliths are widely spread among the territory and variations in the flow parameters between different laccoliths are most likely to be important.

In addition to the data from *Corry* (1988), we also consider in this study the data provided by *Rocchi et al.* (2002) on 9 laccoliths nested in a christmas tree structure at Elba Island, Italy (Figure 2.4). The detailed mapping and reconstruction of tectonic history made by *Rocchi et al.* (2002) provides for the parameters of each intrusive layer in the laccolith complex. In addition, for this dataset, each laccolith is part of a larger intrusive system, and hence variability of the model parameters should be limited, except for the overlying elastic layer thickness, assumed to be the intrusion depth in the model, whose variation between laccoliths is given by *Rocchi et al.* (2002). The dispersion is much smaller for this dataset; the radius ranges from 800 m to 5 km and

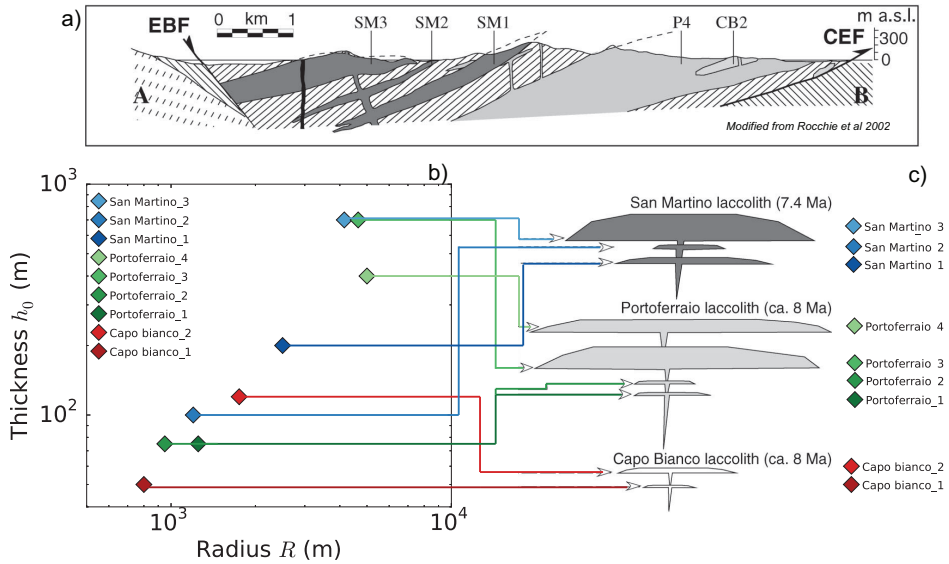


Figure 2.4: a): Cross section of western and central Elba Island where we can see the christmas tree structure of the laccolith complex and the main laccolith units visible at the surface. b) Thickness versus radius of the different laccolith units. c) Sketch of the corresponding location of these laccoliths within the christmas tree structure shortly after their formations. Figure modified from *Rocchi et al.* (2002).

the thickness from 50 m to 700 m (Figure 2.5 a).

Finally, we also show the morphology of 25 large mafic sills whose thicknesses and radii are given by *Cruden et al.* (2012) (Figure 2.5 a). In order to account for the intrinsic scale of different settings for each intrusion and compare them to the model, the data have first to be nondimensionalized using characteristic values for each intrusion parameters and also their depth, when absent from the catalog.

Range of values for the parameters

In terrestrial settings, magma density ρ_m mainly depends on its composition and varies between 2500 kg m^{-3} for felsic magmas to 2900 kg m^{-3} for more mafic magmas. Reported intrusion depths vary from 180 to 2200 m for laccoliths in *Corry* (1988) and from 1.9 to 3.7 km for laccoliths at Elba Island. Hence, for a Young's modulus value of 10 GPa, the characteristic length scale Λ varies between $\sim 1 \text{ km}$ and $\sim 7 \text{ km}$ for laccoliths. The density does not affect much the value of Λ and the characteristic length scale for large mafic sills, whose depths are not reported in *Cruden et al.* (2012) and set to 1.5 km,

2.3. Application to the spreading of shallow magmatic intrusion³³

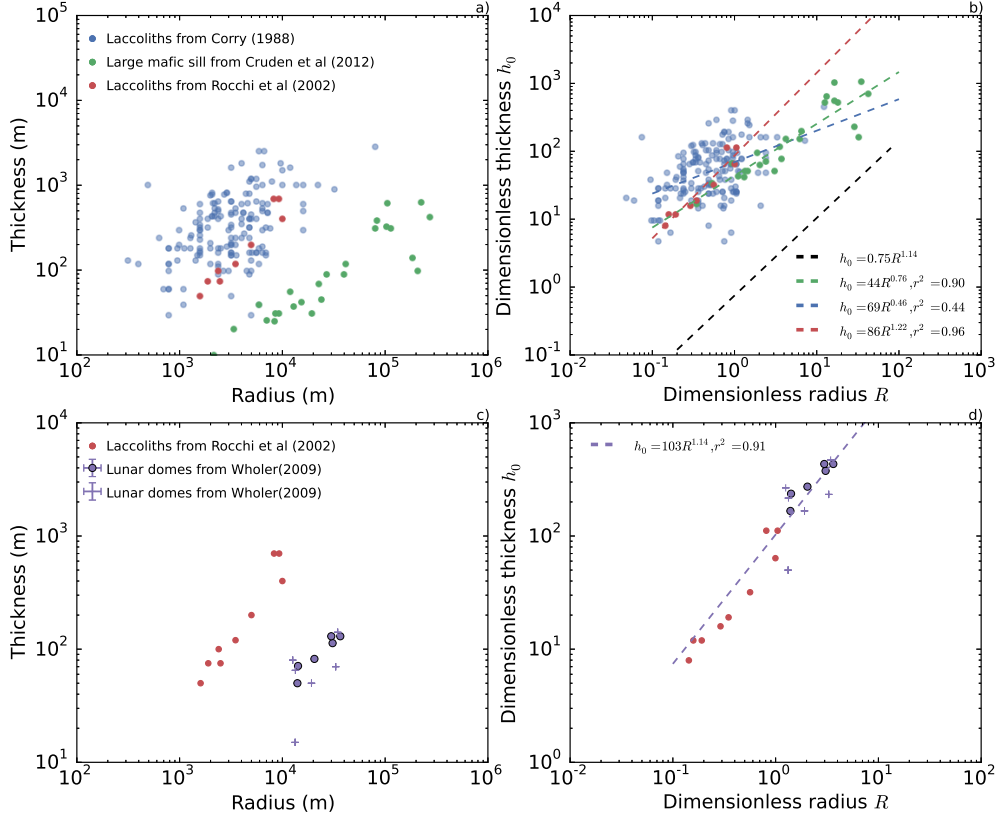


Figure 2.5: a) Thickness at the center h_0 (m) versus radius R (m) for magmatic intrusions from different datasets indicated on the plot. b) Dimensionless thickness as a function of dimensionless radius. Characteristic thickness and length are calculated from (2.13) and (2.12). Dashed lines: predicted scaling law from the simulations (black) and best fit for the power law $h_0 = aR^b$ for each dataset obtained from a linear least-square regression in log-log space. r^2 is the squared of the correlation coefficient, i.e. Pearson product-moment correlation coefficient which gives an indication on the goodness of the fit; 1 is total positive correlation and 0 is no correlation. We use $\rho_m = 2500 \text{ kg m}^{-3}$, $Q_0 = 10 \text{ m}^3 \text{ s}^{-1}$ and $\eta_h = 10^6 \text{ Pa s}$ for felsic laccoliths and $\rho_m = 2900 \text{ kg m}^{-3}$, $Q_0 = 10 \text{ m}^3 \text{ s}^{-1}$ and $\eta_h = 10^2 \text{ Pa s}$ for large mafic sills. Unless the intrusion depth is given by the dataset, we use $d_c = 1500 \text{ m}$. $g = 9.81 \text{ m s}^{-2}$. c) and d), same plots but where we compared the laccoliths from [Rocchi et al. \(2002\)](#) to a set of low-slope lunar domes given by [Wöhler et al. \(2009\)](#). Lunar domes are nondimensionalized using $g = 1.62 \text{ m s}^{-2}$, $\rho_m = 2900 \text{ kg m}^{-3}$, $Q_0 = 10 \text{ m}^3 \text{ s}^{-1}$, $\eta_h = 1 \text{ Pa s}$ and d_c , which is not given in the dataset, is set to 1500 m. Purple dots correspond to morphometry reevaluated with the LOLA instrument topography and crosses to the original data. In all cases, the Poisson's ratio is $\nu^* = 0.25$.

is equal to ~ 3 km.

On Earth, laccoliths are generally formed by relatively evolved lavas that may have differentiated from primitive magma in deep crustal magma chambers, located some 5 to 15 km below the surface. The overpressures driving magma ascent are typically 20 to 50 MPa (*Stasiuk et al.*, 1993; *Barmin et al.*, 2002), which gives overpressure gradients of $\sim 10^3$ Pa m $^{-1}$. Lava viscosity at eruption temperature η_h mainly depends on its composition and water content; close to its liquidus temperature, it can vary from 10^2 Pa s for mafic lavas to 10^6 Pa s for felsic lavas (*Shaw*, 1972; *Giordano et al.*, 2008; *Whittington et al.*, 2009; *Chevrel et al.*, 2013). However, *Wada* (1994) shows that the dyke width tends to increase with viscosity to the power 1/4 (*Kerr and Lister*, 1995) and overall, the injection rate Q_0 should be similar for different magma compositions. Based on common effusion rate for lava flows on Earth, we take $Q_0 \sim 0.1 - 100$ m 3 s $^{-1}$ (*Pieri and Baloga*, 1986; *Harris et al.*, 2000; *Castro et al.*, 2013; *Tuffen et al.*, 2013). The height scale H thus varies between ~ 1 to 10 m for felsic laccoliths and ~ 0.1 and 1 m for large mafic sills.

Table 2.1: Range of values for the model parameters

Parameters	Symbol	Earth	Moon	Unit
Depth of intrusion	d_c	0.2 – 2.7	0.5 – 1.5	km
Young's Modulus	E	10	10	GPa
Poisson's ratio	ν^*	0.25	0.25	
Gravity	g	9.81	1.62	m s $^{-2}$
Magma density	ρ_m	2500 – 2900	2900	kg m $^{-3}$
Magma viscosity	η_h	$10^2 - 10^6$	1 – 10	Pa s
Feeder dyke width	a	1 – 100	10	m
Depth of the melt source	Z_c	1 – 10	500	km
Initial overpressure	ΔP	20 – 50	50	MPa
Injection rate	Q_0	0.1 – 100	$1 - 10^4$	m 3 s $^{-1}$
Characteristic scales	Symbol	Earth	Moon	Unit
Height scale	H	0.1 – 10	0.1 – 1	m
Length scale	Λ	1 – 7	2.2 – 12	km
Time scale	τ	$10^{-3} - 100$	$10^{-3} - 10$	years

The model also considers a thin prewetting film of thickness h_f whose meaning in the application to the spreading of laccolith is unclear. In particular, the model shows no convergence when h_f tends to zero (*Lister et al.*, 2013)

and therefore, the thickness h_f might be linked to some structural length scale at the front of the laccolith or to the natural imperfection of the flow geometry. For the purpose of the application, we choose a film thickness of 1 mm, i.e. the minimum length scale with physical significance for the spreading of laccoliths which give a dimensionless h_f that varies between 10^{-2} and 10^{-4} . In the following, we set h_f to 10^{-3} unless otherwise specified.

Dimensionless data and comparison with the model

Each magmatic intrusion unit is made dimensionless using its characteristic length scale Λ , which depends upon the intrusion depth, and its characteristic height scale, which is taken as either $H = 6$ m for felsic laccoliths or $H = 0.6$ m for large mafic sills (Figure 2.5). When the intrusion depth is not provided, we use $d_c = 1.5$ km. First, the dimensionless radius of laccoliths at Elba Island and 95% of those from [Corry \(1988\)](#) are smaller than 4 consistent with their arrest in the bending regime. The prediction of the model for the evolution of the thickness h_0 of the current as a function of its radius R can be easily derived from the scaling laws (2.22) and (2.21) and should follow

$$h_0 \sim 0.3h_f^{-1/7}R^{8/7} \quad (2.23)$$

in agreement with the power law relationship $h_0 = bR^a$ initially proposed by [McCaffrey and Petford \(1997\)](#) (Section 1.3.2). To characterize the mean trend in each population, we use a linear least-square regression in log-log space to obtain a value for the coefficient a and b that best fit the observations. We found $h_0 = 86R^{1.22}$ for the laccoliths at Elba island which is very close to $R^{1.14}$ predicted by the model (Figure 2.5, $r^2 = 0.96$). Actually, the geometry of these laccoliths is not well known and probably not perfectly axisymmetric. [Hewitt et al. \(2014\)](#) found that for a two dimensional flow, $h_0 \propto h_f^{-1/7}L^{10/7}$ where L is the half-length of the flow ($10/7 \sim 1.43$). The best fit value for the coefficient a then nicely inserts between the expected values for the two geometries as noted by [Michaut \(2011\)](#). In contrast, the prediction for the coefficient b is much smaller than the value derived from the observations. Even for $h_f = 10^{-2}$, which would be an upper bound for this parameter, the model predict $b = 0.15$, which is three orders of magnitudes smaller than the observations (Figure 2.5). Matching the data to the model will require using a viscosity η_h for the magma abnormally high, i.e. $\eta_h \sim 10^{15}$ Pa s or unreasonable injection rate, i.e. $Q_0 \sim 1 \text{ km}^3 \text{ s}^{-1}$.

The best fit power law relationship for the laccoliths from [Corry \(1988\)](#) is $h_0 = 85R^{0.62}$ (Figure 2.5, $r^2 = 0.54$). In that case, the exponent a is smaller than one and does not agree with the model. This value for a , slightly smaller than the value calculated directly on the data by [McCaffrey and Petford](#)

(1997), was interpreted as reflecting the two-stage growth process historically invoked for the formation of laccoliths (Section 1.3.2). However, the dispersion in the data is much more important than in the observation from *Rocchi et al.* (2010) and is not taken into account in the nondimensionalization which assumes the same parameters for all the different laccoliths. It might explain the discrepancy between the model prediction and the observation in this example.

Half of the large mafic sills show dimensionless radius smaller than $R = 4$, not consistent with their arrest in the gravity current regime (Figure 2.5). It might suggest that these mafic sills have intruded shallower into the crust; for instance, for $d_c = 250$ m, the characteristic length scale for the mafic sill is smaller $\Lambda = 800$ m and 95% of the population show dimensionless radius larger than 4. Nevertheless, their dimensionless thickness, which should tend to a constant of order $O(1)$ according to the model, is much larger than the expected value and increases with the radius R . For a gravity current in a two dimensional geometry, the thickness is indeed expected to increase with the length of the sill, but as $L^{1/4}$ (*Michaut*, 2011), i.e. with an exponent much smaller than the value of 0.76 found for the coefficient a for large mafic sills (Figure 2.5, $r^2 = 0.9$). Therefore, the model predictions hardly reconcile with the observations for large mafic sills.

2.3.2 Low-slope domes on the Moon

Observations

On the Moon, 13 elongated low-slope domes, located around the lunar maria, have been recently identified as potentially intrusive domes (*Wöhler et al.*, 2007, 2009). *Wöhler et al.* (2009) used an image-based 3D reconstruction approach which relies on a combination of photocalinometry and shape from shading techniques to determine the morphometric properties of each of these lunar domes which results in a 10% error estimate on the intrusion thickness. These data have since been updated by Mélanie Thiriet, an under graduate student in our laboratory, who used the high resolution of the topography obtained from the 64 ppm, ~ 450 m/pixel (*Zuber et al.*, 2009), LOLA gridded topography data to reevaluate the thickness and the radius of some of these potentially intrusive lunar domes (Figure 2.5).

Range of values for the parameters

Given the basalt composition of most lunar rocks brought back from the lunar maria by the Apollo missions, the lunar magmas are more likely to be mafic in composition and we use $\rho_m = 2900$ kg m⁻³ for the lava density. Intrusion

2.3. Application to the spreading of shallow magmatic intrusion³⁷

depths, which are not given by *Wöhler et al.* (2009), should vary between 500 m and 5 km and in the following, we set $d_c = 1.5$ km for all the lunar domes. Therefore, on the Moon, the larger lava density and the smaller gravity leads to length scale 1.5 times larger than terrestrial ones. For instance, using $E = 10$ GPa and $d_c = 1.5$ km, the characteristic length scale for a lunar intrusion is ~ 5 km and 3.3 km for a terrestrial laccolith.

The source of magma in the lunar interior is poorly constrained and more likely to be deeper than on Earth; most of the mare basalt are thought to be a product of melting initiated deep in the lunar mantle, deeper than 400 km (*Shearer*, 2006). Using the same value for the initial driving pressure, $\Delta P = 50$ MPa, unless lunar magmas are likely to be more mafic and contain less volatiles implying smaller driving pressure, and a depth of 500 km for the magma source region, the overpressure gradient is only of 100 Pa m^{-1} . However, reported run out distance for some lava flows in the lunar maria are very large and implies higher effusion rate than on Earth, i.e. $Q_0 = 10^3 - 10^8 \text{ m}^3 \text{ s}^{-1}$ (*Crisp and Baloga*, 1990; *Zimbelman*, 1998). Mare basalts, which have lower concentration in alkalies than terrestrial basalts, should also have a lower viscosity (*Zimbelman*, 1998). We take $\eta_h = 1 \text{ Pa s}$ and for injection rate between $Q_0 = 1 - 10^4 \text{ m}^3 \text{ s}^{-1}$, the typical height scale for lunar domes varies between 0.5 and 1.5 m.

Predictions versus observations

After nondimensionalization, the lunar low-slope domes show dimensionless radius smaller than 4 consistent with their arrest in the bending regime (Figure 2.5). In addition, if we use $Q_0 = 10 \text{ m}^3 \text{ s}^{-1}$ and the values of the parameters listed above to calculate the height scale H , they are almost perfectly aligned with the terrestrial laccolith from Elba Island (Figure 2.5) (*Michaut*, 2011). Indeed, the best fit for the power law $h_0 = bR^{8/7}$ for all the observations, lunar domes + Elba Island laccoliths, is $h_0 = 103R^{1.14}$ with a high correlation coefficient $r^2 = 0.9$. Given that the same intrusion depth has been arbitrarily chosen for all intrusions, the fit is surprisingly accurate. Therefore, the isoviscous elastic-plated gravity current model supports the intrusive origin of the lunar domes described by *Wöhler et al.* (2009) and their arrest in the bending regime. In addition, it is able to explain the difference between Earth laccolith and lunar intrusive domes (*Michaut*, 2011).

2.3.3 What causes the arrest of a shallow magmatic intrusion?

The model shows promising results in reproducing the overall morphology of terrestrial laccoliths but lacks of a predictive criteria for their arrest. Fracturation is generally considered as the limiting mechanism for the spreading of magmatic intrusions and in the following, we consider fracturation as a possible mechanism for the arrest of magmatic intrusions into the bending regime.

As the flow length increases, the pressure in the intrusion eventually decreases to the critical value equal to the pressure necessary for fracturing the tip. In that case, fracturing at the tip might limit spreading and trigger the arrest of a laccolith in the bending regime. The stress intensity factor K_I for a mode I fracture and a uniformly loaded crack situated close to a boundary (i.e., $d \ll R$) can be approximated by (*Dyskin et al.*, 2000; *Bunger and Emmanuel*, 2005)

$$K_I = K_M M_0 d_c^{-3/2} \quad (2.24)$$

where $K_M = 1.932$ is a constant and M_0 is the bending moment at the crack tip given by

$$M_0 = -D \left(\frac{\partial^2 h}{\partial r^2} + \frac{\nu^*}{r} \frac{\partial h}{\partial r} \right) \Big|_{r=R(t)}. \quad (2.25)$$

Once K_I reaches the fracture toughness limit K_c , which is in the range $\sim 1-10$ MPa m $^{1/2}$ for crustal rocks and a mode I fracture (*Lister and Kerr*, 1991), fracturing at the tip will limit the lateral extent of the intrusion.

Injecting the dimensional scaling law for the thickness h_0 as a function of the radius R (2.23) into the predicted flow shape in the bending regime (2.19) gives the flow shape as a function of the radius $R(t)$ for a fractured-limited flow in the bending regime is

$$h(r, t) = 0.6 H^{8/7} \Lambda^{-8/7} R(t)^{8/7} \left(1 - \frac{r^2}{R^2(t)} \right)^2. \quad (2.26)$$

Injecting this expression into (2.25) and (2.24) and inverting for the radius, one can then found that the critical dimensionless radius R_{cr} for the laccolith is

$$R_{cr} \sim \frac{0.4 E^{7/6} H^{4/3} K_m^{7/6}}{K_c^{7/6} \Lambda^{7/3}} d^{7/4} \quad (2.27)$$

which, in terms of the parameters, reads

$$R_{cr} \sim 2.2 E^{7/12} K_m^{7/6} Q_0^{1/3} \eta_h^{1/3} g^{1/4} \rho_m^{1/4} K_c^{-7/6} \quad (2.28)$$

2.3. Application to the spreading of shallow magmatic intrusion39

and therefore mainly depends in the fracture toughness of the encasing rocks. One can calculate that for typical crustal and magma parameters for terrestrial laccoliths (Section 2.3) and the largest reported value for the parameter $K_c = 10 \text{ MPa m}^{1/2}$, the dimensionless critical radius is equal to ~ 60 and therefore, still much larger than the dimensionless transition radius between the bending and gravity regime $R = 4$. Therefore, while fracturation might explain the arrest for large mafic sills, it does not provide a sufficient mechanism for the arrest of laccoliths.

2.3.4 Discussion

Historical models for intermediate scale magmatic intrusions consider that the main phase of laccolith growth and spreading require a two-stage process: horizontal spreading of a sill followed by vertical inflation when the sill has grown horizontally enough so that the magma has enough leverage on the overlying layer to begin to bend them upward (*Johnson and Pollard, 1973; Koch et al., 1981*). More recent models instead proposed that these intrusions form as a series of sub-horizontally staked magma sheets (*Morgan et al., 2008; Menand, 2011*). While both models are able to account for several geological observations, they both lack a physical description of the intrusion process and are then not able to explain the solidified morphology of these magmatic intrusions in terms of flow parameters (injection rate, volume) at the time of emplacement.

Michaut (2011) has developed a new approach to model intermediate-scale intrusions such as sills, laccoliths or bysmaliths through a dynamic elastic-plated gravity current model that considers both the bending and the own weight of the magma as driving the flow. This model shows promising results in predicting the variety of shapes of intermediate scale magmatic intrusions; from the dome shape of laccolith to the disk-like morphology of large mafic sill. It allows to relate the laccolith morphology to the crustal and magma physical properties, and more importantly, to the injection rate. The prediction of the model, especially the exponent of the thickness to radius power law relationship, also fits the variability in the laccolith units at Elba Island, hence providing for a physical explanation for the observed laccolith morphology. In addition, the model is also consistent with a two-stage growth process; first, the lateral growth of a sill and then, when the conditions of applicability for the model are met, i.e. $R > h_0$ and $R \gtrsim d_c$, spreading and thickening occur simultaneously (*Michaut, 2011*). Finally, the model shows promising results in explaining the discrepancy between terrestrial laccolith and low-slope lunar domes on the Moon. Therefore, it can be used to assess the intrusive origin of intrusive candidates on other terrestrial planets.

However, other questions remain open. First, we have shown that the model hardly accounts for the absolute final value for both the thickness and the radius of these laccoliths and that reconciliating predictions and observations requires abnormally high magma viscosity. In addition, we show that the model does not offer a satisfactory explanation for the increase in large mafic sill thickness with their diameter. Finally, we also show that fracturation is not likely to stop a magmatic intrusion in the bending regime. Therefore, other mechanisms not taken into account in the model of *Michaut* (2011), are required to understand the final morphology of these magmatic intrusions.

2.4 Toward a more realistic model for shallow magmatic intrusions

In this manuscript, we propose to explore two important mechanisms that have been neglected until now and will certainly influence the emplacement of shallow magmatic intrusions in the crust of terrestrial planets: the effect a temperature-dependent rheology for the magma and the effect of an overburden characterized by a non-constant thickness.

The former has already shown important implications for the cooling of lava domes (*Bercovici*, 1994; *Bercovici and Lin*, 1996; *Balmforth and Craster*, 2004; *Garel et al.*, 2014). Indeed, the viscosity of magma can vary by several orders of magnitudes during cooling (*Shaw*, 1972; *Lejeune and Richet*, 1995). As the fluid cools, its composition and crystal content change which, in turn, modifies the viscosity and the dynamics of the flow itself. The first part of the manuscript deals with this matter and try to better understand the dynamics of a cooling elastic-plated gravity current. In particular, in chapter 3, we propose a model for the cooling of an elastic-plated gravity current with a temperature-dependent viscosity and isothermal boundary conditions. This model is next further refined to account for the heating of the wall rocks and compared to the observation in chapter 4.

The second part of the manuscript addresses the second point and in particular, the problem of crater-centered intrusions with application to the endogenous deformations observed at lunar floor-fractured craters. Indeed, these impact craters on the Moon show important deformations that might be related to the emplacement of a shallow magmatic intrusion below their floor (*Schultz*, 1976a). Chapter 5 presents the theoretical model and its application to the deformations observed at floor-fractured craters. Then, chapter 6 takes the study of floor-fractured craters one step further by looking at the gravitational signature of lunar floor-fractured craters in the light of the model predictions.

This thesis, closely combining theoretical models and observations, expands and generalizes the model of *Michaut* (2011) exposed in this chapter, and sheds light on the final morphology of shallow magmatic intrusions on one side and on the origin of lunar floor-fractured craters on the other side.

Part II

Evolution thermique des intrusions magmatiques à faible profondeur

CHAPTER 3

Elastic-plated gravity current with temperature-dependent viscosity

*This chapter is part of a paper submitted for publication to Journal of Fluid Mechanics (JFM) untitled: **Elastic-plated gravity current with temperature-dependent viscosity**.*

Contents

3.1	Introduction	44
3.2	Theory	46
3.2.1	Formulation	46
3.2.2	Pressure	47
3.2.3	Injection rate	47
3.2.4	Heat transport equation	48
3.2.5	Equation of motion	50
3.2.6	Dimensionless equations	51
3.2.7	Further simplifications	53
3.2.8	Summary of the equations	54
3.2.9	Preliminary results for an isothermal flow	55
3.3	Evolution in the bending regime	56
3.3.1	Thermal structure for an isoviscous flow, effect of Pe	56
3.3.2	Thickness and temperature profile, effect of ν	57
3.3.3	Evolution of the thickness and the radius	59
3.3.4	Characterization of the thermal anomaly	61
3.3.5	Effective viscosity of the current	62
3.3.6	Note on the effect of crystallization	64
3.4	Evolution in the gravity current regime	66
3.4.1	Thermal structure for an isoviscous flow, effect of Pe	66
3.4.2	Thickness and temperature profile, effect of ν	66
3.4.3	Evolution of the thickness and radius	69

3.4.4	Characterization of the thermal anomaly	70
3.4.5	Effective viscosity of the current	71
3.4.6	Note on the effect of crystallization	73
3.5	Different evolutions with bending and gravity	74
3.6	Summary and conclusion	78

Temperature-dependent elastic-plated gravity currents have numerous applications in nature, from shallow magmatic intrusions to the flow of melt-water below an ice sheet. We develop the general equations for an elastic-plated gravity current with a temperature-dependent viscosity for constant influx conditions. We show that the coupling between the thermal structure and the flow itself results in important deviations from the isoviscous case. In particular, the bending and gravity asymptotic regimes, characteristic of the isoviscous case, both split into three phases: a first 'hot' isoviscous phase, a second phase where the flow effective viscosity and thickness drastically increase and a third 'cold' isoviscous phase. These three phases are controlled by the extent of the thermal anomaly, for which we develop analytical scaling laws. The effective flow viscosity is governed by the local thermal state at the current tip in the bending regime while it is the average flow viscosity in the gravity regime. In the end, the complete evolution of such an elastic-plated gravity current depends on its thermal state at the transition between the bending and gravity regimes. We provide a phase diagram which predicts the different evolution scenarios as a function of the flow Peclet number and viscosity contrast.

3.1 Introduction

Elastic-plated gravity currents involve the spreading of viscous material beneath an elastic sheet. The applications range from the emplacement of lava in the shallow crust (*Michaut, 2011; Bunger and Cruden, 2011*) and melt-water drainage below ice sheet (*Das et al., 2008; Tsai and Rice, 2010*) in geological setting to the manufacture of flexible electronics and microelectromechanical systems (MEMS) in engineering (*Hosoi and Mahadevan, 2004*).

When the thickness of the flow is small compared to its extent, lubrication approximation applies and the study of elastic-plated gravity currents resumes to the study of a sixth order, non-linear partial differential equation (*Michaut, 2011; Lister et al., 2013; Hewitt et al., 2014*). However, the assumption that the thickness of the fluid tends to zero at the contact line leads

to divergent viscous stresses, and hence, a regularization condition is needed at the front (*Flitton and King*, 2004; *Lister et al.*, 2013; *Hewitt et al.*, 2014). One common approach is to add a thin prewetting film of fluid, thus avoiding the requirement for any boundary conditions at the contact line (*Lister et al.*, 2013; *Hewitt et al.*, 2014).

The dynamics of the spreading has been described in an axisymmetric geometry for a Newtonian fluid with constant viscosity (*Michaut*, 2011; *Lister et al.*, 2013; *Thorey and Michaut*, 2014) and show two distinct regimes of evolution. First, gravity is negligible and the peeling of the front is driven by bending of the overlying layer; the interior is bell-shaped, the radius evolves as $t^{8/22}$ and the thickness as $t^{7/22}$. When the radius becomes larger than 4Λ , where Λ is the flexural wavelength of the upper layer, the weight of the current becomes dominant over the bending terms and the flow enters a gravity current regime (*Huppert*, 1982a). In this regime, the thickness profile develops a flat top with bent edges, the radius evolves as $t^{1/2}$ while the thickness tends to a constant. Different analogue experiments of isoviscous flows confirm these theoretical results (*Dixon and Simpson*, 1987; *Lister et al.*, 2013).

However, in many real geological settings, the isothermal/isoviscous assumption are not valid. For instance, the viscosity of magmas, produced by partial melting of the upper mantle, can vary by several orders of magnitude (*Shaw*, 1972; *Lejeune and Richet*, 1995). Therefore, as the fluid flows, it cools down, its composition and crystal content change which, in turn, modifies the viscosity and the dynamics of the flow. Several studies have shown that, in a gravity current, this coupling between the cooling and the flow itself results in important deviations from the isoviscous case (*Bercovici*, 1994; *Bercovici and Lin*, 1996; *Balmforth and Craster*, 2004; *Garel et al.*, 2014).

In this paper, we examine how the spreading of an elastic-plated gravity current is affected by the cooling itself. In particular, we consider the problem of an elastic-plated gravity current whose viscosity depends on temperature according to a prescribed rheology $\eta(T)$. This gives rise to a set of two coupled non-linear equations that we solve numerically. We study the flow thermal structure and its effect on the dynamics through the rheology in each regime separately. In both regimes, we identify different “thermal” phases of propagation that we characterize by different scaling laws.^x

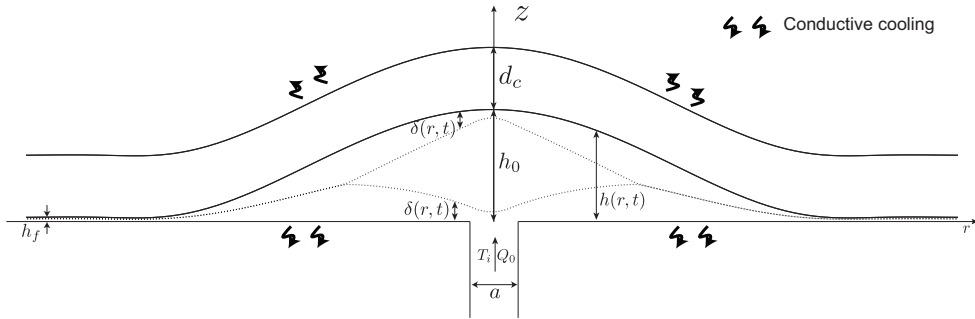


Figure 3.1: Model geometry and parameters. The vertical scale is exaggerated.

3.2 Theory

3.2.1 Formulation

We model the axisymmetric flow of fluid below an elastic layer of constant thickness d_c and above a semi infinite rigid layer (Figure 3.1). The assumption that the thickness of the fluid $h(r, t)$ tends to zero at the contact line leads to divergent viscous stresses and to the theoretical immobility of the current (*Flitton and King, 2004*). To avoid problem at the contact line, we consider a thin pre-wetting film of thickness h_f (*Lister et al., 2013*) (Figure 3.1).

The fluid is injected continuously at the base and center of the current at a constant rate Q_0 through a conduit of diameter a . The hot fluid is intruded at temperature T_i and cools through the top and bottom by conduction in the surrounding medium, whose temperature is considered constant and equal to T_0 . In using a fixed temperature at the flow boundary, we essentially assume that the fluid is bounded by a medium with infinite thermal conductivity.

As it cools, the viscosity of the fluid increases following a prescribed temperature-dependent rheology $\eta(T)$ given by

$$\eta(T) = \frac{\eta_h \eta_c (T_i - T_0)}{\eta_h (T_i - T_0) + (\eta_c - \eta_h)(T - T_0)} \quad (3.1)$$

where η_h and η_c are the viscosities of the hottest and coldest fluid at the temperature T_i and T_0 respectively (*Bercovici, 1994*). Although this rheology is largely simplified, the inverse dependence of viscosity on temperature captures the essential behavior of a viscous fluid, i.e. the viscosity variations are

the largest where the temperature is the coldest (*Shaw*, 1972; *Marsh*, 1981; *Lejeune and Richet*, 1995; *Giordano et al.*, 2008).

3.2.2 Pressure

The intrusion develops over a length scale Λ that is much larger than its thickness H ($\Lambda \gg H$). In the laminar regime and in axisymmetrical coordinates (r, z) , the Navier-Stokes equations within the lubrication approximaton are

$$-\frac{\partial P}{\partial r} + \frac{\partial}{\partial z} \left(\eta(T) \frac{\partial u}{\partial z} \right) = 0 \quad (3.2)$$

$$-\frac{\partial P}{\partial z} - \rho_m g = 0 \quad (3.3)$$

where $u(r, z, t)$ is the radial velocity, ρ_m the fluid density, g the standard acceleration due to gravity and $P(r, z, t)$ the pressure within the fluid. Integration of (3.3) gives the total pressure $P(r, z, t)$ within the flow. When the vertical deflection $h(r, t)$ of the upper elastic layer is small compared to its thickness d_c , i.e $h \ll d_c$, we can neglect stretching of the upper layer and only consider bending stresses. Therefore, the total pressure $P(r, z, t)$ at a level z in the current is the sum of three contributions: the weight of the magma and of the upper layer and the bending pressure

$$P = \rho_m g(h - z) + \rho_r g d_c + D \nabla_r^4 h \quad (3.4)$$

where $h(r, t)$ is the flow thickness, ρ_r the density of the surrounding rocks and D is the flexural rigidity of the thin elastic layer, that depends on Young's modulus E , Poisson's ratio ν^* and on the elastic layer thickness d_c as $D = E d_c^3 / (12(1 - \nu^*))$.

3.2.3 Injection rate

Assuming a Poiseuille flow within the cylindrical feeding conduit, the vertical injection velocity $w_i(r, t)$ and injection rate Q_0 are given by

$$w_i(r, t) = \begin{cases} \frac{\Delta P}{4\eta_h Z_c} \left(\frac{a^2}{4} - r^2 \right) & r \leq \frac{a}{2} \\ 0 & r > \frac{a}{2} \end{cases} \quad (3.5)$$

$$Q_0 = \frac{\pi \Delta P a^4}{128 \eta_h Z_c} \quad (3.6)$$

where ΔP is the initial overpressure within the melt at $z = Z_c$.

3.2.4 Heat transport equation

3.2.4.1 Local energy conservation

In the laminar regime and in axisymmetrical coordinates (r, z) , the local energy conservation equation within the lubrication assumption is

$$\frac{D}{Dt} (\rho_m C_{p,m} T + \rho_m L(1 - \phi)) = k_m \frac{\partial^2 T}{\partial z^2} \quad (3.7)$$

where $T(r, z, t)$ is the fluid temperature and ρ_m , k_m and $C_{p,m}$ are the density, thermal conductivity and specific heat of the fluid. Here, we also account for energy release by crystallization of the fluid, which is a non negligible source of heat for magmas; $\phi(r, z, t)$ is the crystal fraction in the melt and L the latent heat of crystallization. In this model, the crystals are considered only as a source/sink of energy as they melt/form during flow emplacement. In particular, the physical properties of the fluid are not modified by the presence of crystals.

Following a common approximation, we assume that the crystal fraction is a linear function of temperature over the melting interval

$$\phi = \frac{T_L - T}{T_L - T_s} \quad (3.8)$$

where T_S and T_L are the solidus and liquidus temperatures of the magma (*Hort*, 1997; *Michaut and Jaupart*, 2006). In addition, we assume that the fluid is injected at its liquidus temperature, i.e. $T_L = T_i$ and, for simplicity, that the solidus temperature is equal to the surrounding rock temperature $T_S = T_0$. With these approximations, the local energy equation (3.7) resumes to

$$\frac{\partial T}{\partial t} + u \frac{\partial T}{\partial r} + w \frac{\partial T}{\partial z} = \frac{St}{St + 1} \kappa_m \frac{\partial^2 T}{\partial z^2} \quad (3.9)$$

where $u(r, z, t)$ and $w(r, z, t)$ are the radial and vertical fluid velocities, $St = (C_{p,m}(T_i - T_0)) / L$ is the Stefan number and κ_m is the fluid thermal diffusivity $\kappa_m = k_m / (\rho_m C_{p,m})$. We use an integral balance method to solve the heat transport equation (3.9). This theory is based on the integral-balance method of heat-transfer theory of *Goodman* (1958), in which the vertical structure of the temperature field is represented by a known function of depth that approximates the expected solution.

3.2.4.2 Integral balance solution for the temperature $T(r, z, t)$

Following *Balmforth and Craster* (2004), we model the cooling of the flow through the growth of two thermal boundary layers: one growing downward

from the top and a second growing upward from the base. As we consider homogeneous thermal properties for the surrounding rocks, we assume that the two thermal boundary layers grow symmetrically and have the same thickness $\delta(r, t)$ (Figure 3.1). We use the following approximation for the vertical temperature profile $T(r, z, t)$

$$T = \begin{cases} T_b - (T_b - T_0)(1 - \frac{z}{\delta})^2 & 0 \leq z \leq \delta \\ T_b & \delta \leq z \leq h - \delta \\ T_b - (T_b - T_0)(1 - \frac{h-z}{\delta})^2 & h - \delta \leq z \leq h \end{cases} \quad (3.10)$$

where $T_b(r, t)$ is the temperature at the center of the flow. The integral balance solution in (3.10) assumes a symmetry around $z = h/2$ and a decrease of the temperature in the two thermal boundary layers down to the surrounding rock temperature T_0 (*Balmforth and Craster, 2004*). In addition, it assumes a uniform temperature T_b in between the thermal boundary layers. As the fluid is injected at temperature T_i , we have $T_b(r, t) = T_i$ as long as $\delta < h/2$ (Figure 3.1). However, if the two thermal boundary layers connect, then $\delta = h/2$ and $T_b \leq T_i$. This profile assures the continuity of the temperature and heat flux within the flow.

3.2.4.3 Integral balance equation

We begin by integrating the local energy conservation equation (3.9) separately over the two thermal boundary layers. The integration over the bottom thermal layer, i.e. from the base, $z = 0$ to a level $z = \delta$ gives

$$\begin{aligned} & \frac{\partial}{\partial t} (\delta(\bar{T} - T_b)) + \frac{1}{r} \frac{\partial}{\partial r} (r\delta(\bar{u}\bar{T} - \bar{u}T_b)) + \delta \left(\frac{\partial T_b}{\partial t} + \bar{u} \frac{\partial T_b}{\partial r} \right) \\ &= -\frac{\kappa_m}{1 + St} \frac{\partial T}{\partial z} \Big|_{z=0} + w_i(T_i - T_b) \end{aligned} \quad (3.11)$$

where the bars indicate the vertical average over the bottom thermal boundary layer

$$\bar{f} = \frac{1}{\delta} \int_0^\delta f dz,$$

which will be determined once the horizontal flow velocity is derived, $T_b(r, t)$ is the temperature at $z = \delta$, $w_i(r)$ is the vertical injection velocity and we have used the nullity of the thermal gradient at $z = \delta$ and the local mass conservation

$$\frac{1}{r} \frac{\partial ru}{\partial r} + \frac{\partial w}{\partial z} = 0. \quad (3.12)$$

The integration over the top thermal layer, i.e., from the level, $z = h - \delta$ to the top $z = h$ gives

$$\begin{aligned} & \frac{\partial}{\partial t} (\delta(\bar{T} - T_b)) + \frac{1}{r} \frac{\partial}{\partial r} (r\delta(\bar{u}\bar{T} - \bar{u}T_b)) + \delta \left(\frac{\partial T_b}{\partial t} + \bar{u} \frac{\partial T_b}{\partial r} \right) \\ &= \frac{\kappa_m}{1 + St^{-1}} \frac{\partial T}{\partial z} \Big|_{z=h} \end{aligned} \quad (3.13)$$

where, in addition to the local mass conservation (3.12) and the fact that the thermal gradient at $z = h - \delta$ is equal to zero, we have used the kinematic boundary condition in $z = h(r, t)$

$$\frac{\partial h}{\partial t} + u \frac{\partial h}{\partial r} = w. \quad (3.14)$$

Therefore, the heat balance equation, i.e. the heat equation (3.9) integrated over the flow thickness, is obtained by adding (3.11) and (3.13). Using (3.10) to derive the conductive fluxes, we finally obtain

$$\begin{aligned} & \frac{\partial}{\partial t} (\delta(\bar{T} - T_b)) + \frac{1}{r} \frac{\partial}{\partial r} (r\delta(\bar{u}\bar{T} - \bar{u}T_b)) + \delta \left(\frac{\partial T_b}{\partial t} + \bar{u} \frac{\partial T_b}{\partial r} \right) \\ &= -\frac{2\kappa_m}{(1 + St^{-1})} \frac{(T_b - T_0)}{\delta} + \frac{w_i}{2} (T_i - T_b). \end{aligned} \quad (3.15)$$

3.2.5 Equation of motion

A global statement of mass conservation gives

$$\frac{\partial h}{\partial t} + \frac{1}{r} \frac{\partial}{\partial r} \left(r \int_0^h u dz \right) = w_i. \quad (3.16)$$

To obtain an equation for the flow thickness, we first note that the chosen vertical structure of the temperature field (3.10) is symmetric around $h/2$, and thus, because the boundary condition are the same at $z = 0$ and $z = h$, the viscosity and velocity u possess the same symmetry. Taking advantage of this symmetry, we integrate once (3.2) using $\frac{\partial u}{\partial z} \Big|_{z=h/2} = 0$ to get

$$\frac{\partial u}{\partial z} = \frac{1}{\eta(z)} \frac{\partial P}{\partial r} \left(z - \frac{h}{2} \right). \quad (3.17)$$

Using no-slip boundary conditions at the top and the bottom of the flow, i.e. $u(r, z = 0, t) = u(r, z = h, t) = 0$, (3.16) can be rewritten as

$$\frac{\partial h}{\partial t} = \frac{1}{r} \frac{\partial}{\partial r} \left(r \int_0^h \frac{\partial u}{\partial z} z dz \right) + w_i. \quad (3.18)$$

Finally, injecting (3.17) into (3.18) gives the equation for the flow thickness evolution in axisymmetric coordinates

$$\frac{\partial h}{\partial t} = \frac{1}{r} \frac{\partial}{\partial r} \left(r \left(\rho_m g \frac{\partial h}{\partial r} + D \frac{\partial}{\partial r} (\nabla_r^4 h) \right) \left(\int_0^h \frac{1}{\eta(y)} \left(y - \frac{h}{2} \right) y dy \right) \right) + u. \quad (3.19)$$

In addition, integration of (3.17) using the no-slip boundary condition at the base of the flow gives

$$u(r, z, t) = \frac{\partial P}{\partial r} \int_0^z \frac{1}{\eta(y)} \left(y - \frac{h}{2} \right) dy. \quad (3.20)$$

where

$$\frac{1}{\eta(y)} = \frac{1}{\eta_c} + \frac{\eta_c - \eta_h}{\eta_h \eta_c} \frac{T(y) - T_0}{T_i - T_0}. \quad (3.21)$$

$T(y)$ being a polynom, integrals in (3.19), (3.20) as well as the averaged quantities \bar{u} and $\bar{u}T$ over the thermal boundary layer in (3.15) can easily be calculated.

3.2.6 Dimensionless equations

We use the characteristic temperature interval $\Delta T = T_i - T_0$ to nondimensionalize temperatures. The dimensionless integral balance approximation (3.10) becomes

$$\theta(z) = \begin{cases} \Theta_b \left(1 - (1 - \frac{z}{\delta})^2 \right) & 0 \leq z \leq \delta \\ \Theta_b & \delta \leq z \leq h - \delta \\ \Theta_b \left(1 - (1 - \frac{h-z}{\delta})^2 \right) & h - \delta \leq z \leq h \end{cases} \quad (3.22)$$

where $\theta(r, z, t)$ is the dimensionless temperature and $\Theta_b = \frac{T_b - T_0}{T_i - T_0}$. Finally, equations (3.15) and (3.19) are nondimensionalized using a horizontal scale Λ , a vertical scale H and a time scale τ given by

$$\Lambda = \left(\frac{D}{\rho_m g} \right)^{1/4} \quad (3.23)$$

$$H = \left(\frac{12 \eta_h Q_0}{\rho_m g \pi} \right)^{1/4} \quad (3.24)$$

$$\tau = \frac{\pi \Lambda^2 H}{Q_0} \quad (3.25)$$

where Λ represents the flexural wavelength of the upper elastic layer (*Michaut, 2011*), H the characteristic thickness of an isoviscous constant flux gravity current with viscosity η_h (*Huppert, 1982b*) and τ the characteristic time to fill up

a cylindrical flow of radius Λ and thickness H at a constant rate Q_0 . In addition, we can define a horizontal velocity scale $U = \Lambda/\tau = (\rho_m g H^3) / (12\eta_h \Lambda)$ and a pressure scale $\rho_m g H$.

The dimensionless equations are

$$\frac{\partial h}{\partial t} = \frac{12}{r} \frac{\partial}{\partial r} \left(r \left(\frac{\partial h}{\partial r} + \frac{\partial}{\partial r} (\nabla_r^4 h) \right) I_1(h) \right) + w_i \quad (3.26)$$

$$\begin{aligned} \frac{\partial}{\partial t} (\delta(\bar{\theta} - \Theta_b)) &= -\frac{1}{r} \frac{\partial}{\partial r} (r \delta(\bar{u}\bar{\theta} - \bar{u}\Theta_b)) - \delta \left(\frac{\partial \Theta_b}{\partial t} + \bar{u} \frac{\partial \Theta_b}{\partial r} \right) \\ &- 2Pe^{-1} St_m \frac{\Theta_b}{\delta} + \frac{w_i}{2} (1 - \Theta_b) \end{aligned} \quad (3.27)$$

$$w_i = \frac{32}{\gamma^2} \left(\frac{1}{4} - \frac{r^2}{\gamma^2} \right) \text{ if } r < \gamma/2, \quad w_i = 0 \text{ if } r \geq \gamma/2 \quad (3.28)$$

$$u(r, z, t) = 12 \left(\frac{\partial h}{\partial r} + \frac{\partial}{\partial r} (\nabla_r^4 h) \right) I_0(z) \quad (3.29)$$

with

$$I_0(z) = \int_0^z (\nu + (1 - \nu)\theta(y)) \left(y - \frac{h}{2} \right) dy \quad (3.30)$$

$$I_1(z) = \int_0^z (\nu + (1 - \nu)\theta(y)) \left(y - \frac{h}{2} \right) y dy \quad (3.31)$$

and where γ , Pe , St_m and ν are the four dimensionless numbers that control the dynamics of the flow

$$\gamma = \frac{a}{\Lambda} \quad (3.32)$$

$$Pe = \frac{H^2}{\kappa_m \tau} \quad (3.33)$$

$$St_m = \frac{C_{p,m} (T_i - T_0)}{C_{p,m} (T_i - T_0) + L} \quad (3.34)$$

$$\nu = \frac{\eta_h}{\eta_c} \quad (3.35)$$

γ is the dimensionless radius of the conduit, it does not significantly influence the flow and is set to 0.02 in this study (*Michaut and Bercovici*, 2009; *Michaut*, 2011); Pe is the Peclet number which compares the vertical diffusion of heat to the horizontal advection in the interior; St_m is a modified Stefan number which represents the ratio of sensible heat between solidus and liquidus to the total energy of the fluid at the liquidus temperature and ν is the maximum viscosity contrast, i.e. the ratio between the hottest and coldest viscosity.

3.2.7 Further simplifications

3.2.7.1 Heat equation

In the end, the heat balance equation (3.27) can reduce to

$$\frac{\partial}{\partial t} (\delta(\bar{\theta} - 1)) + \frac{1}{r} \frac{\partial}{\partial r} (r\delta(\bar{u}\theta - \bar{u})) = -2Pe^{-1}St_m \frac{\Theta_b}{\delta} \quad (3.36)$$

Indeed, if the thermal boundary layers exist, $\Theta_b = 1$, δ is the variable quantity and (3.27) directly reduces to (3.36). In contrast, if the thermal boundary layers merge, $\delta = h/2$ and the variable quantity is Θ_b . In this case, the heat balance equation (3.27) reduces to

$$\frac{\partial h\bar{\theta}}{\partial t} + \frac{1}{r} \frac{\partial}{\partial r} (rh\bar{u}\theta) - \Theta_b \left(\frac{\partial h}{\partial t} + \frac{1}{r} \frac{\partial}{\partial r} (rh\bar{u}) \right) = -8St_mPe^{-1} \frac{\Theta_b}{h} + w_i \quad (3.37)$$

which, by using (3.16), rewrites

$$\frac{\partial h\bar{\theta}}{\partial t} + \frac{1}{r} \frac{\partial}{\partial r} (rh\bar{u}\theta) = w_i - 8St_mPe^{-1} \frac{\Theta_b}{h}. \quad (3.38)$$

Equation (3.38) also corresponds to (3.36) when $\delta = h/2$.

Following *Balmforth and Craster* (2004), we rewrite (3.36) using a new variable $\xi = \delta(1 - \bar{\theta})$

$$\frac{\partial \xi}{\partial t} + \frac{1}{r} \frac{\partial}{\partial r} (r\bar{u}\xi) - \frac{1}{r} \frac{\partial}{\partial r} (r\delta(\bar{u}\theta - \bar{u}\bar{\theta})) = 2Pe^{-1}St_m \frac{\Theta_b}{\delta}. \quad (3.39)$$

where our unknown Θ_b or δ can be calculated directly from the expression of ξ using $\delta = h/2$ or $\Theta_b = 1$ respectively

$$\Theta_b(r) = \begin{cases} 1 & \text{if } \xi \leq \xi_t \\ \frac{3}{2} - \frac{3\xi}{h} & \text{if } \xi > \xi_t \end{cases} \quad \delta(r) = \begin{cases} 3\xi & \text{if } \xi \leq \xi_t \\ h(r, t)/2 & \text{if } \xi > \xi_t \end{cases}$$

with $\xi_t = h/6$.

The second term on the left hand side of (3.39) contains advection by the vertically integrated radial velocity while the third term contains a correction accounting for the vertical structure of the temperature field. The term on the right is the loss of heat by conduction in the surrounding medium.

3.2.7.2 Average quantities

The average velocity over a thermal boundary layer \bar{u} reads

$$\bar{u} = \frac{1}{\delta} \int_0^\delta u dz = u(r, \delta, t) - \frac{1}{\delta} \int_0^\delta \frac{\partial u}{\partial z} z dz \quad (3.40)$$

$$= \frac{12}{\delta} \frac{\partial P}{\partial r} (\delta I_0(\delta) - I_1(\delta)) \quad (3.41)$$

where $P(r, z, t) = h + \nabla_r^4 h$ is the dimensionless dynamic pressure and we have used (3.17) in (3.40). The average rate of heat advected $\bar{u}\theta$ over a thermal boundary layer reads

$$\begin{aligned} \bar{u}\theta &= \frac{1}{\delta} \int_0^\delta u\theta dz = \frac{1}{\delta} \left([uG(z)]_0^\delta - \int_0^\delta G(z) \frac{\partial u}{\partial z} dz \right) \\ &= \frac{12}{\delta} \frac{\partial P}{\partial r} (G(\delta)I_0(\delta) - I_2(\delta)) \end{aligned} \quad (3.42)$$

where

$$G(z) = \frac{\Theta_b z^2}{3\delta^2} (3\delta - z) \quad (3.43)$$

is a primitive of θ when $z < \delta$ and

$$I_2(z) = \int_0^z (\nu + (1 - \nu)\theta(y)) G(y) \left(y - \frac{h}{2} \right) dy. \quad (3.44)$$

Therefore, we have

$$\bar{u}\theta - \bar{u}\bar{\theta} = \frac{12}{\delta} \frac{\partial P}{\partial r} (I_0(\delta) (G(\delta) - \delta\bar{\theta}) + \bar{\theta}I_1(\delta) - I_2(\delta)) \quad (3.45)$$

where the average temperature over a thermal boundary layer is $\bar{\theta} = 2\Theta_b/3$

3.2.8 Summary of the equations

In the end, the coupled equations governing the cooling of an elastic-plated gravity current are

$$\frac{\partial h}{\partial t} - \frac{12}{r} \frac{\partial}{\partial r} \left(r I_1(h) \frac{\partial P}{\partial r} \right) = \mathcal{H} \left(\frac{\gamma}{2} - r \right) \frac{32}{\gamma^2} \left(\frac{1}{4} - \frac{r^2}{\gamma^2} \right) \quad (3.46)$$

$$\frac{\partial \xi}{\partial t} + \frac{1}{r} \frac{\partial}{\partial r} (r (\bar{u}\xi - \Sigma)) = 2Pe^{-1} St_m \frac{\Theta_b}{\delta} \quad (3.47)$$

with

$$\Theta_b(r) = \begin{cases} 1 & \text{if } \xi \leq \xi_t \\ \frac{3}{2} - \frac{3\xi}{h} & \text{if } \xi > \xi_t \end{cases} \quad \delta(r) = \begin{cases} 3\xi & \text{if } \xi \leq \xi_t \\ h(r, t)/2 & \text{if } \xi > \xi_t \end{cases}$$

$$\bar{u} = \frac{12}{\delta} \frac{\partial P}{\partial r} (\delta I_0(\delta) - I_1(\delta)) \quad (3.48)$$

$$\Sigma = \frac{\partial P}{\partial r} (8I_1(\delta)\Theta_b - 12I_2(\delta)) \quad (3.49)$$

where $P = h + \nabla_r^4 h$ is the dimensionless pressure and \mathcal{H} the Heaviside function. The expression of $I_0(\delta)$, $I_1(h)$, $I_1(\delta)$ and $I_2(\delta)$ as well as the numerical scheme used to solve equations (3.46) and (3.47) are given in Appendix A.

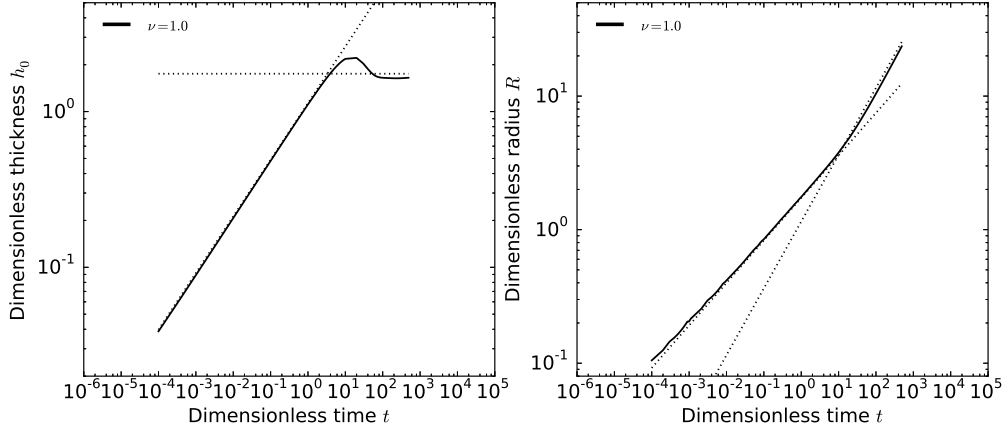


Figure 3.2: Left: Dimensionless thickness at the center h_0 versus dimensionless time t . Dotted-lines: scaling laws in the bending regime $h_0 = 0.7h_f^{-1/11}t^{8/22}$ and in the gravity regime where h_0 tends to a constant. Right: Dimensionless radius R versus dimensionless time t . Dotted-lines: scaling laws in the bending regime $R = 2.2h_f^{1/22}t^{7/22}$ and in the gravity current regime $R \propto t^{1/2}$.

3.2.9 Preliminary results for an isothermal flow

For a constant injection rate, a small pre-wetting film thickness, i.e. $h_f \ll 1$ and a viscosity contrast ν set to 1, numerical resolution of (3.46) shows two asymptotic spreading regimes (*Michaut, 2011; Lister et al., 2013*).

At early times, when $R \ll \Lambda$, gravity is negligible and the spreading dynamics is governed by the bending of the upper layer. The spreading is very slow and the interior has uniform pressure $P = \nabla_r^4 h$. The flow is bell-shaped and its thickness is given by

$$h(r, t) = h_0(t) \left(1 - \frac{r^2}{R^2(t)}\right)^2 \quad (3.50)$$

with $h_0(t)$ the thickness of the current at the center (*Michaut, 2011; Lister et al., 2013*). In this regime, *Lister et al.* (2013) have shown that the spreading is controlled by the propagation of a peeling by bending wave at the flow front with dimensionless velocity c

$$c = \frac{dR}{dt} = h_f^{1/2} \left(\frac{\kappa}{1.35}\right)^{5/2} \quad (3.51)$$

where $\kappa = \partial^2 h / \partial r^2$ is the dimensionless curvature of the interior solution. Using the propagation law (3.51) and the form of the interior solution (3.50), *Lister et al.* (2013) predicted that, in this regime, the flow radius and height

evolve following

$$h_0(t) = 0.7h_f^{-1/11}t^{8/22} \quad (3.52)$$

$$R(t) = 2.2h_f^{1/22}t^{7/22} \quad (3.53)$$

where the numerical pre-factor obtained in our simulations match those of *Lister et al.* (2013) (Figure 3.2).

In contrast, when the radius R becomes larger than 4Λ ($R \gg \Lambda$), the weight of the current becomes dominant over the bending terms. The pressure is given by the hydrostatic pressure $P = h$ and the current enters a classical gravity current regime where bending terms only affect the solution near the edge of the current (Huppert, 1982a; Michaut, 2011; Lister et al., 2013). In this second regime, the radius evolves as $t^{1/2}$ and the thickness tends to a constant (Figure 3.2).

In the following, we study the effect of the cooling on the flow dynamics in both regimes separately. We first describe the thermal structure for an isoviscous flow, i.e. $\nu = 1$ and then study the effect of the temperature-dependent viscosity on the flow dynamics without crystallization, i.e $St_m = 1$. Finally, we introduce crystallization by setting $St_m < 1$. For simplicity, we present the results for a given film thickness ($h_f = 5 \cdot 10^{-3}$); results for different film thicknesses are shown in Appendix C.

3.3 Evolution in the bending regime

We first concentrate on the case in which only bending contributes to the dynamic pressure. The governing equations are thus (3.46) and (3.47) where $P = \nabla_r^4 h$.

3.3.1 Thermal structure for an isoviscous flow, effect of Pe

The current cools by conduction and thermal boundary layers form at the contact with the surrounding medium. These boundary layers first connect at the tip of the flow, where the small thickness induces an important cooling (Figure 3.3). A region of cold fluid forms at the front.

As the current thickens with time, a balance between advection and diffusion of heat is never reached in the interior of the current. The hot thermal anomaly grows in extent with time but slower than the current itself and the cold fluid region at the tip grows. For instance, for $Pe = 100$, while the region of cold fluid extends over about 10% of the current at $t = 0.5$, it extends

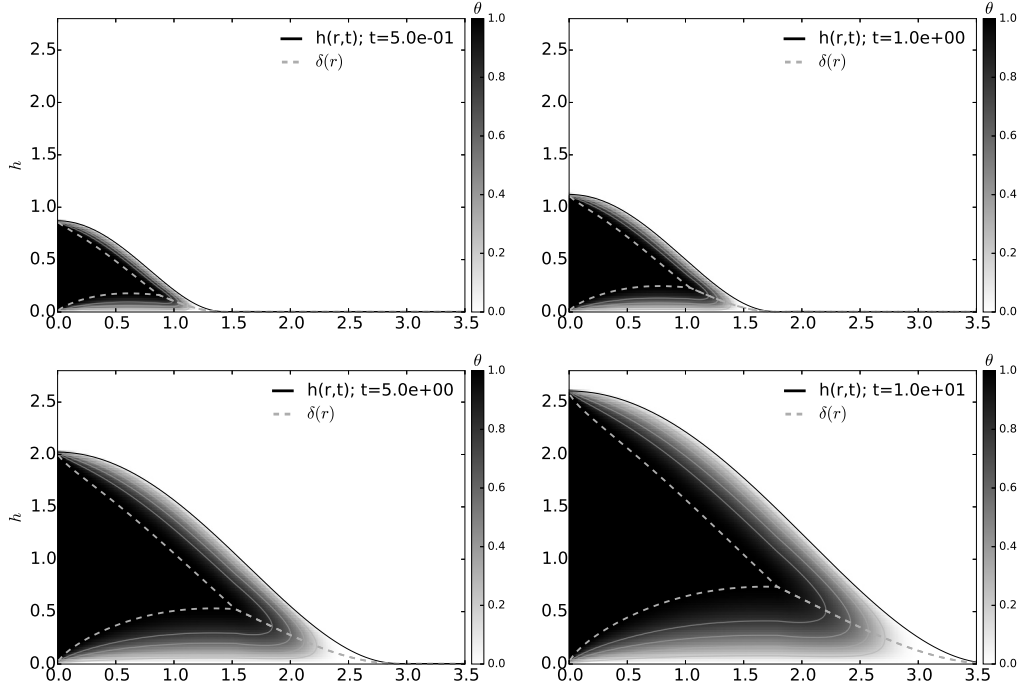


Figure 3.3: Snapshots of the flow thermal structure $\theta(r, z, t)$ at different times indicated on the plot. Dashed lines represent the thermal boundary layers. Solid grey lines are isotherms for $\theta = 0.2, 0.4, 0.6$ and 0.8 . Here, $\nu = 1.0$, $Pe = 100$, $St_m = 1$.

over about 20% at $t = 10$ (Figure 3.3). The smaller Pe , the more important the conductive cooling and the larger the cold region (Figure 3.4 and 3.5). For instance, at $t = 10$, while the cold region extends over about 20% of the current for $Pe = 100$, it extends over more than 70% for $Pe = 1$ (Figure 3.4).

3.3.2 Thickness and temperature profile, effect of ν

When accounting for the temperature dependence of the viscosity, the region of cold fluid at the tip is marked by a higher viscosity and enhances flow thickening at the expense of spreading. The larger the viscosity contrast, the larger the aspect ratio h_0/R (Figure 3.4). For instance, for the same value of $Pe = 1$, while the aspect ratio is 0.7 for $\nu = 1$ at $t = 10$, it is 4.2 at the same time for $\nu = 10^{-3}$ (Figure 3.4). Nevertheless, the shape of the flow remains essentially self-similar, i.e. well described by (3.50) and cannot be differentiated from the shape of an isoviscous current if the thickness and the radial coordinates are rescaled by the thickness at the center $h_0(t)$ and radius $R(t)$ (Figure 3.5).

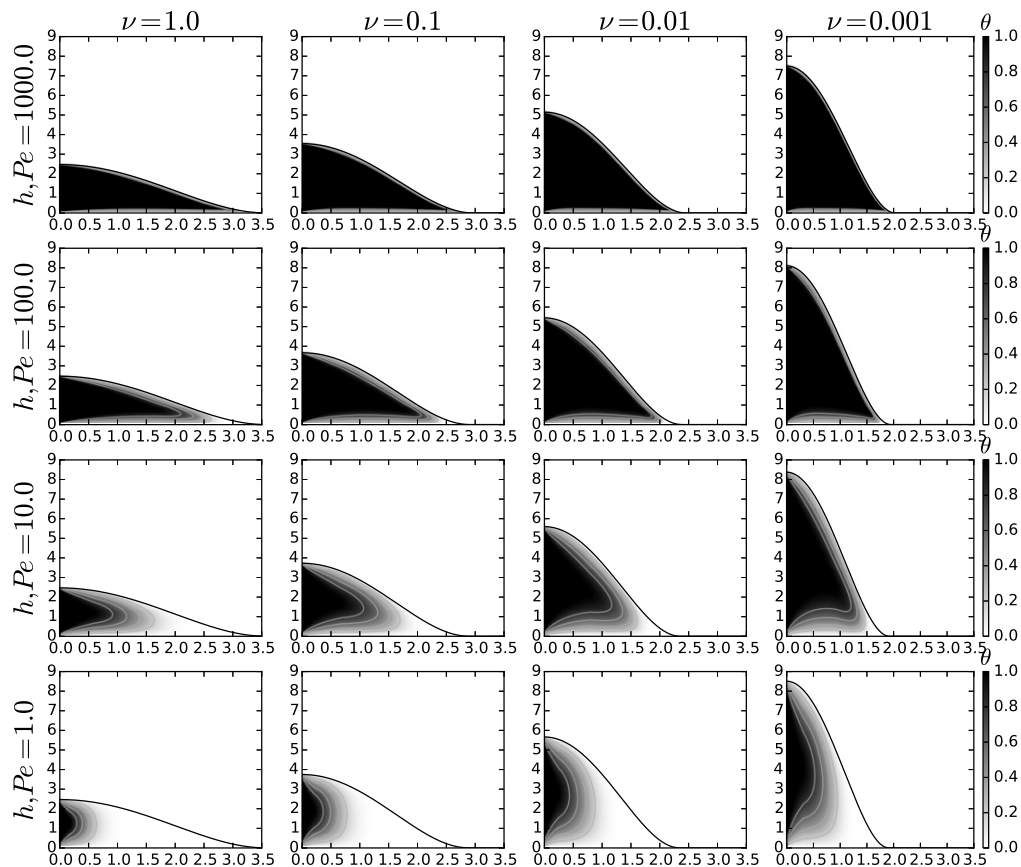


Figure 3.4: Snapshots of the flow thermal structure $\theta(r, z, t)$ for different set (ν, Pe) with $\nu = 1, 0.1, 0.01$ and 0.001 and $Pe = 1, 10, 100$ and 1000 at $t = 10$. While Pe controls the thermal structure of the flow, it has only a small influence on the flow aspect ratio which is controlled by ν .

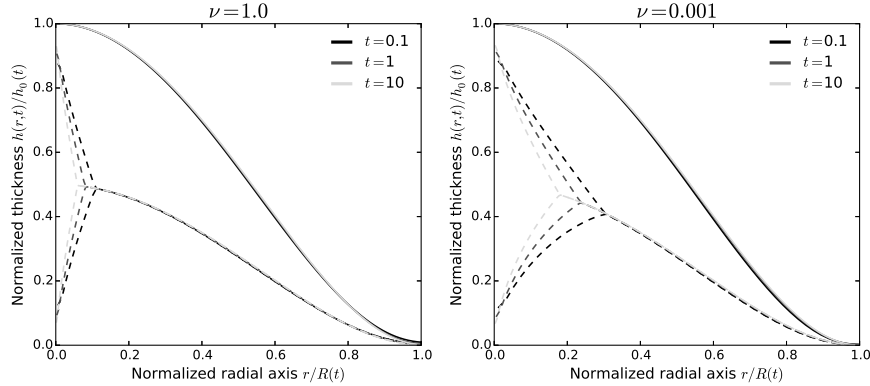


Figure 3.5: Left: thickness normalized by the thickness at the center $h(r,t)/h_0(t)$ versus radial axis normalized by the current radius $r/R(t)$ at different times indicated on the plot for $Pe = 1.0$ and $\nu = 1.0$. Solid-lines represent the thickness profiles. Dashed-lines represent the thermal boundary layers. Right: Same plot but for $\nu = 10^{-3}$.

The flow thermal structure is similar to the isoviscous case (Figure 3.4), the thermal anomaly rapidly detaches from the tip of the current and a region of cold fluid develops at the front where heat loss is the largest. However, the important thickening induced by the viscosity increase limits heat loss to the surrounding. The larger the viscosity contrast ν , the more important the thickening and the larger the thermal anomaly at a given time. For instance, for $Pe = 1$, while the thermal anomaly extends over about 30% of the flow for $\nu = 1$ at $t = 10$, it extends over more than 50% for $\nu = 10^{-3}$ (Figure 3.4).

As expected, a larger Peclet number leads to a larger thermal anomaly (Figure 3.4). However, although different Peclet numbers cause very different thermal structures, the influence of the Peclet number on the flow morphology is small, much smaller than the effect of the viscosity contrast ν (Figure 3.4). For instance, for $\nu = 10^{-3}$ at $t = 10$, the thermal anomaly is still attached to the tip of the current for $Pe = 1000$ whereas it makes about 50% of the current for $Pe = 1$; but, the thickness h_0 and the radius R in both cases differ only by a few percents (Figure 3.4). This suggests that, in this regime, the spreading of the flow is not controlled by the mean temperature or average viscosity of the flow.

3.3.3 Evolution of the thickness and the radius

In this bending dominated regime, the dynamics show three different spreading phases. The thickness as well as the radius first follow the isoviscous

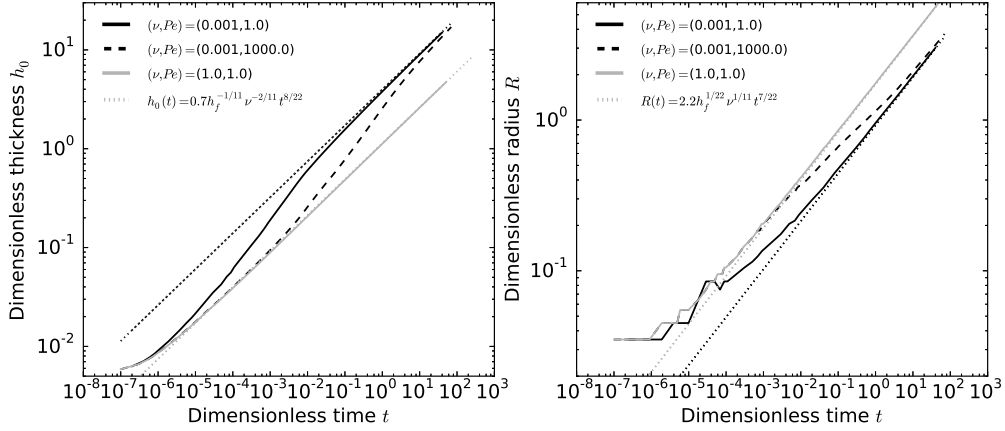


Figure 3.6: Left: Dimensionless thickness at the center h_0 versus dimensionless time t for different sets (ν, Pe) indicated on the plot. Dotted-lines: scaling laws $h_0 = 0.7h_f^{-1/11}\nu^{-2/11}t^{8/22}$ for $\nu = 1.0$ and 0.001 . Right: Dimensionless radius R versus dimensionless time t for the same sets of values (ν, Pe) . Dotted-lines: scaling laws $R = 2.2h_f^{1/22}\nu^{1/11}t^{7/22}$ for $\nu = 1.0$ and 0.001 .

scaling laws for a hot viscosity current $h_0 \propto t^{8/22}$ (3.52) and $R \propto t^{7/22}$ (3.53) (Figure 3.6). In the second phase, thickening occurs at the expense of spreading because the thermal anomaly has detached from the current radius and the viscous cold fluid region at the front slows down the spreading. Finally, the dynamics enters a third phase where the thickness and radius follow the scaling laws for the spreading of an isoviscous current characterized by a dimensionless cold viscosity $1/\nu$. These scaling laws are obtained from (3.52) and (3.53) by rescaling the characteristic thickness and time by $\nu^{1/4}$ and read

$$h_0 = 0.7\nu^{-2/11}h_f^{-1/11}t^{8/22} \quad (3.54)$$

$$R = 2.2\nu^{1/11}h_f^{1/22}t^{7/22}. \quad (3.55)$$

The dependence on the viscosity contrast ν indeed fits very well the third phase of the flow observed in the numerical simulations (Figure 3.6). In the end, the effective viscosity η_e of the flow evolves from the viscosity of the hot fluid in the first phase to asymptotically tend to the one of the cold fluid in the third phase.

The time the flow spends in each phase depends on the Peclet number Pe . For instance, for $\nu = 10^{-3}$, while the current leaves the first phase at $t \sim 10^{-6}$ for $Pe = 1.0$, this transition happens only after $t \sim 10^{-2}$ for $Pe = 10^3$ (Figure 3.6). The larger the Peclet number, the less efficient the cooling and thus the longer the flow remains in the first phase and the later it reaches the third phase.

3.3.4 Characterization of the thermal anomaly

Following *Garel et al.* (2012), we quantify the size of the thermal anomaly through a critical thermal radius $R_c(t)$ where the temperature at the center of the flow Θ_b is 1% of the injection temperature, i.e. $\Theta_b(r = 0) - \Theta_b(r = R_c) = 0.99$. The thermal anomaly is first advected at the same velocity as the current itself, i.e. $R(t) = R_c(t)$ (Figure 3.7 left). After a time that depends on Pe and ν , the thermal anomaly detaches from the tip and $R(t) - R_c(t)$ increases with time (Figure 3.7).

In the bending regime, the interior pressure is constant and the thickness profile $h(r)$ is given by (3.50) (Figure 3.5). The time evolution of the size of the thermal anomaly $R_c(t)$ is characterized by looking at the radius in the flow where heat advection locally balances heat loss, i.e.

$$\frac{d}{dt}(\Theta_b h) \approx Pe^{-1} \frac{\Theta_b}{h}. \quad (3.56)$$

Using the thickness profile (3.50), (3.56) becomes

$$\alpha^2 \left(1 + \frac{R_c}{R}\right)^2 \left(\Theta_b \frac{dh_0}{dt} + h_0 \frac{d\Theta_b}{dt}\right) + \frac{4h_0 R_c^2 \Theta_b}{R^3} \frac{dR}{dt} \alpha \left(1 + \frac{R_c}{R}\right) \approx \frac{Pe^{-1} \Theta_b}{\alpha^2 \left(1 + \frac{R_c}{R}\right)^2 h_0}$$

where $\alpha(t) = (R(t) - R_c(t))/R(t)$ is the normalized region beyond $r = R_c(t)$. In the limit $\alpha \ll 1$, i.e. $R_c/R \sim 1$, the time derivative is locally dominated by its advective part ($\propto \alpha$) and we finally get

$$\alpha^3 \approx \frac{Pe^{-1}}{h_0^2(t)} \frac{R}{\frac{\partial R}{\partial t}}. \quad (3.57)$$

Substituting $h_0(t)$ and $R(t)$ by their respective scaling laws (3.54) and (3.55), the size evolution of the normalized cold front region α reads

$$\alpha(t) \approx Pe^{-1/3} \nu^{4/33} h_f^{2/33} t^{1/11}. \quad (3.58)$$

which is equivalent to

$$R(t) - R_c(t) = 2.1 Pe^{-1/3} \nu^{7/33} h_f^{7/66} t^{9/22} \quad (3.59)$$

where the numerical prefactor, which depends on the definition of the thermal anomaly, has been chosen to fit the simulations.

The predicted scaling law for the evolution of the cold fluid region (3.59) indeed closely fits the numerical simulations for $\nu < 1$ and for different Peclet numbers (Figure 3.7). For $\nu = 1$ and $Pe = 1$, the condition $R - R_c \ll R$ is no more respected for $t > 0.1$, the thermal anomaly is much smaller than the flow itself and the evolution of the cold fluid region diverges from (3.59).

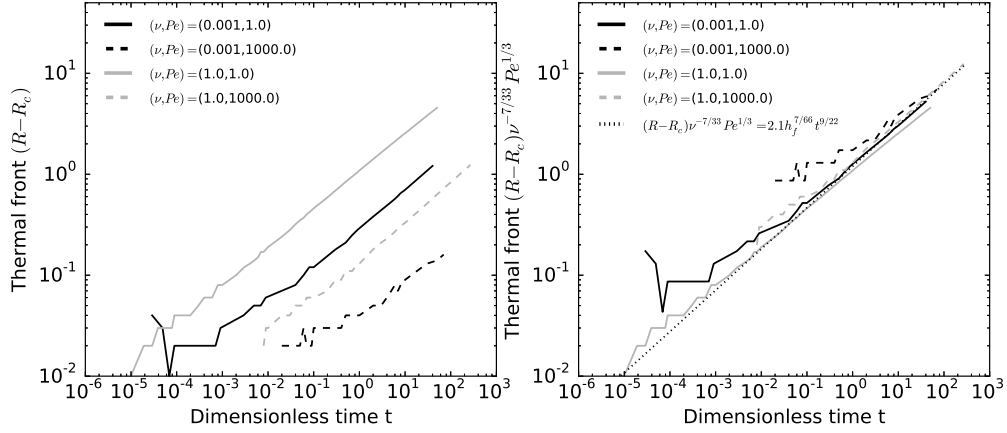


Figure 3.7: Left: Extent of the cold fluid region $R(t) - R_c(t)$ versus dimensionless time for different combinations (ν, Pe) indicated on the plot. Right: Same plot but where we rescale the extent of the cold fluid region by $Pe^{-1/3} \nu^{7/33}$. Dotted-line: scaling law $(R(t) - R_c(t))Pe^{1/3}\nu^{-7/33} = 2.1h_f^{7/66}t^{9/22}$.

3.3.5 Effective viscosity of the current

We use the predicted scaling law for the thickness $h_0(t)$ (3.54) to infer the time evolution of the effective viscosity $\eta_e(t)$. Substituting ν by $\eta_h/\eta_e(t)$ in (3.54) and inverting for $\eta_e(t)/\eta_h$, we get

$$\eta_e(t)/\eta_h = \left(\frac{h_0(t)t^{-8/22}}{0.7h_f^{-1/11}} \right)^{11/2} \quad (3.60)$$

where $h_0(t)$ is given by the simulation.

As suggested by the results of section 3.3.3, the effective viscosity is first close to the hot viscosity η_h , i.e. $\eta_e/\eta_h \sim 1$ (Figure 3.8 a). It rapidly increases in the second phase of propagation and finally tends to the cold viscosity η_c in the third phase, i.e. $\eta_e/\eta_h \sim 1/\nu$. The effective viscosity is however very different from the average viscosity (Figure 3.8 a). Since the spreading is controlled by the propagation of a peeling by bending wave at the tip of the current (Lister et al., 2013), the evolution of the effective viscosity should be linked to the rapid cooling of the front. We calculate the average viscosity $\eta_f(t)$ over a fixed front region of size L in between $R(t) - L$ and $R(t)$

$$\eta_f/\eta_h = \frac{1}{V_f} \int_{R-L}^R \int_0^h r\eta(\theta) dr dz \quad (3.61)$$

where $V_f(t)$ is the volume of this region. The numerical evaluation of $\eta_f(t)$ for a constant size $L \sim 0.1$ fits relatively well the evolution of the effective

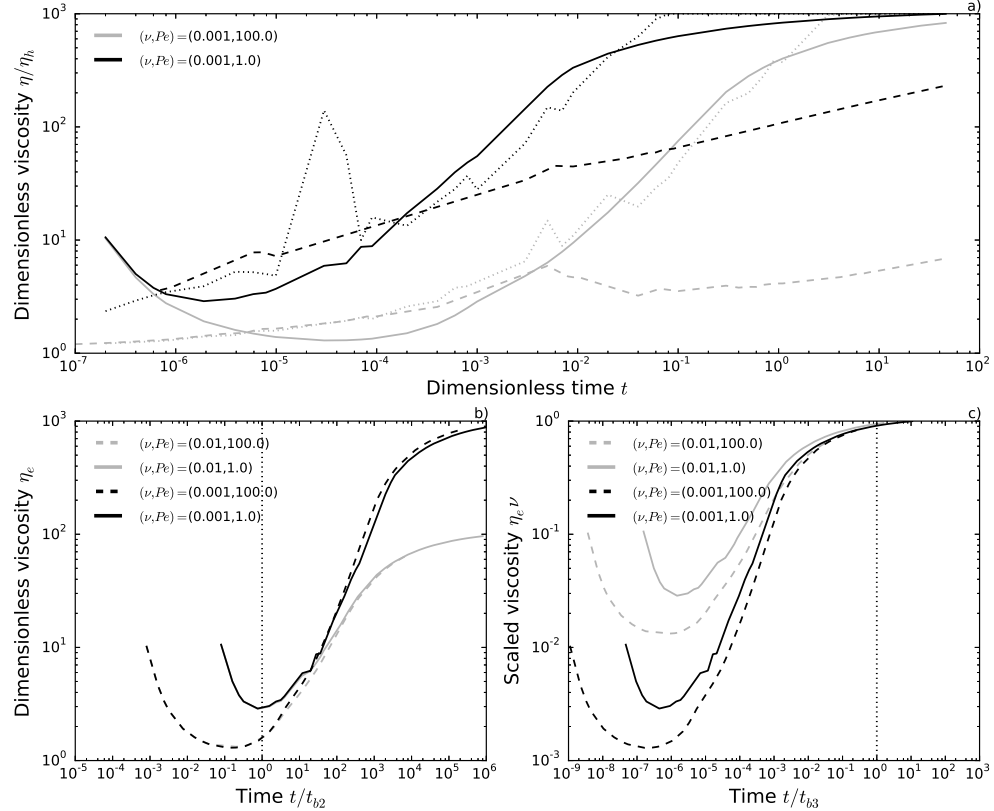


Figure 3.8: a) Dimensionless viscosity $\eta(t)/\eta_h$ versus dimensionless time t for different combinations (ν, Pe) indicated on the plot. Solid lines: effective viscosity η_e/η_h defined by (3.60). Dashed-lines: average flow viscosity defined by $\overline{\eta_a(t)}/\eta_h = \frac{1}{V(t)} \int_0^{R(t)} \int_0^{h(r,t)} r \eta(\theta) dr dz$ where $V(t)$ is the current volume. Dotted-lines: average front viscosity η_f/η_h defined by (3.61). b) Dimensionless effective viscosity η_e versus time where the time has been rescaled by the time for the flow to enter the second phase t_{b2} . c) Same as left but where the time has been rescaled by the time for the flow to enter the third phase t_{b3} .

viscosity η_e for the second phase of propagation (Figure 3.8 a). Therefore, the effective viscosity, and thus the different phases of propagation, are controlled by the average viscosity of a small region at the front of size $L = O(0.1)$.

At the initiation of the flow, the prewetting film is composed by fluid at the injection temperature, the thermal anomaly is attached to the front and the current spreads with a hot viscosity η_h . Once the film has cooled by conduction, which occurs over a time $t_{b2} = 0.1Pe h_f^2$, where the numerical prefactor has been matched to the simulations, the thermal anomaly detaches from the current tip and the effective viscosity starts to increase. Indeed, when rescaling the time of the simulations by t_{b2} , the different simulations enter the second phase simultaneously (Figure 3.8 b). Then, the size of the cold fluid region at the front increases, the effective viscosity increases and the flow finally behaves as an isoviscous current when its effective viscosity becomes close to its maximum value $1/\nu$. In the following, we use $\eta_e = 0.9\eta_c$ to determine the time t_{b3} the current enters this third phase which happens when $R(t) - R_c(t) \lesssim 0.5$. Inverting (3.59) thus gives $t_{b3} \sim 0.03Pe^{22/27}\nu^{-14/27}h_f^{-7/27}$. Indeed, when rescaling the time of the simulations by t_{b3} , the different simulations enter the third phase simultaneously (Figure 3.8 c).

3.3.6 Note on the effect of crystallization

Here, we examine the effect of crystallization on the flow dynamics and use a value of $St_m = 0.17 < 1$, relevant for magmas. Crystallization induces a release of latent heat in the fluid, increasing the amount of available energy at a given time. When $St_m < 1$, the tip of the current remains hot for a longer time and the flow transitions to the second phase later than in the case where $St_m = 1$ (Figure 3.9). As the crystallization acts only to reduce the cooling term by a factor St_m in (3.47), one can easily rewrite (3.59) to account for the effect of crystallization on the size of the cold fluid region

$$R(t) - R_c(t) = 2.1Pe^{-1/3}St_m^{1/3}\nu^{7/33}h_f^{7/66}t^{9/22}. \quad (3.62)$$

Indeed, the dependence with the dimensionless number St_m is well described by the scaling law (3.62) (Figure 3.10). Accordingly, the time t_{b2} and t_{b3} for the current to enter the second and third phase of the flow are delayed when accounting for crystallization and respectively read

$$t_{b2} \sim 0.1Pe St_m^{-1}h_f^2 \quad (3.63)$$

$$t_{b3} \sim 0.03St_m^{-22/27}Pe^{22/27}\nu^{-14/27}h_f^{-7/27} \quad (3.64)$$

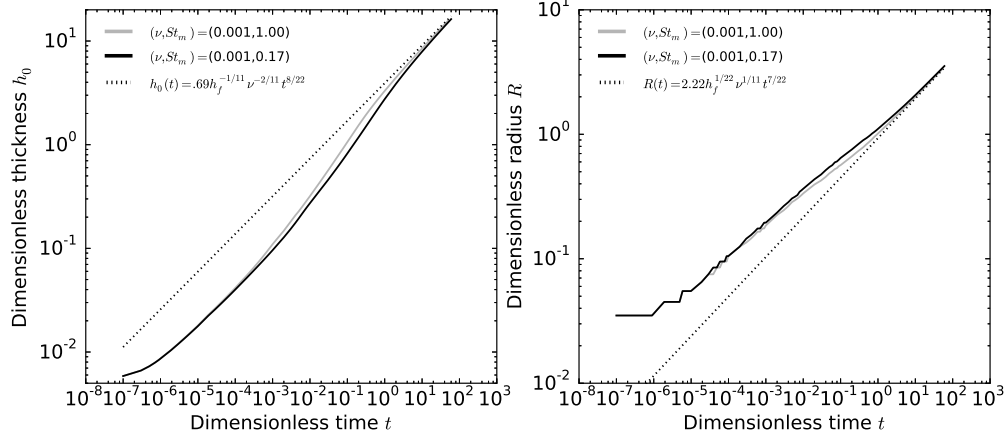


Figure 3.9: Left: Dimensionless thickness at the center h_0 versus dimensionless time t for different values of St_m indicated on the plot, $\nu = 0.001$ and $Pe = 10.0$. Dotted-line: scaling law $h_0 = 0.7h_f^{-1/11} \nu^{-2/11} t^{8/22}$ for $\nu = 0.001$. Right: Dimensionless radius R versus dimensionless time t for the same combinations of dimensionless numbers. Dotted lines: scaling law $R = 2.2h_f^{1/22} \nu^{1/11} t^{7/22}$ for $\nu = 0.001$.

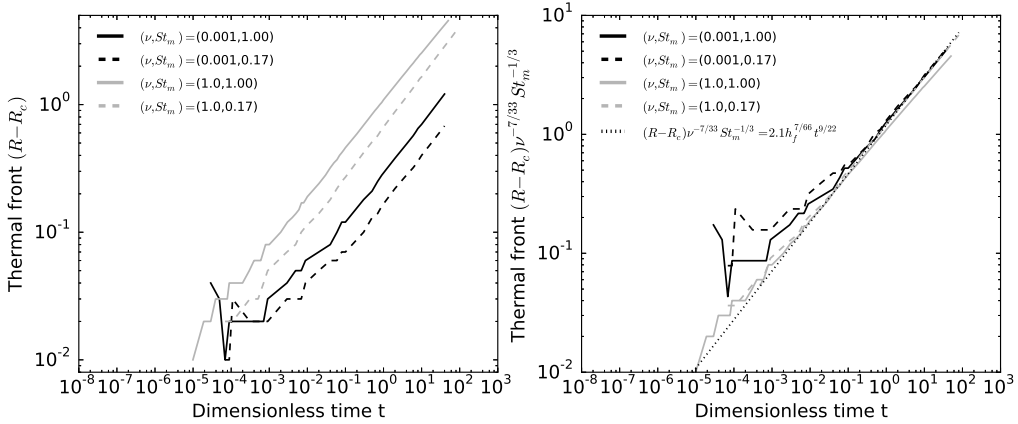


Figure 3.10: Left: Extent of the cold fluid region $R(t) - R_c(t)$ versus dimensionless time for different combinations (ν, St_m) indicated on the plot and $Pe = 1$. Right: Same plot but where we have rescaled the extent of the cold fluid region by $St_m^{1/3} \nu^{7/33}$. Dotted-line: scaling law $(R(t) - R_c(t)) St_m^{-1/3} \nu^{-7/33} = 2.1h_f^{7/66} t^{9/22}$.

3.4 Evolution in the gravity current regime

To study the late time behavior, we concentrate on the case where only the weight of the fluid contributes to the pressure. The governing equations are thus (3.46) and (3.47) where $P = h$. We follow the same framework as in Section 3.3.

3.4.1 Thermal structure for an isoviscous flow, effect of Pe

As in the bending regime, the bulk of the fluid first expands at the injection temperature and $R_c(t) \sim R(t)$. As the bottom and the top cool by conduction, thermal boundary layers form at the contact with the surrounding medium and connect at the tip of the current. However, in the gravity current regime, the thickness of the current tends to a constant. Therefore, conduction in the surrounding medium rapidly balances the input of heat at the center and when the thermal anomaly detaches from the tip of the current, its extent reaches a steady state (Figure 3.11).

The radius of the steady-state thermal anomaly R_c also largely depends on Pe in this regime: the larger the number Pe , the larger the radius R_c (Figure 3.12). For instance, while the thermal anomaly R_c is less than 1 in the steady state regime for $Pe = 1$, it is about 12 for $Pe = 10^3$ (Figure 3.12, $\nu = 1$).

3.4.2 Thickness and temperature profile, effect of ν

For a current with a viscosity that depends on temperature, as soon as the thermal anomaly detaches from the current radius, the cold fluid at the front tends to slow down the spreading and enhance the thickening of the flow (Figure 3.12). For instance, for $Pe = 1$, while the aspect ratio h_0/R is about 0.12 for $\nu = 1$ at $t = 200$, it is ~ 1 for $\nu = 10^{-3}$ (Figure 3.12). The shape of the current is not self-similar and the front steepens when the viscosity increases in comparison to the isoviscous case as noted by *Bercovici (1994)*. However, when the current becomes much larger than the thermal anomaly, the current side slumps to become less steep (Figure 3.12) and recovers a shape similar to the isoviscous flow with cold viscosity.

The thermal structure is similar to the isoviscous case. In particular, after a time that depends on Pe , the thermal anomaly reaches a steady-state profile (Figure 3.12). As in the bending regime, the thickening at the center limits heat loss to the surrounding for large values of the viscosity contrast ν . Therefore, the extent of the thermal anomaly in the steady-state is slightly larger for a larger viscosity contrast. For instance, for $Pe = 10$ at $t = 200$,

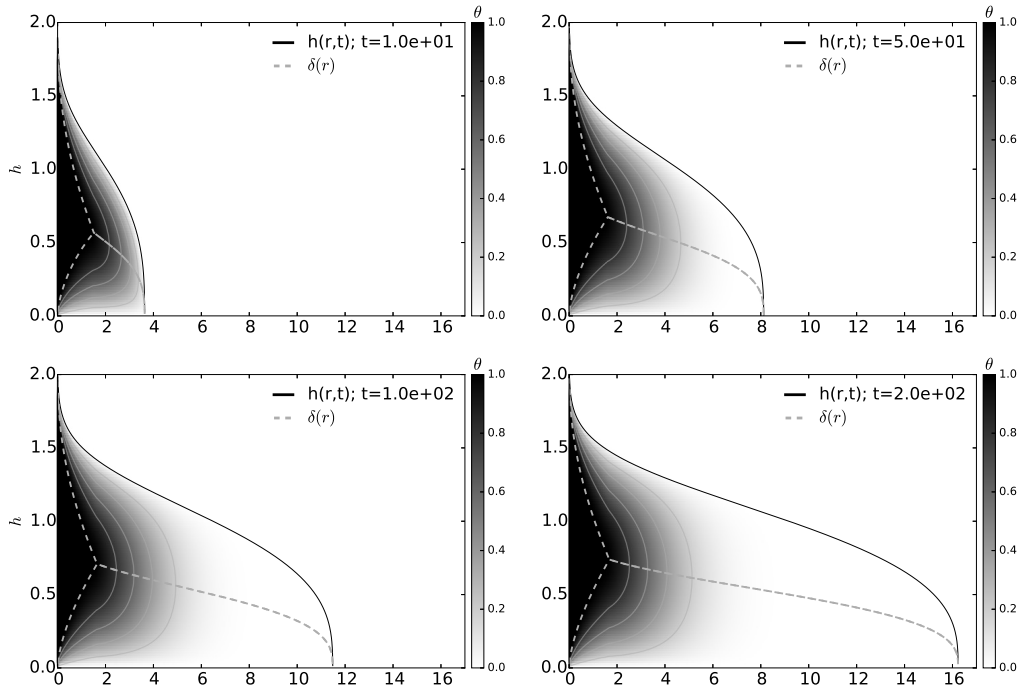


Figure 3.11: Snapshots of the flow thermal structure $\theta(r, z, t)$ at different times indicated on the plot. Dashed lines: thermal boundary layers. Here, $\nu = 1$, $Pe = 100$ and $St_m = 1$.

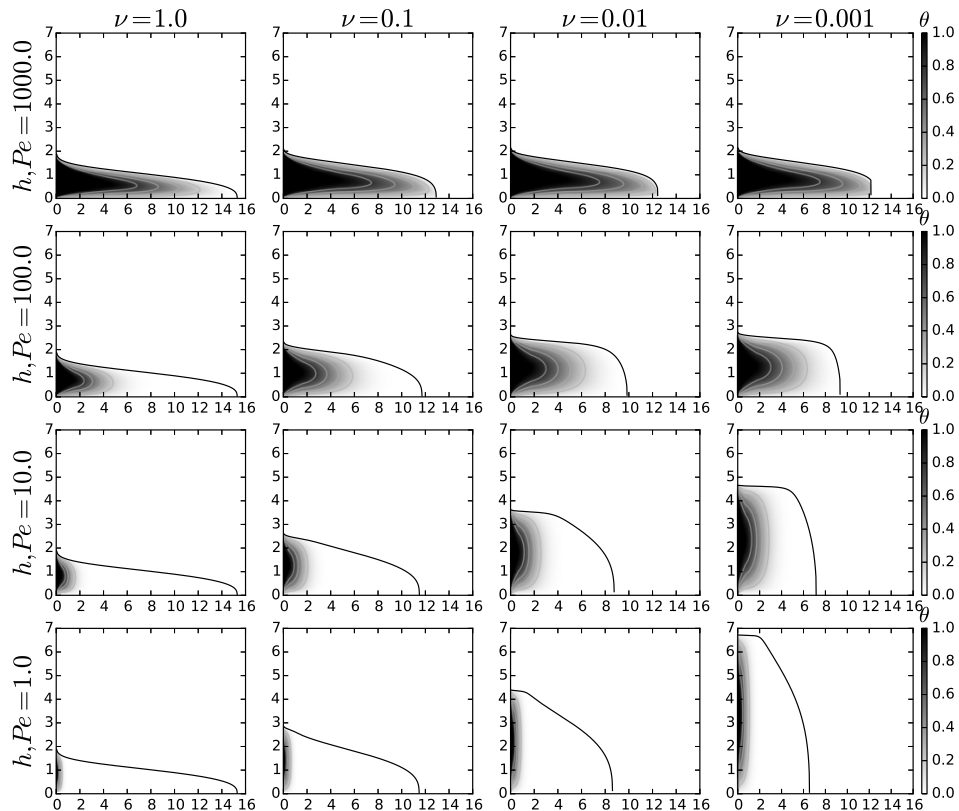


Figure 3.12: Snapshots of the flow thermal structure $\theta(r, z, t)$ for different sets (ν, Pe) with $\nu = 1, 0.1, 0.01$ and 0.001 and $Pe = 1, 10, 100$ and 1000 at $t = 200$.

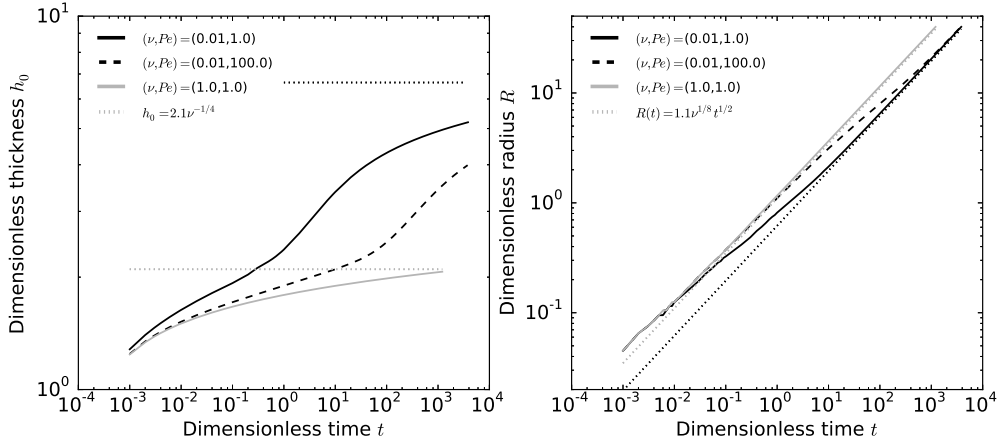


Figure 3.13: Left: Dimensionless thickness at the center h_0 versus dimensionless time t for different sets (ν, Pe) indicated on the plot. Dotted-lines represent the scaling laws $h_0 = 2.1\nu^{-1/4}$ for $\nu = 1.0$ and 10^{-2} . Right: Dimensionless radius R versus dimensionless time t for the same sets (ν, Pe) . Dotted-lines represent the scaling laws $R = 1.1\nu^{1/8}t^{1/2}$ for $\nu = 1.0$ and 10^{-2} .

while the thermal anomaly extends over less than 2 for $\nu = 1$, it reaches $R_c \sim 3$ for $\nu = 10^{-3}$.

The flow morphology is much more sensitive to Pe in the gravity current regime than in the bending regime and different Pe lead to different current morphologies for a given ν (Figure 3.12). For instance, for $\nu = 10^{-3}$ at $t = 200$, the thermal anomaly is still attached to the tip for $Pe = 10^3$ and the aspect ratio of the flow h_0/R is close to 0.15. In contrast, for $Pe = 1$, the thermal anomaly radius R_c is less than 30% of the current radius and the aspect ratio of the flow is much larger $h_0/R = 1.15$ (Figure 3.12).

3.4.3 Evolution of the thickness and radius

As in the bending regime, the dynamics in the gravity current regime shows three different spreading phases. The thickness as well as the radius first follow the isoviscous scaling laws for a given hot viscosity η_h , i.e. h_0 tends to a constant and $R \propto t^{1/2}$ (Figure 3.13). In a second phase, the thickness rapidly increases and the spreading slows down. Finally, the thickness and radius follow the isoviscous scaling laws but for a cold viscosity flow.

These dimensionless scaling laws read, as a function of ν

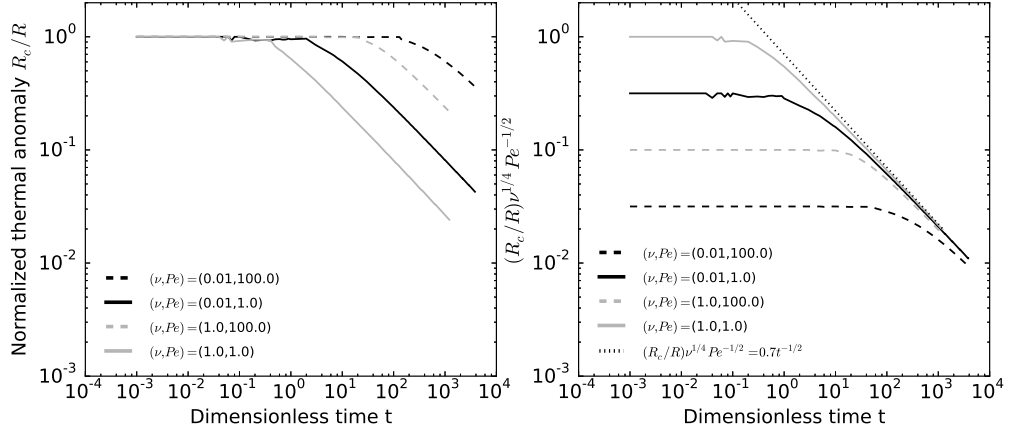


Figure 3.14: Left: Normalized thermal anomaly radius $R_c(t)/R(t)$ versus dimensionless time for different combinations (ν, Pe) indicated on the plot. Right: Same plot but where we rescale the normalized thermal anomaly radius $R_c(t)/R(t)$ by $Pe^{1/2}\nu^{-1/4}$.

$$h_0 = 2.1\nu^{-1/4} \quad (3.65)$$

$$R(t) = 1.1\nu^{1/8}t^{1/2} \quad (3.66)$$

They perfectly match our numerical simulations (Figure 3.13). Therefore, the effective viscosity η_e that controls the flow dynamics is first close to the viscosity of the hot fluid η_h ; it then rapidly increases to asymptotically tend to the viscosity of the cold fluid η_c in the third phase.

As in the bending regime, the time the current spends in each phase depends on Pe (Figure 3.13). For instance, for $\nu = 10^{-2}$, while the current leaves the first phase at $t \sim 10^{-1}$ for $Pe = 1.0$, the transition occurs after $t \sim 10^1$ for $Pe = 10^2$ (Figure 3.13). The larger the Pe , the longer the current remains in the first phase and the later is reached the third phase.

3.4.4 Characterization of the thermal anomaly

The thermal anomaly is first advected at the same velocity as the current itself, i.e. $R_c(t)/R(t) \sim 1$ (Figure 3.14 left). After a time that depends on Pe and ν , the thermal anomaly detaches from the front and reaches a steady-state profile (Figure 3.12 and 3.14).

We develop a simple thermal budget to predict the extent of the thermal anomaly in the steady-state regime. At the steady state radius R_c of

the thermal anomaly, a balance between heat advection and diffusion in the surrounding medium in a dimensional form gives

$$\rho C_p U_0 \frac{\Delta T}{R_c} \approx \frac{8k\Delta T}{h_0^2} \quad (3.67)$$

where ΔT is a mean temperature contrast between the fluid and the surroundings and U_0 is a mean velocity of advection. For a gravity current, and by opposition to the bending regime, the thickness h_0 reaches a constant. Taking U_0 as a horizontal redistribution of the injection rate at $r = R_c$, we write

$$U_0 = Q_0 / (2\pi R_c h_0) \quad (3.68)$$

which gives

$$R_c \approx \frac{1}{4} \sqrt{\frac{h_0 Q_0}{\pi \kappa}} \quad (3.69)$$

By non-dimensionalizing (3.69), we obtain the evolution of the steady-state radius $R_c \approx Pe^{1/2}\nu^{-1/8}$ and hence

$$\frac{R_c}{R(t)} = 0.7Pe^{1/2}\nu^{-1/4}t^{-1/2} \quad (3.70)$$

where we have used (3.66) and the numerical prefactor, which depends on the definition of the thermal anomaly, has been chosen to fit the simulations.

The scaling law (3.70) closely fits the numerical simulations (Figure 3.14). Indeed, when the thermal anomaly enters the steady state, the thermal anomaly radius remains constant and the normalized thermal anomaly radius $R_c(t)/R(t)$ evolves as the inverse of the current radius, i.e. as $t^{-1/2}$ (Figure 3.14). Furthermore, both the dependence with Pe and ν vanish when rescaling $R_c/R(t)$ by $Pe^{1/2}\nu^{-1/4}$ in the steady state regime (Figure 3.14, right).

3.4.5 Effective viscosity of the current

Repeating the same exercise as in section (3.3.5), we use the predicted scaling law for the radius $R(t)$ (3.66) to infer the effective viscosity $\eta_e(t)$ of the current

$$\frac{\eta_e(t)}{\eta_h} = \left(\frac{R(t)t^{-1/2}}{1.1} \right)^{-8} \quad (3.71)$$

where $R(t)$ is given by the simulation.

As expected, the effective viscosity in the gravity current regime represents the average viscosity of the current and the different phases of propagation reflect changes in the average viscosity of the flow (Figure 3.15 a).

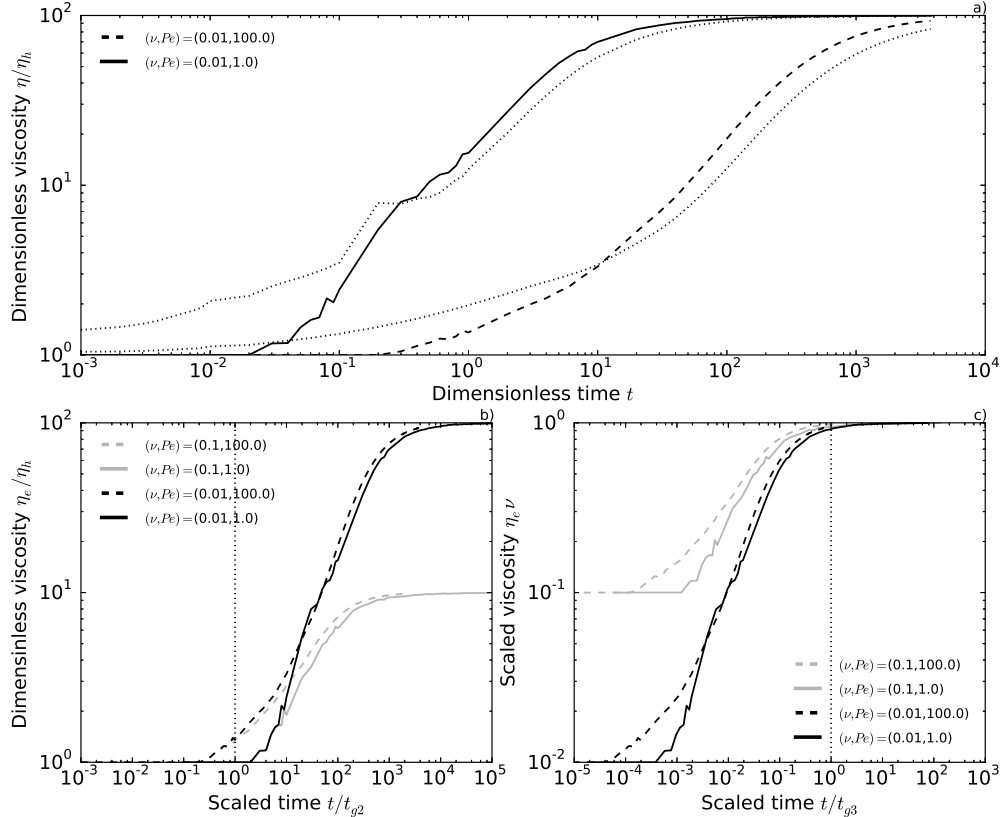


Figure 3.15: a) Dimensionless viscosity $\eta(t)/\eta_h$ defined by (3.60) versus dimensionless time t for different combinations (ν, Pe) indicated on the plot. Black dotted-lines: average flow viscosity defined by $\eta_a(t)/\eta_h = \frac{1}{V(t)} \int_0^{R(t)} \int_0^{h(r,t)} r \eta(\theta) dr dz$ where $V(t)$ is the current volume. b) dimensionless effective viscosity η_e versus time where the time has been rescaled by the time t_{g2} (3.73). c) Same as left but where the time has been rescaled by t_{g3} (3.74).

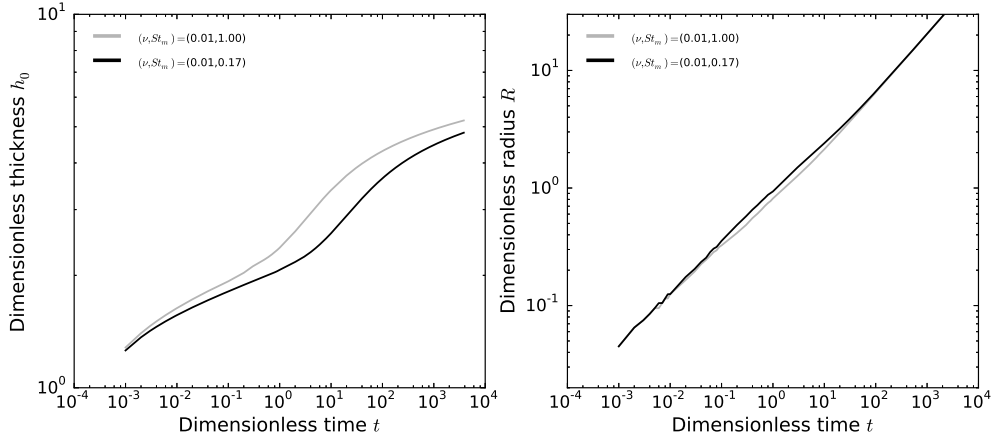


Figure 3.16: Left: Dimensionless thickness at the center h_0 versus dimensionless time t for different sets (ν, St_m) indicated on the plot and $Pe = 1$. Right: Dimensionless radius R versus dimensionless time t for the same sets (ν, St_m) and $Pe = 1$.

At the flow initiation, the thermal anomaly is advected at the same velocity as the current itself and the current spreads with hot viscosity η_h . When the thermal anomaly detaches from the tip and enters a steady state, η_e increases. The time t_{g2} to enter this second phase scales with the time to cool the current by conduction, i.e. $t_{g2} = 10^{-2}Pe$ where the numerical pre-factor has been matched to the simulations. Indeed, when rescaling the time by t_{g2} , the different simulations enter the second phase simultaneously (Figure 3.15 b). Then, the size of the cold fluid region at the front increases, the effective viscosity increases and the flow finally behaves as an isoviscous current when its effective viscosity becomes close to its maximum value $1/\nu$. As in the bending regime, we use $\eta_e = 0.9\eta_c$ to define the time t_{g3} the current enters the third phase of the dynamics which happens when $R_c(t)/R(t) \lesssim 0.3$. Inverting (3.70) thus gives $t_{g3} = 5.2Pe\nu^{-1/2}$. Indeed, when rescaling the time of the simulations by t_{g3} , the different combinations (ν, Pe) enter the third phase simultaneously (Figure 3.15 c).

3.4.6 Note on the effect of crystallization

As in the bending regime, crystallization induces a release of latent heat, increasing the amount of available energy at a given time. As a result, when $St_m < 1$, the current is hotter on average and it transitions to the second phase later than in the case where $St_m = 1$ (Figure 3.16). As in section (3.3.6), one can easily rewrite (3.70) to account for the effect of crystallization

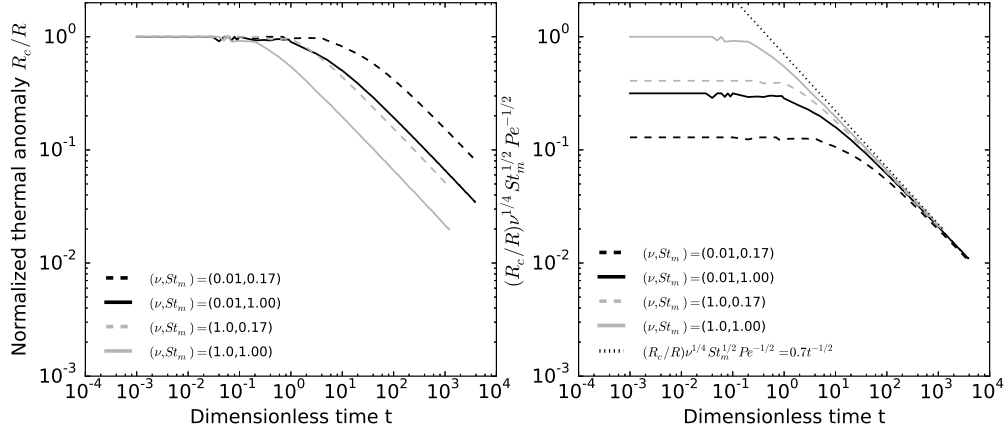


Figure 3.17: Left: Normalized thermal anomaly radius $R_c(t)/R(t)$ versus dimensionless time for different combinations (ν, St_m) indicated on the plot and $Pe = 1$. Right: Same plot but where we have rescaled the normalized thermal anomaly radius $R_c(t)/R(t)$ by $St_m^{-1/2} Pe^{1/2} \nu^{-1/4}$.

on the thermal anomaly evolution

$$\frac{R_c}{R(t)} = 0.7 St_m^{-1/2} Pe^{1/2} \nu^{-1/4} t^{-1/2} \quad (3.72)$$

Indeed, the dependence with the dimensionless number St_m is well described by the scaling law (3.72) (Figure 3.17). Accordingly, the time t_{g2} and t_{g3} for the current to enter the second and third phase of the flow are both delayed and respectively read

$$t_{g2} \sim 10^{-2} Pe St_m^{-1} \quad (3.73)$$

$$t_{g3} \sim 5.2 Pe St_m^{-1} \nu^{-1/2} \quad (3.74)$$

3.5 Different evolutions with bending and gravity

For an isoviscous flow with $h_f \ll h \ll d_c$, in between the bending and gravity regime, Lister et al. (2013) also describe a short intermediate regime where the peeling by bending continues to control the propagation but where the flow shows an interior flat-topped region due to the increasing effect of gravity. For simplicity, we only consider the two asymptotic regimes. At the transition, the isoviscous current is characterized by $R \sim 4$ and for $h_f = 0.005$,

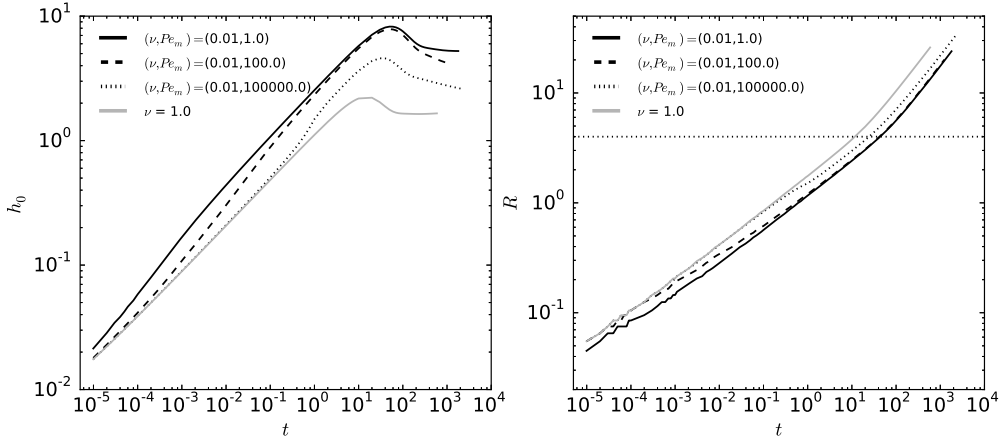


Figure 3.18: Left: Dimensionless thickness at the center h_0 versus dimensionless time for different sets (ν, Pe) indicated on the plot. The grey line represents the isoviscous case $\nu = 1$. Right: Same plot but for the dimensionless radius R . Horizontal black dotted-line represents the transition radius between the bending and the gravity regime.

$h_0 \sim 2$ and $t \sim 10$. In the following, we consider a modified Peclet number $Pe_m = PeSt_m^{-1}$ which integrates the effect of crystallization for clarity.

For a current with a temperature-dependent viscosity, the transition between the bending regime and the gravity regime also occurs when the radius of the current reaches $R \sim 4$ (Figure 3.18). However, the current thickness and time at the transition depend on the thermal state of the flow, i.e. on the combination of (ν, Pe_m) considered (Figure 3.18). For instance, for $\nu = 0.01$ and a small value of Pe , i.e. $Pe = 1.0$, the current transitions to the gravity regime at $t \sim 50$ with $h_0 \sim 8$ while in the third thermal phase of the bending regime. It is then characterized by a cold viscosity $\eta_c = 100$ and a large aspect ratio. In contrast, for a larger value of Pe , i.e. $Pe = 10^5$, the current remains longer in the first phase of the bending regime and it spreads with hot viscosity η_h for a longer period of time. As a consequence, it reaches $R \sim 4$ and enters the gravity regime sooner at $t \sim 30$ while in the second phase of the bending regime and hence characterized by a smaller thickness $h_0 \sim 5$ and a smaller aspect ratio. For even larger Peclet number Pe , the current would transition while in the first thermal phase of the bending regime at $t \sim 10$ and with $h_0 \sim 2$, as in the isoviscous case with viscosity η_h .

Overall, the time for the current to reach the transition t_t is the time for its radius to reach $R(t) = 4$. Setting (3.55) equal to 4, we obtain $t_t = 6.5(\eta_e/\eta_h)^{2/7}h_f^{-1/7}$ where η_e is the effective viscosity of the current (see Section

Chapter 3. Elastic-plated gravity current with temperature-dependent viscosity

Name	From	To	Expression
t_t	Bending	Gravity	$6.5(\eta_e/\eta_h)^{2/7} h_f^{-1/7}$
t_t^h	Bending	Gravity	$6.5h_f^{-1/7}$
t_t^c	Bending	Gravity	$6.5\nu^{-2/7} h_f^{-1/7}$
Bending regime			
t_{b2}	Phase 1	Phase 2	$0.1PeSt_m^{-1}h_f^2$
t_{b3}	Phase 2	Phase 3	$0.03St_m^{-22/27}Pe^{22/27}\nu^{-14/27}h_f^{-7/27}$
Gravity regime			
t_{g2}	Phase 1	Phase 2	$10^{-2}PeSt_m^{-1}$
t_{g3}	Phase 2	Phase 3	$5.2PeSt_m^{-1}\nu^{-1/2}$

Table 3.1: Summary of the different transition times. t_t is the transition time between bending and gravity which is bound by t_t^h , when the current transitions in the first bending thermal phase, and t_t^c , when the current transitions in the third bending thermal phase. t_{b2} (resp. t_{b3}) represents the time to transition from phase 1 to phase 2 (resp. from phase 2 to phase 3) in the bending regime. t_{g2} (resp. t_{g3}) represents the time to transition from phase 1 to phase 2 (resp. from phase 2 to phase 3) in the gravity regime.

3.3.5). In particular, it is bounded by two values corresponding to two end-member cases: the case where the current transitions to the gravity regime while in the first bending phase, i.e. when $\eta_e = \eta_h$ and $t_t^h \sim 6.5h_f^{-1/7}$ and the case where the current transitions to the gravity regime while in the third bending phase, i.e. $\eta_e = \eta_c$ and $t_t^c \sim 6.5\nu^{-2/7}h_f^{-1/7}$. Indeed, when rescaling the time of the simulation by t_t^c , the different simulations, for which the third thermal phase of the bending regime has been reached before the transition to the gravity regime, collapse on the same curve (Figure 3.19, right).

The subsequent evolution in the gravity regime also depends on the combinations (ν, Pe_m) considered. Indeed, in contrast to the bending regime where the effective viscosity is that of a small region at the tip, the effective viscosity is the average flow viscosity in the gravity regime. Therefore, the effective viscosity of the flow can drastically decrease when entering the gravity regime and a flow in the i th thermal phase of the bending regime can transition in the j th thermal phase of the gravity regime with $i \geq j$ which results in 6 possible scenarios. For instance, a current in the second thermal phase of the bending regime can transition into the first or second thermal phase of the gravity current regime. However, the case where a current in the third thermal phase of the bending regime transitions to the first thermal phase of the gravity regime is not possible since the thermal anomaly has already detached from

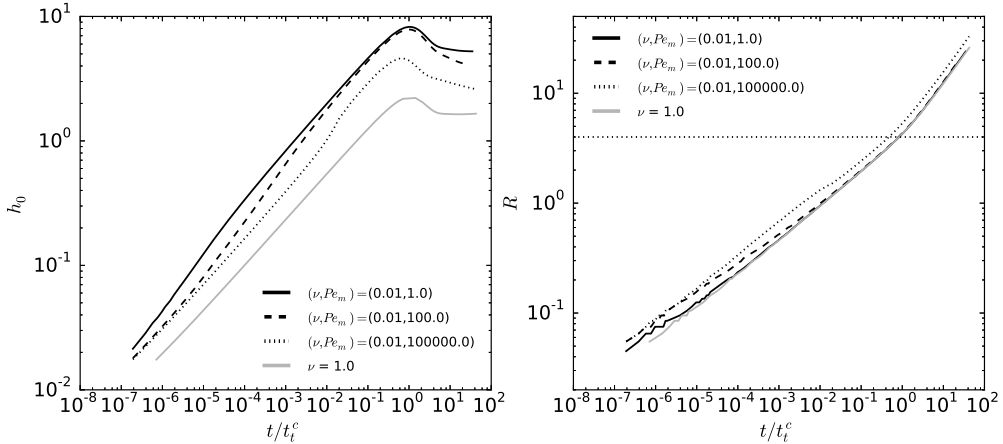


Figure 3.19: Left: Dimensionless thickness at the center h_0 versus time where the time has been rescaled by the time t_t^c the current transitions to the gravity regime while it is in the third bending phase (Table 3.1). The grey line represents the isoviscous case with given viscosity η_h . Right: Same plot but for the dimensionless radius R . Horizontal black dotted-line represents the transition radius between the bending and the gravity regime.

the tip. In the following, we detail the five remaining scenarios in order to build a phase diagram as a function of the combination (ν, Pe_m) considered.

We first consider the case where the current transitions to the gravity regime in the first thermal phase of the bending regime. In that case, the time for the transition is t_t^h ; it is less than the time for the second bending thermal phase change t_{b2} ; comparing t_t^h and t_{b2} gives $Pe > 65h_f^{-15/7}$ (Figure 3.20, Table 3.1). For $Pe > 65h_f^{-15/7}$, as $t_t^h < t_{g2}$, the current transitions to the first thermal phase of the gravity current regime (B_1G_1 in Figure 3.20).

If the current has already reached the third thermal bending phase, the transition occurs at t_t^c and is necessarily larger than t_{b3} ; comparing t_t^c and t_{b3} gives $\nu > 8.3 \cdot 10^{-13} Pe_m^{7/2} h_f^{-1/2}$ (Figure 3.20, Table 3.1). As $t_t^c > t_{g2}$ for $\nu > 8.3 \cdot 10^{-13} Pe_m^{7/2} h_f^{-1/2}$, the current can either transition to the second or third thermal phase of the bending regime. If it transitions to the second phase of the gravity regime, then comparing t_t^c and t_{g3} gives $\nu < 0.3 Pe_m^{14/3} h_f^{2/3}$ (B_3G_2 on Figure 3.20) and if it transitions to the third phase of the gravity current, then $\nu > 0.3 Pe_m^{14/3} h_f^{2/3}$ (B_3G_3 on Figure 3.20).

In the case where the transition occurs when it is in the second bending phase, the time for the transition is not exactly known. However, it is bounded by t_t^h and t_t^c and we can therefore predict some evolution scenarios. Indeed, the transition time is necessarily smaller than t_t^c . Therefore, if $t_t^c < t_{g2}$, i.e.

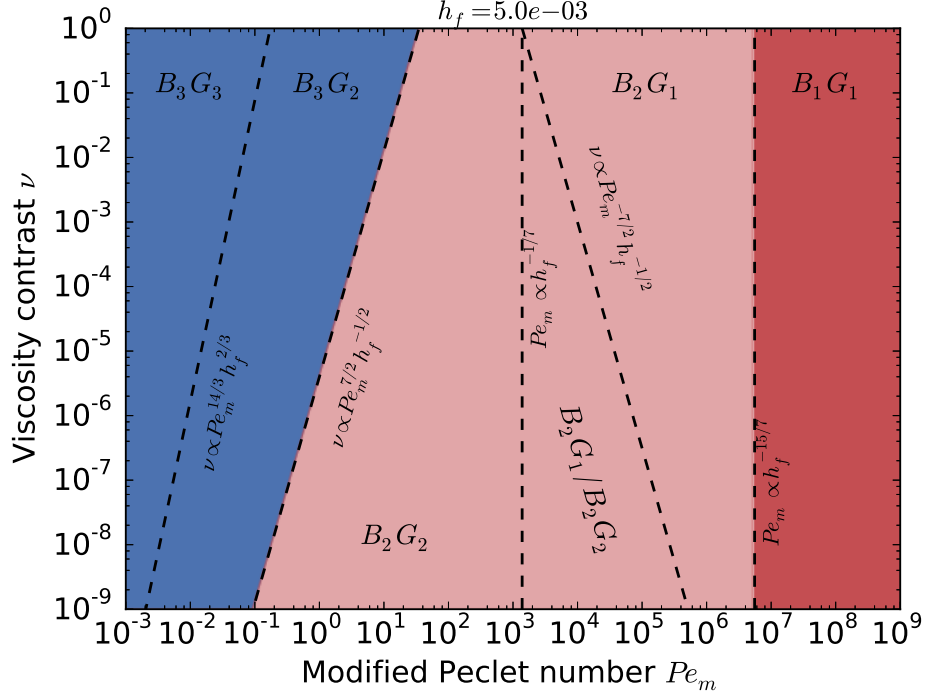


Figure 3.20: Phase diagram for the evolution with bending and gravity for different combinations (ν, Pe_m) and a given value of $h_f = 0.005$. $B_i G_j$ refers to the case where the current transitions from the i th bending thermal phase to the j th gravity thermal phase where i and $j \in \{1, 2, 3\}$.

$\nu > 7.0 \cdot 10^9 Pe_m^{-7/2} h_f^{-1/2}$, the current transitions to the first gravity thermal phase ($B_2 G_1$ on Figure 3.20). Similarly, if $t_t^h > t_{g2}$, i.e. $Pe_m < 650 h_f^{-1/7}$, the current transitions to the second gravity current phase ($B_2 G_2$ on Figure 3.20).

3.6 Summary and conclusion

Isothermal elastic-plated gravity current shows two asymptotic regimes. At early times, the gravity is negligible and the peeling of the front is driven by the bending of the overlying layer. In contrast, at late times, the own flow weight becomes the driving pressure and the current evolves in a gravity current regime. In this study, we have developed a theory for the evolution of an elastic-plated gravity current with a temperature dependent viscosity and studied the response of the flow to its cooling in each regime separately.

In the bending regime, since the flow constantly thickens, the thermal anomaly grows with time but slower than the flow itself and a region of cold

fluid rapidly forms at the front. In contrast, in the gravity current regime, since the flow tends to a constant thickness, the temperature profile diffuses to an almost stationary profile and the thermal anomaly reaches a steady-state. The time to reach this steady-state also scales with the dimensionless numbers of the system. Analyses of the heat transport equation in both regimes allowed us to predict the time evolution of this thermal anomaly as a function of the dimensionless number of the system (Pe, ν, St_m).

Numerical resolution of the equations show that the combine effect of cooling and temperature-dependent viscosity result in important deviations from the isoviscous case. In particular, each regime is split in three different phases: a first phase where the flow behaves as an isoviscous flow with a hot viscosity, a second phase where the flow slows down and drastically thickens and a last phase where the flow returns in an isoviscous flow but with a cold viscosity. These three phases are linked to the coupling between the thermal anomaly and the flow itself and in particular, the second phase of the flow is triggered by the detachment of the thermal anomaly. However, we show that the effective viscosity of the flow is drastically different in the two regimes. While the dynamics is governed by the local thermal state of the front in the bending regime, it is the average thermal structure of the current that controls the flow in the gravity regime.

The final evolution of an elastic-plated gravity current therefore depends on the relative phase change within each regime and on the transition between the bending and the gravity regime itself. We provide a general phase diagram that predicts the different evolution scenarios as a function of the dimensionless parameters. This model for the cooling of an elastic-plated gravity current is further refined and apply to the observation in the next chapter.

CHAPTER 4

Toward a more realistic model and its application to the spreading of shallow magmatic intrusions

Contents

4.1 Motivation	82
4.2 Theory	83
4.2.1 Thermal boundary condition	84
4.2.2 Dimensionless equations	85
4.2.3 Rheology	87
4.2.4 Comparison with the isothermal model	88
4.3 Evolution in the bending regime	89
4.3.1 Relaxing the thermal boundary condition, effect of Ω	90
4.3.2 Considering a more realistic rheology, effect of $\eta(\theta)$	91
4.3.3 Characterization of the thermal anomaly	92
4.4 Evolution in the gravity regime	95
4.4.1 Relaxing the thermal boundary condition, effect of Ω	95
4.4.2 Considering a more realistic rheology, effect of $\eta(\theta)$	97
4.4.3 Characterization of the thermal anomaly	99
4.5 Evolution with bending and gravity in the more realistic model	101
4.6 Application to the spreading of shallow magmatic intrusions	102
4.6.1 Elba Island christmas-tree laccolith complex	102
4.6.2 Low-slope lunar domes	108
4.6.3 Large mafic sills	111
4.6.4 Contact aureole	112
4.7 Summary and discussion	114

The previous chapter was a first step toward the understanding of the coupling between the cooling and the spreading of an elastic-plated gravity current. Hereafter, we investigate the changes in the dynamics caused by both the heating of the wall rocks and a more realistic rheology for the magma. We then compare the model predictions with the observations presented in Chapter 2.

4.1 Motivation

Numerous geological studies demonstrate that magmatic intrusions affect the host rock by developing contact-metamorphic aureoles (*Jaeger*, 1959; *Galushkin*, 1997; *Senger et al.*, 2014). For instance, the Leadville Limestone in Colorado, USA, famous for preserving fossils dating back to the Carboniferous period, was locally transformed into marble following the intrusion of the Treasure Mountain Dome (Figure 4.1). The increase in the geothermal gradient in sedimentary basins also tends to accelerate the thermal maturation of organic matter in the surrounding, promoting hydrocarbon generation (*Senger et al.*, 2014). Release of CO_2 during metamorphic processes has also been proposed to help the formation of ore deposits in the vicinity of magmatic intrusions (*Sillitoe and Thompson*, 1998; *Ganino et al.*, 2008; *Zhou et al.*, 2008).

The size of the contact aureole depends on the context and can reach more than 100% of the intrusion thickness in many regions (*Galushkin*, 1997). This contact aureole, by insulating the flow, may also affect the dynamics of the magmatic intrusion itself. In the following, we relax the isothermal boundary condition used in Chapter 3 to investigate its influence of the dynamics.

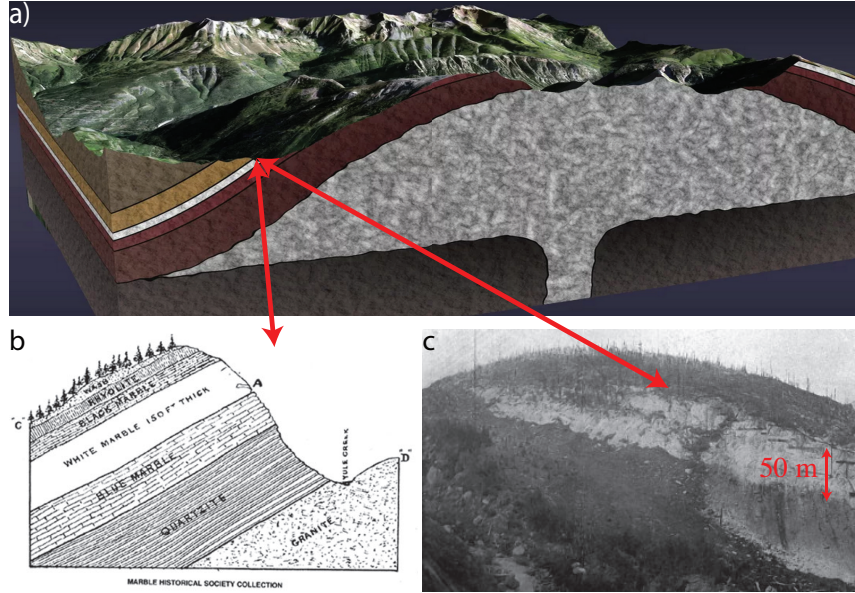


Figure 4.1: a) Sketch of the granitic Treasure Mountain Laccolith intruded roughly ~ 20 Ma years ago in Colorado, USA. The Leadville Limestone (white layer) was metamorphosed by the heat from the intrusion, and was transformed into marble. During the last 10 Ma, the area was eroded, and the marble as well as the laccolith are today exposed at the surface. b) Cross section of the strata from the West flank of the Treasure Mountain dome. c) Marble vein visible from the West flank of the Treasure Mountain. The quality of this Marble was selected to clad the exterior of the Lincoln Memorial and a variety of building throughout the United States.

4.2 Theory

We consider the model of elastic-plated gravity current with temperature-dependent viscosity described in Section 3.2 in which we relax the isothermal boundary condition. In the following, we specify only the changes in theory that come from the new thermal boundary condition and we refer the reader to Section 3.2 for more details about the derivation.

4.2.1 Thermal boundary condition

We now consider the heating of the surrounding medium by the flowing magma. The vertical temperature profile respecting continuity writes

$$T = \begin{cases} T_b - (T_b - T_s)(1 - \frac{z}{\delta})^2 & 0 \leq z \leq \delta \\ T_b & \delta \leq z \leq h - \delta \\ T_b - (T_b - T_s)(1 - \frac{h-z}{\delta})^2 & h - \delta \leq z \leq h \end{cases} \quad (4.1)$$

where $\delta(r, t)$ is the thermal boundary layer thickness, $T(r, z, t)$ is the temperature of the fluid, $T_b(r, t)$ is the temperature at the center of the profile and $T_s(r, t)$ is now the temperature at the surface, i.e. $T(r, z = 0, t) = T(r, z = h, t) = T_s(r, t)$. As in Section 3.2, this profile assures the continuity of the temperature and heat flux within the flow. In addition, continuity of the heat flux across the flow boundaries reads

$$k_m \frac{\partial T}{\partial z} \Big|_{z=0} = k_r \frac{\partial T_r}{\partial z} \Big|_{z=0} \quad (4.2)$$

$$k_m \frac{\partial T}{\partial z} \Big|_{z=h} = k_r \frac{\partial T_r}{\partial z} \Big|_{z=h} \quad (4.3)$$

where $T_r(r, z)$ is the temperature in the surrounding medium and k_r its thermal conductivity. Assuming a semi infinite layer for the rigid layer below the intrusion, *Carslaw and Jaeger* (1959) show that the temperature T_r in the surrounding rocks can be approximated to a first order by

$$T_r(r, z, t) - T_0 = (T_s - T_0) \operatorname{erfc} \left(\frac{-z}{2\sqrt{\kappa_r t}} \right). \quad (4.4)$$

The thickness of the upper layer is equal to the intrusion depth d_c . However, we assume that the depth d_c is large compared to the characteristic length scale for conduction L_c and we use the same approximation to derive T_r above the intrusion

$$T_r(r, z, t) - T_0 = (T_s - T_0) \operatorname{erfc} \left(\frac{z - d_c}{2\sqrt{\kappa_r t}} \right). \quad (4.5)$$

Therefore, the two thermal boundary conditions (4.2) and (4.3) become

$$k_m \frac{\partial T}{\partial z} \Big|_{z=0} = k_r \frac{T_s - T_0}{\sqrt{\pi \kappa_r t}} \quad (4.6)$$

$$k_m \frac{\partial T}{\partial z} \Big|_{z=h} = -k_r \frac{T_s - T_0}{\sqrt{\pi \kappa_r t}}. \quad (4.7)$$

4.2.2 Dimensionless equations

Except for the conduction term, which now accounts for the dimensionless surface temperature Θ_s , the coupled dimensionless equations governing the cooling of the flow are very similar to (3.46) and (3.47) and read

$$\frac{\partial h}{\partial t} - \frac{12}{r} \frac{\partial}{\partial r} \left(r I_1(h) \frac{\partial P}{\partial r} \right) = \mathcal{H} \left(\frac{\gamma}{2} - r \right) \frac{32}{\gamma^2} \left(\frac{1}{4} - \frac{r^2}{\gamma^2} \right) \quad (4.8)$$

$$\frac{\partial \xi}{\partial t} + \frac{1}{r} \frac{\partial}{\partial r} (r (\bar{u} \xi - \Sigma)) = 2Pe^{-1} St_m \frac{\Theta_b - \Theta_s}{\delta} \quad (4.9)$$

with

$$\bar{\theta} = \frac{1}{3} (2\Theta_b + \Theta_s) \quad (4.10)$$

$$\bar{u} = \frac{12}{\delta} \frac{\partial P}{\partial r} (\delta I_0(\delta) - I_1(\delta)) \quad (4.11)$$

$$\Sigma = \frac{12}{\delta} \frac{\partial P}{\partial r} (I_0(\delta) (G(\delta) - \delta \bar{\theta}) + \bar{\theta} I_1(\delta) - I_2(\delta)). \quad (4.12)$$

where $G(z)$ denotes a primitive of $\theta(z)$ when $z < \delta$. The rheology, which couples equations (4.8) and (4.9), is contained in the three integrals $I_0(z)$, $I_1(z)$ and $I_2(z)$ and is discussed in the next section. The thermal boundary conditions (4.6) and (4.7) reduce in a dimensionless form to

$$2 \frac{\Theta_b - \Theta_s}{\delta} = \beta(t) \Theta_s \quad (4.13)$$

where

$$\beta(t) = \frac{\Omega_1 \Omega_2^{-1/2} Pe^{1/2}}{\sqrt{\pi t}}. \quad (4.14)$$

Ω_1 and Ω_2 are two new dimensionless numbers and read

$$\Omega_1 = \frac{\kappa_r}{\kappa_m} \quad (4.15)$$

$$\Omega_2 = \frac{k_r}{k_m} \quad (4.16)$$

They represent the ratio of wall rocks to magma thermal diffusivity (4.15) and thermal conductivity (4.16) respectively. While the former should be close to 1, the later could show small variations depending on the nature of the surrounding rocks as well as its porosity content (*Büttner et al., 1998*). However, variations of both dimensionless numbers will only affect the size of the thermal aureole. In this Chapter, we focus mainly on the dynamics of the

flow itself and for a sake of simplicity, we rather consider only the combination of both which we call Ω and reads

$$\Omega = \Omega_1 \Omega_2^{-1/2} \quad (4.17)$$

$$= \frac{\kappa_r}{\kappa_m} \left(\frac{k_m}{k_r} \right)^{1/2} \quad (4.18)$$

It represents the ratio between heat conduction at the contact with the enclosing rocks and heat diffusion within the fluid and quantify how much heat is transferred to the wall rocks.

As in the precedent chapter, the heat transport equation (4.9) is written in terms of ξ which represents our “thermal variable”. In that case, ξ writes

$$\xi = \frac{\delta}{3} (-2\Theta_b - \Theta_s + 3) \quad (4.19)$$

where we have used (4.10) in (4.19). In addition, from (4.13), we can derive an expression for Θ_s , δ and Θ_b as a function of the other variables

$$\Theta_s = \frac{2\Theta_b}{\beta\delta + 2}, \quad (4.20)$$

$$\delta = \frac{1}{\Theta_s \beta} (2\Theta_b - 2\Theta_s), \quad (4.21)$$

$$\Theta_b = \frac{\Theta_s}{2} (\beta\delta + 2). \quad (4.22)$$

When the thermal boundary layers have just merged, then $\Theta_b = 1$, $\delta = h/2$ and injecting (4.20) into (4.19) gives

$$\xi_t(t) = \frac{\beta(t)h^2(r,t)}{6\beta(t)h(r,t) + 24}. \quad (4.23)$$

Therefore, when $\xi < \xi_t$, the thermal boundary layers are not merged, $\Theta_b = 1$ and injecting (4.21) into (4.19) and solving for Θ_s gives

$$\Theta_s = \frac{3\beta}{4}\xi - \frac{\sqrt{3}}{4}\sqrt{\beta\xi(3\beta\xi + 8)} + 1. \quad (4.24)$$

In contrast, when $\xi > \xi_t$, the thermal boundary layers have merged, $\delta = h/2$ and injecting (4.22) into (4.19) and solving for Θ_s gives

$$\Theta_s = \frac{-12\xi + 6h}{(\beta h + 6)h}. \quad (4.25)$$

In the end, we then have

$$\Theta_s(r,t) = \begin{cases} \frac{3\beta}{4}\xi - \frac{\sqrt{3}}{4}\sqrt{\beta\xi(3\beta\xi + 8)} + 1 & \text{if } \xi \leq \xi_t \\ \frac{-12\xi + 6h(r,t)}{(\beta h(r,t) + 6)h(r,t)} & \text{if } \xi > \xi_t \end{cases} \quad (4.26)$$

and

$$\Theta_b(r) = \begin{cases} 1 & \text{if } \xi \leq \xi_t \\ \frac{\Theta_s}{4} (\beta(t)h(r,t) + 4) & \text{if } \xi > \xi_t \end{cases} \quad (4.27)$$

$$\delta(r) = \begin{cases} \frac{1}{\Theta_s \beta(t)} (-2\Theta_s + 2) & \text{if } \xi \leq \xi_t \\ h(r,t)/2 & \text{if } \xi > \xi_t \end{cases} \quad (4.28)$$

with

$$\xi_t(t) = \frac{\beta(t)h^2(r,t)}{6\beta(t)h(r,t) + 24} \quad (4.29)$$

4.2.3 Rheology

The model derived in Section 4.2.2 does not yet assume a specific relation between viscosity and temperature and the choice of the rheology $\eta(T)$, which is contained in the integrals $I_0(z)$, $I_1(z)$ and $I_2(z)$, remains to be defined. In Section 3.2, we assumed a viscosity inversely dependent on the temperature which reads in a dimensional form

$$\eta(T) = \frac{\eta_h \eta_c (T_i - T_0)}{\eta_h (T_i - T_0) + (\eta_c - \eta_h)(T - T_0)}. \quad (4.30)$$

where η_h and η_c are the viscosities of the hottest and coldest fluid at the temperature T_i and T_0 respectively (Bercovici, 1994). While this model possesses some nice simplification properties, it restricts the change in viscosity to a very narrow range of temperatures close to $T = T_0$, i.e. $\theta = 0$ (Figure 4.2). In contrast, the Arrhenius model ($\eta \sim \exp(-k/T)$), which is a more realistic model to relate temperature and viscosity for lavas (Blatt et al., 2006), describes a viscosity that increases over a much larger range of temperatures (Figure 4.2). To get some insights into the effect of a more realistic temperature-dependent viscosity, we thus also use a first-order approximation of the Arrhenius model as a second rheology $\eta_2(T)$ (Diniega et al., 2013)

$$\eta_2(T) = \eta_h \exp \left(-\log \left(\frac{\eta_h}{\eta_c} \right) \left(1 - \frac{T - T_0}{T_i - T_0} \right) \right) \quad (4.31)$$

In a dimensionless form, they read

$$\eta_1(\theta)/\eta_h = \frac{1}{\nu + (1 - \nu)\theta} \quad (4.32)$$

$$\eta_2(\theta)/\eta_h = \exp(-\log(\nu)(1 - \theta)) \quad (4.33)$$

where ν is the viscosity contrast which described in Section 3.2 and represents the ratio between the hot viscosity η_h and the cold viscosity η_c . The expression of $I_0(\delta)$, $I_1(\delta)$, $I_1(h)$ and $I_2(\delta)$, necessary to close the model, are given in Appendix A for both rheologies.

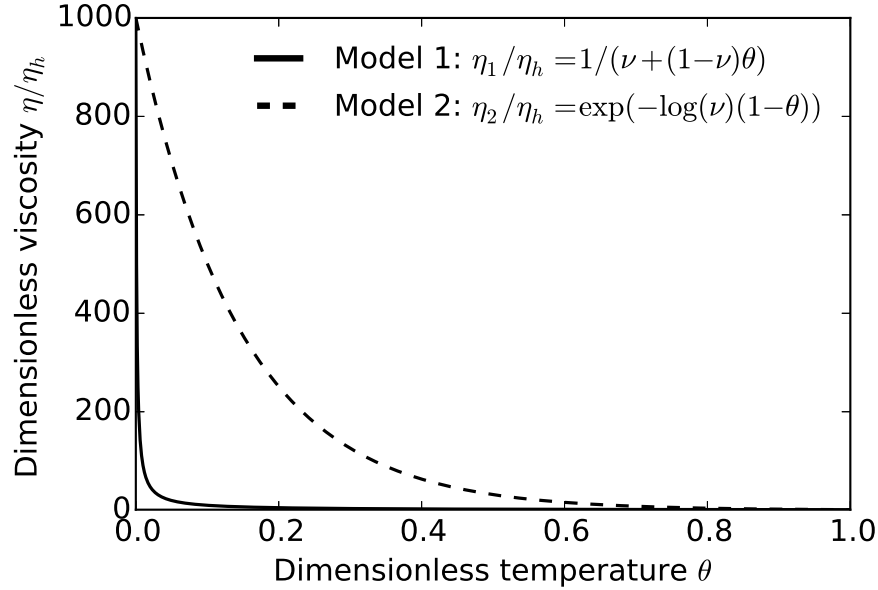


Figure 4.2: Dimensionless viscosity versus dimensionless temperature for both rheologies η_1 (4.32) and η_2 (4.33) using $\nu = 0.001$.

4.2.4 Comparison with the isothermal model

We showed that relaxing the isothermal boundary condition introduces a new dimensionless number Ω which controls how much heat can be transferred to the surrounding rocks. In the limit $\Omega \rightarrow \infty$, the model should thus reduce to the model described in Section 3.2. Indeed, when $\Omega \rightarrow \infty$, the coefficient $\beta \rightarrow \infty$ and then $\xi_t \rightarrow h/6$ (Section 3.2.7.1). When $\xi < \xi_t$, injecting the corresponding expression of Θ_s (4.26) in the corresponding expression of δ (4.28) gives

$$\delta = \frac{3\beta\xi + \sqrt{3}\sqrt{\beta\xi(3\beta\xi + 8)} + 8}{2\beta} \quad (4.34)$$

which indeed tends to 3ξ when $\beta \rightarrow \infty$ as in Section 3.2.7.1. When $\xi > \xi_t$, injecting the corresponding expression of Θ_s (4.26) in the corresponding expression of Θ_b (4.27) gives

$$\Theta_b = \frac{3(\beta h + 4)(h - 2\xi)}{2h(\beta h + 6)} \quad (4.35)$$

which indeed tends to $3/2 - 3\xi/h$ when $\beta \rightarrow \infty$ (Section 3.2.7.1). Finally, taking the limit of Θ_s for both $\xi > \xi_t$ and $\xi < \xi_t$ show that Θ_s indeed tends to zero when $\Omega \rightarrow \infty$.

For magmatic intrusions, the thermal parameters of the magma and the encasing rocks are close and the dimensionless number Ω would be close to 1. In the following, we study the effect of relaxing the isothermal boundary condition on the dynamics by comparing $\Omega = 10^5$ and $\Omega = 1$ in both regimes separately. We also investigate the effect of a more realistic rheology on the flow dynamics.

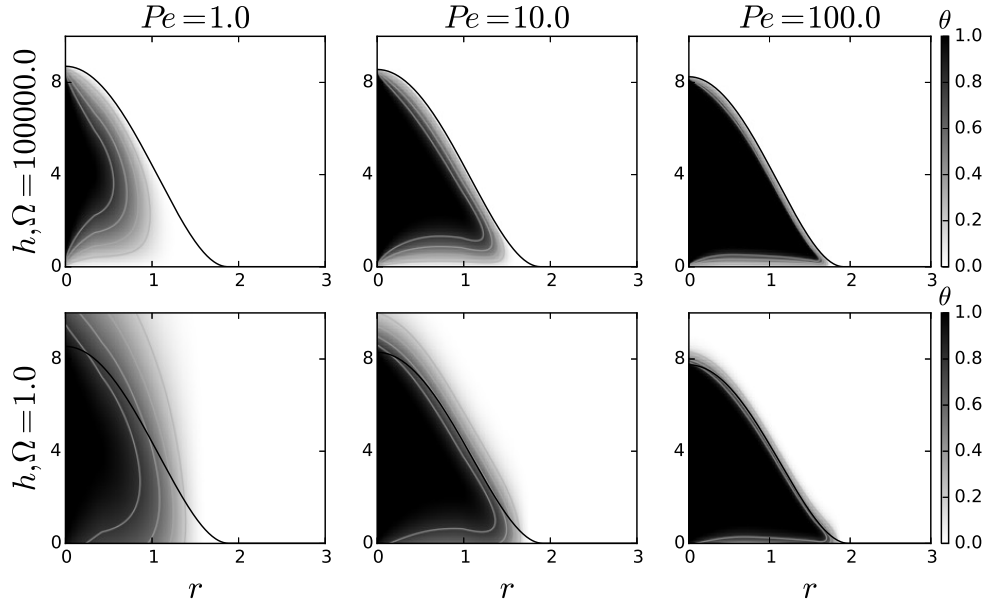


Figure 4.3: Snapshots of the flow thermal structure $\theta(r, z, t)$ for different sets (Pe, Ω) with $Pe = 1.0, 10.0, 100.0$, $\Omega = 10^5$ and 1.0 at $t = 10$ for $\nu = 0.001$. The thermal structure above the intrusion is given by (4.5) and reads in a dimensionless form $\Theta_r(r, z, t) = \Theta_s(r, t) \operatorname{erfc} \left(Pe^{1/2} \Omega_1 \frac{(z-h)}{2\sqrt{t}} \right)$ where Ω_1 is set to 1. The thermal structure below the intrusion is similar and not shown for clarity.

4.3 Evolution in the bending regime

We follow the same approach as in the previous Chapter and first concentrate on the case in which only bending contributes to the dynamic pressure. The governing equations are thus (4.8) and (4.9) where $P = \nabla_r^4 h$. For isothermal boundary conditions, we show that the dynamics in the bending regime depends on the average viscosity of a small region at the front of the current and can be divided into three phases. Hereafter, we first describe how the thermal

boundary condition influences the timing for the phase transition by looking at two values for the dimensionless number Ω , i.e. $\Omega = 1$ and $\Omega = 10^5$ and $\eta(\theta) = \eta_1(\theta)$. We then investigate the effect of changing the rheology.

4.3.1 Relaxing the thermal boundary condition, effect of Ω

Heating of the surrounding medium acts to limit heat loss in the flow central region and the thermal anomaly is larger (Figure 4.3). For instance, for $\nu = 0.001$ and $Pe = 1.0$, while the thermal anomaly extends over 50% of the current for $\Omega = 10^5$ at $t = 10$, it makes up more than 75% of the flow for $\Omega = 1$ (Figure 4.3). Nevertheless, the thin tip of the current is still rapidly cooling and the radius of the flow still grows faster than the thermal anomaly extent when relaxing the thermal boundary condition.

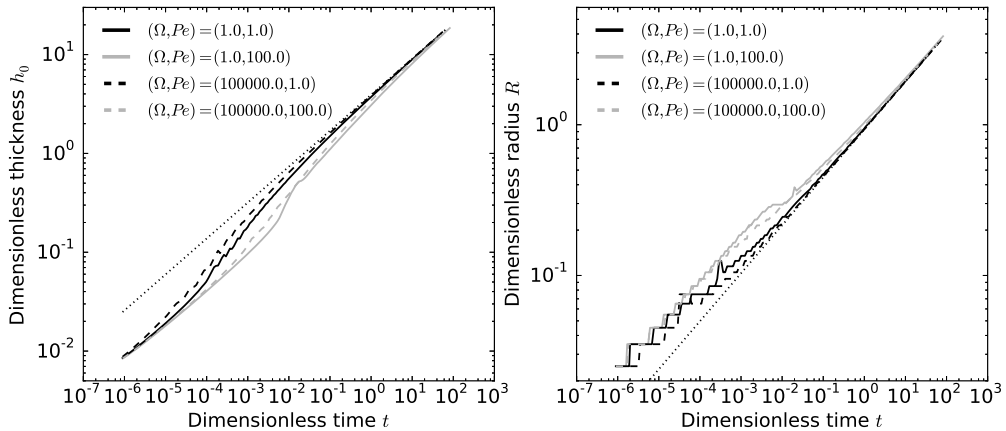


Figure 4.4: Left: Dimensionless thickness at the center h_0 versus dimensionless time t for different sets (Ω, Pe) indicated on the plot. Dotted-line: scaling law $h_0 = 0.7h_f^{-1/11}\nu^{-2/11}t^{8/22}$ for $\nu = 0.001$. Right: Dimensionless radius R versus dimensionless time t for the same sets (Ω, Pe) . Dotted-line: scaling law $R = 2.2h_f^{1/22}\nu^{1/11}t^{7/22}$ for $\nu = 0.001$. In all simulations, $\nu = 0.001$ and $\eta(\theta) = \eta_1(\theta)$.

Hence, the dynamics for $\Omega = 1$ also passes through three different phases. The current first behaves as an isoviscous flow with hot viscosity, it then slows down and thickens to finally behave again as an isoviscous flow but with a cold viscosity (Figure 4.4). As the current tip remains hot for a longer period of time, the transitions to the second and third bending regime are however delayed relatively to the case where $\Omega = 10^5$ (Figure 4.4). For instance, for

$\nu = 10^{-3}$ and $Pe = 1.0$, while the transition to the second bending phase already begins at $t \sim 10^{-6}$ for $\Omega = 10^5$, it occurs only after $t \sim 10^{-5}$ for $\Omega = 1.0$ (Figure 4.4).

In addition, the second phase of thickening shows two different stages for $\Omega = 1.0$ and $Pe = 100.0$, a first stage where the thickness drastically increases and a second stage where it continues to increase but at a much slower rate (Figure 4.4). This transition, enhanced by the new thermal boundary condition, reflects the detachment of the thermal anomaly in the second bending phase and is discussed in Appendix C.2.

4.3.2 Considering a more realistic rheology, effect of $\eta(\theta)$

The first order Arrhenius rheology $\eta_2(\theta)$ widens the range of temperature over which significant viscosity variation occurs, i.e. $\sim 80\%$ of the temperature range against $\sim 10\%$ for $\eta_1(\theta)$ (Figure 4.2).

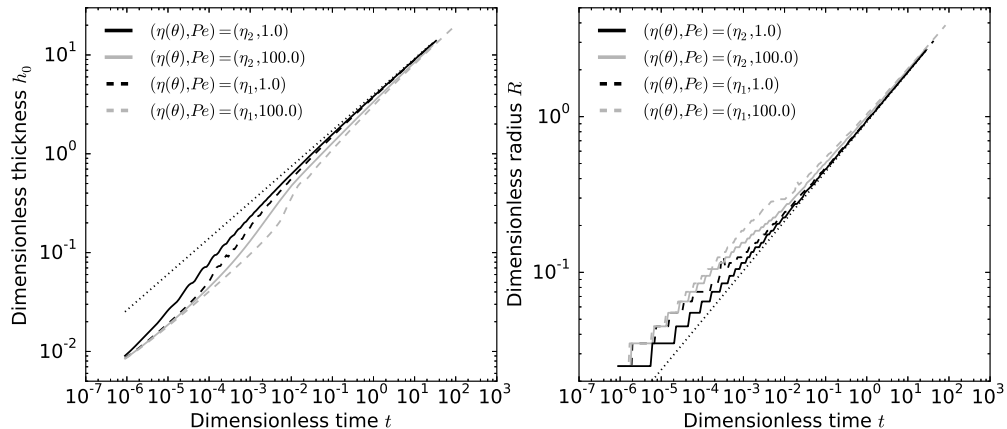


Figure 4.5: Left: Dimensionless thickness at the center h_0 versus dimensionless time t for different sets (η, Pe) indicated on the plot. Dotted-line: scaling law $h_0 = 0.7h_f^{-1/11}\nu^{-2/11}t^{8/22}$ for $\nu = 0.001$. Right: Dimensionless radius R versus dimensionless time t for the same sets (η, Pe) . Dotted-line: scaling law $R = 2.2h_f^{1/22}\nu^{1/11}t^{7/22}$ for $\nu = 0.001$. In all simulations, $\nu = 0.001$ and $\Omega = 1.0$.

Therefore, the effective flow viscosity starts to increase sooner and the transition to the second bending phase occurs sooner than for the rheology previously considered $\eta_1(\theta)$ (Figure 4.5). For instance, for $\nu = 10^{-3}$ and $Pe = 1.0$, while the second phase of the flow starts around $t \sim 10^{-5}$ for the rheology $\eta_1(\theta)$, it starts around $t \sim 10^{-6}$ for the rheology $\eta_2(\theta)$ (Figure 4.5). In particular, the change in rheology almost compensates for the delay caused by

the heating of the surrounding medium. For instance, the transition time for the second bending phase for a flow characterized by $\eta = \eta_1(\theta)$ and $\Omega = 10^5$ is almost the same than for a flow characterized by $\eta = \eta_2(\theta)$ and $\Omega = 1$ (Figure 4.4 and 4.5).

4.3.3 Characterization of the thermal anomaly

As in Chapter 3, we quantify the size of the thermal anomaly through a critical thermal radius $R_c(t)$ where the temperature at the center of the flow Θ_b is 1% of the injection temperature, i.e. $\Theta_b(r = 0) - \Theta_b(r = R_c) = 0.99$. As expected, the thermal anomaly is larger when relaxing the thermal boundary condition and changing the rheology $\eta(\theta)$ has almost no effect on its evolution (Figure 4.6). In addition, the extent of the cold fluid region $R(t) - R_c(t)$ is growing slightly slower with time when considering $\Omega = 1$ in comparison to the isothermal boundary case $\Omega = 10^5$ (Figure 4.6). In the following, we characterize the thermal anomaly evolution in the more realistic case where $\Omega = 1$ and $\eta(\theta) = \eta_2(\theta)$.

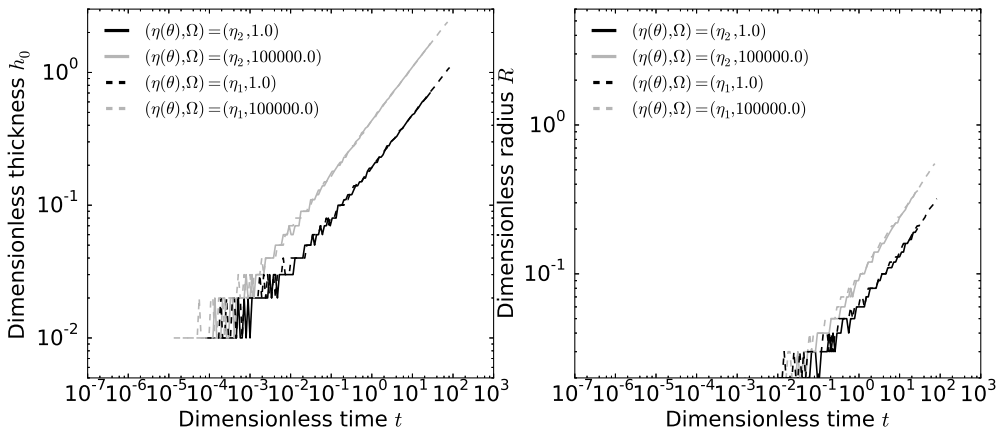


Figure 4.6: Left: Extent of the cold fluid region $R(t) - R_c(t)$ versus dimensionless time for different combinations (η, Ω) indicated on the plot, $\nu = 0.01$ and $Pe = 1.0$. Same plot but for $Pe = 100.0$.

As in Section 3.3.4, the size of the thermal anomaly $R_c(t)$ is given by the radius where advection of heat is equal to heat loss

$$\frac{d}{dt} (\theta(r = R_c, t)) \approx Pe^{-1} \frac{\partial^2}{\partial z^2} (\theta(r = R_c, t)) \quad (4.36)$$

which, by integration over the thickness of the flow h , becomes

$$\begin{aligned} \frac{d}{dt} \left(\int_0^h \theta dz \right) - \Theta_s \frac{dh}{dt} &\approx Pe^{-1} \frac{\Theta_b - \Theta_s}{h} \\ \bar{\theta} \frac{dh}{dt} + h \frac{d\bar{\theta}}{dt} - \Theta_s \frac{dh}{dt} &\approx Pe^{-1} \frac{\Theta_b - \Theta_s}{h} \\ \frac{2}{3} (\Theta_b - \Theta_s) \frac{dh}{dt} + h \frac{d\bar{\theta}}{dt} &\approx Pe^{-1} \frac{\Theta_b - \Theta_s}{h} \end{aligned} \quad (4.37)$$

where $\bar{\theta}$ is equal to $(\int_0^h \theta dz)/h$ here. Using the thickness profile (3.50), (4.37) becomes

$$\begin{aligned} \alpha^2 \left(1 + \frac{R_c}{R} \right)^2 \left(\frac{2}{3} (\Theta_b - \Theta_s) \frac{dh_0}{dt} + h_0 \frac{d\bar{\theta}}{dt} \right) + \\ \frac{8h_0 R_c^2 (\Theta_b - \Theta_s)}{3R^3} \frac{dR}{dt} \alpha \left(1 + \frac{R_c}{R} \right) &\approx \frac{Pe^{-1} (\Theta_b - \Theta_s)}{\alpha^2 \left(1 + \frac{R_c}{R} \right)^2 h_0} \end{aligned} \quad (4.38)$$

where $\alpha(t)$ is the normalized region beyond $r = R_c(t)$, i.e. $\alpha(t) = (R(t) - R_c(t))/R(t)$. In the limit $\alpha \ll 1$, i.e. $R_c/R \sim 1$, and neglecting the higher order terms in (4.38) ($\propto \alpha^2$), we obtain the same scaling law for the size of the normalized cold front region α than the one found in Section 3.3.4. However, it clearly does not match the prediction when $\Omega = 1.0$ (Figure 4.7) and the new thermal anomaly evolution must be linked to a change in the heat advection rate, i.e. the left hand side term in the balance (4.38). Neglecting the advection term to keep only the inflation term instead in (4.38) leads to

$$\alpha^2 \left(1 + \frac{R_c}{R} \right)^2 \frac{dh_0}{dt} \approx \frac{Pe^{-1}}{\alpha^2 \left(1 + \frac{R_c}{R} \right)^2 h_0} \quad (4.39)$$

which, in the limit $\alpha \ll 1$, becomes

$$\alpha^4 \frac{\partial h_0}{\partial t} \approx \frac{Pe^{-1}}{h_0 \frac{\partial h_0}{\partial t}}. \quad (4.40)$$

Substituting $h_0(t)$ by its respective scaling law (3.54), the relative size of the normalized cold front region α reads

$$\alpha(t) \propto h_f^{1/22} \nu^{1/11} Pe^{-1/4} t^{7/44} \quad (4.41)$$

which is equivalent to

$$R(t) - R_c(t) = 0.8h_f^{1/11} \nu^{2/11} Pe^{-1/4} t^{17/44} \quad (4.42)$$

where the numerical prefactor, which depends on the definition of the thermal anomaly, has been chosen to fit the simulations.

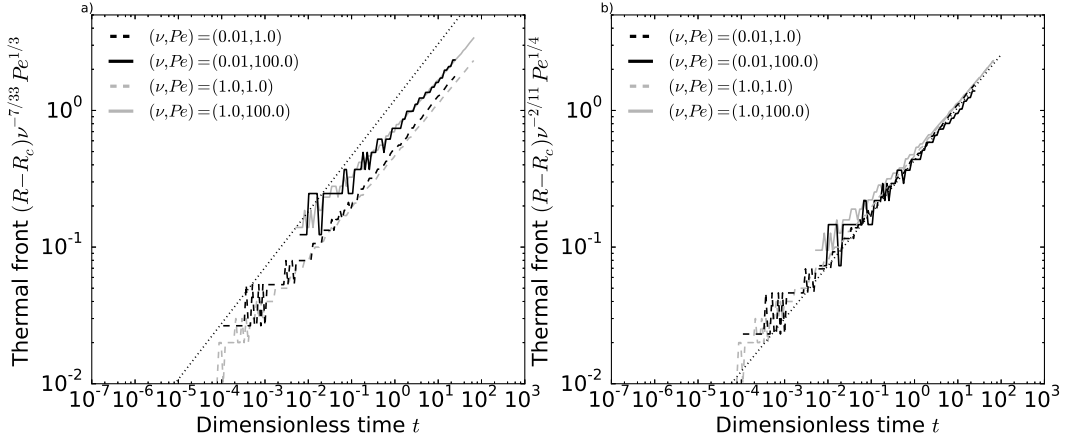


Figure 4.7: a) Extent of the cold fluid region $R(t) - R_c(t)$ rescaled by $P_e^{-1/3}\nu^{7/33}$ versus time for different combinations (ν, Pe) indicated on the plot. Dotted-line: scaling law (3.59) $(R(t) - R_c(t))Pe^{1/3}\nu^{-7/33} = 2.1h_f^{7/66}t^{9/22}$ derived in Section 3.3.5 b) Same plot but where we rescale the extent of the cold fluid region by $P_e^{-1/4}\nu^{2/11}$. Dotted-line: scaling law $(R(t) - R_c(t))Pe^{1/4}\nu^{-2/11} = 0.7h_f^{1/11}t^{17/44}$. In all simulations, $\Omega = 1.0$ and $\eta(\theta) = \eta_2(\theta)$.

This new scaling law for the evolution of the extent of the cold fluid region (4.42) shows a much better fit with the simulations (Figure 4.7 b). Indeed, in that case, the constant heating of the surrounding medium limits the expansion of the cold fluid region in comparison to the isothermal case. In particular, the thermal anomaly reaches the third bending phase much later and therefore, the scaling law corresponds to the evolution of the thermal anomaly in the second bending phase; a phase dominated by inflation. Therefore, the evolution of the thermal anomaly is governed by the inflation rate at the intrusion tip when relaxing the thermal boundary condition.

The cold fluid region grows effectively slightly slower, with a time exponent equal to $17/44$ instead of $9/22$ ($17/44 \sim 0.38$, $9/22 \sim 0.40$) and the dependence in the Peclet number Pe is weaker, i.e. it changes from a power $1/3$ to $1/4$. Indeed, for small Pe , vertical diffusion is efficient on the emplacement time scale and rapidly heats up the surrounding medium. The heat loss in the interior is smaller and the thermal anomaly larger in comparison to the case where $\Omega = 10^5$. In contrast, for large values of Pe , advection dominates and the saving of heat by insulation is less important decreasing the overall difference between small and large values of Pe .

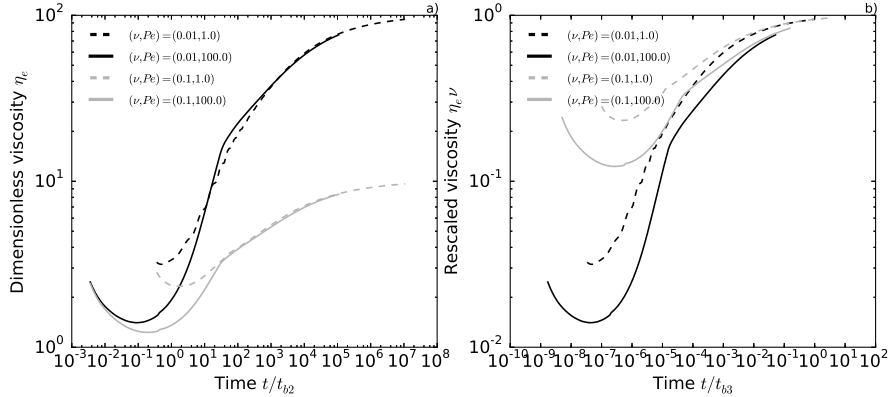


Figure 4.8: a) Dimensionless effective viscosity versus time where the time has been rescaled by the time for the flow to enter the second phase t_{b2} . b) Same as left but where we rescale the viscosity by ν and the time by t_{b3} . In all simulations, $\Omega = 1.0$ and $\eta(\theta) = \eta_2$.

As we show in Section 4.3.2, the time t_{b2} for the current to enter the second bending phase does not change much as the delay induced by the heating of the surrounding medium is offset by the change in rheology. Accordingly, we use the time t_{b2} (3.63) defined in section 3.3.5 as the time to cool the thin prewetting film to characterize the first bending transition (Figure 4.8 a). In contrast, the time t_{b3} for the current to enter the third phase of the flow is now larger. Processing as in Section 3.3.5 but using (4.42) for the evolution of the cold fluid region $R(t) - R_c(t)$ instead of (3.59), we find that t_{b3} is given by

$$t_{b3} = 0.4 h_f^{-4/17} \nu^{-8/17} Pe^{11/17} St_m^{-11/17} \quad (4.43)$$

4.4 Evolution in the gravity regime

As in chapter 3, we now consider the late time behavior in which only the weight of the fluid contributes to the dynamic pressure P . The governing equations are (4.8) and (4.9) where $P = h$. We follow the same framework as in the previous section.

4.4.1 Relaxing the thermal boundary condition, effect of Ω

As in the bending regime, for a small value of Ω , the heating of the surrounding medium insulates the current and the thermal anomaly is larger. For instance,

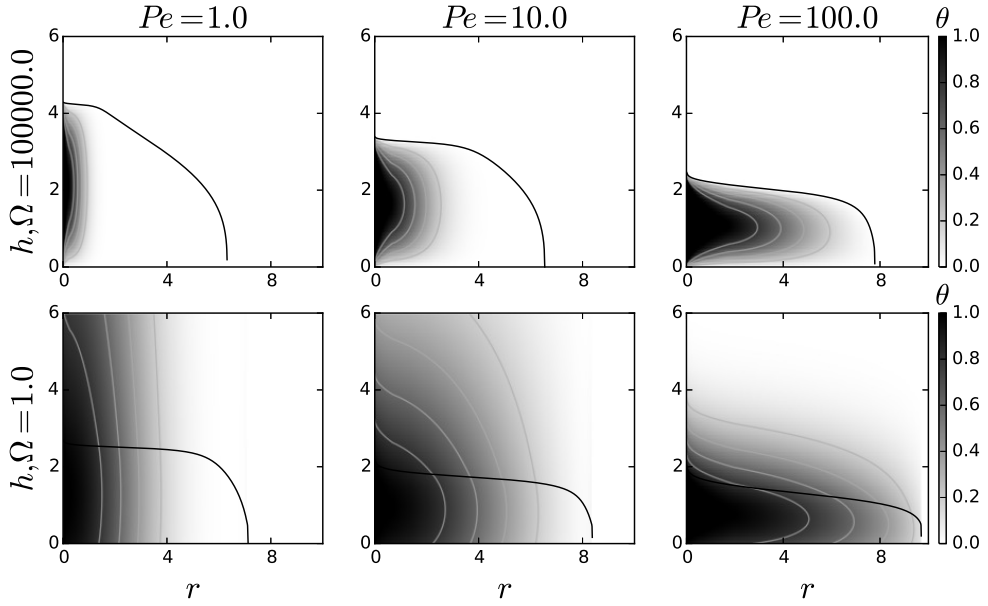


Figure 4.9: Snapshots of the flow thermal structure $\theta(r, z, t)$ for different sets (Pe, Ω) with $Pe = 1.0, 10.0, 100.0$ and $\Omega = 10^5$ and 1.0 at $t = 100$ for $\nu = 0.01$. The thermal structure above the intrusion is given by (4.5) and reads in a dimensionless form $\Theta_r(r, z, t) = \Theta_s(r, t) \operatorname{erfc}\left(Pe^{1/2} \Omega_1 \frac{(z-h)}{2\sqrt{t}} \right)$ where Ω_1 is set to 1. The thermal structure below the intrusion is similar and not shown for clarity.

for $Pe = 1$ and $\nu = 0.01$ at $t = 100$, while $R_c \sim 1$ for $\Omega = 10^5$, R_c is larger than 5 for $\Omega = 1$ (Figure 4.9). In addition, after it detaches from the current tip, the thermal anomaly does not reach a steady-state profile but keeps growing with time instead (Figure 4.10). Indeed, in contrast to the isothermal boundary case, the constant increase of the surface temperature continuously decreases the heat loss in the central region of the current which allows an expansion of the thermal anomaly.

For small values of Pe , the important heating of the surroundings medium results in a flow that is almost vertically isothermal (Figure 4.9 and 4.10). In contrast, for large values of Pe , the vertical diffusion of heat is less efficient, the thermal aureole is restricted to a small region around the intrusion, the thermal anomaly is larger and the temperature gradient within the flow are stronger (Figure 4.9).

While three phases also characterize the dynamics when $\Omega = 1.0$, their durations are modified by the new thermal boundary condition (Figure 4.11). In particular, the current remains hot for a longer period of time and the

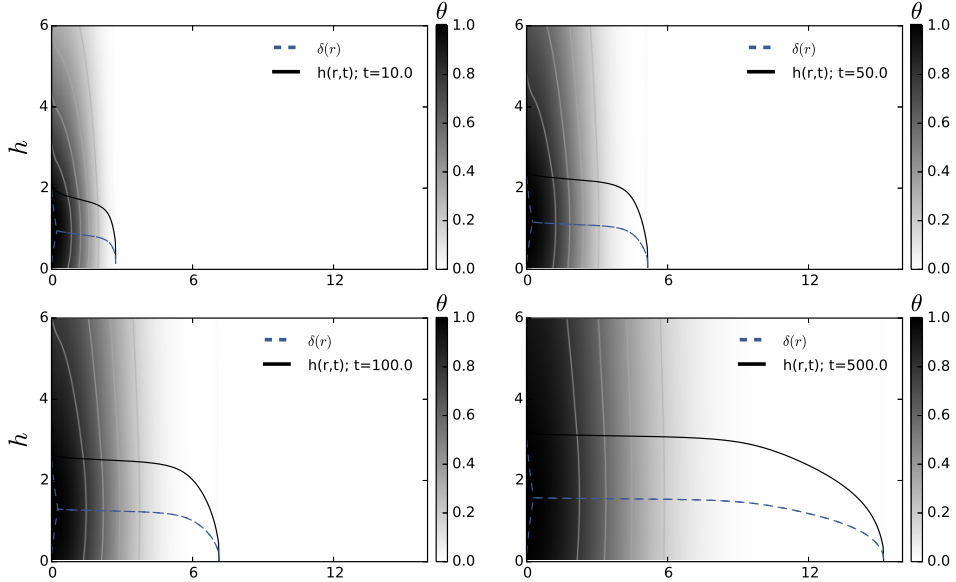


Figure 4.10: Snapshots of the flow thermal structure $\theta(r, z, t)$ at different times indicated on the plot. Dashed lines represent the thermal boundary layers. Solid grey lines are isotherms for $\theta = 0.2, 0.4, 0.6$ and 0.8 . Here, $\nu = 0.01$, $Pe = 1.0$ and $St_m = 1$. The thermal structure above the intrusion is given by (4.5) and reads in a dimensionless form $\Theta_r(r, z, t) = \Theta_s(r, t) \operatorname{erfc} \left(Pe^{1/2} \Omega_1 \frac{(z-h)}{2\sqrt{t}} \right)$ where Ω_1 is set to 1. The thermal structure below the intrusion is similar and not shown for clarity.

second phase is delayed in comparison to the case where $\Omega = 10^5$. For instance, for $\nu = 0.01$ and $Pe = 1.0$, while the first transition occurs at $t \approx 0.1$ for $\Omega = 10^5$, it happens only after $t \approx 1$ for $\Omega = 1$ (Figure 4.11). As the thermal anomaly does not reach a steady state for $\Omega = 1$, the cooling of the current in the second gravity phase is also slower than for $\Omega = 10^5$ and the current reaches the third phase also much later for $\Omega = 1$ (Figure 4.11). In the next section, we consider the effect of the first order Arrhenius rheology on the dynamics for $\Omega = 1.0$.

4.4.2 Considering a more realistic rheology, effect of $\eta(\theta)$

As in the bending regime, the chosen rheology $\eta(\theta)$ also affects the timing for the phase transition, and, in particular, these transitions occur sooner for the first order Arrhenius rheology $\eta_2(\theta)$ than for $\eta = \eta_1(\theta)$. In particular, the delay induced in the phase transitions by the heating of the surrounding medium is almost offset by the first order Arrhenius rheology. For instance,

**Chapter 4. Toward a more realistic model and its application to
100 the spreading of shallow magmatic intrusions**

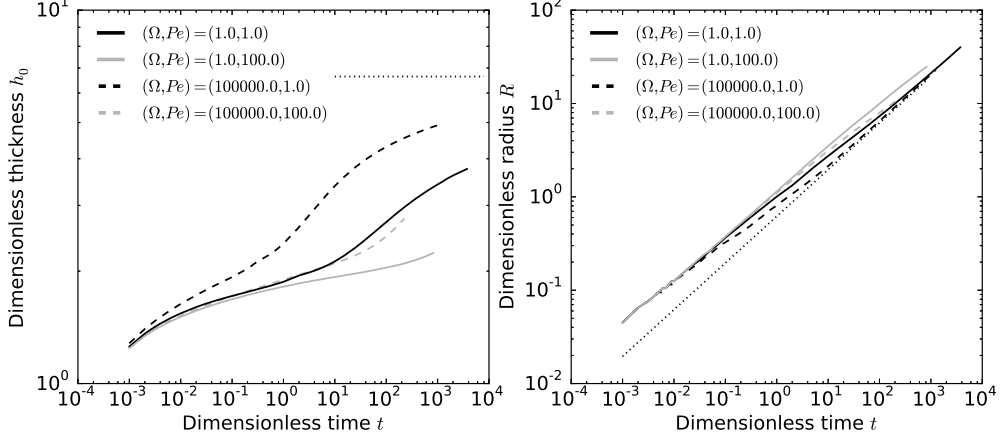


Figure 4.11: Left: Dimensionless thickness at the center h_0 versus dimensionless time t for different sets (Ω, Pe) indicated on the plot. Dotted-line: scaling law $h_0 = 0.7h_f^{-1/11}\nu^{-2/11}t^{8/22}$ for $\nu = 0.01$. Right: Dimensionless radius R versus dimensionless time t for the same sets (Ω, Pe) . Dotted-line: scaling law $R = 2.2h_f^{1/22}\nu^{1/11}t^{7/22}$ for $\nu = 0.01$. In all simulations, $\nu = 0.01$ and $\eta(\theta) = \eta_1$.

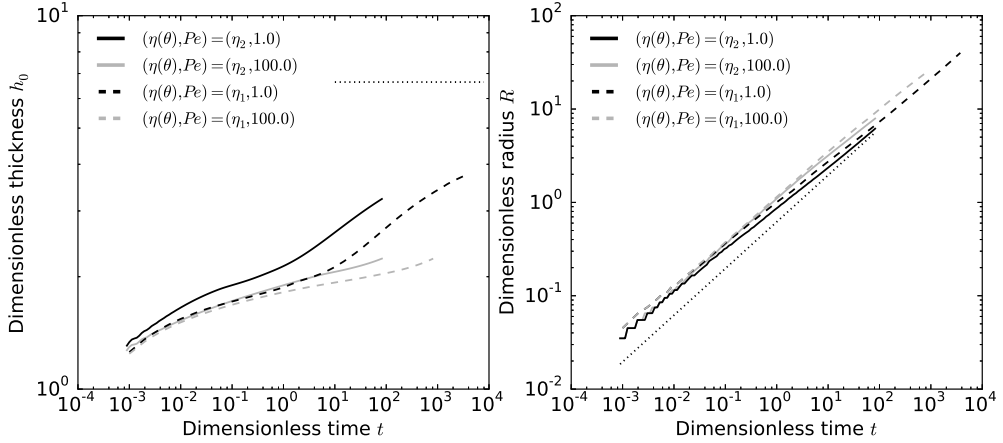


Figure 4.12: Left: Dimensionless thickness at the center h_0 versus dimensionless time t for different sets (η, Pe) indicated on the plot. Dotted-line: scaling law $h_0 = 0.7h_f^{-1/11}\nu^{-2/11}t^{8/22}$ for $\nu = 0.01$. Right: Dimensionless radius R versus dimensionless time t for the same sets (η, Pe) . Dotted-line: scaling law $R = 2.2h_f^{1/22}\nu^{1/11}t^{7/22}$ for $\nu = 0.01$. In all simulations, $\nu = 0.01$ and $\Omega = 1$.

the transition to the second gravity phase occurs around the same time for a current characterized by $\eta(\theta) = \eta_1$ and $\Omega = 10^5$ as for a current characterized

by $\eta(\theta) = \eta_2$ and $\Omega = 1.0$ (Compare Figure 4.11 and 4.12).

4.4.3 Characterization of the thermal anomaly

As in the bending regime, the thermal anomaly is first attached to the tip of the current, i.e. $R_c(t)/R(t) = 1$. After a time that depends on Pe as well as ν , the thermal anomaly detaches from the tip and follows its own evolution. However, in contrast to the isoviscous case, the thermal anomaly does not reach a steady state and R_c/R does not evolve as $t^{-1/2}$ anymore (Figure 4.13 a). We modify the thermal budget of Section 3.4.4 to account for the heating of the surrounding medium.

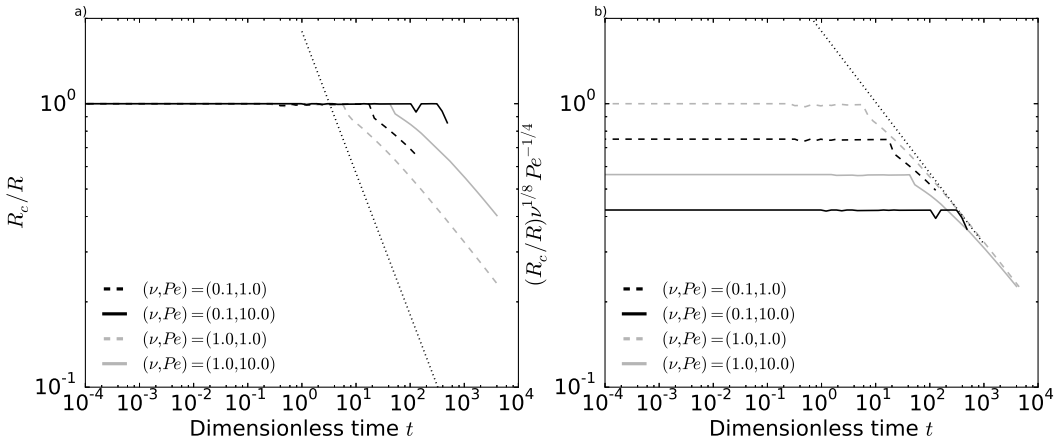


Figure 4.13: a) Normalized thermal anomaly radius $R_c(t)/R(t)$ versus time for different combinations (ν, Pe) indicated on the plot. Dotted-line: Scaling law found in Section 3.4.4 $R_c(t)/R(t) \sim t^{-1/2}$ for comparison. b) Same plot but where we rescale the normalized thermal anomaly by $Pe^{1/4}\nu^{1/8}$. Dotted-line: scaling law $(R_c(t)/R(t))Pe^{-1/4}\nu^{1/8} = 1.8t^{-1/4}$. In all simulations, $\Omega = 1.0$ and $\eta(\theta) = \eta_1$.

When the thermal anomaly has detached from the intrusion front, a balance between heat advection and diffusion in the surrounding medium in a dimensional form reads

$$\rho C_p U_0 \frac{\Delta T}{R_c} \approx k_m \frac{\Delta T}{h_0^2} \quad (4.44)$$

where ΔT is the mean temperature contrast between the fluid and the surroundings and U_0 is a redistribution of the injection rate at $r = R_c$, i.e.

$U_0 = Q_0/(2\pi R_c h_0)$. In addition, the continuity of the heat flux at the boundary (4.6) imposes

$$k_m \frac{\Delta T}{h_0} \approx k_s \frac{\Delta T}{\sqrt{\pi \kappa_r t}}. \quad (4.45)$$

Injecting (4.45) and the expression for the velocity into (4.44) gives

$$R_c \approx \left(\frac{Q_0 \kappa_r^{1/2}}{\kappa_m k_s} \right)^{1/2} t^{1/4}. \quad (4.46)$$

By non-dimensionalizing (4.46), we obtain the evolution of the thermal anomaly when it has detached from the tip $R_c(t) \sim \Omega^{-2} Pe^{1/4} t^{1/4}$ and hence

$$\frac{R_c(t)}{R(t)} = 1.8 \Omega^{-2} Pe^{1/4} \nu^{-1/8} t^{-1/4} \quad (4.47)$$

where we have used the scaling law for $R(t)$ given by (3.66) and the numerical prefactor, which depends on the definition of the thermal anomaly, has been chosen to fit the simulations. The scaling law, which is only valid for $\Omega = O(1)$, indeed closely fits the simulations. In particular, both the dependence with the Peclet number Pe and the viscosity contrast vanishes when rescaling by $Pe^{1/4} \nu^{-1/8}$ (Figure 4.13 b).

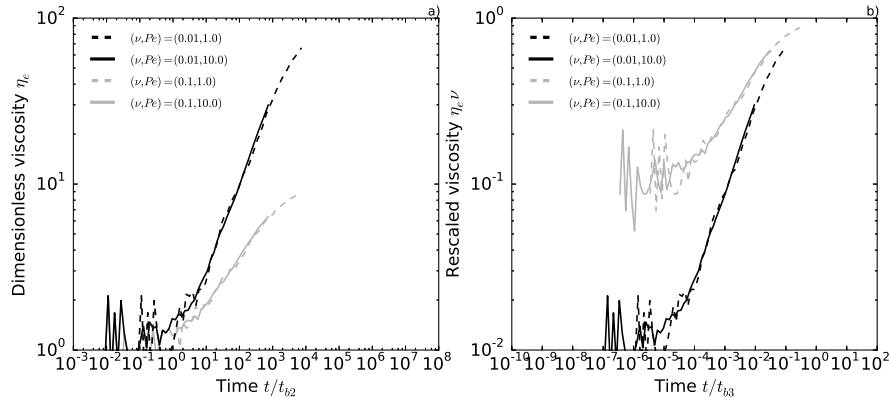


Figure 4.14: a) Dimensionless effective viscosity versus time where the time has been rescaled by the time for the flow to enter the second phase t_{g2} . b) Same as left but where we rescale the viscosity by ν and the time by t_{g3} . In all simulations, $\Omega = 1.0$ and $\eta(\theta) = \eta_1$.

The time t_{g2} for the current to enter the second gravity phase does not change much as the delay induced by the heating of the surrounding medium is offset by the change in rheology. Accordingly, we use the time t_{g2} (3.73)

to characterize the first gravity transition (Figure 4.14 a). In contrast, the time t_{g3} for the current to enter the third phase of the flow is now larger. Processing as in Section 3.4.5 but using (4.47) for the evolution of normalized thermal anomaly $R_c(t)/R(t)$ instead of (3.70), we find that t_{g3} is given by

$$t_{g3} = 80\Omega^{-8}\nu^{-1/2}PeSt_m^{-1} \quad (4.48)$$

Name	From	To	Expression
t_t	Bending	Gravity	$6.5(\eta_e/\eta_h)^{2/7}h_f^{-1/7}$
t_t^h	Bending	Gravity	$6.5h_f^{-1/7}$
t_t^c	Bending	Gravity	$6.5\nu^{-2/7}h_f^{-1/7}$
Bending regime	Phase 1	Phase 2	$0.1PeSt_m^{-1}h_f^2$
	Phase 2	Phase 3	$0.4h_f^{-4/17}St_m^{-11/17}Pe^{11/17}\nu^{-8/17}$
Gravity regime	Phase 1	Phase 2	$10^{-2}PeSt_m^{-1}$
	Phase 2	Phase 3	$80PeSt_m^{-1}\nu^{-1/2}$

Table 4.1: Summary of the different transition times. t_t is the transition time between bending and gravity which is bound by t_t^h , when the current transitions in the first bending thermal phase, and t_t^c , when the current transitions in the third bending thermal phase. t_{b2} (resp. t_{b3}) represents the time to transition from phase 1 to phase 2 (resp. from phase 2 to phase 3) in the bending regime. t_{g2} (resp. t_{g3}) represents the time to transition from phase 1 to phase 2 (resp. from phase 2 to phase 3) in the gravity regime.

4.5 Evolution with bending and gravity in the more realistic model

In the previous chapter, we showed that the final evolution of an elastic-plated gravity current depends on the relative phase changes within each regime and the transition between the bending and the gravity regime itself. The Arrhenius rheology tends to offset the delay caused by the heating of the surrounding medium and overall, the phase diagram presented in section (3.5) shows only minor modifications (Figure 4.15). Except for the transitions from the third bending phase to the second and third gravity phases, which are shifted to the left, the phase diagram is indeed not modified (Appendix B). Therefore, in the framework of our more realistic model, the current is only more likely to

transition to the gravity regime before reaching the third bending phase. In the following, we look at the observations discussed in chapter 2 in the light of our new model.

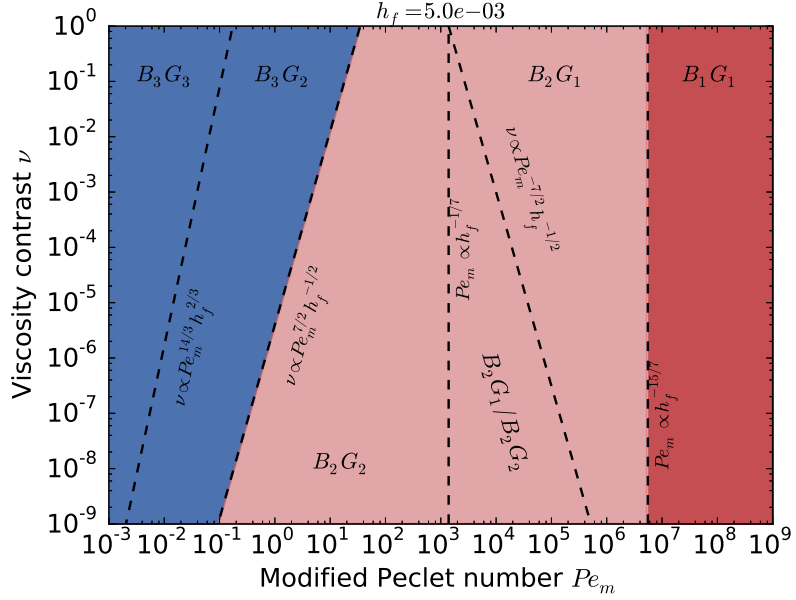


Figure 4.15: Phase diagram for the evolution with bending and gravity for the more realistic case discussed in this chapter for different combinations (ν, Pe_m) and a given value of $h_f = 0.005$. $B_i G_j$ refers to the case where the current transitions from the i th bending thermal phase to the j th gravity thermal phase where i and $j \in \{1, 2, 3\}$.

4.6 Application to the spreading of shallow magmatic intrusions

4.6.1 Elba Island christmas-tree laccolith complex

The isoviscous elastic-plated gravity current model has been used in Chapter 2 to study the laccoliths at Elba Island (*Michaut, 2011*). It shows that, while their final morphologies are consistent with their arrest in the bending regime, their dimensions require unreasonable magma viscosity to agree with the isoviscous model (Chapter 2). In addition, given the fracture toughness of rocks, their radii seem too small to be fractured controlled and their arrest might be better explained by their cooling (*Michaut, 2011*). In the following,

4.6. Application to the spreading of shallow magmatic intrusion

we compare the new model predictions to the size of laccoliths provided by *Rocchi et al.* (2002). In order to account for the intrinsic scale of different settings for each intrusion and compare them to the model, the data have first to be nondimensionalized using characteristic values for the model parameters.

Table 4.2: Range of values for the model parameters

Parameters	Symbol	Earth	Moon	Unit
Depth of intrusion	d_c	0.2 – 2.7	0.5 – 1.5	km
Young's Modulus	E	10	10	GPa
Poisson's ratio	ν^*	0.25	0.25	
Gravity	g	9.81	1.62	m s^{-2}
Magma density	ρ_m	2500 – 2900	2900	kg m^{-3}
Liquidus magma viscosity	η_h	$10^2 – 10^6$	1 – 10	Pa s
Solidus magma viscosity	η_c	$10^6 – 10^{10}$	$10^3 – 10^5$	Pa s
Feeder dyke width	a	1 – 100	10	m
Depth of the melt source	Z_c	1 – 10	500	km
Initial overpressure	ΔP	20 – 50	50	MPa
Injection rate	Q_0	$0.1 – 10^3$	$1 – 10^4$	$\text{m}^3 \text{s}^{-1}$
Magma thermal conductivity	k_m	2.5	2.5	$\text{W K}^{-1} \text{m}^{-1}$
Magma thermal diffusivity	κ_m	10^{-6}	10^{-6}	$\text{m}^2 \text{s}^{-1}$
Magma liquidus temperature	T_L	900-1200	1200	
Magma solidus temperature	T_S	700-1000	1000	
Magma heat capacity	C_p	4.18×10^5	4.18×10^5	$\text{J kg}^{-1} \text{K}^{-1}$
Latent heat of crystallization	L	4.18×10^5	4.18×10^5	J kg^{-1}
Rock thermal diffusivity	κ_r	10^{-6}	10^{-6}	$\text{m}^2 \text{s}^{-1}$
Characteristic scales	Symbol	Earth	Moon	Unit
Height scale	H	0.1 – 10	0.1 – 1	m
Length scale	Λ	1 – 7	2.2 – 12	km
Time scale	τ	$10^{-3} – 100$	$10^{-3} – 10$	years
Dimensionless number	Symbol	Earth	Moon	
Peclet number	Pe	$10^{-4} – 500$	$10^{-3} – 10^4$	
Viscosity contrast	ν	$10^{-4} – 10^{-10}$	$10^{-3} – 10^{-5}$	
Modified Stefan number	St_m	0.1 – 0.5	0.1 – 0.5	
	Ω	1	1	

Range of values for the dimensionless numbers

The different parameters along with a discussion on the possible values for h_f have been provided in Chapter 2 and are summarized in Table 4.2. We refer the reader to Section 2.3.1 for more details about their derivation. In the

following, we quantify the values of the new dimensionless numbers related to the cooling of the flow for the case of the Elba Island laccoliths.

For a latent heat of crystallization $L = 4.18 \times 10^5 \text{ J kg}^{-1}$, a difference between solidus temperature T_S and liquidus temperature T_L between 100 K and 300 K, the number St_m varies from 0.1 to 0.5. For a thermal diffusivity for the magma equal to $\kappa_m = 10^{-6} \text{ m s}^{-2}$, an injection rate Q_0 between 0.1 and 100 $\text{m}^3 \text{s}^{-1}$ and an intrusion depth between 0.2 and 2.7 km, the Peclet number varies from 10^{-3} to 100 and therefore, Pe_m varies from 0.01 to 1000. The increase in viscosity upon cooling varies from 4 to 6 for mafic magmas and can be up to 10 orders of magnitude for felsic magmas (*Shaw, 1972; Lejeune and Richet, 1995; Giordano et al., 2008; Diniega et al., 2013*). We thus consider that the viscosity contrast ν ranges from 10^{-4} to 10^{-10} .

It is generally assumed that the magma stops spreading when its crystal content becomes close to its maximum packing, i.e. $\phi \sim 60\%$ (*Pinkerton and Stevenson, 1992*). Beyond this point, crystal collisions dominate and the viscosity jumps to much higher values (*Lejeune and Richet, 1995; Giordano et al., 2008*). We assume that this is equivalent to η_e tending to η_c in our model. With this assumption, the model thus predicts that a magmatic intrusion would solidify as a laccolith upon reaching the third bending phase.

Do laccoliths stop in the bending regime ?

The dimensionless thickness h_0 as a function of its dimensionless radius R for a current that solidifies in the third phase of the bending regime can be derived from the scaling laws (3.54) and (3.55) and should follow

$$h_0 = 0.3 h_f^{-1/7} \nu^{-2/7} R^{8/7} \quad (4.49)$$

Using the parameters listed in Figure 4.16, the dimensionless observations show a very good agreement with the model for a viscosity contrast close to 8 orders of magnitude ($\nu = 6.9 \pm 2.3 \times 10^{-8}$, $r^2 = 0.9$), which is consistent with the felsic composition of these laccoliths, and $h_f = 0.001$ (Figure 4.16 a) (*Marsh, 1981; Diniega et al., 2013*). Varying h_f has only minor effect on the best fit viscosity contrast and is discussed in Appendix B. This value for the viscosity contrast also depends on the chosen value for the height scale H whose main uncertainty is on the liquidus viscosity η_h and the injection rate Q_0 . Indeed, the larger this two parameters, the larger the height scale, the smaller the dimensionless thicknesses and therefore, the smaller the best fit viscosity contrast. Nevertheless, introducing the cooling in the elastic-plated gravity current model allows to reconcile the model predictions and the observations in the case of laccoliths (Chapter 2). The shape and in particular, the large thickness of the laccoliths at Elba Island is now entirely consistent

4.6. Application to the spreading of shallow magmatic intrusion

with the model predictions and therefore with their arrest in the bending regime. In the following, we use the phase diagram proposed in Section 4.5 to better constrain the viscosity contrast along with η_h and Q_0 .

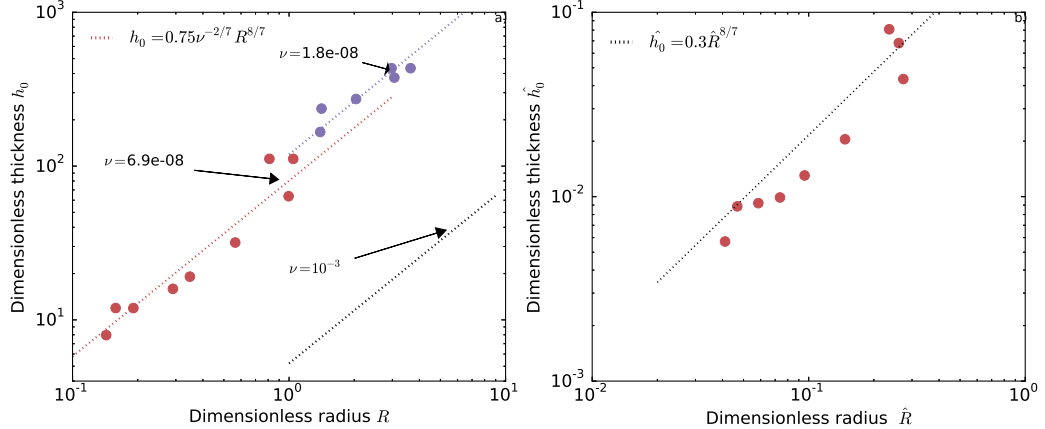


Figure 4.16: a) Dimensionless maximum thickness h_0 versus radius R for laccoliths from Elba Island and revised low-slope lunar domes. Parameters for calculating Λ (3.23) and H (3.24) are $E = 10^9$ GPa, $\nu^* = 0.25$, $\rho_m = 2500$ kg m $^{-3}$, $g = 9.81$ m s $^{-2}$, $\eta_h = 10^6$ Pa s and $Q_0 = 10$ m 3 s $^{-1}$ on Earth and, everything else being equal, $g = 1.62$ m s $^{-2}$, $\eta_h = 1$ Pa s on the Moon. Dotted lines: best fit scaling laws (4.49) with $h_f = 0.001$ for laccoliths at Elba Island (red) and low-slope lunar domes (purple). $\nu = 6.9 \pm 2.3 \cdot 10^{-8}$ ($r^2 = 0.92$) and $\nu = 1.8 \pm 0.4 \cdot 10^{-8}$ ($r^2 = 0.88$) represent the linear least square best fit for the data on Earth and the Moon respectively. b) Dimensionless thickness \hat{h}_0 versus \hat{R} where \hat{h}_0 and \hat{R} are given by (??) with $h_f = 0.001$ for laccoliths at Elba Island. Substituting (3.25) into (3.33), we obtain $Pe = Q_0H/(\pi\kappa\Lambda^2)$; the parameters for calculating Pe for each laccolith are the same than those used for the nondimensionalization, $\kappa = 10^{-6}$ m s $^{-2}$ and St_m is considered constant and set to 0.1. The viscosity contrast is set to $\nu = 6.9 \cdot 10^{-8}$ for all laccoliths. Dotted line: scaling law $\hat{h}_0 \sim 0.3\hat{R}^{8/7}$.

What can we learn from the phase diagram ?

Assuming that the intrusion stops when it reaches the third bending phase, the phase diagram proposed in section 4.5 simplifies (Figure 4.17). It shows that sills and laccoliths are two specific end member regions as a function of Pe and ν . In particular, while the top portion of the phase diagram corresponds to magmatic intrusions more mafic in composition, the bottom should be more

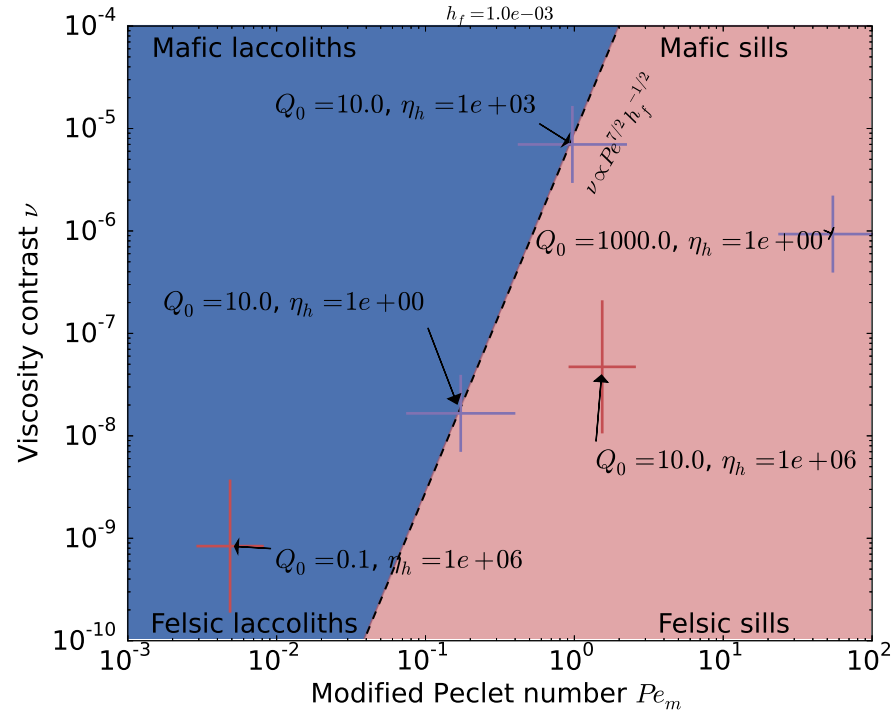


Figure 4.17: Subset of the phase diagram proposed in section 4.5 relevant for the study of terrestrial laccoliths. Red and purple crosses represent a range of value for ν and Pe for Elba Island laccoliths and low-slope lunar domes respectively. The width of each cross is defined by the minimum and the maximum value obtained for the Peclet number given the range of variation of parameters listed in table 4.2 and the injection rate Q_0 and the viscosity at the liquidus temperature η_h indicated on the plot. The height of the cross corresponds to the minimum and maximum values for the viscosity contrast obtain from (4.49) when $h_f = 0.001$.

representative of felsic magmatic intrusions. The boundary between the two regions show that felsic magmatic intrusions should solidify as sills on a larger range of number Pe . Indeed, felsic magmatic intrusions tend to be thicker than their mafic counterparts. In the framework of our model, they then stay hot for a longer period of time and therefore, can reach the gravity regime more easily. Given the felsic composition of Elba island laccoliths, this phase diagram can then be used to constrain their Peclet number, and therefore Q_0 and η_h , for them to fall in the laccolith region. In the following, we use this approach to constrain the injection rate Q_0 for these laccoliths.

We first compute a value for the Peclet number for each laccolith at Elba Island. Injecting the scales (3.23), (3.24) and (3.25) in the expression of Pe

4.6. Application to the spreading of shallow magmatic intrusion

(3.33) gives

$$Pe \approx 4.8 Q_0^{5/4} \eta_h^{1/4} \rho_m^{1/4} g^{1/4} E^{-1/2} d_c^{-3/2} \kappa_m^{-1} \quad (4.50)$$

where we set the Poisson's ratio to $\nu^* = 0.25$. Except for Q_0 , that we want to constrain, and d_c , which is given and depends on the laccolith, we take the parameter values listed in Figure 4.16. Therefore, Pe reads

$$Pe \approx 6 \times 10^4 d_c^{-3/2} Q_0^{5/4} \quad (4.51)$$

For $St_m = 0.1$, the intrusion depths given by *Rocchi et al.* (2002) and $Q_0 = 10 \text{ m}^3 \text{ s}^{-1}$, the modified Peclet number Pe_m ranges from 1 to 6. As the best fit range of values for the viscosity contrast associated with $Q_0 = 10 \text{ m}^3 \text{ s}^{-1}$ is $\nu = 6.9 \pm 2.3 \times 10^{-8}$, as discussed in the previous Section, the phase diagram thus predicts that these laccoliths should have stop in the gravity regime (Figure 4.17). Hence, we might have overestimate the injection rate. Indeed, taking a smaller value for the injection rate of $Q_0 = 0.1 \text{ m}^3 \text{ s}^{-1}$, reasonable for viscous felsic magmas (*Harris et al.*, 2000), the height scale H is smaller and the dimensionless thicknesses are larger. The model thus predicts a larger viscosity contrast $\nu = 1.2 \pm 0.4 \times 10^{-9}$, still consistent with the range of expected values for felsic magmas, and weaker Peclet numbers. In the end, the range of values for the dimensionless numbers now falls within the laccolith regions and is consistent with the observations (Figure 4.17).

Is conduction cooling enough to solidify a laccolith ?

If the laccoliths stopped spreading as soon as they reached the third phase of the bending regime, the variance in thickness and radius in between the different intrusions should also be explained by variations in the Peclet number, most likely due to variations in intrusion depths in this example. Indeed, the time t_{b3} , necessary to reach the third bending phase, the thickness and the radius of the current at this time all depend on the combination (ν, Pe_m) considered (see Section 4.5).

To test this hypothesis, we first rescale the time using the time t_{b3} (4.43) as follow

$$\hat{t} = h_f^{4/17} Pe_m^{-11/17} \nu^{8/17} t \quad (4.52)$$

where \hat{t} is the new variable. Injecting (4.52) into (3.54) and (3.55), we find the corresponding thickness \hat{h}_0 and radius \hat{R} read

$$\hat{R} = h_f^{1/34} Pe_m^{-7/34} \nu^{1/17} R \quad (4.53)$$

$$\hat{h}_0 = h_f^{3/17} Pe_m^{-4/17} \nu^{6/17} h_0 \quad (4.54)$$

In terms of \hat{h}_0 and \hat{R} , the scaling law (4.49) rewrites $\hat{h}_0 \sim 0.3 \hat{R}^{8/7}$ and does not depend on the dimensionless numbers anymore (Figure 4.18). For laccoliths

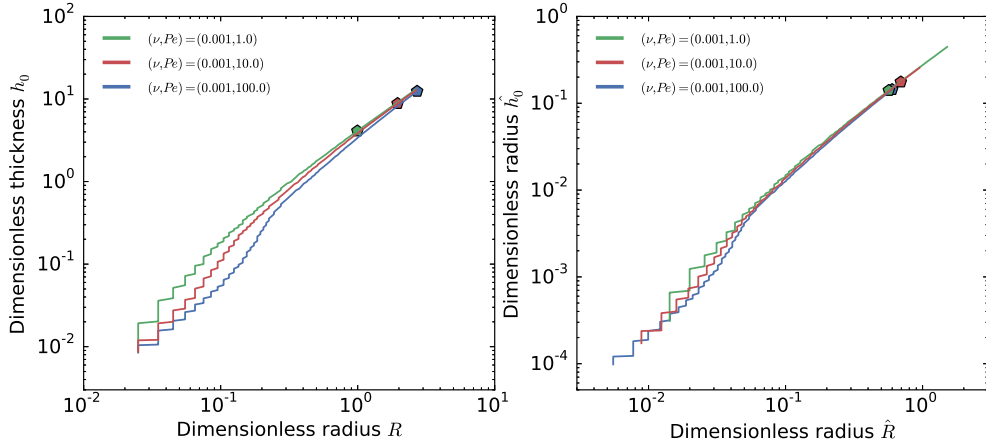


Figure 4.18: a) Dimensionless thickness at the center h_0 versus dimensionless radius R for different sets (ν, Pe) indicated on the plot ($\eta(\theta) = \eta_2$, $\Omega = 1.0$). Pentagons refer to the size where the effective viscosity of the current equal 70% of the maximum viscosity η_c , i.e. $\eta_e = 0.7\eta_c$. b) Dimensionless thickness \hat{h}_0 versus dimensionless radius \hat{R} where \hat{h}_0 and \hat{R} are given by (??) with $h_f = 0.001$. As expected, after rescaling h_0 and R , the sizes of the solidified laccoliths should collapse almost on the same point.

at Elba Island, we use a constant viscosity contrast equal to $\nu = 8.2 \cdot 10^{-9}$, $h_f = 0.001$ and we compute a Peclet number for each laccolith according to (4.51) with $Q_0 = 10 \text{ m}^3 \text{ s}^{-1}$. However, the different laccoliths do not collapse on the same dot after rescaling (Figure 4.16 b). In particular, the dependence in Pe of our scaling, resulting from different intrusion depths, is not enough to explain the variability in the size of terrestrial laccoliths. An additional cooling mechanism, amplifying the effect of Pe , is thus required to explain the exact extent of laccoliths. This could be extraction of heat by circulation of fluid (Senger et al., 2014). To test this hypothesis, we look at the low-slope domes on the Moon where conduction is most likely the only source of cooling.

4.6.2 Low-slope lunar domes

Because the Moon is supposed to be depleted of volatiles, circulation of fluid in the lunar crust is likely to be very limited and the model developed in this chapter should be appropriate for studying the cooling of low-slope lunar domes. In this section, we restrict our analysis to some specific domes whose characteristics have been precisely revisited by Mélanie Thiriet (Purple dots Figure 2.5, see Section 2.3.2). Their shapes and characteristics have already been discussed in Chapter 2 and hereafter, we look at their dimension in the

4.6. Application to the spreading of shallow magmatic intrusions

light of the cooling elastic-plated gravity current model.

Range of values for the dimensionless numbers

Parameters for a lunar setting have been discussed in Chapter 2 and are summarized in Table 4.2. In particular, for the same injection rate, the smaller gravity, together with the higher density and the smaller viscosity of lunar magmas, lead to smaller Peclet numbers. For instance, for an intrusion 1.5 km deep, using $g = 1.62 \text{ m s}^{-2}$, $\eta_h = 1 \text{ Pa s}$ and $\rho_m = 2900 \text{ kg m}^{-3}$ instead of $g = 9.81 \text{ m s}^{-2}$, $\eta_h = 10^6 \text{ Pa s}$ and $\rho_m = 2500 \text{ kg m}^{-3}$ lead to a Peclet number two orders of magnitude smaller on the Moon than on Earth, i.e. $Pe = 0.04$ and $Pe = 1.8$ respectively. However, injection rates on the Moon might be larger than on Earth (*Crisp and Baloga, 1990; Zimbelman, 1998*) (See Section 2.3.2). For an injection rate one to two orders of magnitude larger and d between 0.5 and 1.5 km, the range of Peclet number is in fact very similar, i.e. from 10^{-3} to 10^4 . Therefore, taking $St_m = 0.1$, we have Pe_m that varies between 0.01 and 10^5 for low-slope lunar domes. Finally, lunar basalts are mafic in composition and the viscosity contrast ν should vary between 10^{-3} and 10^{-5} (*Diniega et al., 2013*).

Constraining the magma physical properties

For an injection rate of $Q_0 = 10 \text{ m}^3 \text{ s}^{-1}$, a liquidus viscosity of $\eta_h = 1 \text{ Pa s}$ and the parameters listed in Figure 4.16, the dimensionless thickness of these domes are also consistent with a viscosity contrast close to 10^{-8} (best fit: $\nu = 1.8 \pm 0.4 \times 10^{-8}$) (Figure 4.16). On the Moon, (4.51) becomes

$$Pe \approx 125d_c^{-3/2}Q_0^{5/4}\eta_h^{1/4} \quad (4.55)$$

and assuming that the intrusion depth ranges from 500 m to 5 km, the Peclet number ranges from 0.1 to 1 and the range of values for the dimensionless number falls at the boundary between the two domains in the phase diagram (Figure 4.17). It is consistent with the radius of these lunar domes being close to $R = 4$, i.e. close to the transition radius with the gravity regime (Figure 4.16). However, the estimate for the viscosity contrast is much larger than the value expected for their mafic composition. For the same injection rate and a liquidus viscosity for the magma of $\eta_h = 10^3 \text{ Pa s}$ instead of $\eta_h = 1 \text{ Pa s}$, the height scale H is larger and the dimensionless thickness smaller. The best fit viscosity contrast is now close to 10^{-5} ($\nu = 6.9 \pm 1.8 \times 10^{-6}$), much closer to the expected value, and the Peclet number are slightly larger (Figure 4.17). A similar value for the viscosity contrast can be obtained for $\eta_h = 1 \text{ Pa s}$ and $Q_0 = 1500 \text{ m}^3 \text{ s}^{-1}$. However, in that case, the Peclet numbers are

much larger and the range of values for the dimensionless numbers fall within the sill region (Figure 4.17). In the end, it suggests that the injection rates for these lunar domes were most likely close to $Q_0 \sim 10 \text{ m}^3 \text{ s}^{-1}$, hence a few orders of magnitude smaller than the effusion rates estimated from the runout distances of some lava flows in the lunar maria i.e. $Q_0 \geq 10^6 \text{ m}^3 \text{ s}^{-1}$ (*Gregg and Fink, 1996*).

Is conductive cooling enough to solidify a laccolith on the Moon ?

On the Moon, the dimensionless sizes of the domes vary by less than one order of magnitude and might be explained only by the conductive cooling of the magmatic intrusion (Figure 4.16). Because intrusion depths are not known for these domes, we can not proceed as for Elba Island laccoliths to test this hypothesis. Instead, we estimate a range of intrusion depth that

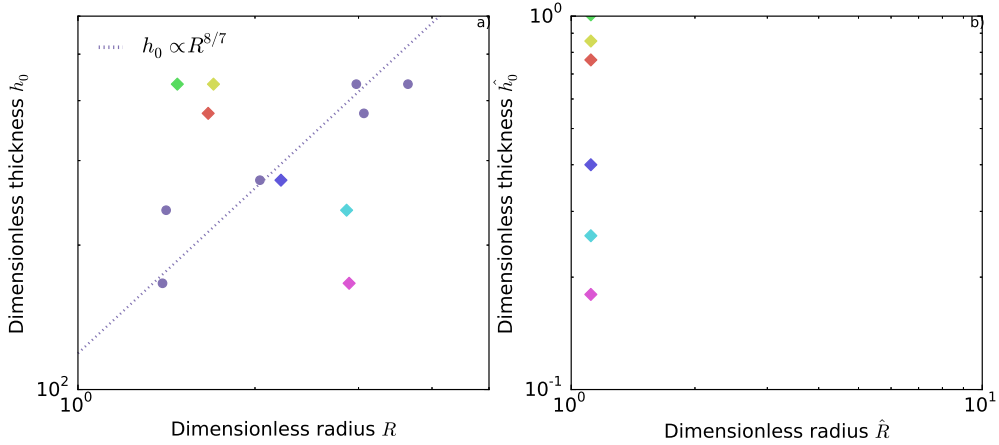


Figure 4.19: a) Dimensionless thickness h_0 versus dimensionless radius R for some lunar low-slope domes. Purple dots: characteristics length scale Λ (3.23) and thickness H (3.24) are calculated the same way as in Figure 4.16. Colored diamonds: characteristics length scale Λ (3.23) and thickness H (3.24) are calculated the same way as in Figure 4.16 except for the intrusion depth, taken from (4.57) with $R^r = 36.6 \text{ km}$ and $d_c^r = 5 \text{ km}$. b) Dimension thickness \hat{h}_0 versus dimensionless radius \hat{R} . Colored polygons refers to the colors in a).

would produce a collapse of the rescaled size of the domes on a reference dome size given by \hat{R}^{ref} and \hat{h}_0^{ref} . Indeed, using (4.53), $\hat{R} = \hat{R}^{\text{ref}}$ implies that

$$\Lambda^{-1} h_f^{1/34} Pe_m^{-7/34} \nu^{1/17} R = (\Lambda^{\text{ref}})^{-1} (h_f^{\text{ref}})^{1/34} (Pe_m^{\text{ref}})^{-7/34} (\nu^{\text{ref}})^{1/17} R^{\text{ref}} \quad (4.56)$$

where the topscript ref denotes a reference dome and the radii R and R^{ref} are with dimension. Assuming that the different lunar domes differ only by their

4.6. Application to the spreading of shallow magmatic intrusion¹³

intrusion depth, (4.56) simplifies and reads

$$d_c = \left(R/R^{\text{ref}} \right)^{34/15} d_c^{\text{ref}} \quad (4.57)$$

We take the largest dome as a reference and we set its depth to the largest reasonable value, i.e. $d_c = 5$ km, mainly to ensure that the dimensionless radius of the other domes remains smaller than 4. Injecting the dome radii in (4.57) then give intrusion depths between 0.5 km and 5 km and Peclet numbers between 10^{-2} and 0.5, consistent with the expected values. However, while this new parameters result in the collapse of \hat{R} for the different domes, the variation in Peclet number can not account for the dispersion in the dome thicknesses (Figure 4.19). In addition, the dimensionless thickness as a function of the dimensionless radius does not follow the scaling law (4.49) anymore (Figure 4.19). The same observations are obtained using different reference domes or by setting the constrain on the rescaled thickness instead of the radius, i.e. $\hat{h}_0 = h_0^{\text{ref}}$. Therefore, conductive cooling does not appear to be responsible for the arrest of terrestrial laccoliths.

4.6.3 Large mafic sills

As we discussed in Chapter 2, the size of large mafic sills reported by *Cruden et al.* (2012) show an increasing thickness with diameter apparently in contradiction with the constant thickness predicted by the elastic-plated gravity current model (Figure 2.5). One possible explanation is that different sills are characterized by different injection rates, i.e. by different height scales. Forcing the dimensionless thicknesses of different sills to be constant imposes that

$$Q_0 = (h_0/h_0^{\text{ref}})^4 Q_0^{\text{ref}} \quad (4.58)$$

where h_0 is the sill thickness with dimension, Q_0 its injection rate and h_0^{ref} and Q_0^{ref} are reference values for this parameters. Taking the thickest sill as a reference with $Q_0^{\text{ref}} = 10^4 \text{ m}^3 \text{ s}^{-1}$, we find that in order to collapse all the data on a constant thickness, the injection rate have to vary by at least 7 orders of magnitudes, i.e. from $Q_0 = 10^{-3}$ to $Q_0 = 10^4 \text{ m}^3 \text{ s}^{-1}$. It is much larger than the expected range of variations for this parameter and hence, these mafic sills do not appear to have all stop in the third gravity regime. Another possible explanation is that fracturation at the tip, instead of cooling, have triggered the arrest of these magmatic intrusions in the second gravity phase. Indeed, while fracturation is not sufficient to stop a magmatic intrusion in the bending regime, it might be responsible for the arrest of large mafic sills (*Michaut*, 2011). The increasing thickness with diameter would thus be consistent with the thickness increase induced by the cooling of the sill in the

second gravity phase. However, more information about the intrusion depth and the relationship between the different sill units, which are not given by *Cruden et al.* (2012), would be required to precisely test this hypothesis.

4.6.4 Contact aureole

Contact metamorphism often occurs in the vicinity of magmatic intrusion (*Jaeger*, 1959; *Sillitoe and Thompson*, 1998; *Senger et al.*, 2014). Metamorphism is a complex process and in the following, we discuss only the dimension of the thermal aureole in the vicinity of laccoliths which have stopped in the third bending regime.

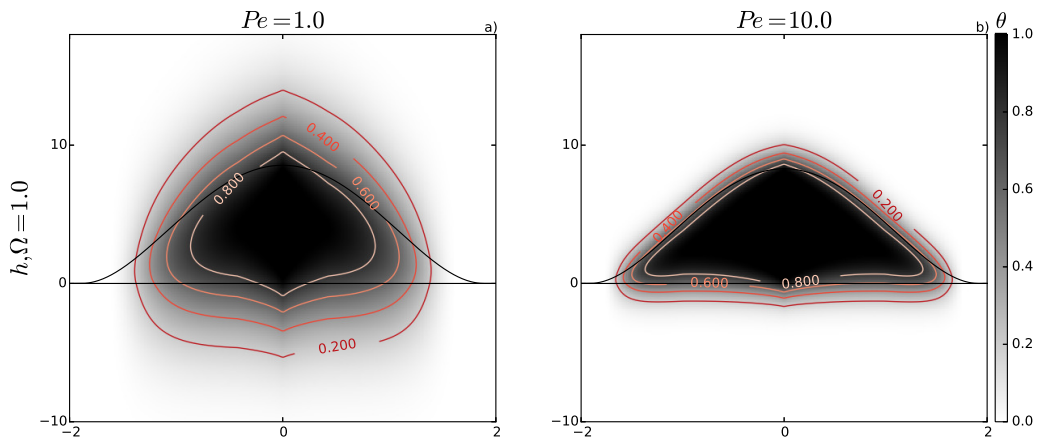


Figure 4.20: a) Snapshot of the flow thermal structure with its surrounding thermal aureole at $t = 10$ for $Pe = 1.0$ and $\nu = 10^{-3}$. Isotherms are indicated on the plot. b) Same plot but for $Pe = 10.0$.

We define the thickness of the thermal aureole by the region where $\Theta_r > 0.1$ above the center of the flow. Therefore, inverting (4.5) gives $L_h(t)$, the maximum thickness of the thermal aureole above the intrusion at $r = 0$

$$L_h(t) = \operatorname{erf}^{-1} \left(\frac{0.1}{\Theta_s(r=0, t)} \right) 2Pe^{-1/2} t^{1/2} \quad (4.59)$$

L_h scales as $Pe^{-1/2}$ and hence, is larger for small values of Pe (Figure 4.20). Indeed, for large Pe , advection dominates on the emplacement time scale and the thermal aureole is restricted to a small zone around the current (Figure 4.20). For instance, the thickness of the contact aureole $L_h(t)$ at $t = 10$ is almost equal to the current thickness h_0 for $Pe = 1$ whereas it is only a few percent of h_0 for $Pe = 10.0$ (Figure 4.3).

4.6. Application to the spreading of shallow magmatic intrusion

The dimension of the thermal aureole also depends on the emplacement time t ; the longer the injection, the longer the heating and the larger the thermal aureole. An upper limit for the emplacement time is given by the time t_t for the intrusion to transition in the gravity regime while it is in the third bending regime, i.e. $t_t = 6.5(\eta_e/\eta_h)^{2/7}h_f^{-1/7}$ (See Section 3.5). Injecting t_t into (4.59) gives

$$L_h^{\max} = 5.0 \operatorname{erf}^{-1} \left(\frac{0.1}{\Theta_s(r=0, t_t)} \right) h_f^{-1/14} \nu^{-1/7} Pe^{-1/2} \quad (4.60)$$

and therefore, using (3.54), we get

$$L_h^{\max}/h_0(t_t) = 3.7 \operatorname{erf}^{-1} \left(\frac{0.1}{\Theta_s(r=0, t_t)} \right) h_f^{1/14} \nu^{1/7} Pe^{-1/2} \quad (4.61)$$

While the absolute size of the thermal aureole L_h^{\max} increases with decreasing Pe and ν (4.60), the ratio L_h^{\max}/h_0 is smaller for larger viscosity contrasts (Figure 4.21).

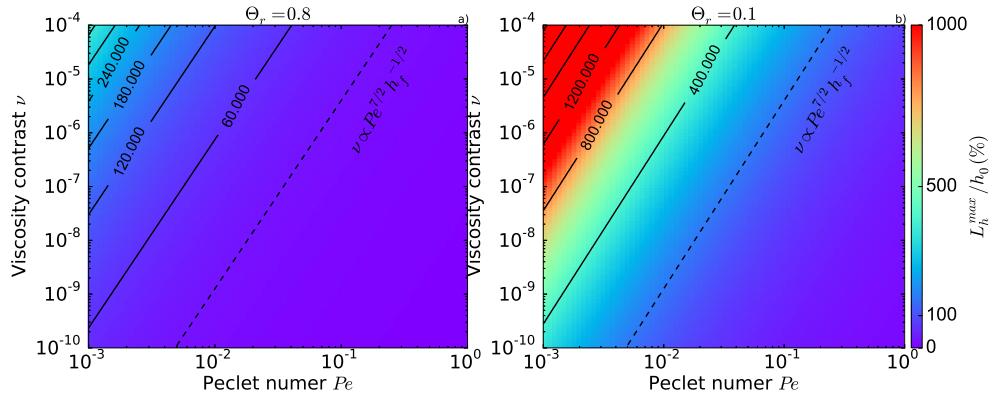


Figure 4.21: a) Maximum Size of the thermal aureole above the intrusion L_h^{\max} normalized by the intrusion thickness at the center h_0 (%) (4.61) as a function of the number Pe and ν . b) Same plot but where the thermal aureole is defined with $\Theta_r = 0.8$ instead of 0.1 in (4.61). In both plot, we set $h_f = 0.001$ and $\Theta_s(r=0, t_t) = 1$.

For the felsic laccoliths at Elba Island, we estimated $\nu \sim 10^{-9}$ and $Pe \sim 10^{-3}$ (Figure 4.21 a) and thus, the thermal aureole should reach 400% of the intrusion thickness at the center of the flow. Important temperature variations however, i.e. $\Theta_r > 0.8$, should be restricted to the vicinity of the current, i.e. $\sim 60\%$ of the intrusion thickness (Figure 4.21 b). These estimates represent upper bound as the temperature at the surface $\Theta_s(r=0, t)$ might be smaller

than 1 for $Pe < 0.1$. In addition, the model neither accounts for horizontal thermal conduction, nor for circulation of fluid in the wall rocks, both effects that should also limit the size of the thermal aureole.

4.7 Summary and discussion

In this chapter, we discuss a more realistic model for the emplacement of magmatic intrusions in the shallow crust of terrestrial planets. In particular, we describe the dynamics of a magma characterized by an Arrhenius rheology and heating the wall rocks as it spreads. We show that relaxing the thermal boundary condition insulates the flow and therefore, allows the intrusion to stay hot for a longer period of time. In particular, the thermal anomaly detaches slower from the tip of the intrusion. It also does not reach a steady state anymore in the gravity regime as the heating of the surrounding medium constantly decreases the heat loss in the central region. Nevertheless, the Arrhenius rheology largely compensates for the delay in the transitions induced by the heating of the surrounding medium. In the end, except for the third phase in both regimes which is reached slightly later, the dynamics shows only small variations in comparison to the one described in chapter 3.

Application of this model to the christmas-tree laccolith complex at Elba Island shows that cooling allows to reconcile the elastic-plated gravity current model with the observations. Indeed, their size is consistent with their felsic composition ($\nu \approx 10^{-8}$) and their arrest in the third bending phase. However, the model does not capture the second order variation in the laccolith dimensions. Indeed, while the mean trend in the data is consistent with the model, conduction alone is not able to explain the variability around this trend. Further application to low-slope lunar domes, where conduction is more likely to be the only cooling mechanism, leads to the same conclusions. The model thus suggests that other mechanism than cooling are responsible for the arrest of laccoliths.

In the end, while some progress has been made in the understanding of the emplacement of these shallow magmatic intrusions, a complete picture of the solution, in regard to the final size and thickness of the intrusion as a function of the parameters of the problem (elasticity and toughness of the host rock, viscosity of the magma, injection rate of the feeder dyke, and depth of emplacement), has not yet been obtained. In general, more detailed observations, especially at the tip of these shallow magmatic intrusions, may provide further insights in the arrest mechanism. Precise information on the extent of the thermal aureole, which has not yet been reported in the literature, could also provide precious constrain for the model. We discuss some

possible extensions of this work in the last part of this manuscript.

Part III

Cratères à sol fracturée: Témoins
d'un magmatisme intrusif lunaire

CHAPTER 5

Floor-fractured craters

*This chapter is a reproduction of the paper published in Journal of Geophysical Research untitled: **A model for the dynamics of crater-centered intrusion: Application to lunar floor-fractured craters** ([Thorey and Michaut, 2014](#)).*

Contents

5.1	Introduction	120
5.2	Floor-fractured craters	122
5.3	An axisymmetric model for a magmatic intrusion spreading below a crater-like topography	125
5.3.1	Crater topography and overlying layer characteristics	125
5.3.2	Equations of Motion	128
5.3.3	Nondimensionalization	130
5.3.4	Range of values for the dimensionless numbers	132
5.4	Results	134
5.4.1	Intrusion below a brecciated zone with no elastic strength (effect of Ξ)	134
5.4.2	Intrusion below an elastic layer of constant thickness	136
5.4.3	Spreading beneath a complex crater topography	138
5.4.4	Spreading beneath a simple crater	144
5.4.5	Effect of a variable injection rate	144
5.5	Discussion	148
5.5.1	Floor appearance	148
5.5.2	Depth of the intrusion	150
5.5.3	Injection rate and formation time scale	152
5.6	Conclusion	154

Lunar Floor-Fractured Craters (FFCs) are a class of craters modified by post impact mechanisms. They are defined by distinctive shallow floors that

are convex or plate-like, sometimes with a wide floor moat bordering the wall region. Radial, concentric and polygonal floor fractures suggest an endogenous process of modification. Two mechanisms have been proposed to account for such deformations: viscous relaxation and spreading of a magma intrusion at depth below the crater. To test the second assumption and bring more constraints on the intrusion process, we develop a model for the dynamics of magma spreading below an elastic overlying layer with a crater-like topography. As predicted in precedent more qualitative studies, the increase in lithostatic pressure at the crater wall zone prevents the intrusion from spreading laterally, leading to the thickening of the intrusion. Additionally, our model shows that the final crater floor appearance after the uplift, that could be convex or flat, with or without a circular moat bordering the wall zone, depends on the elastic thickness of the layer overlying the intrusion and on the crater size. As a result, our model provides a simple formula to derive the elastic thickness of the layer overlying the intrusion, and hence a minimum estimate for the intrusion depth. Finally, our model suggests that crust redistribution by cratering must have controlled magma ascent below most of these craters.

5.1 Introduction

A large fraction of the magma produced by mantle melting never reaches the surface as it intrudes the shallow layers of the planet. On Earth, the volume of intrusive magma is estimated to be 10 times (resp. 5 times) the volume of extrusive lava for the continental crust (resp. the oceanic crust) (*Crisp*, 1984). Buoyancy is the main mechanism driving up the magma from the interior to the shallow layers or the surface of the planets. It has been shown that dykes stop their propagation when they become neutrally buoyant relative to their surroundings (*Walker*, 1989; *Rivalta et al.*, 2005; *Taisne and Jaupart*, 2009). Therefore, the intrusive to extrusive ratio largely depends on the respective density of the crust and magma.

The density of the lunar crust is particularly low. The last estimate from the GRAIL NASA mission provides for a mean density for the highlands of 2550 kg.m^{-3} , even lower than what was previously assumed (*Wieczorek et al.*, 2013). Both the light anorthite minerals that form the lunar crust and impact induced fractures and brecciation contribute to its low density (*Wilhelms et al.*, 1987). Given the large density of magma inferred from the composition of the mare basalts that are generally rich in FeO and TiO₂ (*Wieczorek et al.*, 2001), the intrusive to extrusive ratio on the Moon might be even higher than on Earth (*El-Baz*, 1970; *Wilson and Head III*, 1981; *Hiesinger*, 2006; *Glotch et al.*, 2010). *Head and Wilson* (1992) estimated an

upper limit of 50 : 1 for this ratio. However, there are no solid constraints supporting this estimate and although it is an important parameter in lunar thermal evolution models (*Laneuville et al.*, 2013), it is poorly constrained.

Extrusions of lava preferentially occurred within large impact basins on the near side of the Moon where a large fraction of the low-density crust has been removed. However, the trajectory of the magma from its source to the surface is unknown. The magma could have ascended directly from the source to the surface (*Wieczorek et al.*, 2001); alternatively, it might have first accumulated at the crust-mantle interface before erupting where the crust was thinner (*Wilson and Head III*, 1981).

Possible sites for intrusions on the Moon are below floor-fractured craters (FFCs). These craters have been identified by *Schultz* (1976a); they have shallow floors with a plate-like or convex appearance, wide floor moats and radial, concentric and polygonal floor fractures. *Schultz* (1976a) has classified about 200 FFCs. Similar FFCs have been observed on Mercury (*Head et al.*, 2008), Mars (*Schultz*, 1978; *Schultz and Glicken*, 1979; *Sato et al.*, 2010) and Venus (*Wichman and Schultz*, 1995a). The database and classification proposed by *Schultz* (1976a) have recently been updated by *Jozwiak et al.* (2012) who used new data from the Lunar Orbiter Laser Altimeter (LOLA) and Lunar Reconnaissance Orbiter Camera (LROC). The deformations affecting these craters are contained within the crater interior. Two mechanisms have been proposed to explain the features observed at FFCs: 1) spreading of a magmatic intrusion at depth below the crater floor (*Schultz*, 1976a; *Wichman and Schultz*, 1993, 1995b, 1996; *Jozwiak et al.*, 2012) and 2) viscous relaxation of the crater floor induced by a local thermal gradient caused by the impact (*Hall et al.*, 1981). However, viscous relaxation of the crater floor has been modeled by *Dombard and Gillis* (2001) but, for typical elastic parameters, the lunar crust is too rigid and shallowing of craters smaller than 100 km is not significant. Hence, if the deformations observed at FFCs resulted indeed from magmatic intrusion, they might give us important constraints and clues on the process of magmatic intrusion in the lunar crust.

The classical, static, model of laccoliths of *Pollard and Johnson* (1973) has previously been applied to the case of FFCs to deduce the intrusion depth and magma pressure (*Wichman and Schultz*, 1993, 1996; *Jozwiak et al.*, 2012). In this static model, the intrusion radius is known a priori. The intrusion shape is controlled by the elastic deformation of a thin elastic layer on top of the laccolith and the elastic pressure necessary for deforming the overlying layer is assumed to be equilibrated by magma weight. However, *Michaut* (2011) and *Bunger and Cruden* (2011) have shown that, if the elastic deformation of the overlying layer controls the flow shape and its dynamics during a first spreading phase, the own weight of the flow becomes dominant during a second

phase where the flow shape shows a flat top. Furthermore, in all these models, the possible effect of a thickening of the overlying layer has been ignored.

Here, we modify the model proposed by *Michaut* (2011) for the dynamics of a magma intrusion below an elastic overlying layer in order to account for the effects of the crater topography, i.e. for an overlying layer of variable thickness. We show that different types of deformations of the crater floor are expected, as initially predicted by *Schultz* (1976a), and that they mainly depend on the elastic thickness of the layer overlying the intrusion and on the crater size.

5.2 Floor-fractured craters

Floor-fractured craters are craters that have undergone endogenous deformations after the impact. About two hundreds FFCs have been observed on the Moon and precisely described by *Schultz* (1976a) who studied their structure and geology using Lunar Orbiter and Apollo stereo sets. *Schultz* (1976a) proposed a classification into 6 categories based on their sizes, morphological features and degrees of modification; classification which has recently been updated by *Jozwiak et al.* (2012) using the Lunar Orbiter Laser Altimeter (LOLA) and Lunar Reconnaissance Orbiter Camera (LROC) (Table 5.1).

Radial and concentric fracture networks generally cross the floors of these craters (*Schultz*, 1976a). Another striking feature of FFCs is their shallow floors: except for class 1 FFCs, they all exhibit a significant shallowing of their floors compared to fresh craters the same size (*Schultz*, 1976a; *Jozwiak et al.*, 2012).

Floor uplift mainly results in two different modes of crater floor appearance (*Schultz*, 1976a). In particular, FFCs of classes 3 and 5 show a flat central floor, characteristic of a piston-like uplift of the crater floor; additionally, a large circular U-shaped moat adjacent to the wall zone borders the flat floor of class 3 FFCs (*Schultz*, 1976a; *Jozwiak et al.*, 2012). A typical example of a class 3 FFC is the crater Warner, which is 35 km in diameter and is located at 4.0°S, 87.3°E in the southern part of the Mare Smythii (Figure 5.1 b). In contrast, the floors of craters of classes 2 and 4 appear convex, indicating a different mechanism of crater floor uplift (*Schultz*, 1976a; *Jozwiak et al.*, 2012). Briggs is a good archetype of class 2 FFC, it is a crater of 37 km in diameter and is located at 26.5°N, 69.1°W, in the western part of the Oceanus Procellarum (Figure 5.1 a). Craters showing a convex floor may also exhibit moats adjacent to their wall zone but these are V-shaped; this is the case for classes 4a, 4b and 4c FFCs. In addition, craters of class 4b also exhibit an inner wall zone.

Table 5.1: A summary of Floor-Fractured Craters classification as proposed by *Jozwiak et al.* (2012) following *Schultz* (1976a)

Class	Description
1	Large craters: 50 – 300 km (average 140 km) Deep floor Absence of moats Radial or concentric fractures
2	Mid-size craters: 13 – 75 km (mean 30 km) Shallow convex floor Absence of moats Strong concentric fractures
3	12 – 170 km (mean 50 km) Shallow central flat floor Wide U-Shaped moat Radial or polygonal fractures
4a	Small craters: 4 – 38 km (mean 15km) Shallow convex floor Weak V-shaped moat Strong radial and concentric fractures
4b	Small craters: 7 – 45 km (average:25km) Shallow convex floor Pronounced V-shaped moat + inner ridges Subtle radial fractures
4c	Small craters: average 15 km Flat or concave up floor V-shaped moats Hummocky, lack of fracture
5	Large craters: 12 – 177 km (average 70km) Shallow old and degraded central flat floor Absence of moats Strong radial, concentric and/or polygonal fractures
6	Large craters: 50 – 200km Completely flooded by basalt Absence of moats Concentric fractures

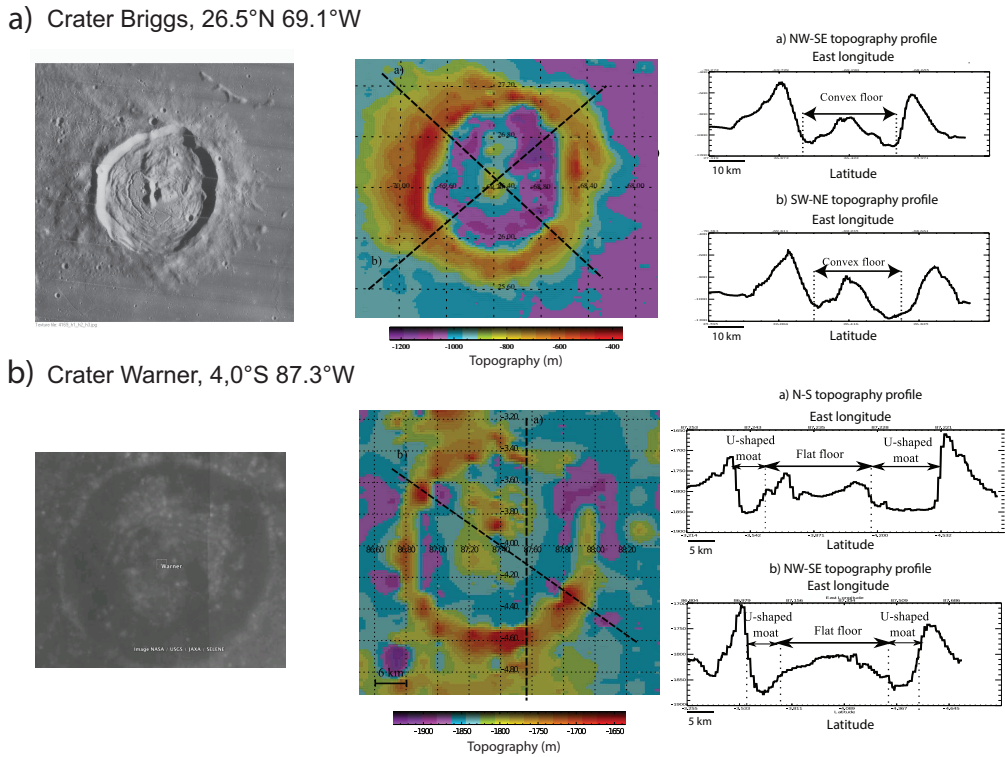


Figure 5.1: **a)** Class 2 floor-fractured crater Briggs ($26.5^{\circ}\text{N}, 69.1^{\circ}\text{W}$), 37 km in diameter: **Left**, high resolution scan from USGS Lunar Orbiter Digitization Project. **Center**, topographic map extracted from LOLA data. Latitudes and longitudes are indicated on the figure. Color scale indicates the topography in meters. The scale origin is given by the zero level of the geoid. **Right**, at the top, Northwest-Southeast topographic profile extracted from line a) on the central topographic map, at the bottom, Southwest-Northeast topographic profile extracted from line b) on the central topographic map. **b)** Same plots for the class 3 FFC Warner ($4.0^{\circ}\text{S}, 87.3^{\circ}\text{E}$) that is 35 km in diameter.

Finally, class 1 FFCs show only limited deformations while the floor of class 6 FFCs has been flooded by mare lavas, illustrating the close relationship between magmatism and deformations at these craters (*Schultz*, 1976a; *Jozwiak et al.*, 2012).

5.3 An axisymmetric model for a magmatic intrusion spreading below a crater-like topography

In this model, we consider the spreading of an axisymmetric intrusion above a rigid layer and below a thin overlying layer with a crater-like topography.

5.3.1 Crater topography and overlying layer characteristics

On the Moon, fresh impact craters have been classified into three categories according to their shapes following crater formation and collapse: simple craters, complex craters and basins (*Pike, 1974; Schultz, 1976b; Pike, 1980; Baker et al., 2011*). Simple craters are bowl-shaped craters that do not exhibit any slope-break (*Pike, 1980*). With increasing diameter, impact craters transition to complex craters that are characterized by an inner flat floor, terraced rims and a central peak. On the Moon, the transition from simple to complex craters occurs at a diameter of ~ 15 km (*Pike, 1980; Hiesinger, 2006; O'Keefe and Ahrens, 1999; Kalynn et al., 2013*). Although not all do, most craters larger than 100 km exhibit rings on their flat floors and are defined as basins (*Wilhelms et al., 1987; Schultz, 1988*). In our model, we do not consider basins and study the spreading of a magmatic intrusion at depth below simple and complex craters.

In this model, we account for the effects of the crater topography on the intrusion dynamics. The normalized sigmoid function $\xi(r)$ is used to parameterize the crater topography

$$\xi(r) = \frac{1}{1 + e^{-\frac{4\alpha(r-C)}{D_c}}} - \frac{1}{1 + e^{\frac{4\alpha C}{D_c}}} \quad (5.1)$$

where D_c is the intrusion depth, C the crater radius, defined as the distance from the crater center to the center of the wall zone, and α the average slope of the wall zone (Figure 5.2). The elevation in height relatively to the crater center, i.e the crater topography, is then given by

$$T_p(r) = D_c \xi(r) \quad (5.2)$$

and results in an increase in lithostatic pressure at the crater wall zone.

For simple craters, our definition of the crater radius C corresponds to half of the observed crater radius. *Pike (1980)* shows that the average wall slope α increases gradually from about 0.3 (19°), for craters 0.5 km in diameter,

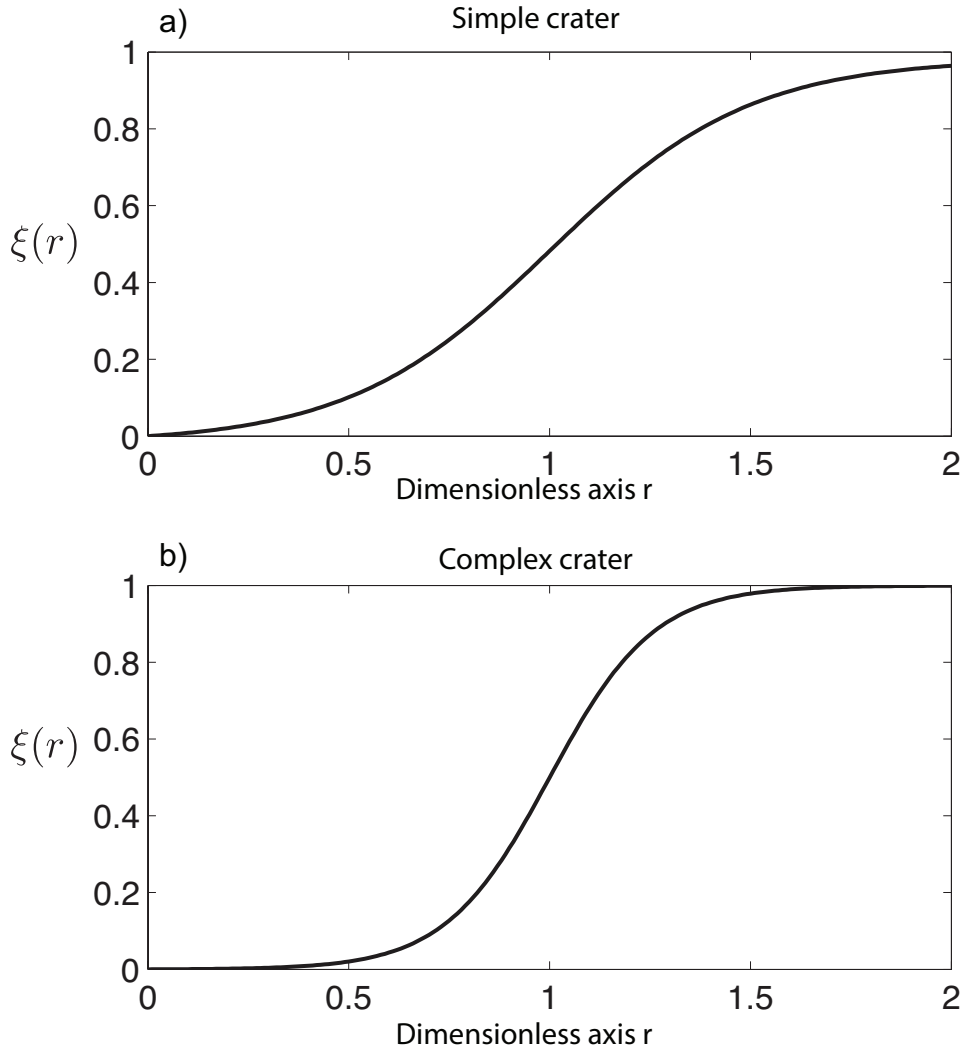


Figure 5.2: Here, we show the two normalized sigmoid function $\xi(r)$ used to parameterize the two end-member crater topographies (see Section 5.3.1). **a)** The sigmoid function of a simple crater is modeled using $D_c/4\alpha C = \zeta = 0.25$. **b)** The sigmoid function of a complex crater is modeled using $D_c/4\alpha C = \zeta = 0.13$.

to 0.4 (25°) for craters 15 km in diameter (*Kalyann et al., 2013*). To model a simple crater, we thus use $D_c/4\alpha C = 0.25$ (Figure 5.2 a), which, for $C = 2.5$ km and $\alpha = 0.4$ (25°) gives a corresponding D_c of 1 km in agreement with *Pike (1980)*. For complex craters, the size of the central flat floor, relatively to the crater radius, increases from 25%, for a crater 20 km in diameter, to 50%, for a crater that is 100 km crater in diameter. The wall of complex craters exhibits walls at the angle of repose ($\sim 30^\circ$), terraces, and hilly toes

that combine to form a wall zone of effective slope value that decreases from $\alpha = 0.5$ (30°) to $\alpha = 0.2$ (12°) as the crater diameter increases from 20 to 100 km (*Pike*, 1980; *Bray et al.*, 2008; *Kalynn et al.*, 2013). To model a complex crater, we use a ratio $D_c/4\alpha C = 0.13$ (Figure 5.2 b) which, for $C = 14$ km and $\alpha = 0.4$, i.e. a crater that is 40 km in diameter, gives $D_c = 3$ km in agreement with *Pike* (1980) and *Kalynn et al.* (2013).

Impact induces fracture and brecciation beneath the crater floor (*Willehelms et al.*, 1987; *Melosh*, 1989; *Jolliff et al.*, 2000) and also causes melting and compaction of the pores (*Melosh*, 1989; *Schultz*, 1976a). If the melting during impact is negligible and the neutral buoyancy zone of the magma lies immediately beneath an impact brecciated lens, as is commonly assumed (*Schultz*, 1976a; *Wichman and Schultz*, 1996; *Jozwiak et al.*, 2012), the overlying layer would not respond elastically due to its lack of coherent structure. We consider the case of a strengthless overlying layer with a crater like topography given by (5.2) in Section 5.4.1. However, a coherent impact melt unit commonly stands on top of the brecciated lens (*Melosh*, 1989; *Schultz*, 1976a). The neutral buoyancy zone of the magma depends on the crust and magma density and could also be situated deeper than the bottom of the brecciated lens. As a result, the overlying layer would deform elastically above the intrusion. In our model, we thus consider the case of an overlying layer with an elastic thickness $T_e(r)$ that varies with radial coordinate r and thickens at the crater wall zone (Figure 5.3). The elastic layer is characterized by a Young's modulus E and a Poisson's ratio ν . For simplicity, the thickness of the elastic layer, showing a simple or a complex crater topography, is considered to be equal to the intrusion depth and is given by

$$T_e(r) = T_e^0(1 + \Psi\xi(r)) \quad (5.3)$$

where $\Psi = D_c/T_e^0$ is the ratio of the crater depth D_c to the intrusion depth at the center T_e^0 and characterizes the thickening of the upper elastic layer at the crater wall zone. As a result of this assumption, the intrusion depth is underestimated in the model, but if a constant thickness brecciated layer overlies the intrusion and underlies such an elastic layer, it does not have any effect on the intrusion dynamics. The crater topography T_p is then given by

$$T_p(r) = T_e(r) - T_e^0 = T_e^0\Psi\xi(r) = D_c\xi(r). \quad (5.4)$$

Central peaks are common features of complex craters. Their dimensions depend on both projectile and target properties as well as on the impact angle (*Schultz et al.*, 1994; *Bray et al.*, 2008). However, their width can reach one fourth of the crater floor and they can be as high as half of the crater depth; hence such a structure could influence the intrusion dynamics. The effect of

a central peak on the spreading of an intrusion is examined in Appendix D. Moreover, a raised rim, uplifted relative to the pre-impact surface, is usually present at the exterior of the crater wall zone (Pike, 1976, 1980). Although, for simplicity, we do not model the effect of this feature, we discuss its possible influence on intrusion emplacement in Section 5.5.3.

5.3.2 Equations of Motion

We assume that the flow spreads along a thin bedding plane and neglect fracturing at the tip. The magma is considered to behave as a newtonian fluid with a constant viscosity μ and density ρ_m . The intrusion is fed at a constant rate through a cylindrical conduit of diameter a . The vertical coordinate z is oriented upward (Figure 5.3).

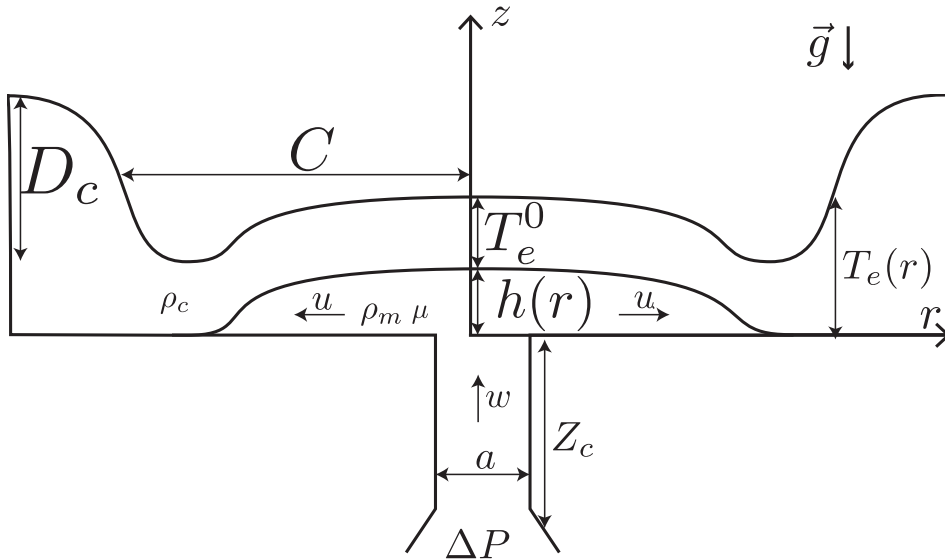


Figure 5.3: Sketch of the intrusion spreading below an impact crater topography. D_c (resp. C) represents the initial depth (resp. radius) of the impact crater. The intrusion spreads above a rigid homogeneous and horizontal bedrock at depth $T_e(r)$ below the crater floor. At the center, the intrusion depth is noted T_e^0 .

5.3.2.1 Momentum equation

The dynamics of the flow is given by the solution of the Navier-Stokes equation in cylindrical geometry. The magma has a relatively large viscosity, hence the flow is in a laminar regime and the inertia terms can be neglected. The

intrusion develops over a length scale comparable to the crater size that is much larger than its thickness H ($C \gg H$), hence the lubrication assumption allows further simplifications (*Huppert, 1982a; Michaut and Bercovici, 2009*). The Navier-Stokes equations in the radial and vertical directions for an axisymmetric, incompressible flow of newtonian fluid resume to

$$-\frac{\partial P}{\partial r} + \mu \frac{\partial^2 u}{\partial z^2} = 0 \quad (5.5)$$

$$-\frac{\partial P}{\partial z} - \rho_m g = 0. \quad (5.6)$$

Integration of (5.6) gives the pressure within the flow

$$P(r, t) = \rho_m g(h(r, t) - z) + \rho_c g T_e(r) + P_e(r, t) \quad (5.7)$$

where $h(r, t)$ is the intrusion thickness and ρ_c is the overlying layer density. The pressure is the sum of three different contributions: the weight of the magma and of the overlying layer and the elastic pressure P_e due to the deformation of the overlying elastic layer. In the absence of radial forces within the elastic plate, the elastic pressure required for bending the plate is given by the force per unit area that is necessary for a vertical displacement h of the thin elastic plate (*Turcotte and Schubert, 1982*)

$$P_e(r, t) = \nabla_r^2 (D(r) \nabla_r^2 h(r)) \quad (5.8)$$

where

$$D(r) = \frac{ET_e(r)^3}{12(1 - \nu^2)} \quad (5.9)$$

is the flexural rigidity of the plate which depends on the elastic layer thickness $T_e(r)$, Young's modulus E and Poisson's ratio ν .

Substituting (5.7) and (5.8) into (5.5) and integrating twice using no-slip boundary conditions at the top and bottom of the intrusion, i.e. $u_{z=0} = u_{z=h} = 0$, we get the radial velocity within the flow

$$u(r, z, t) = \frac{1}{2\mu} \left(\rho_m g \frac{\partial h(r, t)}{\partial r} + \rho_c g \frac{\partial T_e(r)}{\partial r} + \frac{\partial}{\partial r} (\nabla_r^2 (D(r) \nabla_r^2 h(r, t))) \right) (z^2 - zh(r, t)) \quad (5.10)$$

5.3.2.2 Injection rate

Assuming a Poiseuille flow within the cylindrical feeding conduit, the vertical injection velocity $w(r, t)$ and injection rate Q_0 are given by:

$$w(r, t) = \begin{cases} \frac{\Delta P}{4\mu Z_c} \left(\frac{a^2}{4} - r^2 \right) & r \leq \frac{a}{2} \\ 0 & r > \frac{a}{2} \end{cases}$$

$$Q_0 = \frac{\pi \Delta P a^4}{128 \mu Z_c} \quad (5.11)$$

where ΔP is the initial overpressure within the melt at $z = Z_c$.

5.3.2.3 Final equation

To obtain the final equation of motion, we write mass conservation integrated over the flow thickness:

$$\frac{\partial h(r, t)}{\partial t} = -\frac{1}{r} \frac{\partial}{\partial r} \left(r \int_0^{h(r, t)} u(r, z, t) dz \right) + w(r, t) \quad (5.12)$$

Injecting (5.10) into (5.12) and substituting $T_e(r)$ by (5.3) gives the evolution equation for the intrusion thickness h :

$$\begin{aligned} \frac{\partial h}{\partial t} &= \frac{\rho_m g}{12\mu} \frac{1}{r} \frac{\partial}{\partial r} \left(rh^3 \frac{\partial h}{\partial r} \right) + \frac{\rho_c g \Psi T_e^0}{12\mu} \frac{1}{r} \frac{\partial}{\partial r} \left(rh^3 \frac{\partial \xi(r)}{\partial r} \right) \\ &+ \frac{ET_e^{0^3}}{144\mu(1-\nu^2)} \frac{1}{r} \frac{\partial}{\partial r} \left(rh^3 \frac{\partial}{\partial r} (\nabla_r^2 ((1+\Psi\xi(r))^3 \nabla_r^2 h)) \right) + w(r, t). \end{aligned} \quad (5.13)$$

As expected, this evolution equation accounts for four different contributions. The first term on the right hand side represents gravitational spreading of the intrusion; except for a constant arising from a no-slip boundary at the top of the flow, it is the same as for a gravity current (*Huppert*, 1982a). This term is negative and induces magma spreading. The second term is associated with the increase in lithostatic pressure at the crater wall zone and represents the lithostatic barrier the flow has to face when spreading below the crater wall zone; it is not present in the case of an overlying layer of constant thickness (*Michaut*, 2011). This term is positive and opposes to the flow. The third term represents squeezing of the flow in response to the elastic deformation of the overlying layer. This term is negative and induces spreading in the case of an elastic layer of constant thickness (*Michaut*, 2011). However, in the case of a layer that thickens with r , it can become positive and oppose to the flow if the thickening is rapid and important, i.e. at the crater wall zone. The last term represents the injection rate.

5.3.3 Nondimensionalization

Because the model depends on a large set of parameters (see Table 5.2), we nondimensionalize the flow equation (5.13) using the crater radius C , as defined in Section 5.3.1, as the characteristic length scale, as well as a height

scale H and a time scale τ given by

$$H = \left(\frac{12\mu Q_0}{\rho_m g \pi} \right)^{\frac{1}{4}} = a \left(\frac{3\Delta P}{32\rho_m g Z_c} \right)^{\frac{1}{4}} \quad (5.14)$$

$$\tau = \frac{\pi C^2 H}{Q_0} = \left(\frac{12\mu}{\rho_m g \pi} \right)^{\frac{1}{4}} \pi C^2 Q_0^{-\frac{3}{4}} \quad (5.15)$$

The height scale and the time scale are defined by equating the nondimensional group in front of the gravity current term to 1, i.e., $(\tau \rho_m g H^3)/(12\mu C^2) = 1$. The height scale H is the characteristic height scale of a gravity current flow (*Huppert*, 1982a). τ is the time scale for a gravity current to fill in the crater; it mainly depends on the injection rate. In the case of an upper layer with constant thickness T_e^0 , a characteristic length scale for the flow is the flexural parameter Λ , as defined by *Turcotte and Schubert* (1982), given by

$$\Lambda = \left(\frac{ET_e^{0^3}}{12(1 - \nu^2)\rho_m g} \right)^{\frac{1}{4}} \quad (5.16)$$

it represents the wavelength over which the upper layer deforms elastically. However, in this problem, the crater radius C imposes a horizontal length scale to the flow, as the lithostatic barrier the flow faces at the wall zone imposes a limitation to the intrusion spreading. The choice of C as the length scale is then more relevant. Variables are then written as:

$$r = Cr^* \quad h = Hh^* \quad t = \tau t^* \quad (5.17)$$

where r^* , h^* and t^* are the dimensionless radius, thickness and time. Substituting (5.17) into (5.13) and dropping the stars, we finally get the dimensionless equation for the flow:

$$\begin{aligned} \frac{\partial h}{\partial t} &= \frac{1}{r} \frac{\partial}{\partial r} \left(rh^3 \frac{\partial h}{\partial r} \right) + \Xi \frac{1}{r} \frac{\partial}{\partial r} \left(rh^3 \frac{\partial \xi(r)}{\partial r} \right) \\ &+ \Theta \frac{1}{r} \frac{\partial}{\partial r} \left(rh^3 \frac{\partial}{\partial r} \nabla_r^2 ((1 + \Psi \xi(r))^3 \nabla_r^2 h) \right) + \frac{32}{\gamma^2} \left(\frac{1}{4} - \frac{r^2}{\gamma^2} \right) \end{aligned} \quad (5.18)$$

where $\xi(r)$ is also made dimensionless

$$\xi(r) = \frac{1}{1 + e^{-\frac{(r-1)}{\zeta}}} - \frac{1}{1 + e^{\frac{1}{\zeta}}} \quad (5.19)$$

and where γ , ζ , Ξ , Ψ and Θ are five dimensionless numbers that control the dynamics of the flow.

$$\gamma = \frac{a}{C} \quad (5.20)$$

$$\zeta = \frac{D_c}{4\alpha C} \quad (5.21)$$

$$\Xi = \left(\frac{\rho_c g D_c}{\rho_m g H} \right) \quad (5.22)$$

$$\Psi = \frac{D_c}{T_e^0} \quad (5.23)$$

$$\Theta = \left(\frac{\Lambda}{C} \right)^4 \quad (5.24)$$

The number γ represents the dimensionless source width. The number ζ is four times the normalized crater wall zone width; its range of values has been discussed in Section 5.3.1. The number Ξ is the ratio between the lithostatic pressure increase at the crater wall zone and the hydrostatic pressure due to a magma column of thickness H . The number Ψ is the dimensionless thickening of the upper elastic layer at the crater wall zone, as described in Section 5.3.1. Finally, the number Θ is the dimensionless flexural wavelength of the upper layer elevated to the power 4; it quantifies the length scale over which the elastic deformation is effective relative to the crater radius.

Additionaly, we define a last dimensionless number Ω

$$\Omega = \frac{\rho_m}{\rho_c} \quad (5.25)$$

which is the ratio between the magma and crust density. The value of Ω is set equal to 1.2. The dimensionless topography is then given by:

$$T_p(r) = \Xi \Omega \xi(r) \quad (5.26)$$

To obtain the crater floor appearance in the different figures, we add to the dimensionless expression of the topography, the dimensionless thickness $h(r)$ of the intrusion.

5.3.4 Range of values for the dimensionless numbers

For a conduit diameter varying between 10 and 100 m and a crater radius between 10 and 50 km, the normalized source width γ (5.20) varies between 10^{-5} and 10^{-2} (Table 5.3). Its variation does not significantly influence the results and in particular, does not play on the shape of the intrusion (*Michaut, 2011*) ; it is fixed at a value of 0.02 in this study. For a Young's modulus

between 1 and 10 GPa, a gravity of 1.62 m.s^{-2} , a magma density ρ_m between 2800 and 3200 kg.m^{-3} and an elastic thickness T_e^0 ranging from 0.5 to 5 km, the flexural wavelength of the upper layer Λ , given by (5.16), varies between 1 and 12 km (Table 5.2). Accordingly, for complex craters between 20 and 100 km in diameter, our length scale C is between 6 km and 40 km and the number Θ takes values between 10^{-7} and 1 (Table 5.3). For simple craters between 10 and 20 km in diameter, the number Θ is between 10^{-3} and 10.

Table 5.2: Range of values for the model parameters

Parameters	Symbol	Range of values
Depth of intrusion	T_e^0	0.5 – 5 km
Young's Modulus	E	1 – 10 GPa
Poisson's ratio	ν	0.25
Gravity	g	1.62 m.s^{-2}
Magma density	ρ_m	2800 – 3200 kg.m^{-3}
Magma viscosity	μ	$1 - 10^4 \text{ Pa.s}$
Feeder dyke width	a	10 – 100 m
Depth of the melt source	Z_c	200 – 500 km
Initial overpressure	ΔP	1 – 20 MPa
Injection rate	Q_0	$0.1 - 2.10^8 \text{ m}^3.\text{s}^{-1}$
Crust density	ρ_c	2500 kg.m^{-3}
Crater depth	D_c	500 – 4000 m
Characteristic scales	Symbol	Range of values
Height scale	H	1 – 35 m
Length scale	C	1 – 50 km
Time scale	τ	$10^{-3} - 1 \text{ years}$
Flexural wavelength	Λ	1 – 12 km

For complex craters, the crater depth ranges from 2 to 4 km and the number Ψ varies between 0.3 and 8 for intrusions between 0.5 and 5 km depth. For simple craters 1 to 2 km deep, this number is between 0.2 and 4 (Table 5.3). Additionally, we use $\zeta = 0.25$ for simple craters and $\zeta = 0.13$ for complex craters (see Section 3.1). Hence, we investigate the influence of four dimensionless numbers on the flow dynamics: the number ζ , through the effect of 2 end-member topographies (see Section 3.1), and the numbers Ξ , Θ and Ψ .

Table 5.3: Dimensionless numbers

Symbol	Description	Complex craters	Simple craters
		Range of values	Range of values
γ	Normalized source width	$10^{-4} - 10^{-2}$	$10^{-4} - 10^{-2}$
ζ	Normalized wall zone width	$0.05 - 0.13$	0.25
Ψ	Thickening term	$0.3 - 8$	$0.2 - 4$
Ξ	Hydrostatic term	$20 - 400$	$20 - 200$
Θ	Elastic term	$10^{-7} - 0.1$	$10^{-3} - 10$
Ω	Density ratio	1.2	1.2
Φ	Upper layer aspect ratio	4500	1200
σ	Normalized pressure head	$0.6 - 100$	$0.6 - 100$

5.4 Results

Equation (5.18) is solved numerically using a fully implicit finite-volume method detailed in Appendix A.3. In all solutions, we compute the mass conservation as a test for the accuracy of the convergence. We first examine the case of an intrusion below a strengthless overlying layer and a thickness that varies radially according to (5.3). We then consider the case of an intrusion that lies beneath an elastic layer whose thickness is also given by (5.3).

5.4.1 Intrusion below a brecciated zone with no elastic strength (effect of Ξ)

If the layer overlying the intrusion is highly fractured and brecciated, it is strengthless and $\Theta = 0$. In that case, we solve:

$$\frac{\partial h}{\partial t} = \frac{1}{r} \frac{\partial}{\partial r} \left(rh^3 \frac{\partial h}{\partial r} \right) + \Xi \frac{1}{r} \frac{\partial}{\partial r} \left(rh^3 \frac{\partial \xi(r)}{\partial r} \right) + \frac{32}{\gamma^2} \left(\frac{1}{4} - \frac{r^2}{\gamma^2} \right) \quad (5.27)$$

which corresponds to (5.18) without the elastic term.

We first consider an intrusion below a complex crater characterized by a topography given by (5.19) using $\zeta = 0.13$. In that case, at the crater wall, the overlying layer thickens and the flow faces an increase in lithostatic pressure which becomes more important as Ξ increases. To examine the effect of the lithostatic pressure increase at the wall zone on the intrusion spreading, we consider $\zeta = 0.13$ and different values of $\Xi = 20, 50$ and 200 in (5.27).

Up to $t = 1$, the flow spreads as a classical gravity current below a flat floor as the lithostatic term (i.e. second term on the right hand side of (5.27)) is

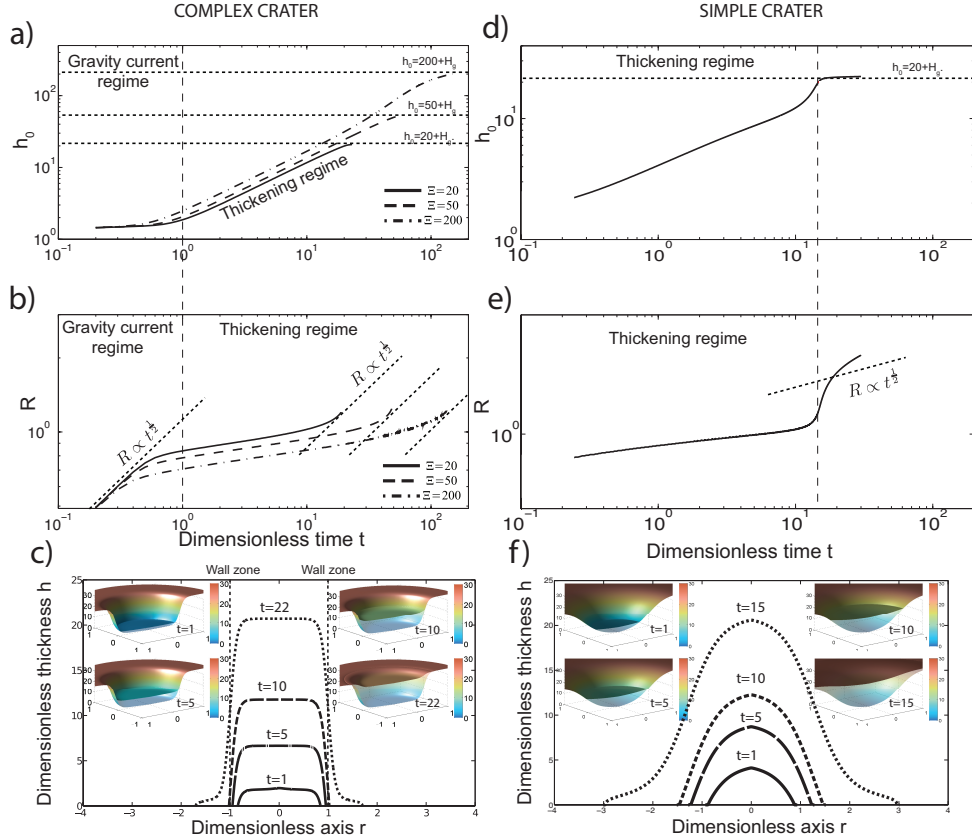


Figure 5.4: **a) and b):** Dimensionless thickness at the center $h_0 = h(0)$ and edge radius R versus dimensionless time t for the case of an intrusion below a strengthless layer, i.e. $\Theta = 0$, with a complex crater topography and for different values of Ξ indicated on the graph. Dimensional values are obtained by multiplying the dimensionless ones by their characteristic scales i.e. C , H (5.14) and τ (5.15). The vertical dashed line indicates $t = 1$, when the intrusion reaches the wall zone. Horizontal dotted lines on a) represent asymptotical behaviors for the different values of Ξ . On b) The dashed lines $R \propto t^{1/2}$ indicate the scaling law in the gravity current regime. **c)** Dimensionless intrusion profiles for different times indicated on the plot using $\Xi = 20$. For each time, a corresponding dimensionless 3D graph, showing the dimensionless floor appearance $T_p(r) + h(r)$, where $T_p(r)$ is given by (5.26), superimposed to the initial dimensionless floor appearance $T_p(r)$ (low opacity), is represented to see the deformation induced by the intrusion on the crater floor. We use $\gamma = 0.02$, $\zeta = 0.13$ and $\Theta = 0$. **d), e) and f)** Same plots but for an intrusion below a strengthless layer with a simple crater topography, i.e. $\zeta = 0.25$, using $\Xi = 20$ only.

negligible. In this regime, the flow thickness goes toward a constant, noted H_g , of order 1 (which depends on the source width (*Michaut and Bercovici, 2009*)) while the radius evolves as $t^{1/2}$ as predicted by the gravity current theory (*Huppert, 1982a*) (Figure 5.4 a, b). The intrusion shows a characteristic flat top profile with a steep front (Figure 5.4 c). When the intrusion reaches the wall zone, at $t \sim 1$, the lithostatic pressure increase prevents the intrusion from spreading laterally. The second term on the right of (5.27) is positive, it increases with Ξ and causes the thickening of the intrusion (Figure 5.4 a, c). In this thickening regime, the edge radius remains close to a constant (Figure 5.4 b). At the surface, the thickening of the flat top intrusion results in an important piston-like uplift of the crater floor. However, no moat is formed adjacent to the wall zone (Figure 5.4 c).

In contrast to complex craters, the topography of simple craters, and hence the lithostatic pressure, gradually increases from the center to the exterior of the crater wall zone. We use $\zeta = 0.25$ and $\Xi = 20$ in (5.27). In that case, there is no gravity current phase; the gradual lithostatic pressure increase slows down the spreading from the beginning and induces a gradual thickening phase (Figure 5.4 d, e, f). The intrusion shape almost accommodates the topography (Figure 5.4 f). Indeed, because the overlying layer is less dense than the magma, the crater floor appears slightly concave up, the concavity increasing with the density difference between the overlying layer and the magma, i.e. on Ω (Figure 5.4 f).

For both types of craters, the phase of thickening ends when the hydrostatic pressure due to the weight of the magma equals the lithostatic pressure outside of the wall zone, i.e. $h_0 \sim \Xi$. When h_0 becomes larger than Ξ , the gravity current term compensates for the lithostatic term in (5.27) and the intrusion can flow down the wall zone and return in a gravity current regime (Figure 5.4 a, b, d, e). In the gravity current regime, the flow evolves toward a constant value equal to $\Xi + H_g$. Thus, for a constant injection rate, the number Ξ mostly controls the final intrusion thickness and hence the shallowing of the crater floor. However, the injection rate might decrease as the intrusion grows, as the intrusion weight compensates for the overpressure at the origin of magma ascent. This effect should control the final shallowing of the crater floor and is discussed in Section 5.4.5.

5.4.2 Intrusion below an elastic layer of constant thickness

In the previous section, we considered that the intrusion stalls beneath a highly fractured and brecciated zone with no strength. However, an impact melt unit might be present on top of the brecciated lens. Furthermore, the

intrusion might also emplace deeper than the brecciated lens; both cases imply the deformation of an upper coherent elastic layer during the spreading of the intrusion. In *Michaut* (2011), the model was developed for an upper elastic layer of constant thickness in a 2D Cartesian geometry and the behavior of the flow was predicted for an axisymmetric geometry. Here, we first show the results for an elastic layer with a constant thickness in an axisymmetric geometry and verify the predictions of *Michaut* (2011). In the next sections, we examine the case of an upper elastic layer with a crater-like topography and a thickness that varies with the radius according to (5.3).

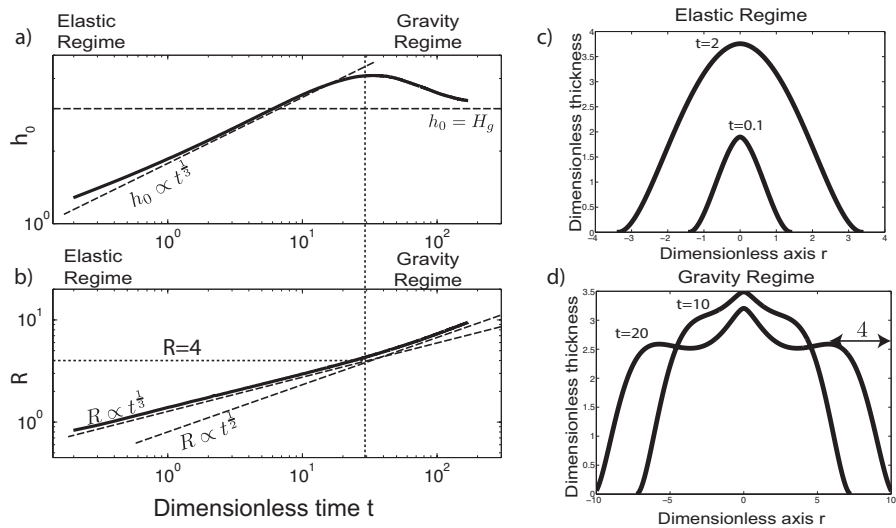


Figure 5.5: **a)** and **b)**: Dimensionless thickness at the center $h_0 = h(0)$ and edge radius R versus dimensionless time t for the case of an intrusion below a constant thickness elastic layer. For $R < 4$, the flow dynamics is controlled by the elastic deformation of the overlying layer, while for a $R > 4$, it is controlled by its own weight. In a), the dashed lines correspond to $h_0 \propto t^{1/3}$ and $h_0 = H_g$ which provide for scaling laws for the elastic and gravity current regimes. In b) the dashed lines $R \propto t^{1/3}$ and $R \propto t^{1/2}$ represent scaling laws for the elastic and gravity current regimes (*Michaut*, 2011). The vertical dashed line indicates the time when the intrusion reaches a radius of 4. The intrusion shape is shown at different times in the elastic regime in c) and in the gravity current regime in d). We use $\gamma = 0.02$, $\Xi = 0$, $\Psi = 0$ and $\Theta = 1$.

We first solve Equation (5.18) using $\Theta = 1$, $\Xi = 0$ and $\Psi = 0$, i.e. $T_e(r) = T_e^0$ to model the case of a magma that flows beneath an upper elastic layer of constant thickness. Equation (5.18) becomes:

$$\frac{\partial h}{\partial t} = \frac{1}{r} \frac{\partial}{\partial r} \left(rh^3 \frac{\partial h}{\partial r} \right) + \frac{1}{r} \frac{\partial}{\partial r} \left(rh^3 \frac{\partial}{\partial r} (\nabla_r^4 h) \right) + \frac{32}{\gamma^2} \left(\frac{1}{4} - \frac{r^2}{\gamma^2} \right) \quad (5.28)$$

In this case, there is no limitation to the flow as both the gravity current term and the elastic term, i.e. the first and second terms on the right side of (5.28), cause spreading. As expected, the intrusion dynamics follows two different spreading regimes (*Michaut*, 2011; *Michaut et al.*, 2013; *Bunger and Cruden*, 2011). During the first phase, the thickening is important and the intrusion shows a bell-shaped profile (Figure 5.5 a, c). As shown by *Michaut* (2011), the flow dynamics is controlled by the elastic deformation of the overlying layer up to a radius $R = 4\Lambda$. In this regime, the elastic pressure is dominant over the pressure due to magma weight. In the magma, the pressure is constant below the elastic layer, except at the tip (*Bunger and Cruden*, 2011; *Michaut*, 2011), which explains the bell-shaped profile of the intrusion (Figure 5.5 c). Indeed, for a constant pressure P_d in the magma, $P_e(r) = D\nabla_r^4 h = P_d$ implies

$$h(r) = \frac{P_d R^4}{64D} \left(1 - \left(\frac{r}{R} \right)^2 \right)^2 \quad (5.29)$$

D is the flexural rigidity of the upper layer of constant thickness as defined by (5.9). Results show that the thickness and radius evolve with time with an exponent close to $1/3$, as predicted by *Michaut* (2011) when neglecting the gravity current term and considering a constant injection rate (Figure 5.5 a, b). Beyond $R = 4\Lambda$, the size of the intrusion becomes much larger than the flexural parameter and the gravitational term becomes prevalent in the dynamics. The intrusion thus transitions to a gravity current regime characterized by a flat top profile (Figure 5.5 d). In this regime, the flow thickness evolves toward a constant H_g while the radius follows $t^{1/2}$ as predicted by the gravity current theory (*Huppert*, 1982a) (Figure 5.5 a, b). The elastic term is negligible when considering the dynamics of the whole flow in this regime. However, the overlying layer is unable to accommodate the steep front of a typical gravity current flow (*Huppert*, 1982a) and the intrusion develops a small scale bent edge whose width is equal to 4Λ (Figure 5.5 d).

5.4.3 Spreading beneath a complex crater topography

In this section, we consider an intrusion below an elastic overlying layer with a complex crater topography, hence we use $\zeta = 0.13$ in (5.19). We first examine the effect of varying the dimensionless flexural parameter, i.e. the dimensionless number Θ and then examine the influence of the thickening at the wall by varying the number Ψ .

5.4.3.1 Effect of the dimensionless flexural parameter (effect of Θ)

We consider equation (5.18) for which we set $\Xi = 20$ and $\Psi = 0.3$ and consider two different values of the dimensionless flexural parameter $\Theta = 10^{-2}$ and $\Theta = 10^{-5}$. Up to $t \sim 1$, the central flat floor of the crater acts as a constant thickness upper layer and the lithostatic term (second term on the right hand side of (5.18)) is negligible.

For $\Theta = 10^{-2}$, the flexural wavelength is close to the crater size, i.e. $4\Lambda \sim C$. The intrusion spreads in an elastic regime below the crater flat floor, the dimensionless radius and dimensionless thickness evolve close to $t^{1/3}$ (Figure 5.6) and the intrusion shows a characteristic bell-shaped profile (Figure 5.7 a). At $t \sim 1$, the second term on the right hand side of (5.18), representing the lithostatic pressure increase at the crater wall zone, becomes important and opposes to the flow. The intrusion enters in a thickening dominated regime, where the thickness increases significantly and the radius remains close to constant (Figure 5.6 and 5.7 a), while it has not yet transitioned into a gravity current regime and still shows a bell shape. The thickening of the bell-shaped intrusion results in a convex uplift of the crater floor (Figure 5.7 a).

For $\Theta = 10^{-5}$, the intrusion first spreads in an elastic regime and the dimensionless radius and thickness evolve as $t^{1/3}$ (Figure 5.6). However, the flexural wavelength is much smaller than the crater size in this case (i.e. $4\Lambda \ll C$). The flow transitions to a gravity current regime far in front of the wall zone, at $t = 0.06$, which is evident as, beyond this time, the dimensionless radius evolves as $t^{1/2}$ while the dimensionless thickness goes toward a constant (Figure 5.6 a and b). In consequence, the intrusion shows a flat top profile and a small scale bent edge while reaching the crater wall zone (Figure 5.7 b). At $t \sim 1$, the lithostatic pressure increase prevents the intrusion from spreading radially and the intrusion thickens. The thickening of the flat top intrusion results in a piston-like uplift of the central part of the crater floor (Figure 5.6 a and 5.7 b) as in the previous case of a gravity current below a strengthless overlying layer (Figure 5.4 c). However, the bending of the upper layer above the intrusion at its edge leads to the formation of a circular moat, adjacent to the wall zone, whose extent corresponds to the size of the intrusion edge and is $\sim 4\Lambda$ (Figure 5.7 b).

The thickening rate of the intrusion, as it reaches the wall zone, depends on its spreading regime (Figure 5.6 a, b) and hence on the value of Θ . For larger values of Θ , the elastic pressure that squeezes the flow is more important and it is easier for the magma to overcome the lithostatic barrier and spread below the wall zone. In any case, when the sum of the pressures due to elastic bending of the overlying layer and to magma weight compensates for the hydrostatic pressure due to the crater wall zone weight, the flow passes

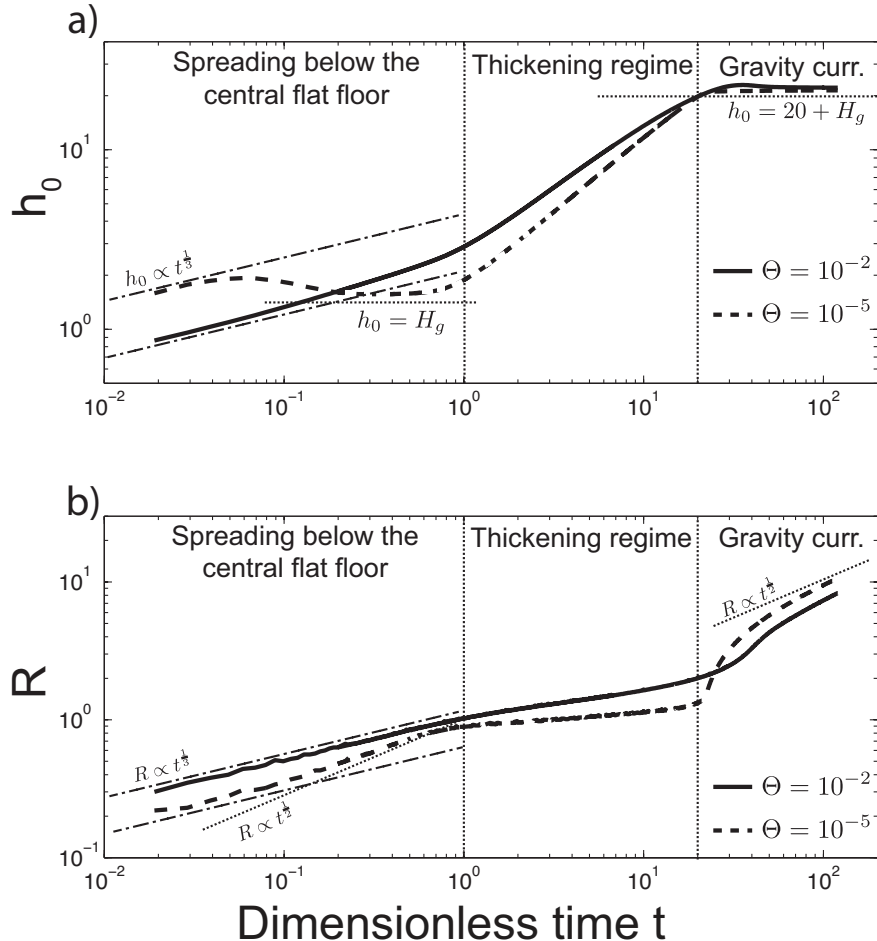


Figure 5.6: Dimensionless thickness at the center $h_0 = h(0)$ and edge radius R versus dimensionless time t for the case of an intrusion spreading below an overlying elastic layer with a topography characteristic of a complex crater, i.e. $\zeta = 0.13$, and using a constant injection rate. Vertical dotted lines: dimensionless times when the intrusion enters and leaves the thickening regime. Thick solid lines, $\Theta = 10^{-2}$, thick dashed lines, $\Theta = 10^{-5}$. Scaling laws are shown in dash-dotted lines for the elastic regime ($R \propto t^{1/3}$, $h_0 \propto t^{1/3}$) and in dotted lines for the gravity current regime ($R \propto t^{1/2}$, $h_0 \rightarrow H_g$, $h_0 \rightarrow \Xi + H_g$). We use, $\gamma = 0.02$, $\zeta = 0.13$, $\Xi = 20$ and $\Psi = 0.3$.

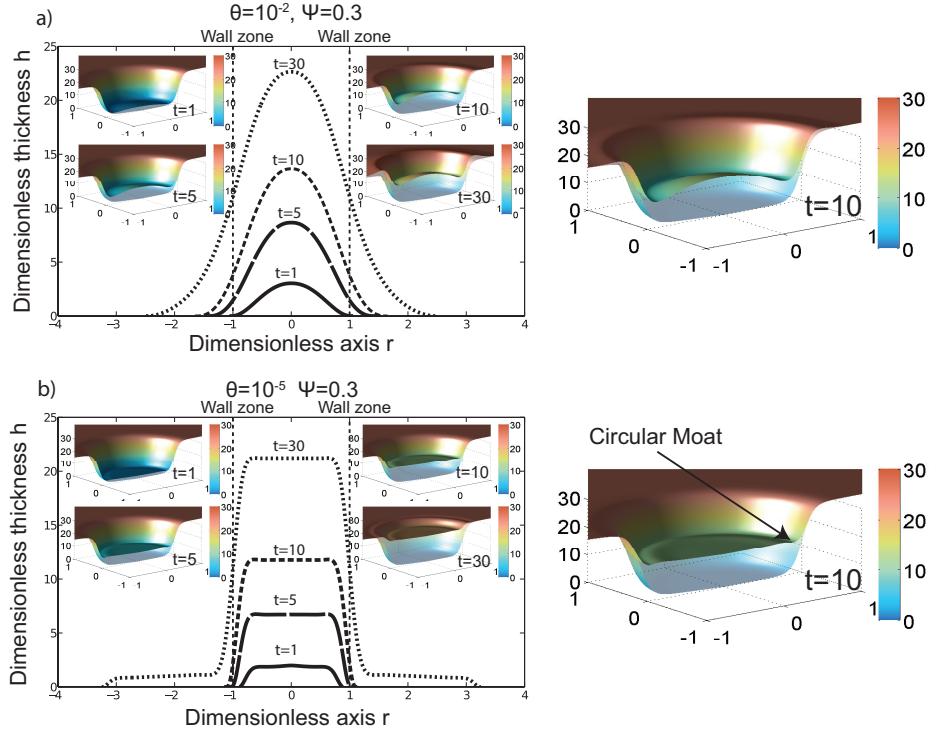


Figure 5.7: **a)** Profiles for an intrusion spreading below an elastic overlying layer with a complex crater topography at different times indicated on the plot for $\Theta = 10^{-2}$, i.e. corresponding to a small crater and/or an intrusion below a thick elastic layer. Units are dimensionless. For each time, a corresponding 3D graph showing the dimensionless crater floor appearance given by $T_p(r) + h(r)$ where $T_p(r)$ is given by (5.26), is represented. For each plot, the dimensionless initial topography $T_p(r)$ is superimposed in low opacity. **b)** Same plot but for a large crater and/or a shallow intrusion, i.e. $\Theta = 10^{-5}$. Here, we use $\gamma = 0.02$, $\zeta = 0.13$, $\Xi = 20$ and $\Psi = 0.3$.

the wall zone. For both values of Θ , as it passes down the wall zone, the intrusion is in a gravity current regime as R is or becomes larger than 4Λ : the radius evolves as $t^{1/2}$ and the thickness evolves toward the final value of $\Xi + H_g$ (Figure 5.6 a, b).

5.4.3.2 Effect of the local increase in the flexural parameter at the wall zone (effect of Ψ)

Due to the elastic thickness increase at the crater wall zone, the flexural wavelength of the overlying elastic layer increases from Λ at the crater center

to a value equal to

$$\Lambda_b = \left(\frac{E(T_e^0 + D_c)^3}{12(1 - \nu^2)\rho_m g} \right)^{\frac{1}{4}} = \Lambda(1 + \Psi)^{\frac{3}{4}} \quad (5.30)$$

beyond the wall zone. To understand the effect of the local increase in flexural wavelength at the wall zone, we consider a constant value of the number $\Xi = 20$ and increasing values of the number $\Psi = 0.3, 3, 6$ for the two different values of the number $\Theta = 10^{-2}$ and $\Theta = 10^{-5}$ used previously and representing two possible end-member floor deformations.

For $\Theta = 10^{-2}$, the elastic term is dominant over the gravity current term as the flow arrives to the wall zone and the effect of the local increase in flexural wavelength of the overlying layer is to increase the thickening rate with time (Figure 5.8 a). The increase in flexural wavelength enhances the barrier effect of the lithostatic pressure increase at the crater wall zone and, in response, the flow thickens rapidly in the center, where the bending is easier (Figure 5.8 a and c). The elastic pressure increases with the bending and after a time that increases with Ψ , it becomes important enough to compensate for the lithostatic pressure increase at the wall zone and induce a squeezing of the intrusion below the wall zone. For large values of Ψ , the local increase in flexural wavelength is important at the wall zone and forces the flow to extend and deform the overlying layer over a much larger distance, beyond the crater, than for smaller values of Ψ (compare $\Psi = 0.3$ and 6 on Figure 5.8 a). As a result, for large values of Ψ , the intrusion profile relaxes, the thickness at the center collapses (Figure 5.8 a and c) and the radius increases quickly. After the relaxation of the profile, the intrusion is still in an elastic regime but characterized by a flexural parameter Λ_b . Once the dimensionless radius reaches $r = 4\Lambda_b/C = 4\Lambda(1 + \Psi)^{3/4}/C = 4\Theta^{1/4}(1 + \Psi)^{3/4}$, the intrusion transitions to a gravity current regime where the thickness evolves toward a constant and the radius grows as $t^{1/2}$ (Figure 5.8 a). For instance, for $\Psi = 3$, the transition to a gravity current regime occurs when $R = 4\Theta^{1/4}(1 + \Psi)^{3/4} = 3.6$ (Figure 5.8 a).

For $\Theta = 10^{-5}$, the gravity current term is dominant when the intrusion reaches the wall zone and the elastic term only controls the shape of the front (Figure 5.8 b and d). And hence, the thickening rate only increases by a few percent between $\Psi = 0.3$ and $\Psi = 6$, while it increases by a factor of 3 in the case of $\Theta = 10^{-2}$ (Figure 5.8 a and b). Nevertheless, the local increase in the flexural wavelength below the wall zone tends to enlarge the size of the intrusion edge and to result in a deeper circular moat at the surface (Figure 5.8 d and f).

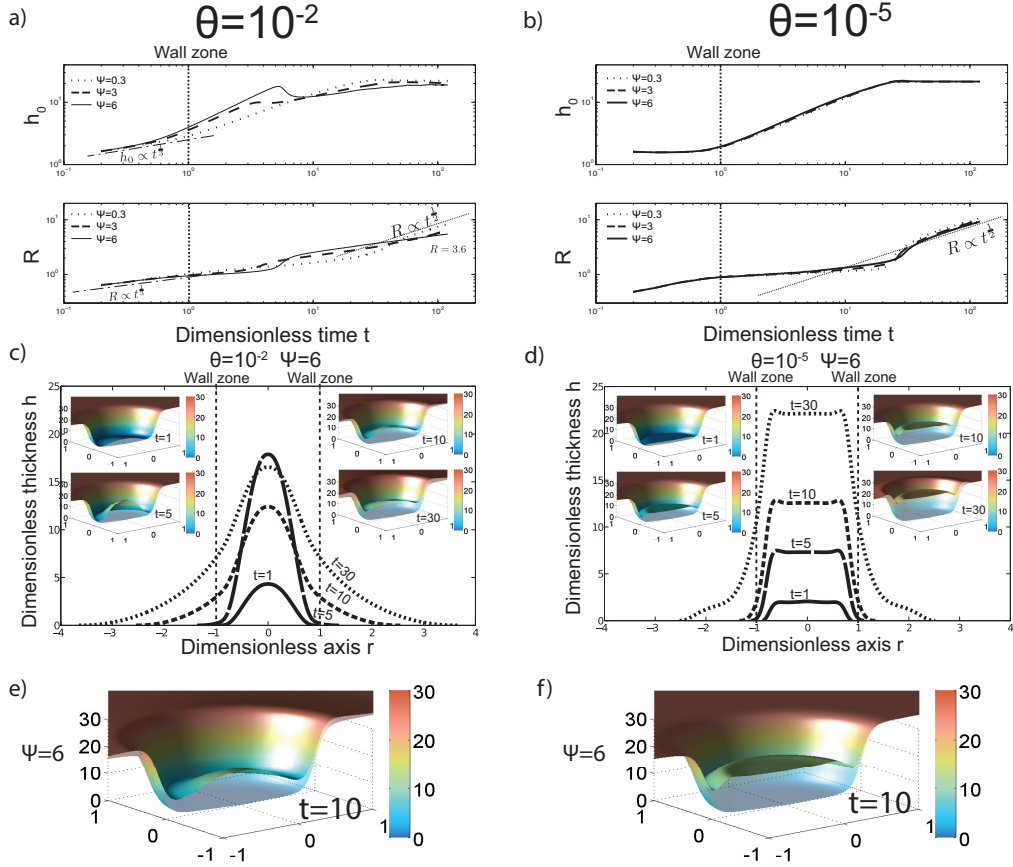


Figure 5.8: **a)** Dimensionless thickness at the center $h_0 = h(0)$ and edge radius R versus dimensionless time t , for an intrusion spreading below an overlying layer with a complex crater topography, for $\Theta = 10^{-2}$ and different values of $\Psi = 0.3, 3$ and 6 . The vertical dotted lines indicate $t = 1$, i.e. the time at which the intrusion reaches the wall zone. **c)** Intrusion profiles for different times indicated on the plot for $\Theta = 10^{-2}$, i.e. corresponding to a small crater and/or a deep intrusion and $\Psi = 6$. Units are dimensionless. For each time, the corresponding dimensionless crater floor appearance given by $T_p(r) + h(r)$, where $T_p(r)$ is given by (5.26), is represented. For each plot, the dimensionless initial topography $T_p(r)$ is superimposed in low opacity. **e)** Dimensionless crater floor appearance at $t = 10$ for $\Psi = 6$, $\Theta = 10^{-2}$. **b), d) and f)** Same plots as a), c) and e) but for $\Theta = 10^{-5}$. We use $\gamma = 0.02$, $\zeta = 0.13$ and $\Xi = 20$.

5.4.4 Spreading beneath a simple crater

In comparison to complex craters, the lithostatic pressure as well as the flexural wavelength of the upper layer gradually increase from the center to the exterior of the crater wall zone. Given the appropriate range of values for the number $\Theta = 10^{-3} - 10$, as discussed in Section 5.3.4, the flexural parameter is between 0.2 and 1 times the crater radius C . The bending of the upper layer thus controls the intrusion shape and dynamics during the whole flow and the intrusion always shows a bell shaped geometry (Figure 5.9). To represent the case of an intrusion below a bowl-shaped crater, we use $\zeta = 0.25$, $\Xi = 20$, $\Theta = 0.1$ and we study the effect of the thickening at the wall zone by using different values of $\Psi = 0.1$ and $\Psi = 4$.

For $\Psi = 0.1$, the thickening at the wall zone $\Psi\xi(r)$ is negligible and the elastic term is similar to that of a constant thickness layer. However, the lithostatic pressure increase slows down the spreading and the evolution of the radius with time is slower than for an elastic regime below a constant thickness layer. The intrusion shows a bell-shaped profile with an important curvature because the weight of the lithostatic barrier constrains the intrusion edge (Figure 5.9 a). For $\Psi = 4$, the local flexural wavelength rapidly rises up to $\Lambda_b = \Lambda(1 + \Psi)^{3/4}$. As a consequence, the intrusion squeezes more rapidly and thickens more slowly than for smaller values of Ψ (Figure 5.9 b). For a larger value of Ψ , the deformation occurs over a larger wavelength and the shallowing is smaller at a given time. However, the overall deformation at the surface is very similar in both cases: the crater floor appears convex and shows an important curvature which overlaps the initial bowl shape of the crater (Figure 5.9 a, b).

5.4.5 Effect of a variable injection rate

So far, we have assumed a constant injection rate; and hence the intrusion grows indefinitely in volume and the flow passes the crater wall zone. However, the driving pressure in the feeder conduit should decrease as the intrusion grows during the thickening phase. In particular, the increase in hydrostatic pressure due to magma weight and in elastic pressure due to bending above the dyke might finally compensate for the initial overpressure ΔP in the magma at the origin of the flow. As the increase in lithostatic pressure at the crater wall zone prevents the intrusion from spreading laterally, the intrusion might reach a steady state profile such that no more magma can intrude. New expressions for the vertical injection velocity and injection rate, taking into account the

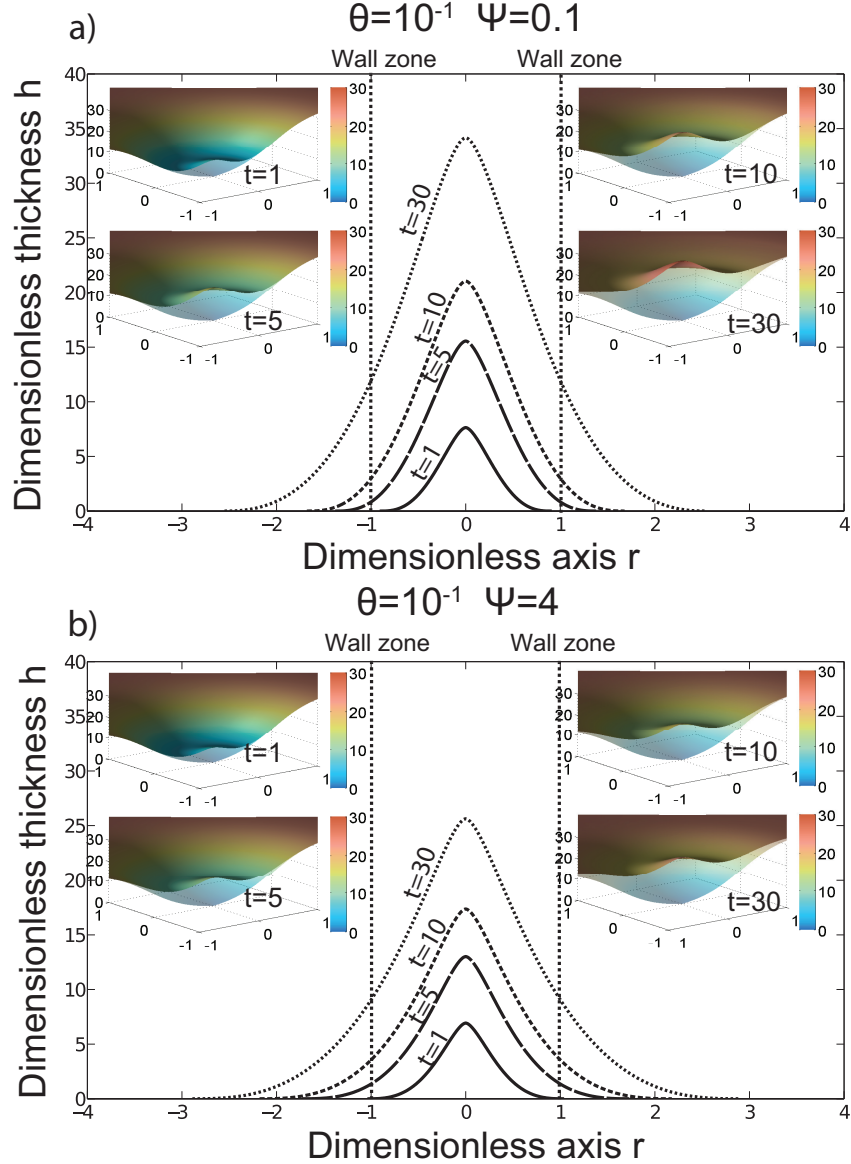


Figure 5.9: **a)** Dimensionless profiles, of an intrusion spreading below an overlying elastic layer with a simple crater topography, i.e. $\zeta = 0.25$, for different dimensionless times indicated on the plot for $\Theta = 10^{-1}$ and $\Psi = 0.1$. For each time, a corresponding 3D graph, showing the dimensionless crater floor appearance given by $T_p(r) + h(r)$, where $T_p(r)$ is given by (5.26), is represented. For each plot, the initial topography $T_p(r)$ is superimposed in low opacity. **b)** Same plot but for $\Psi = 4$. We use, $\gamma = 0.02$ and $\Xi = 20$.

increase in pressure in the magma at the top of the feeder dyke, are given by:

$$w(r, t) = \frac{32}{\gamma^2} \left(1 - \frac{1}{\sigma} (h_0 + P_{e,r=0}) \right) \left(\frac{1}{4} - \frac{r^2}{\gamma^2} \right) \quad (5.31)$$

and

$$Q_0 = \left(1 - \frac{1}{\sigma} (h_0 + P_{e,r=0}) \right) \quad (5.32)$$

where

$$\sigma = \frac{\Delta P}{\rho_m g H} \quad (5.33)$$

and

$$P_{e,r=0} = \Theta \nabla_r^2 ((1 + \Psi \xi(r))^3 \nabla_r^2 h) \Big|_{r=0} \quad (5.34)$$

The dimensionless number σ represents the normalized pressure head, $P_{e,r=0}$ is the dimensionless elastic pressure at the center and Q_0 the dimensionless total injection rate. As discussed in [Michaut \(2011\)](#), the elastic pressure $P_{e,r=0}$ required to bend the upper layer tends to infinity as $R \rightarrow 0$, but rapidly decreases with the radius as $P_{e,r=0}$ scales with h_0/R^4 (see (5.8)). However, here we assume a large aspect ratio for the intrusion (lubrication assumption), and this initial transient regime, where the flow is very narrow and $P_{e,r=0}$ is very large, is thus not representative of the initiation phase of the intrusion. Hence, to investigate the effect of the elastic pressure on the injection rate, we neglect this initial transient phase.

Given that the deformations are limited to craters, it is possible that excavation of material during the impact has controlled the intrusion of magma. In that case, the driving pressure ΔP at the origin of the flow should be lower or equal to the weight of crust that has been removed by cratering, i.e. $\Delta P \leq \rho_c g D_c$, which implies $\sigma < \Xi$ (see (5.22) and (5.33)). Hence, given the range of values for the parameters (Table 5.2), the value of the number σ varies between 0.6 and 100 (Table 5.3). We consider a complex crater with $\zeta = 0.13$ and we set $\Xi = 50$, $\Psi = 1$, $\sigma = 22$ and two values of Θ , equal to 10^{-2} and 10^{-5} , to consider the effect of a variable injection rate.

For $\Theta = 10^{-2}$, the elastic pressure governs the spreading of the intrusion below the crater flat floor; as $P_{e,r=0}$ scales with h_0/R^4 , $P_{e,r=0}$ decreases as the flow spreads and its radius increases (Figure 5.10 a) inducing an increase in the total injection rate Q_0 (5.32). Then, as the intrusion thickens, both the pressure due to magma weight and the elastic pressure increases at the center, in response (Figure 5.10 a). The total injection rate decreases and the system reaches a steady state shape when $Q_0 \rightarrow 0$, i.e when the initial overpressure is compensated by the sum of the elastic pressure and of the pressure due to magma weight (Figure 5.10 a,b).

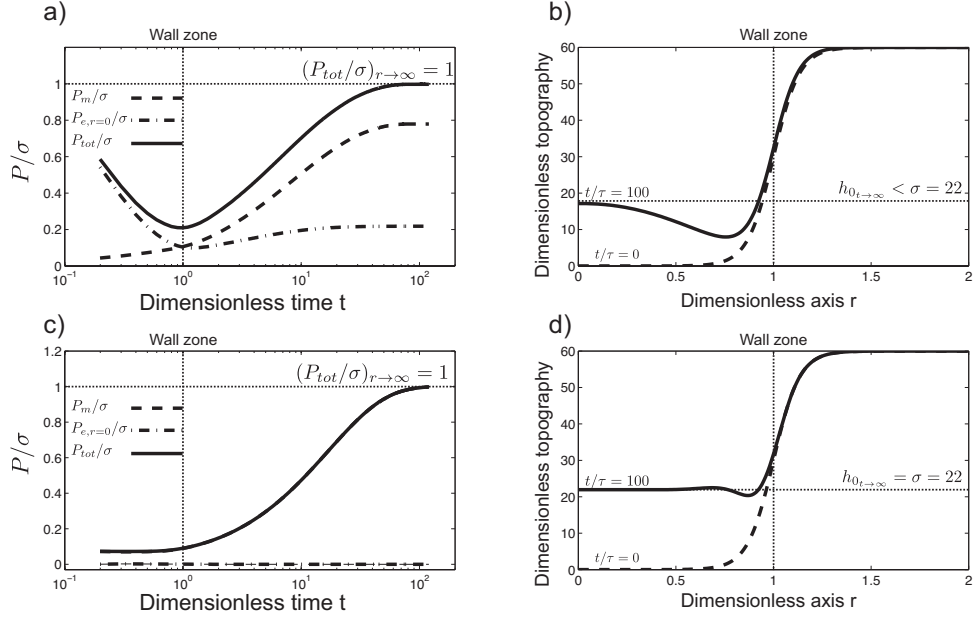


Figure 5.10: **a)** Dimensionless pressure in the magma P normalized by the value of σ versus dimensionless time t for $\Theta = 10^{-2}$, for an intrusion spreading below an elastic overlying layer with a complex crater topography. The solid line represents the dimensionless pressure at the center of the flow normalized by σ , i.e. $P_{tot}/\sigma = (h_0 + P_{e,r=0})/\sigma$, the dashed line indicates the magma weight contribution $P_m/\sigma = h_0/\sigma$ and the dash-dotted line represents the elastic pressure contribution $P_{e,r=0}/\sigma$. The vertical dotted line indicates the dimensionless time when the intrusion reaches the wall zone. **b)** Initial (dashed line) and final, i.e. steady state, (solid line) dimensionless topography of the crater. **c)** and **d)** Same plots as **a)** and **b)** but for $\Theta = 10^{-5}$. In **c)**, the dashed line representing the magma weight contribution is not distinguishable from the total pressure. For all plots, horizontal dotted lines represent asymptotic behaviors. We use $\gamma = 0.02$, $\Xi = 50$, $\zeta = 0.13$, $\Psi = 1$ and $\sigma = 22$.

For $\Theta = 10^{-5}$, the weight of the magma is the dominant contribution to the pressure during the whole flow (P_m and P_{tot} are not distinguishable on Figure 5.10 c) and the injection rate remains close to a constant while the intrusion spreads below the crater flat floor in a gravity current regime (Figure 5.10 c). As the intrusion thickens, the weight of magma increases at the center (Figure 5.10 c) leading to a decrease in the total injection rate (5.32). When, $h_0 = \sigma = 22$, no more magma intrudes below the crater, the intrusion thickness as well as the radius stabilized and the intrusion reaches its steady state shape (Figure 5.10 c, d).

The normalized pressure head thus controls the amount of shallowing of

the crater floor. If the pressure head is larger than the weight of the crust that has been removed by cratering, the intrusion would pass the wall zone and reach a constant thickness, but it would still continue to flow laterally beyond the wall zone (see lateral spreading regime in *Michaut (2011)*). In contrast, if the pressure head is less than the weight of the crust that has been removed by cratering, the intrusion reaches a steady-state shape and deformations are constrained within the crater. In that case, for small values of Θ , the amount of shallowing is directly the normalized pressure head σ while for relatively large values of Θ , the intrusion reaches a steady state profile for a thickness $h_0 \leq \sigma$.

5.5 Discussion

5.5.1 Floor appearance

Viscous relaxation tends to relax large wavelength structures without affecting or creating small-scale features. In particular, viscous relaxation is not able to explain the presence of moats bordering the wall region observed in different classes of FFCs (*Schultz, 1976a; Jozwiak et al., 2012*). Relaxation of the crater floor also tends to produce a convex profile at the end of the deformation (*Dombard and Gillis, 2001*) and cannot account for central flat floors observed for FFCs of class 3 and 5 (*Jozwiak et al., 2012*).

In contrast, our model is able to reproduce the different kinds of floor appearances observed at FFCs and thus confirms the predictions initially made by *Schultz (1976a)*. In particular, for a given crater size, the thickening caused by the increase in lithostatic pressure at the crater wall zone induces either a convex uplift of the crater floor, if the intrusion occurs below a thick elastic layer, or a piston-like uplift of the crater floor if the intrusion occurs below a strengthless and highly brecciated zone or below a thin elastic layer. This piston-like uplift results in a large, shallowed plate like floor as predicted by *Schultz (1976a)*.

In addition, the model shows that the final appearance of the crater floor is controlled by the ratio between the flexural wavelength of the overlying layer, that mainly depends on the elastic layer thickness, and the crater size, i.e. on the number $\Theta = (\Lambda/C)^4$. Indeed, because the deformation of the overlying elastic layer is accommodated along a width of 4Λ , our model predicts a transition between a flat floor and a convex floor when $4\Lambda \sim C$, i.e. at $\Theta = 10^{-3}$. For large values of $\Theta > 10^{-3}$, i.e. small craters and/or a thick elastic layer overlying the intrusion, the bending of the upper elastic layer affects the whole crater width resulting in a convex crater floor (Figure 5.7

a). On the contrary, for large craters and/or a thin elastic layer overlying the intrusion, i.e. small values of $\Theta < 10^{-3}$, the thickening of the flat top intrusion results in a flat central floor with a circular moat that borders the interior of the wall zone (Figure 5.7 b). This circular moat results from the elastic deformation of the overlying layer at the intrusion front and its size is equal to 4Λ . Finally, if the overlying layer is strengthless and $\Theta = 0$, the crater floor appears flat or slightly concave up because of the density difference between the magma and the overlying layer.

FFCs of classes 3 and 5 show a central uplifted flat floor; they generally have a large diameter: the mean diameter is of 50 km for craters of class 3, and 70 km for craters of class 5 (Table 5.1) (*Schultz*, 1976a; *Jozwiak et al.*, 2012). These large diameters are coherent with a small value of Θ (5.24), i.e. with an intrusion in the gravity current regime as it reaches the wall zone and a piston-like uplift of the central flat floor of the crater. A moat bordering the wall region is observed for craters of class 3 in agreement with our results for small values of Θ (see for instance the topography of FFC Warner Figure 5.1 b). Craters of class 5 have a central shallowed flat floor but do not show a moat bordering the wall region (Table 5.1). One possibility is that the intrusion has emplaced below a strengthless layer. Another possibility is that these craters have been partially infilled before deformation by basin ejecta (*Schultz*, 1976a); as a result, the thickening of the intrusion was limited and not important enough to form a moat. Furthermore, for large craters and/or intrusions below a thin elastic layer, our model predicts that the maximum stresses are concentrated upon the intrusion edge within a crown bordering the wall region (Figure D.1 c). This stress concentration in front of the crater wall could induce new fractures or reactivate preliminary fractures caused by the impact, providing privileged paths for the magma to rise to the surface (*Schultz*, 1976a). Indeed, pyroclastic deposits have been observed in floor-fractured craters of classes 3 and 5, preferentially located within fractures adjacent to the wall zone (*Schultz*, 1976a).

Convex floors characterize FFCs of classes 2 and 4 (see for instance FFC Briggs, Figure 5.1 a). Craters of classes 2 and 4 are in fact generally small; their average diameters are 30 and 20 km respectively (*Jozwiak et al.*, 2012) with some of them being initially simple craters (Table 5.1); this is coherent with large values of Θ and a final convex floor appearance according to our model. In FFCs of class 4, a more or less pronounced narrow V-shaped moat is observed adjacent to the wall zone as well as pronounced inner ridges for FFCs of class 4 b. In the frame of our model, we can interpret these features as resulting from the rupture of the upper layer during the thickening regime. Indeed, our model predicts that the radial stress might not be maximum at the crater center, even for a convex floor, but at a given radial coordinate $r_{\sigma_{max}}$

such that $0 < r_{\sigma_{max}} < 1$ (see Appendix D.1, Figure D.1 a, b) because the intrusion might transition from an elastic to a gravity current shape before the wall zone and because the elastic thickness increases towards the wall zone. The location of $r_{\sigma_{max}}$ depends on time and on the values of Θ and Ψ . This location of maximum stress provides a preferred location for a concentric failure of the upper elastic layer.

Furthermore, our model can also explain the variable characteristics of central peaks of FFCs (*Schultz*, 1976a). In the case where an elastic layer is present, our model predicts that the central peak would be leveled up during the uplift and slightly smaller than initially (see Appendix D.2, Figure D.2 b,c). *Schultz* (1976a) indeed observed that there is a tendency for central peaks of FFCs to be smaller than those for well-preserved impact craters. Furthermore, a small circular moat borders the central peak if this elastic layer is relatively thin, such $4\Lambda < C$ (see Appendix D.2, Figure D.2 b). The build up of stress resulting from the flexure within this moat could be coherent with the fracture pattern observed in the vicinity of central peaks at some FFCs (*Schultz*, 1976a). Finally, if the layer overlying the intrusion is formed by incoherent breccias, the central peak would be buried during the uplift, or its initial size significantly reduced if the shallowing is smaller than the central peak height, and could thus be absent from the uplifted floor, as observed in a few cases (*Schultz*, 1976a) (see Appendix D.2, Figure D.2 a).

5.5.2 Depth of the intrusion

The deformation of a layer overlying a shallow magmatic intrusion such as a laccolith has been classically modeled by the upward deflection of a thin elastic layer submitted to the pressure P_d within the intrusion (5.29). In this kind of static model, the internal pressure P_d within the intrusion is usually assumed to be a constant and equal to the hydrostatic pressure due to the weight of the magma at the center of the intrusion. The solution to this problem gives a floor deflection, or maximum intrusion thickness h_0 , that varies with radius to the fourth (5.29) (*Johnson and Pollard*, 1973; *Pollard and Johnson*, 1973). In the case of an intrusion below the floor of a crater, the crater radius clamps the elastic overlying layer and the intrusion radius can be considered equal to the crater radius, if the deformation affects the whole crater floor. And hence, this approach has motivated many previous studies to derive the intrusion depth from the estimated uplift at a given floor-fractured crater (*Wichman and Schultz*, 1996; *Jozwiak et al.*, 2012).

However, there is an inconsistency in equating the pressure due to magma weight and the elastic pressure deforming the overlying plate since both pressures act in favor of flow spreading. Assuming that the final steady-state

shape of the flow has been reached, i.e. that the intrusion has reached the wall zone and that the pressure above the feeding conduit is equal to the initial overpressure driving the flow in the conduit (see Section 4.4), and assuming that the overlying elastic layer making the crater floor has a constant thickness up to the wall zone, the function (5.29) may indeed describe the vertical displacement of the overlying layer due to an elastic pressure P_e . But this is true only in the case where the intrusion is in the elastic regime, i.e. if the elastic pressure is dominant over the pressure due to magma weight and in this case, the pressure necessary for deforming the overlying plate P_e is then not supported by magma weight but by the driving pressure within the feeding dyke (see (*Michaut, 2011*), Section 6.1). Furthermore, if the thickening at the wall zone is significant, the curvature of the intrusion is accentuated by the interaction with the wall zone and (5.29) is not accurate anymore. Moreover, for large craters or shallow intrusions, i.e. $4\Lambda < C$, the intrusion lies in the gravity current regime when it reaches the crater wall zone. In that case, the dominant pressure comes from magma weight and, assuming the intrusion has reached the wall zone and its steady-state shape, then the overpressure driving the injection is compensated by magma weight and, $P_d = \rho_m g h$ is a good estimate of the pressure within the flow. However in this case, the intrusion is characterized by a flat top and its profile is very different from (5.29) (see Section 4.2.2) (*Bunger and Cruden, 2011; Michaut, 2011*) and hence, (5.29) is no longer accurate to derive the intrusion depth.

Finally, using (5.29) and equating $P_d = \rho_m g h_0$ to derive the intrusion depth T_e^0 at FFCs leads to an intrusion depth that scales with the crater diameter to the power four third, i.e. the larger the crater, the deeper the intrusion. But, there is no reason to suppose that the intrusion depth scales with the crater size.

In contrast, the model we develop provides a simple method to estimate the elastic thickness of the layer overlying the intrusion from the floor appearance. As discussed above, the floor of a crater appears convex if the flexural wavelength of the layer overlying the intrusion is such that $4\Lambda \geq C$. As Λ mainly depends on T_e^0 , and assuming the intrusion has reached the crater wall zone, this inequality provides for a lower bound on the elastic thickness of the upper layer:

$$T_e^0 \geq \left(\frac{12(1 - \nu^2)\rho_m g C^4}{4^4 E} \right)^{1/3} \quad (5.35)$$

For instance, Briggs is a class 2 FFC of 37 km in diameter, it shows a large convex floor (Figure 5.1 a). Hence (5.35) applies and we estimate that the intrusion lies beneath an elastic layer whose thickness is equal to or deeper than 1.6 km for this specific crater, using parameter values listed in Table

(5.2). This value is only a minimum value for the intrusion depth, as it does not take into account the potential presence of a brecciated layer on top or below the elastic layer.

In the case of a crater showing a flat floor with a circular moat, the intrusion should be in a gravity current regime, and, assuming it has reached the wall zone (which is likely to be the case if the shallowing is significant), then the width of the moat directly provides for an estimate of the flexural wavelength of the overlying elastic layer, and hence for the elastic thickness. Indeed, the size of the moats corresponds to the width of the intrusion edge, i.e. to 4Λ (see Figure 5.5 d, Figure 5.7 b and Section 5.4.2). For instance, for the class 3 FFC Warner, which is 35 km in diameter, the deformation shows a plate-like central flat floor, with a moat bordering the wall region of about one third of the crater radius (Figure 5.1 b). Hence, $(4\Lambda)/C \sim 1/3$ and the elastic thickness T_e^0 varies between 300 and 600 m. Again, this estimate provides a minimum value for the intrusion depth.

5.5.3 Injection rate and formation time scale

Precedent works have shown that, for craters smaller than 100 km in diameter, the shallowing associated with viscous relaxation is small or almost nonexistent (*Dombard and Gillis, 2001*). In contrast, our model of magmatic intrusion is able to reproduce the large discrepancy in crater floor shallowing observed at FFCs. Two mechanisms might control the final amount of shallowing: the injection rate and the cooling of the intrusion.

If the cooling time scale of the intrusion is large compared to its formation time scale, then the intrusion reaches the wall zone and thickens. In that case, assuming a constant injection rate, the maximum amount of shallowing corresponds to the intrusion thickness that evolves toward a dimensionless thickness of $\Xi + H_g$. However, as explained in Section 5.4.5, the injection rate should decrease as the intrusion grows, in particular during the thickening phase. Indeed, when the magma reaches the wall zone, the pressure due to magma weight and to elastic deformation of the overlying layer increases as the crater floor is uplifted and might finally compensate for the initial pressure driving the flow in the melt source. An estimate of this initial overpressure can be derived from our model in some cases. Indeed, for small values of Θ , i.e. for craters that show a flat floor like those of classes 3 and 5, the overpressure in the melt source might be estimated from the final thickness of the intrusion at the center h_0^f , i.e. $\Delta P = \rho_m g h_0^f$ as proposed by *Jozwiak et al. (2012)* (Figure 5.10 c, d). However, for large values of Θ , i.e. for craters that show a convex floor, as craters of classes 2 and 4, this assumption is inappropriate as both the pressure due to magma weight and the elastic pressure contribute to

compensate for the initial overpressure ΔP , i.e. $\Delta P > \rho_m g h_0^f$ (Figure 5.10 a and b).

For most FFCs, the deformation is contained within the crater floor (*Schultz*, 1976a) suggesting that the removal of material during the impact controlled the initial overpressure in the melt source. However, impact craters commonly show a raised rim, which is uplifted relative to the pre-impact surface and this structure could also contribute to prevent the intrusion from growing beyond the wall zone. Finally, in a few cases such as crater Haldane (*Schultz*, 1976a), the deformations extend well beyond the wall zone and suggest that the intrusion passed the wall zone, i.e. that the initial overpressure might have been larger than $\rho_c g D_c + P_r$ where P_r is the lithostatic pressure excess induced by the raised rim.

The deep floor of Class 1 FFCs suggests that these craters didn't undergo the thickening phase (Table 5.1). However, the network of fractures on their floor is coherent with the spreading of an underlying intrusion that might be an aborted sill that cooled before reaching the wall zone. In that case, the time scale for the intrusion to reach the wall zone $\tau = (\pi C^2 H)/Q_0$ is larger than the time scale for cooling of the intrusion. The time scale for cooling can be estimated from the characteristic time for conductive cooling of an intrusion of average thickness \bar{h}

$$\tau_c = \frac{\bar{h}^2}{\pi \kappa} \quad (5.36)$$

where $\kappa = 10^{-6} \text{ m}^2.\text{s}^{-1}$ is the thermal diffusivity of basalt. For large craters of class 1, the intrusion is more likely to be in a gravity current regime with an average thickness close to $\bar{h} \sim 2H$. The inequality $\tau_c \leq \tau$ ((5.15) and (5.36)) provides for an upper bound for the average injection rate:

$$Q_0 \leq 408(C^8 \kappa^4 \rho_m g)^{\frac{1}{5}} \quad (5.37)$$

For instance, for the crater Atlas, which is 87 km in diameter and is located at 46.7N, 44.4E in the southeast of Mare Frigoris, the injection rate should be smaller than $10^{-2} \text{ m}^3.\text{s}^{-1}$, using parameter values listed in Table (5.2). This value is for instance in agreement with the extrusion rate of lavas on the Moon estimated at the end of the Imbrian and during the Eratosthenian period by *Head and Wilson* (1992). However, most of the FFCs have undergone a thickening stage and hence are such that $\tau_c \geq \tau$, and this inequality provides for a lower bound for the average injection rate for these craters.

5.6 Conclusion

The model shows that the spreading of an intrusion at depth below a crater is able to reproduce the deformations observed at FFCs and thus confirms the different predictions made by *Schultz* (1976a). In particular, the increase in lithostatic pressure and in flexural wavelength of the overlying layer at the crater wall zone prevent the intrusion from spreading radially and induce a thickening of the intrusion that leads to the shallowing of the crater floor. When the time scale for conductive cooling of the intrusion is large compared to the formation time scale, the amount of shallowing is controlled by the initial overpressure in the melt source. The model predicts that the final appearance of the crater floor, including the presence/disappearance of a central peak, is mainly controlled by the upper layer flexural wavelength Λ , i.e. its structure and thickness, and the crater radius C .

For an overlying layer with no elastic strength, i.e. an intrusion emplaced within or immediately beneath a brecciated lens, the crater floor is flat at the end of the deformation. If an elastic layer lies on top of the intrusion, but is sufficiently thin such that $C \geq 4\Lambda$, the crater shows a central plate-like floor separated from the wall zone by a circular moat. This moat results from the deformation of the thin elastic overlying layer above the intrusion front and its width is equal to 4Λ . The depth of the moat is controlled by the amount of thickening of the overlying layer at the crater wall zone. Finally, if the intrusion is emplaced beneath a thick elastic layer such that $C < 4\Lambda$, the crater shows a convex floor.

Within the framework of this model, FFCs of class 1 would result from aborted sills that have cooled before reaching the wall zone. Craters showing a convex floor, such as those of classes 2 and 4, would result from the spreading of an intrusion below a relatively thick elastic layer, such that $\Lambda \geq C/4$. On the contrary, craters showing a flat floor, such as those of classes 3 and 5, would result from the spreading of an intrusion beneath a relatively thin elastic layer, such that $\Lambda << C/4$. The wide circular U-shaped moat of class 3 FFCs is well explained by the elastic deformation of the thin elastic layer overlying the intrusion while the V-shaped moat of class 4 FFCs, showing a convex floor, could be explained by the rupture of the overlying layer, which is predicted to occur at a radial coordinate intermediate between the center and the wall zone. The absence of a moat for craters of class 5 could suggest that the intrusion develops immediately beneath or within a breccia lens and that not sufficiently impact melt stands above the breccia to form an elastic layer. Finally, class 6 FFCs are filled up by lavas that have reached the surface.

In addition, the model allows to constrain the elastic thickness of the layer lying on top of the intrusion, which provides a lower bound for the intrusion

depth.

CHAPTER 6

Gravitational signature of lunar floor-fractured craters

*This chapter is a reproduction of the paper published in Earth and Planetary Science Letters (EPSL) untitled: **Gravitational signatures of lunar floor-fractured craters** ([Thorey et al., 2015](#)).*

Contents

6.1	Introduction	158
6.2	Theoretical considerations	159
6.2.1	Constitutive equations	160
6.2.2	End-member modes of deformation	163
6.2.3	Gravitational signature of FFCs: two case studies	164
6.2.4	Filtered GRAIL gravity	167
6.3	Gravitational signature of lunar craters	168
6.3.1	Normal and floor-fractured crater populations	169
6.3.2	Crater gravitational signatures	171
6.4	Magmatic intrusion characteristics	174
6.4.1	Intrusion thickness	175
6.4.2	Density contrast $\Delta\rho$ of the intrusion	177
6.5	Discussion	178
6.6	Conclusion	179

Lunar floor-fractured craters are impact craters characterized by distinctive shallow floors crossed by important networks of fractures. Different scenarios have been proposed to explain their formations but recent studies showed that the intrusion of magma at depth below the crater floor is the most plausible explanation. The intrusion of dense magma within the light upper-most part of the lunar crust should have left a positive signature in the gravity field. This study takes advantage of the unprecedented resolution of the lunar gravity field obtained from the NASA's Gravity Recovery

and Interior Laboratory (GRAIL) mission, in combination with topographic data obtained from the Lunar Orbiter Laser Altimeter (LOLA) instrument, to investigate the gravitational signatures of both normal and floor-fractured craters. Despite the large variability in their gravitational signatures, the floor-fractured and normal craters in the Highlands show significant differences: the gravitational anomalies are significantly larger at floor-fractured craters. The anomaly amplitudes for floor-fractured craters are in agreement with synthetic gravity anomalies based on the predicted intrusion shapes from a theoretical flow model. Our results are consistent with magmatic intrusions intruding a crust characterized by a 12% porosity and where the intrusion has no porosity. Similar studies have been carried out in the lunar maria and South Pole Aitken basin. Although the average gravitational signature of floor-fractured craters is larger than at normal craters in these regions, they cannot be distinguished statistically due to the small number of craters and the large variability of the anomalies. In general, a better characterization of the signal due solely to the initial impact crater is needed to isolate the magmatic intrusion signal and characterize the density contrast between the magma and crust.

6.1 Introduction

There are a class of impact craters on the Moon that are distinguished by having uplifted floors and radially/concentric floor-fractured networks. About 200 of these floor-fractured craters (FFCs) have been identified by *Schultz* (1976a) and these impact craters are interpreted to have undergone endogenous deformations after their formation. The most striking feature of these craters is their shallow floors compared to normal craters of the same size, with the uplift reaching 50% of the initial crater depth in some cases (*Schultz*, 1976a). Due to this deformation, their floors show large networks of radial, concentric and pentagonal fractures. Additionally, depending on local conditions, the uplift results in either a convex floor or a flat plate-like floor, sometimes with a wide circular moat just interior to the rim (*Schultz*, 1976a; *Jozwiak et al.*, 2012).

Intrusion of magma beneath the crater floor and viscous relaxation of the crater topography after the impact are two proposed scenarios to explain these deformations (*Schultz*, 1976a; *Hall et al.*, 1981; *Wichman and Schultz*, 1995a; *Dombard and Gillis*, 2001). The recent theoretical model for the dynamics of crater-centered intrusions of *Thorey and Michaut* (2014) and recent morphological and geological studies by *Jozwiak et al.* (2012) showed that intrusion of magma beneath the crater floor is the most plausible scenario to produce

the morphological features observed at floor-fractured craters.

Magmatic intrusions should be emplaced at their level of neutral buoyancy (*Walker*, 1989; *Taisne and Tait*, 2009; *Wichman and Schultz*, 1995a). Upon cooling and solidification, however, their densities will be larger than the surrounding crustal material and hence, leave a positive signature in the gravity field. *Schultz* (1976a) looked at the gravitational signature of some floor-fractured craters with gravity derived from radio tracking data acquired during the Apollo 15 and 16 missions (*Sjogren et al.*, 1972, 1974). Except at the floor-fractured crater Taruntius, where a strong gravity anomaly was detected, no pronounced gravity anomalies were observed at other floor-fractured crater sites. However, the gravity data from these two experiments only covered a narrow swath along the equator and the resolution of the data used in these studies were not able to detect gravity anomalies for objects smaller than about 100 km in diameter (*Schultz*, 1976a; *Sjogren et al.*, 1974), which includes about 88% of the floor-fractured crater population.

Data from the NASA Gravity Recovery and Interior Laboratory (GRAIL) NASA mission have provided a global map of the Moon's gravity field with an unprecedented resolution. These data have been used to construct a model of the gravity field to spherical harmonic degree and order 900, which corresponds to a half-wavelength resolution of ~ 6 km at the lunar surface (*Zuber et al.*, 2013; *Konopliv et al.*, 2014). These data, used in combination with the topographic data obtained from the Lunar Orbiter Laser Altimeter (LOLA) instrument allow to investigate mass anomalies located in the lunar crust. In particular, these data allow to resolve small-scale density variations in the shallow crust (*Besserer et al.*, 2014; *Wieczorek et al.*, 2013) and they have been used to detect ancient igneous intrusions (*Andrews-Hanna et al.*, 2013).

In this paper, after some theoretical considerations on the expected gravitational signal at floor-fractured craters in section 6.2, we use GRAIL gravity to detect the presence of magmatic intrusions at floor-fractured crater sites in section 6.3. Then, we develop a method to derive the density contrast between the magma and crust in section 6.4. We discuss its geological implications in section 6.5 and conclude in section 6.6.

6.2 Theoretical considerations

The Bouguer anomaly associated with a magmatic intrusion beneath a crater depends upon the intrusion characteristics, namely its density and shape. Recently, we showed that the morphology of crater-centered intrusions depends mainly upon the thickness of the overlying elastic layer and on the crater size (*Thorey and Michaut*, 2014). Guided by the results and predictions of our

model that is briefly summarized below, we here calculate and discuss the expected gravitational signal at floor-fractured crater sites.

6.2.1 Constitutive equations

In our model, the intrusion is fed at a constant rate through a cylindrical conduit located below the center of a crater floor and spreads horizontally along a thin bedding plane (Figure 6.1). The magma makes rooms for itself

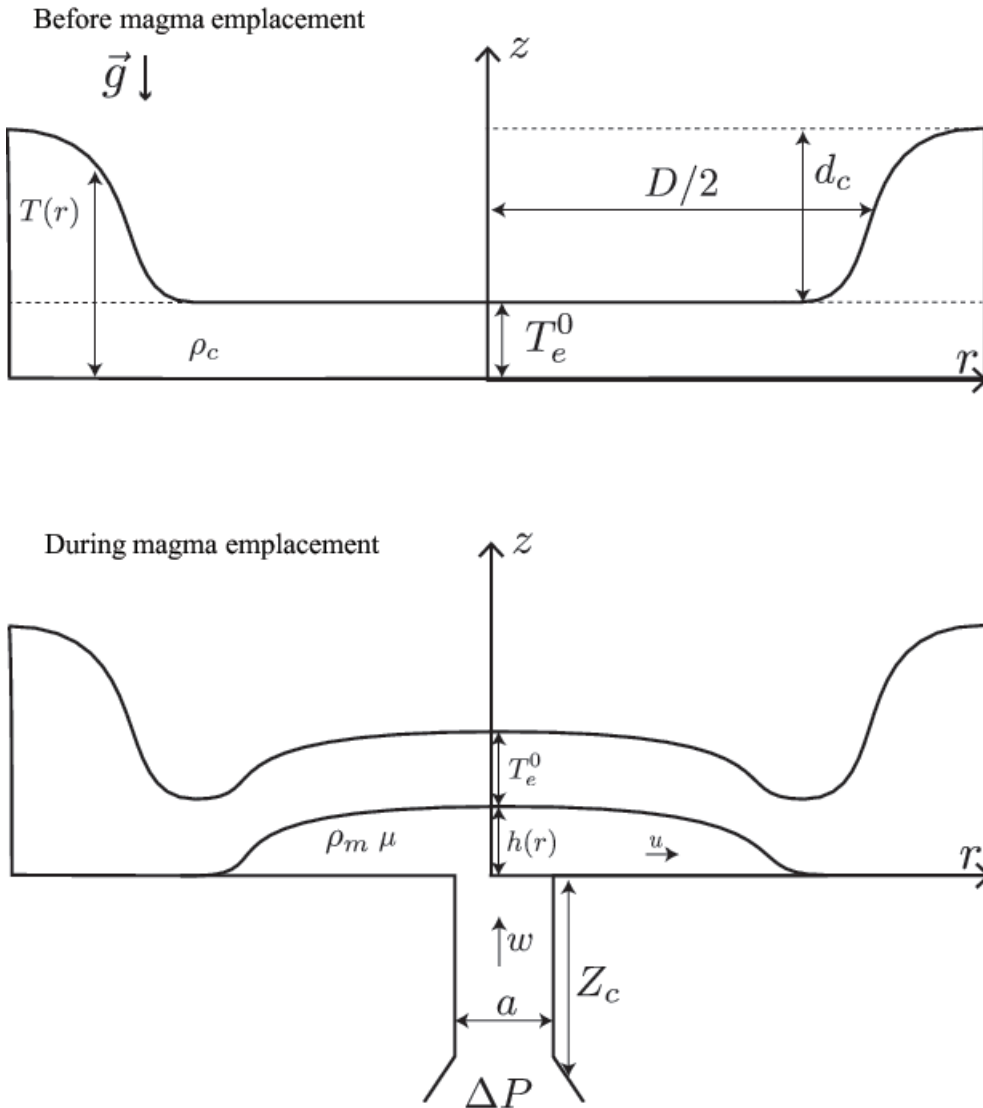


Figure 6.1: Model geometry and parameters.

by lifting the overlying assumed elastic layer, which is characterized by a

Young's modulus E , a Poisson's ratio ν and an elastic thickness $T_e(r)$ given by

$$T_e(r) = T_e^0 + d_c \xi(r), \text{ with } \xi(r) = \frac{1}{1 + e^{-\frac{2\alpha(2r-D)}{D}}} - \frac{1}{1 + e^{2\alpha}} \quad (6.1)$$

where T_e^0 is the overlying layer thickness at the crater center, d_c the crater depth with respect to the pre-impact surface and $\xi(r)$ a normalized sigmoid function which reproduces a typical complex crater depression in terms of the crater diameter D and wall slope α (Figure 6.1, top).

The thickness evolution equation in cylindrical coordinates for the flow of a newtonian fluid is given by (*Thorey and Michaut, 2014*)

$$\begin{aligned} \frac{\partial h}{\partial t} &= \frac{\rho_m g}{12\mu} \frac{1}{r} \frac{\partial}{\partial r} \left(rh^3 \frac{\partial h}{\partial r} \right) + \frac{\rho_c g \Psi T_e^0}{12\mu} \frac{1}{r} \frac{\partial}{\partial r} \left(rh^3 \frac{\partial \xi(r)}{\partial r} \right) \\ &\quad + \frac{ET_e^{0^3}}{144\mu(1-\nu^2)} \frac{1}{r} \frac{\partial}{\partial r} \left(rh^3 \frac{\partial}{\partial r} (\nabla_r^2 ((1+\Psi\xi(r))^3 \nabla_r^2 h)) \right) \\ &\quad + w(r, t) \end{aligned} \quad (6.2)$$

$$w(r, t) = \begin{cases} \frac{\Delta P}{4\mu Z_c} \left(\frac{a^2}{4} - r^2 \right) & r \leq \frac{a}{2} \\ 0 & r > \frac{a}{2} \end{cases} \quad (6.3)$$

where $h(r, t)$ is the intrusion thickness, r is the radial coordinate, t is time, ρ_m and ρ_c are the magma and crust density, μ is the viscosity, $\Psi = d_c/T_e^0$ is the thickening of the overlying layer at the wall, $w(r, t)$ is the injection velocity and $\Delta P/Z_c$ is the overpressure gradient driving magma ascent in the feeder dyke.

The terms on the right side of (6.2) respectively represent, from left to right, spreading due to magma weight, the lithostatic barrier the magma has to face at the crater wall, squeezing of the flow in response to elastic deformation of the overlying layer and injection rate. Equation (6.2) is non-dimensionalized using the crater radius $D/2$ as a horizontal scale, a height scale H and a time scale τ given by

$$H = \left(\frac{12\mu Q_0}{\rho_m g \pi} \right)^{\frac{1}{4}} \quad (6.4)$$

$$\tau = \frac{\pi D^2 H}{4Q_0} \quad (6.5)$$

where H is the characteristic height scale of a gravity current (*Huppert, 1982a*) and τ is the characteristic time to fill up the crater depression for a constant injection rate

$$Q_0 = \frac{\pi \Delta P a^4}{128\mu Z_c}. \quad (6.6)$$

Another useful lengthscale in the problem is the flexural wavelength Λ (*Michaut, 2011*)

$$\Lambda = \left(\frac{ET_e^{03}}{12(1 - \nu^2)\rho_m g} \right)^{\frac{1}{4}} \quad (6.7)$$

which represents the wavelength of deformation of the elastic layer.

Equation (6.2) made dimensionless becomes

$$\begin{aligned} \frac{\partial h}{\partial t} &= \frac{1}{r} \frac{\partial}{\partial r} \left(rh^3 \frac{\partial h}{\partial r} \right) + \Xi \frac{1}{r} \frac{\partial}{\partial r} \left(rh^3 \frac{\partial \xi(r)}{\partial r} \right) \\ &+ \Theta \frac{1}{r} \frac{\partial}{\partial r} \left(rh^3 \frac{\partial}{\partial r} \nabla_r^2 ((1 + \Psi \xi(r))^3 \nabla_r^2 h) \right) + \frac{32}{\gamma^2} \left(\frac{1}{4} - \frac{r^2}{\gamma^2} \right) \end{aligned} \quad (6.8)$$

where $\xi(r)$ is also made dimensionless

$$\xi(r) = \frac{1}{1 + e^{-\frac{(r-1)}{\zeta}}} - \frac{1}{1 + e^{\frac{1}{\zeta}}} \quad (6.9)$$

and where

$$\gamma = \frac{2a}{D} = 0.02 \quad (6.10)$$

$$\zeta = \frac{d_c}{2\alpha D} = 0.13 \quad (6.11)$$

$$\Xi = \left(\frac{\rho_c g d_c}{\rho_m g H} \right) = 20 \quad (6.12)$$

$$\Psi = \frac{d_c}{T_e^0} = 1. \quad (6.13)$$

γ is the dimensionless source width, ζ is four times the normalized crater wall width and characterizes the crater geometry, Ξ is the ratio between the lithostatic pressure increase at the crater wall and the hydrostatic pressure due to a magma column of thickness H , which quantifies the importance of the lithostatic barrier at the crater wall, and Ψ is the dimensionless thickening of the upper elastic layer, which characterizes the elastic thickness increase at the crater wall. These are dimensionless parameters that do not significantly affect our results and are considered fixed in our analysis (*Thorey and Michaut, 2014*). The dimensionless number Θ

$$\Theta = \left(\frac{2\Lambda}{D} \right)^4 \quad (6.14)$$

is the dimensionless flexural wavelength of the upper layer raised to the power 4 that quantifies the length scale over which the elastic deformation is effective relative to the crater radius. It varies between 10^{-5} and 10^{-1} and has a strong influence on the intrusion shape and final floor appearance.

6.2.2 End-member modes of deformation

For a constant injection rate and no crater depression, i.e a constant upper elastic layer ($\xi(r) = 0$ and $T_e(r) = T_e^0$), the numerical resolution of the equations shows two spreading regimes (*Michaut, 2011; Michaut et al., 2013*). The flow is first driven by the bending of the upper elastic layer. The intrusion is bell-shaped and both the radius and the thickness evolve close to $t^{1/3}$. When the radius becomes larger than 4Λ , the weight of the intrusion becomes dominant over the bending terms and the intrusion enters a gravity current regime. In this second regime, the intrusion shows a flat top with bent edges, the radius evolves as $t^{1/2}$ and the thickness tends to a constant (*Huppert, 1982a; Michaut, 2011*).

For a constant injection rate and a crater-like topography for the upper layer, i.e. $T_e(r)$ given by (6.1), the spreading regimes are perturbed by the presence of the crater wall. The central flat floor of the crater first acts as a constant elastic upper layer and the intrusion spreads as described above. However, when it reaches the crater wall, the important increase in lithostatic pressure prevents the magma from spreading horizontally. The intrusion thickens in response and the crater floor is uplifted (*Thorey and Michaut, 2014*). Accordingly, the intrusion thickness can be estimated from the amount of uplift of the crater floor at the center.

The final morphology of the crater floor depends mainly on the ratio between the flexural wavelength and the crater radius, i.e. on the dimensionless number Θ (6.14). For a large value of Θ , i.e. a deep intrusion and/or a small crater, the intrusion reaches the wall in the bending regime. The intrusion is bell-shaped and the uplift of the crater floor leads to a shallowed convex floor (Figure 6.2, left). In contrast, for a small value of Θ , i.e. a shallow intrusion and/or a large crater, the intrusion is in a gravity current regime when it reaches the crater wall. The thickening of the cylinder-like intrusion leads to a piston-like uplift of the crater floor and to a shallowed central flat floor for the crater (Figure 6.2, right).

Accordingly, this model results into two main types of floor-fractured craters: craters with convex floors corresponding to bell-shaped intrusions (Figure 6.2, left) and craters with plate-like floors corresponding to cylinder-shaped intrusions (Figure 6.2, right). In the following, we consider craters of classes 2 and 4 of *Schultz (1976a)* to represent manifestations of bell-shaped intrusions, and craters of classes 1, 3, 5 and 6 to be manifestations of cylinder-shaped intrusions.

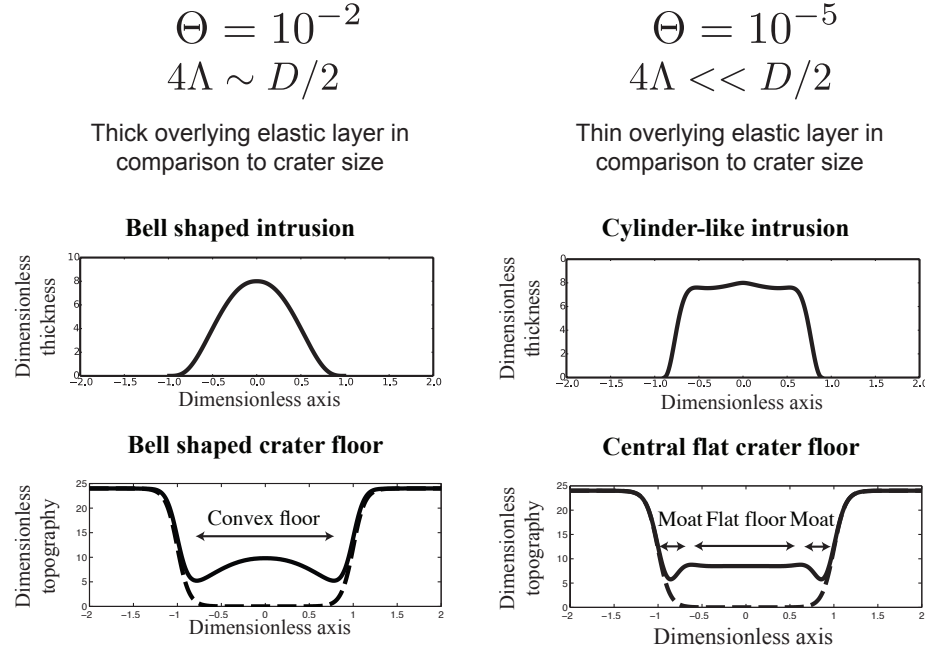


Figure 6.2: Two end-member intrusion shapes producing the two end-member floor deformations observed at FFC sites: convex floor (left) and plate-like floor (right).

6.2.3 Gravitational signature of FFCs: two case studies

The Bouguer gravity is the gravity anomaly that remains after taking into account the gravitational signature of surface topography. Thus, if there are no lateral variations in crustal density, the Bouguer anomaly of a floor-fractured crater should be entirely the result of the magmatic intrusion. The Bouguer anomaly associated with a magmatic intrusion depends upon the intrusion morphology, the intrusion depth and the density contrast $\Delta\rho$ between the intrusion and the surrounding crust.

We investigate the signal expected at floor-fractured craters as a function of the intrusion shape, diameter and depth. In particular, for the bell and cylinder shaped intrusion, we study the signal for an intrusion diameter that varies between 20 and 180 km, i.e. the minimum and maximum diameter of floor-fractured craters observed by [Schultz \(1976a\)](#) and two intrusion depths, i.e. $T_e^0 = 0$ km and a reasonable upper bound of 5 km ([Thorey and Michaut, 2014](#)). We set the intrusion thickness H_0 to a value of 2 km, which is the maximum uplift observed by [Schultz \(1976a\)](#) and the density contrast between the magma and the crust to a value of $\Delta\rho = 600 \text{ kg m}^{-3}$, the maximum density contrast between mafic and crustal lunar rocks using the bulk densities of

Kiefer et al. (2012).

The two end-member intrusion profiles are obtained by solving equation (6.8) for two different values of the dimensionless number Θ (6.14), $\Theta = 10^{-2}$ for the bell-shaped intrusion and $\Theta = 10^{-5}$ for the cylinder-like intrusion (*Thorey and Michaut, 2014*). We stop the simulations when the uplift at the center h_0 is significant and such that the pressure due to the intrusion weight at the center is about half the lithostatic pressure due to the crater wall ($h_0 = 10$). Finally, each profile is redimensionalized: the axial coordinate of the dimensionless thickness profile is multiplied by $D/2$ and the dimensionless thickness profile is multiplied by H_0/h_0 , where h_0 is the dimensionless thickness of the intrusion at the end of the simulation.

We calculate the synthetic radial gravity anomaly (more precisely, the gravity disturbance) δ_g^s corresponding to each intrusion profile using the spherical harmonics expansion

$$\delta_g^s(r, \theta, \phi) = \frac{GM}{r^2} \sum_{l=0}^{L_{\max}} \sum_{m=-l}^l \left(\frac{R_i}{r} \right)^l (l+1) C_{lm} Y_{lm}(\theta, \phi) \quad (6.15)$$

where r, θ and ϕ are the coordinates of observation, G is the gravitational constant, M the mass of the Moon, R_i the reference radius of the spherical harmonic coefficients taken as the mean radius at the site of intrusion, i.e. $R_i = R_0 - T_e^0 + \bar{h}$ where R_0 is the mean lunar radius and \bar{h} the mean intrusion thickness, C_{lm} , and Y_{lm} the spherical harmonic functions of degree l and order m (*Wieczorek and Phillips, 1998*). Gravitational accelerations are considered positive when directed downward (see Appendix E for the expression of the spherical harmonic coefficients associated with the intrusion thickness profile and the calculation details).

The two different intrusion shapes result in two different types of anomaly (Figure 6.3, left). For a bell-shaped intrusion, with a convex crater floor, the gravity anomaly is also bell-shaped. It decreases gradually from the center to the crater wall (Figure 6.3, top left). For an intrusion placed at the surface, $T_e^0 = 0$, the signal barely depends on the crater diameter. The mean gravity anomaly measured interior to the crater wall is almost constant and about 15 mGal (Figure 6.3, top right). Although an increased intrusion depth decreases the mean value of the anomaly by a factor that is less than two for craters smaller than 50 km, it barely affects the anomaly for craters larger than 50 km (Figure 6.3; top right).

For a cylinder-like intrusion and a plate-like crater floor, the gravity anomaly is relatively uniform and sharply decreases at the crater wall (Figure 6.3, bottom left). Consequently, although the maximum amplitude of the anomaly is similar to the one produced by a bell-shaped intrusion, the

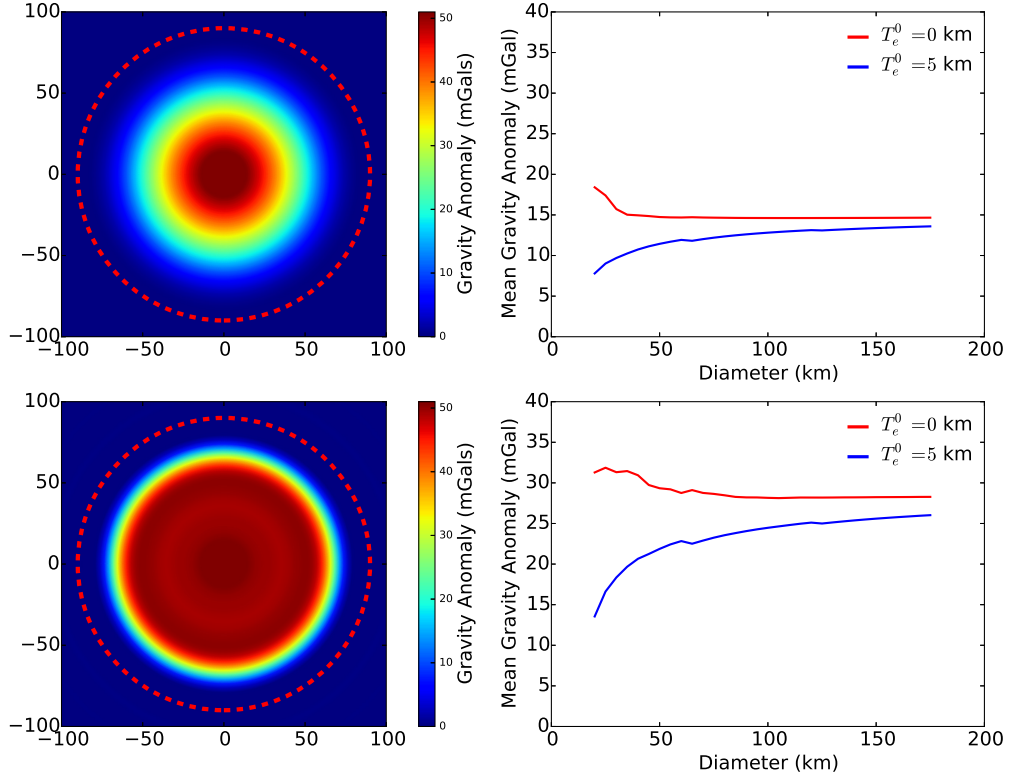


Figure 6.3: Top left: Calculated synthetic gravity anomaly for a bell-shaped intrusion at the surface for $T_e^0 = 0 \text{ km}$, $H_0 = 2 \text{ km}$, $D = 180 \text{ km}$ and $\Delta\rho = 600 \text{ kg m}^{-3}$. Dotted red line represents the crater rim. Top right: Mean synthetic gravity anomaly as a function of the crater diameter D for a bell-shaped intrusion with $H_0 = 2 \text{ km}$ and $\Delta\rho = 600 \text{ kg m}^{-3}$. Red solid line: the intrusion is at the surface, $T_e^0 = 0 \text{ km}$. Blue solid line: the intrusion is 5 km below the surface, $T_e^0 = 5 \text{ km}$. Bottom: Same as above, but for a cylinder-shaped intrusion.

mean gravity anomaly, measured interior to the crater wall, is twice larger and about 30 mGal. Similar to bell-shaped intrusion, an increased intrusion depth decreases the mean value of the anomaly by a factor that is less than two for craters smaller than 50 km but barely affects the anomaly for craters larger than 50 km (Figure 6.3, bottom right).

One important observation of our modeling is that even for an extreme case of a 2 km thick and a 180 km diameter intrusion placed at the surface with a large density contrast of 600 kg m^{-3} , the expected signal is only of a few tens of mGal. Though GRAIL can easily detect such small amplitude anomalies, this gravity signals could be masked by both large-scale regional signals and short-

wavelength signals that are unrelated to our idealized model of Figure 6.1. Therefore, we need to filter out these other contributions to be able to detect the potential presence of magmatic intrusions at floor-fractured craters. In the following, we present the gravity model that we use and consider the remaining expected signal after filtering the synthetics the same way the observed gravity are filtered.

6.2.4 Filtered GRAIL gravity

The observed gravity field on the Moon is a result of several contributions, including surface topography, relief along the crust-mantle interface and density heterogeneities in both the mantle and the crust. In order to detect the presence of magmatic intrusions in the shallow crust, which have predicted anomalies of only a few tens of mGal, we first remove all known signatures from the observed gravity field in order to highlight those signals that remain.

To construct this model, we start with JGGRAIL 900C11A gravity field, which is developed to spherical harmonic degree 900 and which is based on all data obtained during the GRAIL primary and extended mission (*Konopliv et al.*, 2014). From the free-air gravity model, we first compute the Bouguer anomaly by removing the gravitational contribution of surface topography and the long-wavelength variations in crustal density that are predicted from remote sensing data, as described in *Wieczorek et al.* (2013). The most prominent signals that remain are either associated with large impact basins or are anticorrelated with long-wavelength topography. We interpret the majority of this signal as being the result of crustal thickness variations, and use the Bouguer anomaly to invert for the gravitational signal of relief along the crust-mantle interface, as described in *Wieczorek et al.* (2013).

Since the shortest wavelength signals in the Bouguer anomaly are unlikely to be the result of crustal thickness variations, and since short-wavelength signals become highly amplified when extrapolated with depth below the surface, we apply the low-pass filter of *Wieczorek and Phillips* (1998) to the Bouguer anomaly before inverting for crustal thickness variations. This filter is parameterized by having a value of 0.5 at spherical harmonic degree λ . The choice of λ is subjective, and λ is chosen such that the obtained crustal thickness map does not contain excessive power at the shortest wavelengths. In *Wieczorek et al.* (2013), λ was chosen to have a value of 80. Here, we test several values for λ and find that $\lambda = 80$ is also a good trade-off between the removal of regional trends and the removal of signals due to the magmatic intrusion itself (see Appendix E Figure 1 for details on the effects of λ).

After removing the gravitational signal of the crustal-mantle interface from the Bouguer anomaly, the remainder of the signal is attributed to lateral vari-

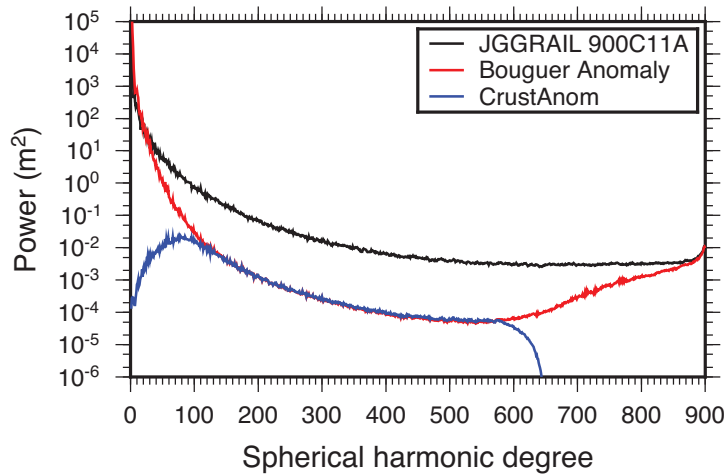


Figure 6.4: Power spectra for various gravity models. Black solid line: free-air gravity from the GRAIL gravity model JGGRAIL 900C11A. Red solid line: Bouguer gravity anomaly assuming a constant crustal density of 2550 kg m^{-3} . Blue solid line: Crustal gravity anomaly of our model CrustAnom with $\lambda = 80$ and which removes long-wavelength variations in crustal density as predicted by remote sensing data.

ations in density within the crust of the Moon. To remove short wavelength noise in the gravitational field, we also apply a cosine filter to the spherical harmonic coefficients between degree 550 and 650. It is from this map, here referred to as CrustAnom, that we search for gravitational anomalies associated with floor-fractured craters. Our model CrustAnom is roughly equivalent to a band-passed Bouguer anomaly, where both the shortest and longest wavelength signals are removed (Figure 6.4).

Upon applying the same filtering to synthetic gravity anomalies, the expected signal at floor-fractured craters is reduced with respect to those considered in section (6.2.3) (Figure 6.5). The filtering, which affects mostly large craters, leads to a drop in the amplitude of the gravity anomaly by a factor larger than two for craters larger than about 80 km. As an example, the mean anomaly for the extreme case of a 2 km thick and 180 km large intrusion should only be of a few mGal in the model CrustAnom (Figure 6.5).

6.3 Gravitational signature of lunar craters

The gravitational signal associated with magmatic intrusions at floor-fractured craters will be superimposed on the signal of a normal impact crater.

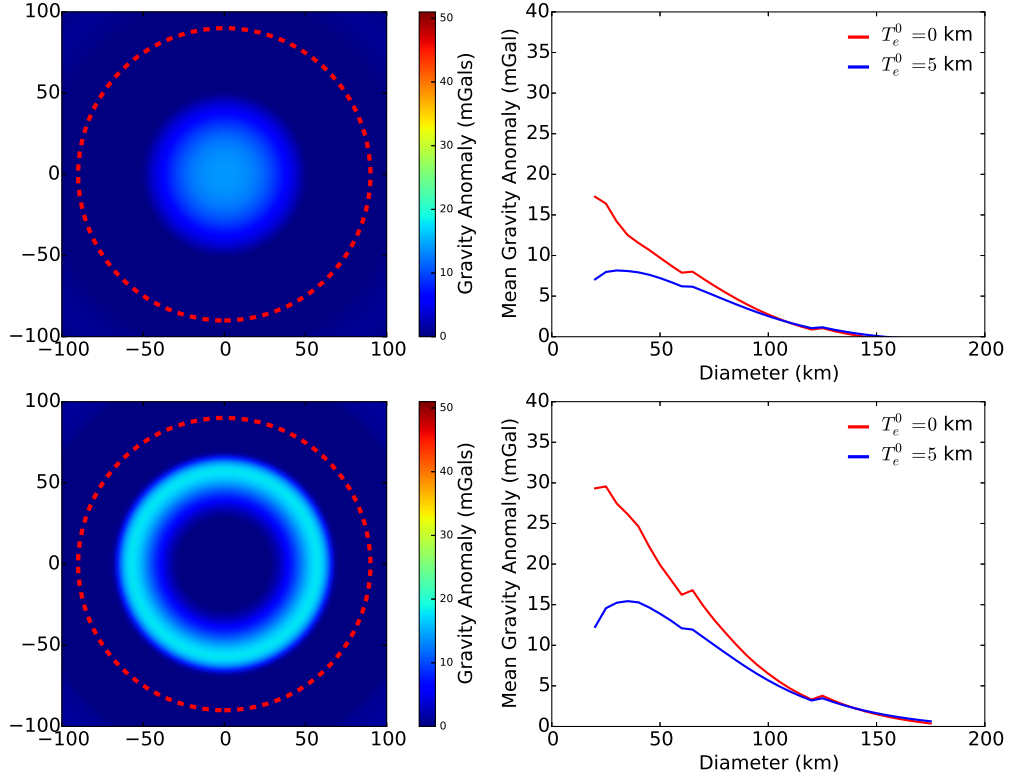


Figure 6.5: Top left: Calculated synthetic gravity anomaly filtered the same way as the model CrustAnom for a bell-shaped intrusion at the surface with $T_e^0 = 0 \text{ km}$, $H_0 = 2 \text{ km}$, $D = 180 \text{ km}$ and $\Delta\rho = 600 \text{ kg m}^{-3}$. Dotted red line represents the crater rim. Top right: Mean filtered synthetic gravity anomaly as a function of the crater diameter D for a bell-shaped intrusion with $H_0 = 2 \text{ km}$ and $\Delta\rho = 600 \text{ kg m}^{-3}$. Red solid line: $T_e^0 = 0 \text{ km}$. Blue solid line: $T_e^0 = 5 \text{ km}$. Bottom: Same as above, but for a cylinder-shaped intrusion.

We use the model CrustAnom to first quantify the gravity signal at normal impact craters and then compare to the signal at found floor-fractured craters.

6.3.1 Normal and floor-fractured crater populations

We use the dataset of [Head et al. \(2010\)](#) as a reference catalog for normal craters and the dataset of [Jozwiak et al. \(2012\)](#) as a reference catalog for floor-fractured craters. We consider only complex craters and thus use a minimum crater diameter of 20 km, which is the transitional crater diameter between simple and complex lunar craters ([Pike, 1974, 1980](#)). We use a maximum crater diameter of 180 km, because for larger craters, the mantle uplift

associated with basin formation becomes apparent in the gravity data (*Melosh et al.*, 2013). These criteria result in a population of 116 floor-fractured and 5101 normal craters covering the whole lunar surface.

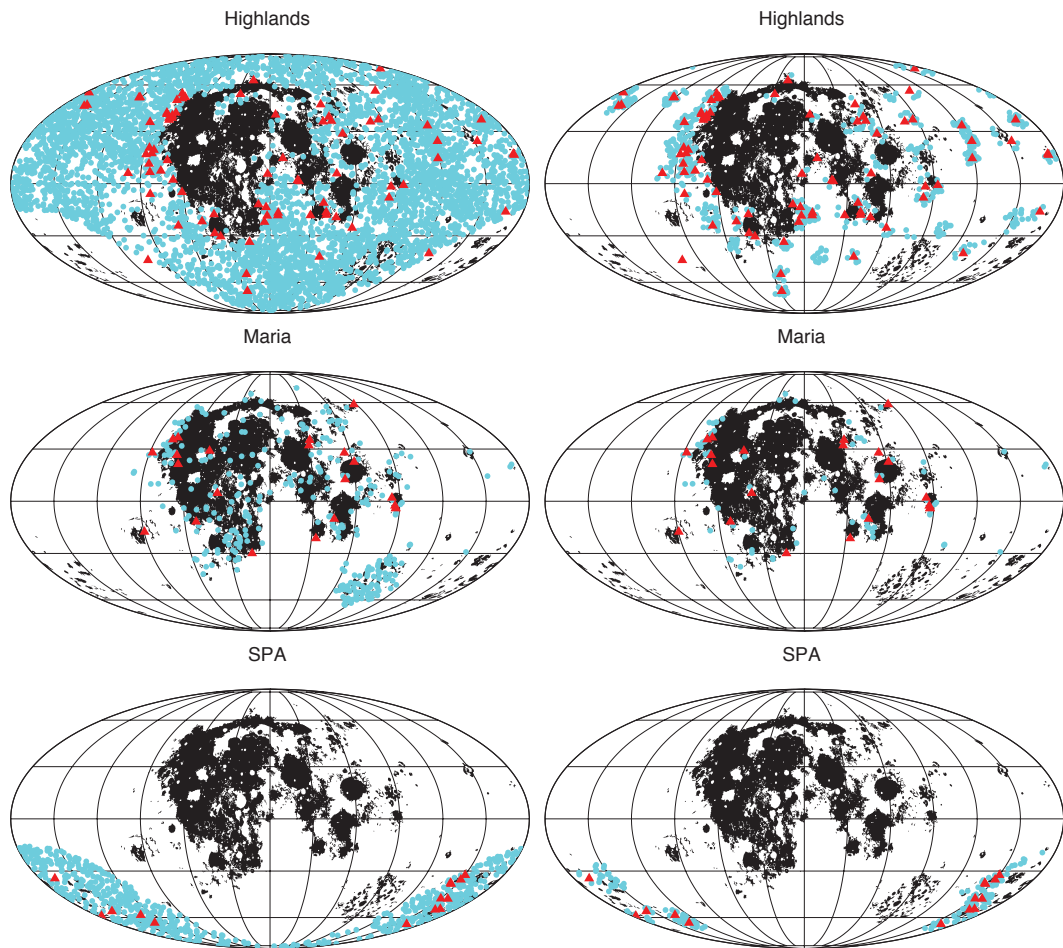


Figure 6.6: **Top row)** Left: All FFCs (red triangles) and normal craters (light blue circles) in the highlands. Right: All FFCs (red triangles) and normal craters that have the same spatial distribution as the FFCs (light blue circles). **Middle row)** Same plots but for craters in the maria. **Bottom row)** Same plots but for craters in South Pole Aitken basin (SPA).

The observed gravity field of an impact crater will depend upon the density of the crust. GRAIL gravity data show that crustal density is not constant, and that regional variations of $\pm 250 \text{ kg m}^{-3}$ exist, primarily between the highlands and the South Pole Aitken basin (SPA). In addition, surface densities in the maria are considerably higher than in the highlands (*Besserer*

(*et al.*, 2014). To minimize potential biases that might arise from regional variations in crustal density or geologic evolution, we divide each crater population (normal and floor-fractured craters) into three sub-populations. The first is constituted by craters that lie within the highlands, outside of both the maria and South Pole-Aitken basin. We use the USGS geological maps to define the mare borders and the SPA basin is defined using the best-fit outer ellipse of *Garrick-Bethell and Zuber* (2009). In the highlands, there are 80 floor-fractured and 4054 normal craters (Figure 6.6, top left). The second sub-population is constituted by craters that lie within the maria and outside of SPA basin of which there are 22 floor-fractured and 306 normal craters (Figure 6.6, middle left). The last sub-population is constituted by craters within the SPA of which there are 14 floor-fractured and 603 normal craters (Figure 6.6, bottom left).

In each region defined above, the spatial distribution of floor-fractured and normal craters is different (Figure 6.6, left). To minimize any biases that might result from different regional characteristics, we also consider, for each region, a second sub-population of normal craters that shares the same spatial distribution as the floor-fractured craters (Figure 6.6, right). In this sub-population, we consider all normal craters that are less than 150 km away from a floor fractured crater.

6.3.2 Crater gravitational signatures

In analyzing the gravitational signature of lunar impact craters, we make use of a single number, the crater gravity anomaly, that is defined as the average gravitational anomaly with respect to the regional value. In calculating this number, we first calculate the average gravitational anomaly from our model CrustAnom within the main crater rim, i.e. within a circular region defined by its radius $D/2$ where D is the crater diameter reported by *Head et al.* (2010) and *Jozwiak et al.* (2012). We then subtract from this value the average value of the gravity field in an annulus extending from the crater rim to a radius of one crater diameter D (Appendix E, Figure 2). Both gravitational anomalies are calculated at the average elevation of the crater.

6.3.2.1 Highlands

The magnitude of the gravity anomalies at normal crater sites shows an important variability (Figure 6.7). On average, the anomaly is positive at the smallest craters, slowly decreases with increasing diameters, and approaches a constant negative value near a diameter of about 100 km. For crater diameters between 100 and 180 km, the mean magnitude of the gravity anomalies

is independent of the diameter and close to -5 mGal. The mean of the gravity anomalies for the whole population μ_{δ_g} is negative and equal to -0.71 mGal. This number is well constrained due to the large number of craters. In particular, the uncertainty in the mean (the standard error, which is the standard deviation divided by the square root of the number of observations) is equal to 0.12 mGal. The population that shares the spatial distribution of floor-fractured craters shows similar trends (Figure 6.7). A Kolmogorov-Smirnov (KS) test was conducted to compare this population to the whole population of normal craters. The test reports a value of p , which is the probability that the two populations are drawn from the same distribution, larger than 10% , which confirms that no significant differences exist between the two populations (Appendix E, Table 1).

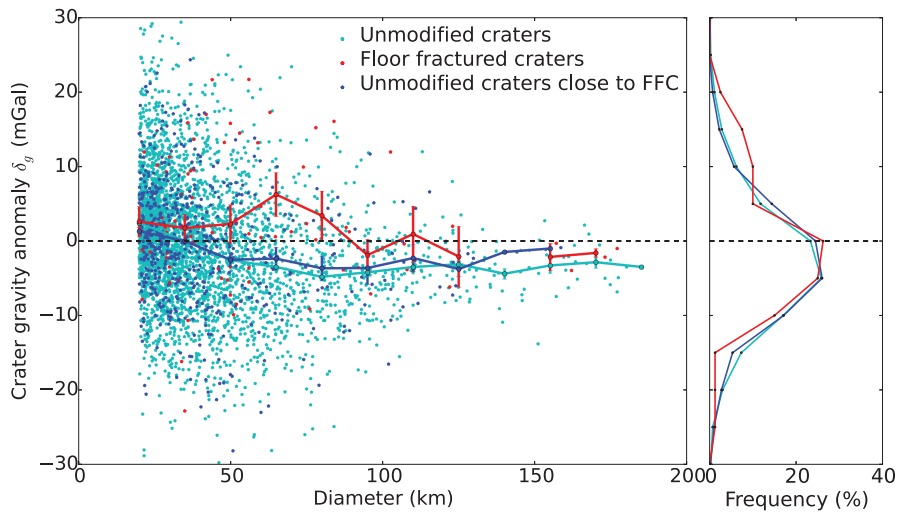


Figure 6.7: Magnitude of the gravity anomaly δ_g versus diameter D for the normal crater population (blue dots), the normal crater population that shares the FFC spatial distribution (light blue dots) and the floor-fractured crater population (red triangles) in the highlands. Solid line: Mean of the gravity anomalies binned in 15 km diameter intervals. Error bars correspond to the standard error for each bin. Right plot: Corresponding gravity anomaly density distribution for each population in frequency (%).

The magnitude of the gravity anomalies at floor-fractured craters shows a different dependence with diameter than at normal craters (Figure 6.7). Although the variance of the data with respect to the average is of the same order, the gravity anomalies at floor-fractured craters are larger. In particular, the mean of the floor-fractured crater gravity anomalies is positive and approximately 2.7 mGal larger than the mean of the normal crater gravity anomalies.

We made use of a t-test to determine the robustness of the difference between the mean magnitude of the gravity anomalies of the two populations. This test quantifies the significance of a difference between the means of two populations assuming the two populations have the same variance. We found that there was only less than a 5% chance that the difference in the mean of the two populations could have occurred by chance (Appendix E, Table 1). The same result holds for the comparison with the normal crater population that shares the spatial distribution of floor-fractured craters (Appendix E, Table 1).

6.3.2.2 Lunar maria and SPA

The magnitude of the gravity anomalies at the sites of complex craters in the lunar maria shows a variability that is similar to craters in the highlands (Figure 6.8, top). The gravity anomaly remains close to 0 mGal and is independent of the crater diameter (Figure 6.8, top). The mean of the whole population μ_{δ_g} is positive and equal to 1.51 ± 0.68 mGal. A KS test shows that there is no significant difference between the entire normal crater population and the one that shares the spatial distribution of floor-fractured craters (Figure 6.8, top, Appendix E, Table 1).

The normal craters in the South Pole Aitken basin show gravity anomalies that are somewhat more negative than in the highlands (Figure 6.8, bottom). On average, the signal decreases with increasing diameter up to $D \sim 100 - 120$ km (Figure 6.8, bottom) and increases somewhat again for crater diameters between 120 and 180 km (Figure 6.8, bottom). A KS test shows that there is no significant difference between the two populations of normal craters (Figure 6.8, bottom, Appendix E, Table 1).

Although the mean magnitude of the gravity anomalies at FFC sites is about 3 mGal larger than the mean value observed at normal craters in the maria and SPA, the variability in the signal is large and there is no significant statistical difference between the mean of the gravity anomalies of normal and floor-fractured craters in those two different regions. Indeed, a t-test, realized for both regions, shows that there was more than a 10% chance that these differences in the mean of the two populations could have occurred by chance (Appendix E, Table 1). Nevertheless, the small number of FFCs in the maria and in the SPA makes difficult to obtain a significant statistic due to the low accuracy in measuring the FFC population mean ($\mu_{\delta_g} = 4.43 \pm 3.52$ mGal in the maria and $\mu_{\delta_g} = -0.25 \pm 2.52$ mGal in SPA).

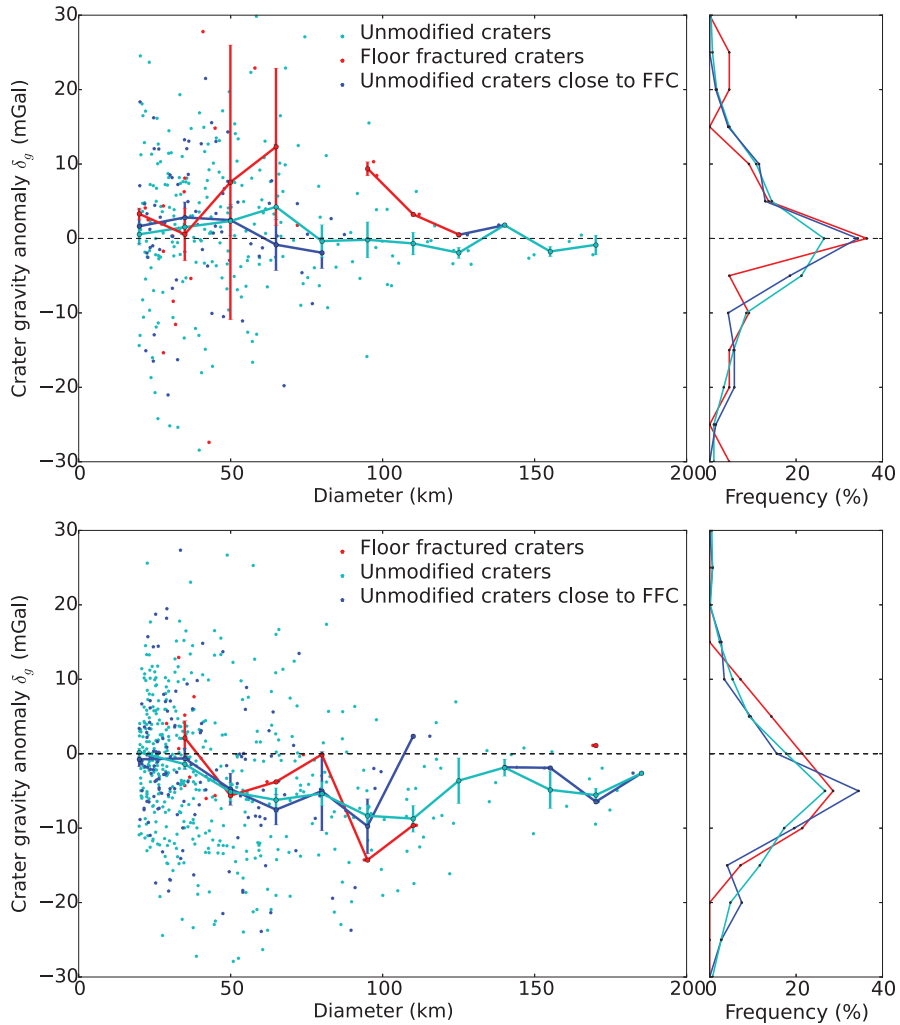


Figure 6.8: **Top:** Magnitude of the gravity anomaly δ_g versus diameter D for the normal crater population (blue dots), the normal crater population that shares the FFC spatial distribution (light blue dots) and the floor-fractured crater population (red triangles) in the maria. Solid line: Mean of the gravity anomalies binned in 15 km diameter intervals. Error bars correspond to the standard error for each bin. Right plot: Corresponding gravity anomaly density distribution for each population in frequency (%). **Bottom:** Same plots but in South Pole-Aitken basin.

6.4 Magmatic intrusion characteristics

Our results show that, on average, crustal gravity anomalies at floor-fractured craters are larger than at normal craters, but also that this result is statistically significant only for the highlands. This is in agreement with the pres-

ence of dense magmatic intrusions at depth below floor-fractured crater floors. In addition, the amplitudes of the gravitational signatures at floor-fractured craters are only of a few mGal, comparable to the predictions based on the theoretical model of *Thorey and Michaut* (2014) (Figure 6.5). In the following, we compare the observed gravity signals at each floor-fractured crater to a synthetic gravity anomaly constructed based on the theoretical model of *Thorey and Michaut* (2014) in order to derive the mean density contrast between the intrusion and the surrounding crust. To that purpose, the thickness of each intrusion is needed and we use LOLA topographic data to estimate this quantity for each floor-fractured crater.

6.4.1 Intrusion thickness

The intrusion thickness H_0 at the center of the crater is taken as the amount of shallowing of the crater floor with respect to the expected depth (*Schultz*, 1976a; *Jozwiak et al.*, 2012). Given the observed crater depth, the problem is to estimate the original crater depth before the intrusion formed. In the study of *Jozwiak et al.* (2012), the scaling law which gives the depth d_c as a function of the crater diameter D , derived by *Pike* (1974), was used as an estimate for the initial crater depth. However, this scaling law was calculated using only recent, Erastosthenian, and well preserved craters, and it is generally acknowledged that floor-fractured craters are generally older and more degraded than this population. In the absence of information on the state of degradation of lunar craters in the dataset of *Head et al.* (2010), we thus use the characteristics of the normal craters that share the spatial distribution of floor-fractured craters described in section 6.3.1 as a reference.

We characterize the depths of both normal and floor-fractured craters using the 64 ppm (~ 450 m/pixel) LOLA gridded topography data (*Zuber et al.*, 2009) obtained from the planetary data system geosciences node. We followed the method described by *Kalynn et al.* (2013) to derive the crater depth d_c and its uncertainty σ_d (see Appendix E for details). Our d_c - D results for normal craters show trends that are consistent with previous works in the highlands, the lunar maria and the SPA (Figure 6.9). Indeed, the crater depth of normal craters increases with increasing diameter and craters in the maria are on average shallower than in the highlands or SPA (Figure 6.9) (*Pike*, 1974, 1980; *Kalynn et al.*, 2013). Nevertheless, the variability in the degradation state of each crater results in an important variance in the crater depth with diameter with respect to the mean trend.

The same variability holds for the floor-fractured crater population depth (Figure 6.9). This variability makes the identification of the uplift difficult at floor-fractured craters. Although the mean crater depth of floor-fractured

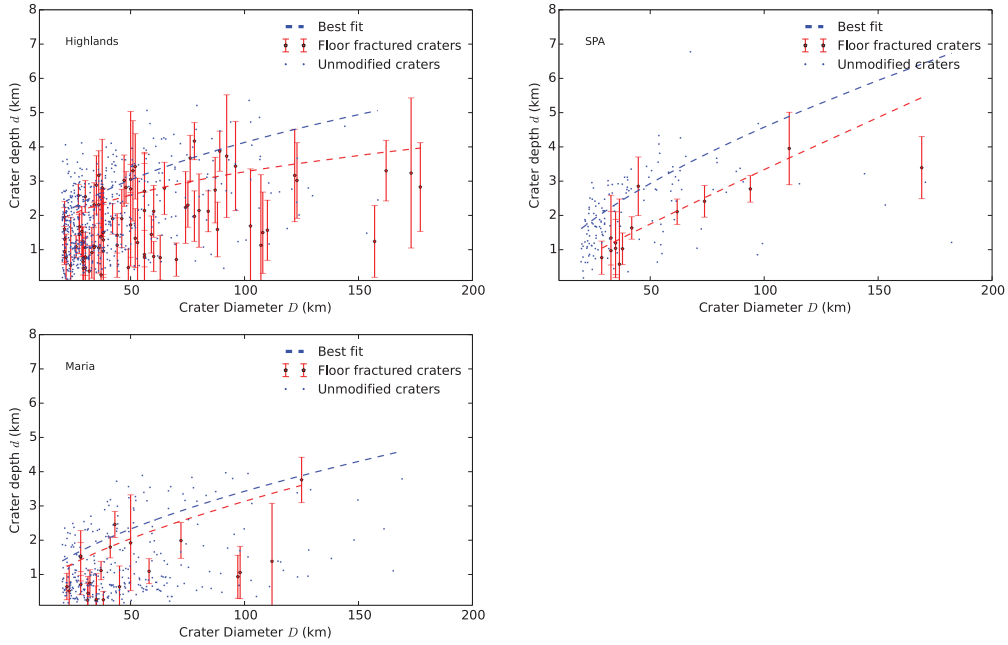


Figure 6.9: Crater depth d_c (km) versus diameter D (km) for floor-fractured craters (red) and normal craters (blue) in the highlands, SPA and the maria. The normal craters in the highlands reference to the populations close to floor-fractured craters. Error bars are the uncertainties in the measurement of the crater depth and for clarity, the uncertainties are not shown for normal craters. Dashed lines: best fit using the equation $d_c = AD^B$ for the floor-fractured crater (red) and the normal crater (blue) populations in log-log space. Values of the coefficient A, B as well as the dispersion around the best fit line σ_{fit} are given in Appendix E, Table 2.

craters in the highlands and SPA is slightly smaller than the mean of the normal crater population, the means of the two populations are not significantly different in the three regions (t-test: $p > 0.5$, Appendix E, Table 2). A detailed geological study at each crater would be necessary to precisely identify the crater morphological structures and decrease the uncertainty in the depth estimation, but such a study is out of the scope of this article. We decided to estimate the intrusion thickness at floor-fractured craters only to a first order by considering the difference in the mean trends between normal and floor-fractured craters.

To characterize the mean trend of normal craters, we make use of a linear least-squares regression in log-log space to obtain a power law relationship of the form $d_c = AD^B$ (Pike, 1974; Kalynn et al., 2013). We use the same method to characterize the mean dependence of floor-fractured crater depth

with crater diameter. In addition of determining the constant A and B , we also calculated the root-mean-squared dispersion σ_{fit} around the best fit (Appendix E, Table 2). Subtracting the two best fit lines, we finally obtain a first-order estimate for the intrusion thickness at the center H_0 for each floor-fractured crater of given diameter D to which we assign an error $\sigma_{H_0} = (\sigma_{\text{fit-FFC}}^2 + \sigma_{\text{fit-Unmod.Crater}}^2)^{1/2}$.

6.4.2 Density contrast $\Delta\rho$ of the intrusion

We consider two different shapes for the intrusions beneath floor-fractured craters: a bell-shaped intrusion for craters that show a convex floor (class 2 and 4 in the classification of *Schultz* (1976a)) and a cylindrical-shaped intrusion for craters that show a plate-like floor (class 1, 3, 5 and 6 in the classification of *Schultz* (1976a)). The two dimensionless profiles are described in section 6.2.2 and each profile is redimensionalized using the thickness of the intrusion H_0 and its radius $D/2$ (see section 6.4.1). The method used to derive the synthetic gravity anomaly from the intrusion thickness profile is detailed in section 6.2.3. We use a unit density contrast, i.e. $\Delta\rho = 1 \text{ kg m}^{-3}$ and then filter the predicted gravity anomaly in exactly the same way than the observed gravity is filtered (section 6.2.4). The synthetic gravity anomaly δ_g^s associated with each floor-fractured crater is defined as the mean of the synthetic gravity anomaly measured interior to the crater rim.

Finally, the density contrast between the magma and the crust at a specific floor-fractured crater location is given by the difference of the observed gravity anomaly δ_g^{obs} and the value of the gravity anomaly for normal craters δ_g^c of the same diameter, divided by the synthetic gravity anomaly for a unit density contrast δ_g^s

$$\Delta\rho = \frac{\delta_g^{obs} - \delta_g^c}{\delta_g^s} \quad (6.16)$$

where $\Delta\rho$ is in kg m^{-3} .

We find that the corrected gravity anomalies observed at floor-fractured crater sites in the highlands are consistent with a mean density contrast between the magma and the crust of $\mu_{\Delta\rho} = 913 \pm 269 \text{ kg m}^{-3}$ (Appendix E, Table 4). In the maria, the corrected gravity anomalies observed in the 22 floor-fractured craters are consistent with a mean density contrast equal to $\mu_{\Delta\rho} = 484 \pm 669 \text{ kg m}^{-3}$ (Appendix E, Table 4). However, the difference between the mean density contrast in the highlands and the maria is not significant (a t-test gives a probability greater than 10% that this could occur by chance, $p > 0.1$). In the South Pole Aikten basin, the corrected gravity anomalies observed in the 14 floor-fractured craters are consistent with a

mean density contrast equal to $\mu_{\Delta\rho} = 974 \pm 846 \text{ kg m}^{-3}$ (Appendix E, Table 4). But, the difference between the mean density contrast in the highlands and SPA is also not significant (a t test gives a probability greater than 50% that this could occur by chance, $p > 0.5$).

6.5 Discussion

In this study, we used the gravity field obtained by the GRAIL mission, in combination with the topographic data obtained by the LOLA instrument, to resolve mass anomalies below floor-fractured craters. We studied separately the craters in the farside highlands, South Pole-Aitken basin and maria to prevent potential bias from regional effects.

We show that the average gravitational signature of normal craters in the highlands is negative, whereas the average gravitational signature of floor-fractured craters is positive. Although a large variability characterizes the magnitude of gravity anomalies in both populations, the difference between the mean of the two populations, equal to $\sim 3 \text{ mGal}$, is statistically significant. In addition, the floor-fractured crater gravity anomalies do not follow the same dependence with diameter as normal craters. Our results are consistent with the emplacement of magmatic intrusions below floor-fractured craters as originally proposed by *Schultz* (1976a). Furthermore, the observed gravity anomalies (after filtering) of a few mGal are in agreement with the values expected from the model of crater-centered intrusion of *Thorey and Michaut* (2014). In particular, measured gravity anomalies at floor-fractured craters imply an average density contrast between the magma and the surrounding crust equal to $\mu_{\Delta\rho} = 913 \pm 269 \text{ kg m}^{-3}$. Thermal annealing could also participate to the measured gravity anomaly, which would then decrease the estimated density contrast, though this effect should be limited to a few percents (*Michaut and Jaupart*, 2011; *Kiefer*, 2013).

The grain density of lunar basalt can vary from 3270 kg m^{-3} for low Ti basalt to 3450 kg m^{-3} for high Ti basalt (*Kiefer et al.*, 2012). In contrast, the lunar crust, which is mainly anorthositic, shows grain densities that vary from 2800 kg m^{-3} to 2900 kg m^{-3} . The grain density contrast between the magma and the crust should thus be between 370 and 650 kg m^{-3} , with an average of 510 kg m^{-3} . Impacts have induced fractures and created pore space in the lunar rocks decreasing their bulk densities. GRAIL data are consistent with an average porosity of about 12% in the crust (*Wieczorek et al.*, 2013), and this porosity could be present in either, or both, of the two units (the surrounding crust and the magmatic intrusion).

First, the observed density contrast could be due to a pore-free magmatic

intrusion and a pore free highland crust. From the sample densities, this would give rise to a density contrast of about 510 kg m^{-3} , which is smaller than the observed $1-\sigma$ lower bound, and thus is probably too small to account for the observations. Second, the density contrast could be the result of a fractured intrusions and a surrounding fractured highland crust. If each had the same level of porosity, this would give rise to an even smaller density contrast. Lastly, if the intrusion were unfractured, but the surrounding highland crust had a porosity of 12%, a density contrast of about 852 kg m^{-3} could be achieved, which is close to the observed value.

The best scenario that can account for the observed density contrast at floor-fractured craters in the highlands is an unfractured basaltic intrusion that forms within a fractured highland crust. Overall, this implies that the intrusion is sufficiently young to have escaped being fractured by subsequent impact events. Given that most basaltic eruptions occurred between 3 and 4 billion years ago, this suggests that the majority of the lunar crust was fractured before this date.

Our analyses of the gravity anomalies in the South Pole-Aitken basin and in the maria are less conclusive and are associated with much larger uncertainties. In regard to the SPA basin, although the mean magnitude of the gravity anomalies for floor-fractured craters is larger than for normal craters, we show that the difference between the two populations is not significant. We note, however, that the average density contrast associated with floor-fractured craters in the South Pole-Aitken basin is nearly identical to that obtained for the highlands.

Concerning the mare regions, the corrected gravity anomalies for floor-fractured craters are consistent with a mean value for the density contrast that is considerably smaller than in the highlands. This is in fact consistent with expectations. If the density contrast were the result of an unfractured intrusion forming in a fractured basaltic crust (both having the same grain density), the density contrast would be only about 403 kg m^{-3} , which is nearly identical to the mean value found from our analysis.

6.6 Conclusion

The gravitational signature of the floor-fractured crater population, first observed by *Schultz* (1976a), has been investigated using the unprecedented resolution of the global gravity model provided by the GRAIL's mission. We show that the signal at floor-fractured craters in the highlands is consistent with the presence of a magmatic intrusion at depth below the crater floor. Derived synthetic gravity anomalies at each FFC compared to observations

show that on average, the density contrast between the magma and the crust is about 913 kg m^{-3} . This value is in agreement with the intrusion being composed of unfractured basaltic material and forming in a pre-existing fractured crust (*Wieczorek et al., 2013*)

Similar studies have been carried out for floor-fractured craters located in the South Pole Aitken basin and in the lunar maria. However, the small number of craters as well as the large variability in these two regions prevent from clearly differentiating the signal due to magmatic intrusions from the background. In general, two major questions need to be addressed before carrying out further investigations at floor-fractured crater sites: 1) What is the origin of the large variability in the magnitude of the gravity anomaly at normal crater? And 2), how can we better quantify the intrusion thickness at floor-fractured craters?

Indeed, our results suggest that the impact itself, combined with preexisting density variations within the crust, results in a wide range of Bouguer anomalies at normal impact craters. Such density structures should also pre-exist below floor-fractured craters before magma emplacement. To enhance the intrusion signal, an estimate of the expected initial gravity signature is desirable.

Additionally, we show that the large variability in the crater depth-diameter relationship makes difficult the determination of the crater depth itself, and by consequence, the thickness of the magmatic intrusion. This variability comes from the degradation state of the crater. A quantification of the degradation state of normal and floor-fractured craters might help to reduce the uncertainty in the determination of the initial and current floor-fractured crater depths and would result in a more accurate derivation of the density contrast between the magmatic intrusion and the surrounding crust.

Part IV

Summary and perspectives

Intrusive magmatism is a major process at the scale of a planetary body and play a fundamental role in the accretionary processes of the terrestrial crust. However, it takes place deep beneath the surface and remain difficult to study without a proper model for magmatic intrusion emplacement. The objective of this thesis was two-fold: to characterize the dynamics of a cooling magmatic intrusion and to shed light on the origin of floor-fractured craters.

Dynamics of shallow magmatic intrusions

Summary

Intermediate-scaled shallow magmatic intrusions are the building blocks of larger plutons intruded into the crust (*Petford et al., 2000; Glazner et al., 2004*). We show in Chapter 1 that the topographic deformation that could be caused by shallow intrusions can be constrained by observations of planetary surfaces; that is, volume, shape and other dimensions of intrusions can be quantified. These observations have been previously used to draw a first view of their formation. However, they must be linked to models of magma intrusion dynamics in order to provide insights into magma physical properties and injection rate.

Michaut (2011) provides a consistent 2D model for such elastic-plated gravity current intrusions which directly link the observed deformations to physical parameters of the magmas. In particular, depending mainly on the injection rate and the intrusion depth, two regimes of propagation are identified and characterized by specific morphologies and scaling laws for intrusion thickness versus length and time. In Chapter 2, we develop the model in an axisymmetric geometry and compare the model predictions to the morphology of several terrestrial shallow magmatic intrusions. We show that laccoliths and low-slope lunar domes are consistent with their arrest in the early times bending regime. In addition, the model predictions are consistent across different planetary settings. However, the absolute dimension of these magmatic intrusions is underestimated by the model; in particular, abnormally high viscosity are required to reconcile both observations and predictions.

To get some insight in the effective flow viscosity, we provide in chapter 3 and 4 an extension of the model of *Michaut (2011)* that accounts for the cooling of the elastic-plated gravity current. We show that the coupling between the temperature field and the flow itself results in important deviation from the isoviscous case. In particular, in the bending regime, the effective flow viscosity is governed by the local thermal condition at the tip of the current; as the fluid is cooling, the thermal anomaly detaches from the tip and the flow

effective viscosity rapidly increases to stabilize when it reaches its maximum value. Applications to terrestrial laccoliths indeed show that their dimensions are in agreement with their arrest in the third bending phase. A phase diagram as a function of the Peclet number Pe and the viscosity contrast ν is provided which allows to constrains the parameters of the intrusions given its composition. We then show that lunar intrusive domes have probably been characterized by larger injection rate than on Earth, though much smaller than the effusion rates estimated from the runout distance of some lunar lava flows.

In chapter 4, we proposed that the entrance in the third phase of both regimes might have triggered the arrest of shallow magmatic intrusions. However, even for laccoliths, we have shown that conduction cooling alone is probably not a sufficient mechanism for their arrest, neither on Earth, nor on the Moon. Available data for large mafic sills on Earth also show less agreement with the model prediction. Indeed, in chapter 3 and 4, we show that sills should behave as isoviscous gravity current when the thermal anomaly is small compared to the flow itself, i.e. in similar settings, their thickness should tend to a constant. The increase in thickness with diameter preserved in the data might thus suggest that they instead stop in the second gravity phase. However, the model lacking of a stopping criteria for the flow, this hypothesis can not be tested properly. In the end, while the cooling of the intrusion has allowed us to predict the mean in the observations, a complete picture of the solution, in regard to the final radius and thickness of the intrusion as a function of the parameters of the problem (elasticity and toughness of the host rock, viscosity of the magma, injection rate of the feeder dyke, and depth of emplacement), has yet not been obtained.

Perspectives

In Chapter 2, 3 and 4, we show that the dynamics in the bending regime is controlled by the local condition at the tip of the current. For a sake of simplicity, we used a thin prewetting film at the tip to avoid the requirement of any boundary condition at a genuine front. While this approach allowed us to get insights into the coupling between the thermal structure and the flow itself, a more precise characterization of the front might help predict the final morphology of laccoliths.

Detail description of the tip

A first step could be to describe the tip in term of a fluid driven fracture instead of the thin prewetting film. As seen in Section 2.3.3, linear elastic

fracture mechanics requires that the mode I intensity factor K_I equal a critical value, the fracture toughness K_{Ic} for the propagation to occur, condition that is usually expressed in term of an asymptotic condition on the crack opening at $r = R$ (*Savitski and Detournay, 2002; Bunger et al., 2005; Bunger and Detournay, 2007; Detournay and Peirce, 2014*). In such problem, the lubrication equation is thus coupled to a description of the fracture opening based on the linear elastic fracture mechanics. *Bunger and Cruden* (2011) use this approach to solve the problem of shallow magmatic intrusion and found similar results than *Michaut* (2011). Interestingly, they needed values for the fracture toughness K_c two or three orders of magnitudes larger than laboratory measurements in order to agree with the observations, which they attribute to potentially crack blunting mechanism at the tip of laccoliths. This observation is consistent with the rapid cooling of the current tip describe in Chapter 3 and 4. However, this model also falls short to reproduce the geometry of large mafic sills. In addition, more realistic model should also address the question of plastic deformation in the fracture potentially caused by the heating (*Bunger, 2008*). Furthermore, the large negative pressure that developed at the front might cause desolved gasses to exsolve from the magma. With the formation and the evolution of a gap filled with gas at the tip of the current, the fluid and the fracture front do not coincide with one another, thus requiring the tracking of two moving boundaries.

Along with the prewetting film regularization, *Hewitt et al. (2014)* propose a second regularization condition where the tip of the elastic-gravity current consists of a lag region filled with gas at constant negative pressure (Figure 6.10). They show that the solution depends on the gas pressure in the tip region in similar fashion that the solution depends on the prewetting film thickness in Chapter 2, 3 and 4. In particular, they show that

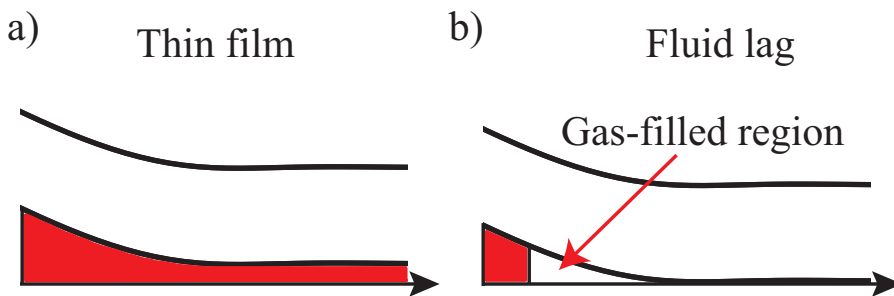


Figure 6.10: Two different regularization condition at the front of the current:
a) thin prewetting film with thickness h_f b) gas -filled region.

$$h_0 \propto h_f^{-1/7} \nu^{-2/7} L^{10/7} \text{ (Thin film)} \quad (6.17)$$

$$h_0 \propto \sigma^{1/9} \nu^{-2/9} L^{14/9} \text{ (Fluid lag)} \quad (6.18)$$

where L is the half length of the flow, $-\sigma$ is the constant negative pressure in the fluid lag and we have rescaled the characteristic thickness and time by $\nu^{1/4}$ in [Hewitt et al. \(2014\)](#). As expected, the two different regularization condition leads to only minor change in the thickness to length relationship ($10/7 \sim 1.4$, $14/9 \sim 1.5$). Nevertheless, a complete description of the dynamics of the cooling gas-filled region, whose properties are expected to vary a lot with the temperature, might also be required.

In the end, further works should couple the model derived in Chapter 3 and 4 to a more careful description of the different processes involved at the scale of the current tip. Such approach should surely give interesting insights and a more complete view of the dynamics of shallow magmatic intrusion.

Contact zone

In chapter 4, we show that a significant thermal aureole should develop in the wall rocks above the central flow region. Apart from plastic rock deformation that might develop in the encasing rocks, studying the possible thermal erosion could also be an interesting thing to look at. For instance, above the feeder dyke, the temperature are expected to be maximum on the roof and might favor subsequent dyke propagation. This could potentially explain the nested structure of several laccolith complexes reported in the literature ([Corry, 1988](#); [Rocchi et al., 2010](#)).

Multiple magma pulses

The results developed in this thesis mostly account for a constant injection rate Q_0 . [Michaut \(2011\)](#) suggests that the weight of the magma at the center might compensate the initial overpressure ΔP ; when $\Delta P/(\rho_m g H) = h_0$ the flow is thick enough to accommodate the overpressure below and enters a regime of lateral propagation ([Michaut, 2011](#)). For the larger overpressure ΔP and the typical parameters listed in Table 4.2, this would happen when $h_0 \sim 200$, which can be reached for $\nu < 10^{-6}$ in the third bending regime. It would be interesting to see how the regime of lateral propagation is affected by the rapid cooling of the tip.

In addition, this model assumes that the overpressure ΔP driving magma ascent remains constant. For instance, on Earth, gas pressure build up within the magma chamber is the most likely source of overpressure and should decrease as the magma is evacuated through the dyke ([Rivalta, 2010](#)). It would be interesting to see how the model developed in Chapter 3 react to a multiple

pulse injection separated by rest period. For instance, *Macedonio et al.* (2014) have used the isoviscous model of *Michaut* (2011) and show that the dynamics of such multiple pulse injection fed magmatic intrusion share similar pattern with the unrest of volcanic caldera observed in different location across the world.

Influence of the topography

In Chapter 5, we study the influence of a depression on top of the emplacement zone on the intrusion dynamics. Instead, the model can be easily adapted to study the presence of a volcanic edifice. It could then be used to study ground deformations experienced by active volcano as a response to the dynamics of underground magmatic systems (*Cayol et al.*, 2014; *Pedersen and Sigmundsson*, 2004; *Patanè et al.*, 2006; *Bonaccorso*, 2001; *Chadwick Jr. and Dieterich*, 1995; *Cannavò et al.*, 2015).

Lunar intrusive magmatism

Summary

While it provides for important constraints on the Moon's thermal and petrogenetic evolution, the total volume of melt produced into the Moon interior is poorly known. Indeed, although the total extrusive volume is quantified through analyses of the lunar maria, the volume of intrusive magma, which should be large due to the low density of the lunar crust, remains unknown. A first step in the quantification of the intrusive activity on the Moon is the detection of shallow magmatic systems.

Low-slope lunar domes and floor-fractured craters are two proposed evidences for shallow magmatic intrusion activity in the upper lunar crust. However, these observations must be linked to shallow magmatic intrusion models to asses their intrusive origin. In this thesis, we first show that lunar-low slope domes morphology are indeed consistent with a model of a cooling magmatic intrusion. In addition, adapting the model of elastic-plated gravity current model to account for a crater-centered intrusion, we show in Chapter 5 that the deformations observed at floor-fractured craters are also consistent with the emplacement of magmatic intrusions below their floor. Consistently, taking advantage of the resolution of the lunar gravity field obtained from the NASA's Gravity Recovery and Interior Laboratory (GRAIL) mission, in combination with topographic data obtained from the Lunar Orbiter Laser Altimeter (LOLA) instrument, we show in Chapter 6 that their gravitational signatures is significantly larger than the one of normal impact craters.

Perspectives

Around 10 low-slope lunar domes and about 200 floor-fractured craters have been detected at the lunar surface, most of them located close or within the lunar maria. While the total volume of these magmatic intrusion should not exceed 1% of lunar maria volume, it advocates the presence of numerous shallow magmatic intrusions in the lunar crust. This suggests that deeper and probably larger intrusion might stands at the base of the lunar crust.

Local stress field

In Chapter 5, we argue that the absence of deformation surrounding floor-fractured craters suggests that the unload pressure associated with the crater might have drive magma ascent below these craters. However, the unload pressure, associated with the depression, should decrease with depth on a length scale equal to the crater diameter, some tens of kilometers. Therefore, for the average FFC diameter, ~ 30 km, the depression caused by the crater can drive magma flow only if the magma is already present at depth smaller than 30 km, i.e. within the crust. It thus raises the question of deeper and larger magmatic reservoir within the lunar crust which might be observable in the the lunar gravity field obtained from the GRAIL mission.

This idea is also supported by recent works on rift volcanism on Earth that show that depression can play a crucial role in the trajectory of magma on the local scale (*Maccaferri et al., 2014*). In particular, in the extensive tectonic setting of rift, *Maccaferri et al.* (2014) show the presence of a stress barrier, consequence of the graben depression, where σ_3 turns to be vertical, i.e. preventing vertical dyke propagation. Interestingly, dyke nucleated below the stress barrier are deviated from their vertical trajectory and off-rift volcanism occur. While important extensive stress field should not exist at floor-fractured crater sites, this work thus not favor dykes initiated deep in the lunar interior, which should have been deviated from the crater center, to feed these shallow intrusions.

Meanwhile, a details analysis of the stress field below the crater depression could thus explain why these craters, apart from the underlying low density breccia, provide a favorable environment for magmatic intrusions. At a regional scale, it could also prove fruitful to investigate the link between the load of the lunar maria and the distribution of floor-fractured craters, which is mainly at the edge of the maria itself.

Thickness of the lunar maria

Approximately 16% of the Moon's surface is covered by basaltic lava flows that comprise the lunar maria. Although the total extent of these lava flows is known, their thicknesses are more difficult to constrain (*Thomson et al.*, 2009). Many different approaches, including indirect techniques as gravity, seismic or radar data, or direct measurements, through analyses of impact that have completely penetrated the maria, have been proposed to estimate their thicknesses. The elastic-plated gravity current models provided in this thesis can also be used to provide estimate useful to constrain thickness model of the lunar maria. Indeed, if the intrusion has stop in the bending regime, the inequality $R < 4\Lambda$ in the case of lunar domes or $R < 4\Lambda/C$ in the case of floor-fractured craters, provide for an estimate for the elastic thickness and thus, a lower bound for the maria thickness.

Floor-fractured craters on other terrestrial planets

As proven of the Moon, floor-fractured crater are a good first basis to probe the importance of intrusive magmatism on terrestrial planets. While they have first been observed and described on the Moon, many evidences show now that floor-fractured crater might be a common landscape on terrestrial planets.

- **Mars:** On Mars, almost 200 floor-fractured craters have also been reported located mostly along a narrow band south of the dichotomy boundary in Arabia Terra (*Bamberg et al.*, 2014). The observed deformations within these craters is very similar to the one observed on the Moon, though Martian floor-fracture craters tend to exhibit a more extensive and wider fracture network (Figure 6.11 a, b and c). This is attributed to complex interaction of the magmatic intrusion with potential ice/water in the subsurface (*Sato et al.*, 2010; *Bamberg et al.*, 2014). In particular, the melting of the water (or possibly CO₂) trapped in the subsurface would enhance erosion of the floor-fractured which is consistent with some small and medium size fluvial outlets (*Sato et al.*, 2010). Interestingly, deformations on Martian floor-fractured craters is not localized within the crater wall but can also extend further the crater rim (Figure 6.11 b,c). In contrast to the Moon, the overpressure driving the intrusion might have been larger than the unloading pressure associated with the depression. In addition, Martian magma, at the difference of their lunar counterpart, are most likely to be buoyant until the surface and the mechanism favorable to intrusion below Martian crater is still debated. Again on Mars, studying the stress field associated with the

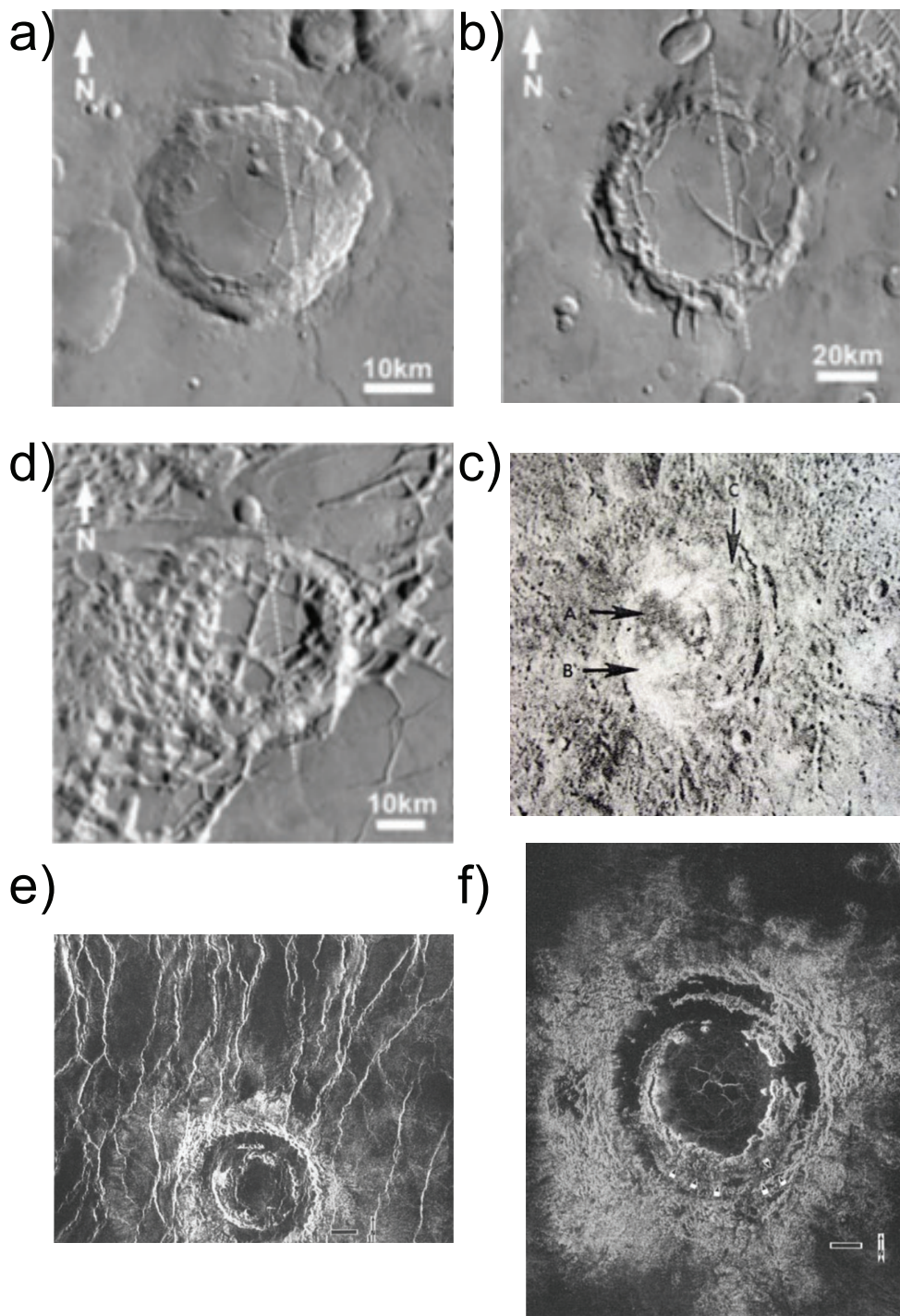


Figure 6.11: a), b) and c) Sample from the Marsian FFC population located respectively at ($0.0^{\circ}\text{N}, 337.3^{\circ}\text{E}$), ($5.5^{\circ}\text{S}, 322.6^{\circ}\text{E}$) and ($6.7^{\circ}\text{S}, 333.4^{\circ}\text{E}$). All are TEHMIS daytime IR image taken modified from [Sato et al. \(2010\)](#). d) Potential FFC on Mercury reproduced from [Schultz \(1977\)](#). e) Barrymore crater, 50 km diameter, located near Imdr Regio. f) Mona lisa Crater, 85 km in diameter, located on the edge of Eistla Regio. Both are potential FFCs on Venus. Reproduced from [Wichman and Schultz \(1995a\)](#).

crater depression could provide a viable mechanism to trigger magma spreading at depth below these craters.

- **Mercury** *Schultz (1977)* propose several candidates searching for intra-crater dark haloes or other color variations indicating post-impact emplacement of mafic materials onto the floor. They did find several crater floors with contrasting deposits, and additionally a few rimmed moat-like depression (Figure 6.11 d).
- **Venus:** Venus geologic record have been largely cut off by resurfacing events constantly reworking the Venusian surface. Nevertheless, several candidates have also been proposed on Venus by *Wichman and Schultz (1995a)*.

Though most of these observations, except for Marsian FFCs, have been made in the late nineties, they provide an extremely good basis for work using new data and x new methods at hand today. In addition, it provides a good opportunity to study and constrain the important of shallow intrusive magmatism outside of the Moon.

Part V

Appendices and bibliography

APPENDIX A

Numerical schemes

A.1 Numerical scheme for a cooling elastic-plated gravity current

In this section, we present the numerical scheme used to solve the coupled nonlinear partial differential equations (4.8) and (4.9). The governing equations presented in Chapter 3 are just a particular case where $\Omega \rightarrow \infty$ and can be solved using $\Omega = 10^5$ for instance.

A.1.1 General procedure

The coupled nonlinear partial differential equations (4.8) and (4.9) are solved on a grid of size M defined by the relation $r_i = (i - 0.5)\Delta r$ for $i = 1, \dots, M$. The grid is shifted at the center to avoid problem arising from the axisymmetrical geometry. We index the grid point by the indice i and denote the solution on this grid h_i and ξ_i and the secondary variables $\Theta_{b,i}$, $\Theta_{s,i}$ and δ_i . Both equations can be expressed on the convenient form

$$\frac{\partial u}{\partial t} - f = 0 \quad (\text{A.1})$$

where u is the function we want to integrate and f a non-linear function that depends on u . We solve these equations by first discretizing all the spatial derivatives using Finite Difference. The accuracy of the scheme is determined by the higher order derivatives since their numerical approximation requires the largest number of sample points. We then get two systems of M ordinary differential equations with the form

$$\frac{\partial u_i}{\partial t} - f_i = 0 \quad i = 1, \dots, M \quad (\text{A.2})$$

The time derivatives are first order and, since explicit schemes tend to be very sensitive and unstable, we use a fully implicit backward Euler scheme to get

$$\frac{u_i^{n+1} - u_i^n}{\Delta t} - f_i(u_i^{n+1}) = 0 \quad i = 1, \dots, M \quad (\text{A.3})$$

Since $f_i(u_i^{n+1})$ is not a linear function, the system above cannot be re-arranged to solve u_i^{n+1} in term of u_i^n and an iterative method has to be employed instead. Fixed point iteration method have shown poor results in converging toward the solution and we finally apply second order Newton's method to obtain the solution at each time step. In particular, we first linearize u^{n+1} around a guess of the solution by assuming $u^{n+1} = u^* + \delta u^n$, where u^* is a guess and δu^n is the error and we drop the i for clarity. Then, we expressed the non-linear part using a Taylor's expansion

$$f^{n+1} = f(u^{n+1}) = f(u^* + \delta u^n) = f(u^*) + J_f^h(u^*)\delta u^n$$

where $J_f^h(u^*)$ is the jacobian matrix for the function f evaluated in h^* . Injecting the expansion into (A.3) finally gives a system of M linear equations for the correction term δ_h^n which can be expressed as

$$(I - \Delta t J_f^h(u^*))\delta u^n = u^n - u^* + \Delta t f(u^*) \quad (\text{A.4})$$

where I is the identity matrix. Therefore, each iteration solves for δu^n and we use $u_n + \delta u^n$ as a new guess u^* in each iteration. This is repeated until δu^n becomes sufficiently small. Finally, since the equations are coupled, we use a fixed-point iteration method to converge toward the solution (h, ξ) at each time step. Therefore, the algorithm is the following at each time step

- Start with a guess for the values of all variables.
- Solve the thickness equation (4.8) for h^{n+1} using Newton-Rhapsod method.
- Solve the heat equation (4.9) for ξ^{n+1} using h^{n+1} as a new guess for h^* and Newton-Rhapsod method.
- Repeat step one until further iterations cease to produce any significant changes in the values of both h^{n+1} and ξ^{n+1} .

The computational scheme is summarized in the following.

A.1.2 Thickness equation

The thickness equation (4.8) is written as

$$\frac{\partial h}{\partial t} - f(h, \xi) = 0 \quad (\text{A.5})$$

with

$$f = \frac{1}{r} \frac{\partial}{\partial r} \left(r \phi \left(\frac{\partial}{\partial r} (h + P) \right) \right) + w_i \quad (\text{A.6})$$

$$\phi = 12I_1(h) \quad (\text{A.7})$$

and where P is the dimensionless bending pressure $P = \nabla^4 h$.

Spatial discretization of f

The spatial discretization is obtained using a central difference scheme over a sub-grid shifted by $0.5\Delta r$ from the main grid. Therefore, we have

$$\begin{aligned} f_i &= \frac{1}{r_i \Delta r} \left(r_{i+1/2} \phi_{i+1/2} \left(\frac{\partial h}{\partial r} + \frac{\partial P}{\partial r} \right) \Big|_{i+1/2} - r_{i-1/2} \phi_{i-1/2} \left(\frac{\partial h}{\partial r} + \frac{\partial P}{\partial r} \right) \Big|_{i-1/2} \right) \\ &= A_i \phi_{i+1/2} (h_{i+1} - h_i) - B_i \phi_{i-1/2} (h_i - h_{i-1}) \\ &\quad + A_i \phi_{i+1/2} (P_{i+1} - P_i) - B_i \phi_{i-1/2} (P_i - P_{i-1}) \\ &\quad + w_i \end{aligned} \quad (\text{A.8})$$

where $A_i = r_{i+1/2}/(r_i \Delta r^2)$ and $B_i = r_{i-1/2}/(r_i \Delta r^2)$. The bending pressure term P is very stiff and needs a careful treatment. In particular, the fourth order derivative requires a fourth order central difference scheme and therefore, P_i is expressed over a seven point stencil on the main grid such that

$$P_i = \alpha_i h_{i-3} + \beta_i h_{i-2} + \gamma_i h_{i-1} + \lambda_i h_i + \kappa_i h_{i+1} + \delta_i h_{i+2} + \varepsilon_i h_{i+3} \quad (\text{A.9})$$

with

$$\begin{aligned} \alpha_i &= \frac{1}{24 \Delta r^4} (-4 + 3p_3 \Delta r) \\ \beta_i &= \frac{1}{24 \Delta r^4} (48 - 24p_3 \Delta r - 2p_2 \Delta r^2 + 2p_1 \Delta r^3) \\ \gamma_i &= \frac{1}{24 \Delta r^4} (-156 + 39p_3 \Delta r + 32p_2 \Delta r^2 - 16p_1 \Delta r^3) \\ \lambda_i &= \frac{1}{24 \Delta r^4} (224 - 60p_2 \Delta r^2) \\ \kappa_i &= \frac{1}{24 \Delta r^4} (-156 - 39p_3 \Delta r + 32p_2 \Delta r^2 + 16p_1 \Delta r^3) \\ \delta_i &= \frac{1}{24 \Delta r^4} (48 + 24p_3 \Delta r - 2p_2 \Delta r^2 - 2p_1 \Delta r^3) \\ \varepsilon_i &= \frac{1}{24 \Delta r^4} (-4 - 3p_3 \Delta r) \end{aligned}$$

and where $p_1 = 1/r_i^3$, $p_2 = 1/r_i^2$ and $p_3 = 2/r_i$. Finally, the term $\phi_{i-1/2}$ and $\phi_{i+1/2}$, which depend on the variable Θ_b , δ as well as different power of h , are evaluated in $i - 1/2$ and $i + 1/2$ respectively. Different choices for the value of the variable at the mid-cell grid point do not show any significant difference and a simple average is taken such that the variable $u_{i+1/2}$ is taken as $0.5(u_i + u_{i+1})$.

Expression of the jacobian J_f^h

The discretized function f_i can be break down in three part, the gravitational part f_i^g which is expressed in term of the value of h on three grid points $\{i-1, i, i+1\}$, the bending part f_i^b which is expressed in term of the value of h on nine grid points $\{i-4, i-3, \dots, i+3, i+4\}$ and the injection term which depends only on the grid point i such that

$$f_i = f_i^g + f_i^b + w_i \quad (\text{A.10})$$

Therefore, the jacobian is nona-diagonal and its coefficient J_{il} are

$$J_{il} = \begin{cases} \frac{\partial f_i^b}{\partial h_l} & l = \{i-4, i-3, i-2, i+2, i+3, i+4\} \\ \frac{\partial f_i^g}{\partial h_l} + \frac{\partial f_i^b}{\partial h_l} & l = \{i-1, i, i+1\} \\ 0 & \text{otherwise} \end{cases} \quad (\text{A.11})$$

The different terms can be easily derived from (A.8) and (A.9) with just slight adjustment coming from the boundary conditions.

Boundary condition

We begin with $h_i = h_f$ for $i = 1, \dots, M$. Since the flow is symmetric in $r = 0$, we require that

$$\left. \frac{\partial h}{\partial r} \right|_{r=0} = \left. \frac{\partial P}{\partial r} \right|_{r=0} = 0 \quad (\text{A.12})$$

and therefore for $i = 1$, we have

$$\begin{aligned} f_i &= A_1 \phi_{i+1/2} (h_{i+1} - h_i) \\ &+ A_i \phi_{i+1/2} (P_{i+1} - P_i) \\ &+ w_i \end{aligned} \quad (\text{A.13})$$

The expression of the bending pressure, evaluated over a 7 point stencils, is problematic close to the boundary and reflection formulae will be used in order to accommodate the boundary conditions [Patankar \(1980\)](#). In particular, we have $h_0 = h_1$, $h_{-1} = h_2$ and $h_{-2} = h_3$. Similarly, boundary condition at the end of the mesh is accounted by using a grid much larger than the flow itself and requiring

$$\left. \frac{\partial h}{\partial r} \right|_{r=r_M} = \left. \frac{\partial P}{\partial r} \right|_{r=r_M} = 0 \quad (\text{A.14})$$

which gives for $i = M$

$$\begin{aligned} f_i &= B_i \phi_{i-1/2} (h_i - h_{i-1}) \\ &+ B_i \phi_{i-1/2} (P_i - P_{i-1}) \\ &+ w_i \end{aligned} \quad (\text{A.15})$$

with $h_{i>=M} = h_f$.

Newton-Rhapsod method

The Newton-Rhapsod method reads

$$(I - \Delta t J_f^h(h_k^*)) \delta h_k^n = h^n - h_k^* + \Delta t f(h_k^*) \quad (\text{A.16})$$

where the k refers to the k iterations, I is a $M \times M$ diagonal matrix and $J_f^h(h^*)$ is a $M \times M$ nona-diagonal matrix. This system of linear equations can be solved using a nona-diagonal algorithm. At the first iteration, we use $h_1^* = h^n$ as a first guess and then we iterate using $h_k^* = h^n + \delta h_{k-1}^n$ as a new guess for each iterations until δh_k^n becomes sufficiently small. In particular, we require that

$$\delta h_k^n / h_k^* < \varepsilon \quad (\text{A.17})$$

with $\varepsilon = 10^{-4}$.

A.1.3 Heat equation

The heat equation (4.9) is written as

$$\frac{\partial \xi}{\partial t} - g(h, \xi) = 0 \quad (\text{A.18})$$

with

$$g = \frac{1}{r} \frac{\partial}{\partial r} (r \Gamma \xi) + \frac{1}{r} \frac{\partial}{\partial r} (r \Sigma) + 2Pe^{-1} St_m \frac{(\Theta_b - \Theta_s)}{\delta} \quad (\text{A.19})$$

$$\bar{\theta} = \frac{1}{3} (2\Theta_b + \Theta_s) \quad (\text{A.20})$$

$$\Gamma = -\frac{12}{\delta} \frac{\partial P}{\partial r} (\delta I_0(\delta) - I_1(\delta)) \quad (\text{A.21})$$

$$\Sigma = \frac{12}{\delta} \frac{\partial P}{\partial r} (I_0(\delta) (G(\delta) - \delta \bar{\theta}) + \bar{\theta} I_1(\delta) - I_2(\delta)). \quad (\text{A.22})$$

Spatial discretization of g

As for the thickness equation, the spatial discretization is obtained using a central difference scheme over a sub-grid shifted by $0.5\Delta r$ from the main grid. Therefore, we have

$$g_i = (C_i \Gamma_{i+1/2} \xi_{i+1/2} - D_i \Gamma_{i-1/2} \xi_{i-1/2}) \quad (\text{A.23})$$

$$+ (C_i \Sigma_{i+1/2} - D_i \Sigma_{i-1/2}) \quad (\text{A.24})$$

$$+ 2Pe^{-1} St_m \frac{\Theta_{b,i} - \Theta_{s,i}}{\delta_i} \quad (\text{A.25})$$

with $C_i = r_{i+1/2}/(r_i \Delta r)$ and $D_i = r_{i-1/2}/(r_i \Delta r)$. We use the average between the grid point i and $i - 1$ (resp. $i + 1$) to evaluate the quantity in Γ and Σ at $i - 1/2$ (resp. $i + 1/2$). In addition, we use a classical upwind scheme to handle ξ at the mid grid point which requires

$$\xi_{i+1/2} = \xi_i \quad (\text{A.26})$$

$$\xi_{i-1/2} = \xi_{i-1} \quad (\text{A.27})$$

Expression of the Jacobian J_g^ξ

The expression of the Jacobian is much straightforward in that case and its coefficient J_{il} are

$$J_{il} = \begin{cases} -D_i \Gamma_{i-1/2} & l = i - 1 \\ C_i \Gamma_{i+1/2} & l = i \\ 0 & \text{otherwise} \end{cases} \quad (\text{A.28})$$

with only slight adjustment coming from the boundary conditions.

Boundary conditions

We consider $\Theta_b = 1$ and $\delta = 10^{-4}$ in the film at $t = 0$. In this way, we ensure that the average temperature across the film at $t = 0$ is close to 1. By construction, $D_1 = 0$ and therefore, for $i = 1$ we have

$$g_i = C_i \Gamma_{i+1/2} \xi_i + C_i \Sigma_{i+1/2} + 2Pe^{-1} St_m \frac{\Theta_{b,i} - \Theta_{s,i}}{\delta_i} \quad (\text{A.29})$$

For $i = M$, we consider that $\Gamma_{i+1/2} = \Gamma_i$ and $\Sigma_{i=1/2} = \Sigma_i$. However, the choice for the boundary condition at the border of the grid $i = M$ is not important as we solve the problem over a grid much larger than the flow itself.

Newton-Rhapsod method

The Newton-Rhapsod method reads

$$(I - \Delta t J_g^\xi(\xi_k^*)) \delta \xi_k^n = \xi^n - \xi_k^* + \Delta t f(\xi_k^*) \quad (\text{A.30})$$

where the k refers to the k iterations, I is a $M \times M$ diagonal matrix and $J_f^\xi(\xi^*)$ is a $M \times M$ tri-diagonal matrix. This system of linear equations can be solved using a tri-diagonal algorithm. As for the thickness equation, at the first iteration, we use $\xi_1^* = \xi^n$ as a first guess and then we iterate using

$\xi_k^* = \xi^n + \delta\xi_{k-1}^n$ as a new guess for each iterations until $\delta\xi_k^n$ becomes sufficiently small. In particular, we require that

$$\delta\xi_k^n / \xi_k^* < \varepsilon \quad (\text{A.31})$$

with $\varepsilon = 10^{-4}$. In addition, at each iteration, the quantity $\Theta_{s,k}^*$, $\Theta_{b,k}^*$ and δ_k^* , that are needed to evaluate Γ and Σ , are derived from the value of ξ_k^* using (4.26), (4.27) and (4.28)

A.1.4 Integral expressions

The model developed in Section 4.2 depends on the integrals

$$I_0(z) = \int_0^z \frac{1}{\eta(y)} \left(y - \frac{h}{2} \right) dy \quad (\text{A.32})$$

$$I_1(z) = \int_0^z \frac{1}{\eta(y)} \left(y - \frac{h}{2} \right) y dy \quad (\text{A.33})$$

$$I_2(z) = \int_0^y \frac{1}{\eta(y)} \left(y - \frac{h}{2} \right) G(y) dy \quad (\text{A.34})$$

where $G(z)$ is a primitive of $\theta(z)$ where $z < \delta$ and is given by

$$G(z) = \frac{z (3\delta^2\Theta_s + 3\delta z(\Theta_b - \Theta_s) + z^2(\Theta_s - \Theta_b))}{3\delta^2}. \quad (\text{A.35})$$

In particular, the model requires the expression of $I_0(\delta)$, $I_1(\delta)$, $I_1(h)$ and $I_2(\delta)$.

Rheology 1: $\eta(\theta) = \eta_1(\theta)$

In that case, the four integrals can be easily derived and read

$$\begin{aligned} I_0(\delta) &= \frac{\delta}{12} (6\delta\nu + (1-\nu)(-\alpha_1\delta + 2\alpha_1h + 6\Theta_b\delta - 6\Theta_bh) - 6h\nu) \\ I_1(\delta) &= \frac{\delta^2}{120} (40\delta\nu + (1-\nu)(-4\alpha_1\delta + 5\alpha_1h + 40\Theta_b\delta - 30\Theta_bh) - 30h\nu) \\ I_1(h) &= \frac{1}{60} ((1-\nu)(-4\alpha_1\delta^3 + 10\alpha_1\delta^2h - 10\alpha_1\delta h^2 + 5\Theta_bh^3) + 5h^3\nu) \\ I_2(\delta) &= -\frac{\delta^2}{2520} (378\alpha_1\delta\nu - 315\alpha_1h\nu - 840\Theta_b\delta\nu + 630\Theta_bh\nu) \\ &\quad -\frac{\delta^2}{2520} (1-\nu)(-50\alpha_1^2\delta + 70\alpha_1^2h + 462\alpha_1\Theta_b\delta - 420\alpha_1\Theta_bh - 840\Theta_b^2\delta + 630\Theta_b^2h) \end{aligned}$$

where $\alpha_1 = \Theta_b - \Theta_s$ has been introduced for clarity.

Rheology 2: $\eta(\theta) = \eta_2(\theta)$

For cases where $\nu < 1$, we have

$$\begin{aligned}
I_0(\delta) &= -\frac{\delta\nu^{1-\Theta_b} (\sqrt{\pi}\sqrt{\alpha_1}(2\delta-h)\sqrt{-\alpha_2}\operatorname{erf}(\sqrt{\alpha_1}\sqrt{-\alpha_2}) + 2\delta(\nu^{\alpha_1}-1))}{4\alpha_1\alpha_2} \\
I_1(\delta) &= \frac{\delta^2\nu^{1-\Theta_b} (\sqrt{\pi}\operatorname{erf}(\sqrt{\alpha_1}\sqrt{-\alpha_2})(\alpha_1(h-2\delta)\alpha_2+\delta))}{4\alpha_1^{3/2}(-\alpha_2)^{3/2}} \\
&\quad + \frac{\delta^2\nu^{1-\Theta_b} (\sqrt{\alpha_1}\sqrt{-\alpha_2}(2\delta(\nu^{\alpha_1}-2)-h\nu^{\alpha_1}+h))}{4\alpha_1^{3/2}(-\alpha_2)^{3/2}} \\
I_1(h) &= \frac{\nu^{1-\Theta_b} (\sqrt{\alpha_1}\sqrt{-\alpha_2}(12\delta^2(\delta(\nu^{\alpha_1}-2)-h\nu^{\alpha_1}+h)+\alpha_1(2\delta-h)^3\log(\nu)))}{12\alpha_1^{3/2}(-\alpha_2)^{3/2}} \\
&\quad - \frac{\nu^{1-\Theta_b} (3\sqrt{\pi}\delta\operatorname{erf}(\sqrt{\alpha_1}\sqrt{-\alpha_2})(\alpha_1(h-2\delta)^2\alpha_2-2\delta^2))}{12\alpha_1^{3/2}(-\alpha_2)^{3/2}} \\
I_2(\delta) &= \frac{\delta^2\nu^{1-\Theta_b} (\sqrt{\pi}\operatorname{erf}(\sqrt{\alpha_1}\sqrt{-\alpha_2})(-2\alpha_1(2\delta-h)(\alpha_1-3\Theta_b)\alpha_2^2-6\delta\Theta_b\alpha_2-3\delta))}{24\alpha_1^{3/2}(-\alpha_2)^{5/2}} \\
&\quad + \frac{\delta^2\nu^{1-\Theta_b} (2\sqrt{\alpha_1}\nu^{\alpha_1}\sqrt{-\alpha_2}(\nu^{-\alpha_1}(\alpha_2(-2\delta(\alpha_1-6\Theta_b)-3h\Theta_b)+2\delta-h)))}{24\alpha_1^{3/2}(-\alpha_2)^{5/2}} \\
&\quad + \frac{\delta^2\nu^{1-\Theta_b} (2\sqrt{\alpha_1}\nu^{\alpha_1}\sqrt{-\alpha_2}(2\delta\alpha_1\alpha_2-6\delta\Theta_b\alpha_2+\delta-\alpha_1h\alpha_2+3h\Theta_b\alpha_2+h))}{24\alpha_1^{3/2}(-\alpha_2)^{5/2}}
\end{aligned}$$

where in addition to α_1 , we also introduced $\alpha_2 = \log(\nu)$ for clarity. In the case where $\nu = 1$, the expression above simplify and read

$$\begin{aligned}
I_0(\delta) &= \frac{1}{2}\delta(\delta-h) \\
I_1(\delta) &= \frac{1}{12}\delta^2(4\delta-3h) \\
I_1(h) &= \frac{h^3}{12} \\
I_2(\delta) &= -\frac{1}{120}\delta^2(18\delta\alpha_1-40\delta\Theta_b-15\alpha_1h+30h\Theta_b)
\end{aligned}$$

A.2 Numerical scheme for crater-centered intrusion

A.3 Numerical scheme

We use a fully implicit finite-volume method to solve (5.18). The discretization is obtained by integrating over a finite number of non overlapping control

volumes, each control volume surrounding one grid point (*Patankar*, 1980). The grid is defined by the relation $r_i = (i - 0.5)\Delta r$ in order to avoid problems at the center. The point b and a define the face of the control volume surrounding i such that $r_a = r_i + \Delta r/2$ and $r_b = r_i - \Delta r/2$. Because we are using an axisymmetric geometry, the control volume is an annulus of interior radius r_b and exterior radius r_a and its surface is $S = \pi(r_a^2 - r_b^2)$. Integration of (5.18) over the control volume surrounding i during a time Δt gives:

$$\int_t^{t+\Delta t} \int_{r_b}^{r_a} \frac{\partial h^*}{\partial t} 2\pi r dr dt = \int_t^{t+\Delta t} \int_b^a \Phi(r, t) 2\pi r dr dt \quad (\text{A.36})$$

where $\Phi(r, t)$ stands for the right hand side of (5.18). The classical second-order ($\propto \Delta r^2$) approximations is taken to derive the successive space derivatives (i.e. $\frac{\partial \Phi(r)}{\partial r} |_{r_a} = \frac{\Phi(i+1) - \Phi(i)}{\Delta r}$). In this way, we ensure that our final scheme is of second-order. Moreover, for more precision, the elastic pressure is calculated using a fourth-order scheme (see A.3.1.3). In the following, we derive each term of the right hand side of (5.18) separately, h refers to the value of the thickness at a time $t + \Delta t$ and h^n to the value at a time t .

A.3.1 Discretization

1. **Time derivative** To discretize the time derivative, we shall consider that the value of the grid point h_i prevails throughout the control volume such that:

$$\int_t^{t+\Delta t} \int_{r_b}^{r_a} \frac{\partial h^*}{\partial t} 2\pi r dr dt = (h_i - h_i^n) S \quad (\text{A.37})$$

2. **Gravitational term**

$$\begin{aligned} & \int_t^{t+\Delta t} \int_{r_b}^{r_a} \frac{1}{r^*} \frac{\partial}{\partial r^*} \left(r^* h^3 \frac{\partial h}{\partial r^*} \right) 2\pi r dr dt \\ &= A_i^g h_{i+1} + B_i^g h_{i-1} - (A_i^g + B_i^g) h_i \end{aligned} \quad (\text{A.38})$$

with $A_i^g = A = (2\pi \Delta r r_a h_a^3)/\Delta r$ and $B_i^g = B = (2\pi \Delta r r_b h_b^3)/\Delta r$ where the value of h_a^3 (resp. h_b^3) is approximated by $(h_{i+1}^3 + h_i^3)/2$ (resp. $(h_i^3 + h_{i-1}^3)/2$).

3. **Elastic term**

$$\begin{aligned} & \int_t^{t+\Delta t} \int_{r_b}^{r_a} \Theta \frac{1}{r^*} \frac{\partial}{\partial r^*} \left(r^* h^3 \frac{\partial P_e}{\partial r^*} \right) 2\pi r dr dt \\ &= A_i^e P_{e,i+1} + B_i^e P_{e,i-1} - (A_i^e + B_i^e) P_{e,i} \end{aligned} \quad (\text{A.39})$$

where $A_i^e = \Theta A$, $B_i^e = \Theta B$ and $P_e = \nabla_r^2(\Pi(r)\nabla_r^2 h(r))$, with $\Pi(r) = (1 + \Psi\xi(r))^3$, is the dimensionless elastic pressure which is discretized using a fourth order finite difference scheme:

$$P_{e,i} = \alpha_i h_{i-3} + \beta_i h_{i-2} + \gamma_i h_{i-1} + \lambda_i h_i + \kappa_i h_{i+1} + \delta_i h_{i+2} + \varepsilon_i h_{i+3} \quad (\text{A.40})$$

with

$$\begin{aligned} \alpha_i &= \frac{1}{24\Delta r^4} (-4p_4 + 3p_3\Delta_r) \\ \beta_i &= \frac{1}{24\Delta r^4} (48p_4 - 24p_3\Delta_r - 2p_2\Delta_r^2 + 2p_1\Delta_r^3) \\ \gamma_i &= \frac{1}{24\Delta r^4} (-156p_4 + 39p_3\Delta_r + 32p_2\Delta_r^2 - 16p_1\Delta_r^3) \\ \lambda_i &= \frac{1}{24\Delta r^4} (224p_4 - 60p_2\Delta r^2) \\ \kappa_i &= \frac{1}{24\Delta r^4} (-156p_4 - 39p_3\Delta_r + 32p_2\Delta_r^2 + 16p_1\Delta_r^3) \\ \delta_i &= \frac{1}{24\Delta r^4} (48p_4 + 24p_3\Delta_r - 2p_2\Delta_r^2 - 2p_1\Delta_r^3) \\ \varepsilon_i &= \frac{1}{24\Delta r^4} (-4p_4 - 3p_3\Delta_r) \end{aligned}$$

where

$$\begin{aligned} p_1 &= \frac{\Pi''_i}{r_i} - \frac{\Pi'_i}{r_i^2} + \frac{\Pi}{r_i^3} \\ p_2 &= \Pi''_i + \frac{3\Pi'_i}{r_i} + \frac{\Pi}{r_i^2} \\ p_3 &= 2\Pi'_i + \frac{2\Pi_i}{r_i} \\ p_4 &= \Pi_i \end{aligned}$$

and where $\Pi_i = (1 + \Psi\xi_i)^3$ and Π'_i and Π''_i are its first and second derivatives with respect to the radial coordinate.

4. Hydrostatic term

$$\begin{aligned} S_i^h &= \int_t^{t+\Delta t} \int_{r_b}^{r_a} \Xi \frac{1}{r^*} \frac{\partial}{\partial r^*} \left(r^* h^3 \frac{\partial \xi}{\partial r} \right) 2\pi r dr \\ &= U^h \left(r_a h_a^3 \frac{\partial \xi}{\partial r} \Big|_a - r_b h_b^3 \frac{\partial \xi}{\partial r} \Big|_b \right) \end{aligned} \quad (\text{A.41})$$

where $U^h = 2\pi\Xi\Delta t$.

5. Injection term

$$\begin{aligned} S_i^i &= \int_t^{t+\Delta t} \int_{r_b}^{r_a} \frac{32}{\gamma^2} \left(\frac{1}{4} - \frac{r^2}{\gamma^2} \right) 2\pi r dr dt \\ &= U^i (\gamma^2 - 2(r_a^2 + r_b^2)) \end{aligned} \quad (\text{A.42})$$

where $U^i = \frac{8S\Delta t}{\gamma^4}$.

6. Implicit scheme

Substituting (A.37), (A.38), (A.39), (A.41) and (A.42) in (A.36) and injecting (A.40), we get the final scheme given by the following equation:

$$a_i h_{i-4} + b_i h_{i-3} + c_i h_{i-2} + d_i h_{i-1} + e_i h_i + f_i h_{i+1} + g_i h_{i+2} + k_i h_{i+3} + l_i h_{i+4} = J_i \quad (\text{A.43})$$

where the different coefficients are defined by:

$$a_i = -B_i^e \alpha_{i-1} \quad (\text{A.44})$$

$$b_i = (B_i^e + A_i^e) \alpha_i - B_i^e \beta_{i-1} \quad (\text{A.45})$$

$$c_i = (B_i^e + A_i^e) \beta_i - B_i^e \gamma_{i-1} - A_i^e \alpha_{i+1} \quad (\text{A.46})$$

$$d_i = (B_i^e + A_i^e) \gamma_i - B_i^e \lambda_{i-1} - A_i^e \beta_{i+1} - B^g \quad (\text{A.47})$$

$$e_i = S + (B_i^e + A_i^e) \lambda_i - B_i^e \kappa_{i-1} - A_i^e \gamma_{i+1} + B^g + A^g \quad (\text{A.48})$$

$$f_i = (B_i^e + A_i^e) \kappa_i - B_i^e \delta_{i-1} - A_i^e \lambda_{i+1} - A^g \quad (\text{A.49})$$

$$g_i = (B_i^e + A_i^e) \delta_i - B_i^e \varepsilon_{i-1} - A_i^e \kappa_{i+1} \quad (\text{A.50})$$

$$k_i = (B_i^e + A_i^e) \varepsilon_i - A_i^e \delta_{i+1} \quad (\text{A.51})$$

$$l_i = -A_i^e \varepsilon_{i+1} \quad (\text{A.52})$$

$$J_i = (Sh_i^n + S_i^i + S_i^h) \quad (\text{A.53})$$

A.3.2 Boundary conditions

Since the flow is symmetric in $r = 0$, we require that:

$$\left. \frac{\partial h}{\partial r} \right|_{r=0} = 0 \quad (\text{A.54})$$

$$\left. \frac{\partial P_e}{\partial r} \right|_{r=0} = 0 \quad (\text{A.55})$$

Boundary conditions at the front of the intrusion are accounted for by using a grid much larger than the intrusion where $h = 0$ beyond the flow.

A.3.3 Algorithm

The fully implicit discretization (A.43) can be rewritten as a linear system $\Omega(h^3)\bar{h} = \bar{J}$ where \bar{h} is a vector containing the value of h at $t + \Delta t$ and \bar{J} containing the right hand side of (A.43). The matrix $\Omega(h^3)$ is a septadiagonal matrix and is solved by using a septadiagonal algorithm. However, due to the non-linearity of the problem (i.e. the coefficients A_e, B_e, A_g, B_g and S^h within the matrix $\Omega(h_i^3)$ and \bar{J} depend on h_i^3), we first have to assume values for h_i at each grid point to inverse for the matrix and get the value of h at $t + \Delta t$. We use the following iterative scheme:

- (a) Start with a guess at all grid-point for $h_i = h_i^n$.
- (b) Calculate tentative values for the different coefficients of the system (non linear terms).
- (c) Apply the septadiagonal matrix algorithm to solve (A.43) and get a new value of h_i .
- (d) With this new h_i , we return to step 2 and repeat step 2 to 4 until further repetitions cease to produce any significant change in h_i (i.e. $|h_i^{new} - h_i| < \varepsilon$ where $\varepsilon = 10^{-4}$).

The final unchanging state is considered as the solution for the thickness of the flow at $t + \Delta t$.

APPENDIX B

Details on the phase diagram

A current in the i th thermal phase can transition in the j th phase of the gravity regime where $i \geq j$. Indeed, the effective viscosity being that of a small region at the tip in the bending regime and the average flow viscosity in the gravity regime, it cannot increase during the transition. Hence, B_1G_2 , B_1G_3 and B_2G_3 are unfeasible (Table B.1 and Figure B.1 a). In addition, the transition from the third thermal phase of the bending regime to the first thermal phase of the gravity regime implies that $t_t^c < t_{b2}$ and $t_t^c > t_{g3}$, which is not possible (Table B.1 and Figure B.1 a). Therefore, the five possible sequences that remain are B_1G_1 , B_2G_1 , B_2G_2 , B_3G_2 and B_3G_3 (Table B.1 and Figure B.1 a).

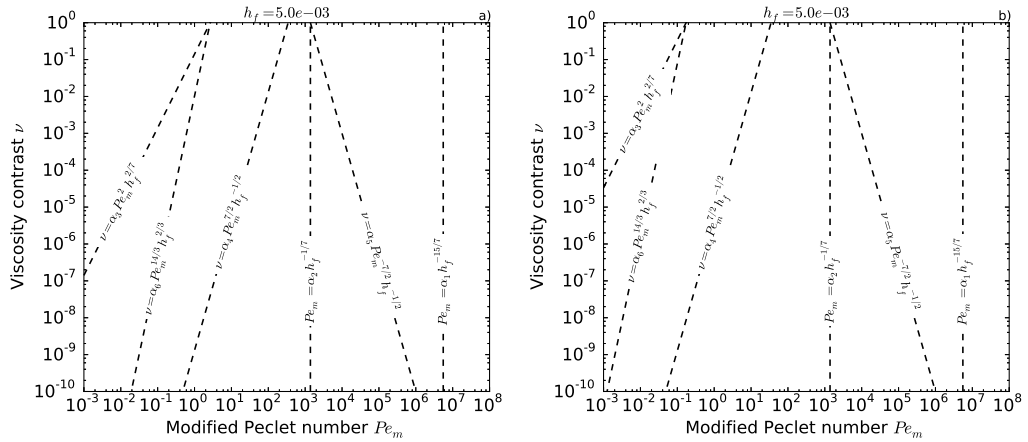


Figure B.1: a) Phase transitions reported in Table B.1 for the model described in Chapter 3. Same plot but for the more realistic model described in Chapter 4.

In the more realistic model described in Chapter 4, the time to enter the third flow phase is slightly delayed in both regimes. In particular, for the current that has reached the third bending phase, $t_t^c > t_{b3}$ now implies $\nu > 2.8 \cdot 10^{-7} Pe^{7/2} h f^{-1/2}$ (Figure B.1 b). In addition, comparing t_t^c and t_{g3} now reads $\nu < 1.2 \cdot 10^5 Pe_m^{14/3} h_f^{2/3}$ (Figure B.1 b).

Transition	Condition 1	Condition 2	Condition 3	Output
		Transition in the first bending thermal phase $B1$		
$t_t = t_t^h$	$t_t^h < t_{b2}$ $Pe_m > \alpha_1 h_f^{-15/7}$	$t_t^h < t_{g2}$ $Pe_m > \alpha_2 h_f^{-1/7}$	-	$B_1 G_1$
$t_t = t_t^h$	$t_t^h < t_{b2}$ $Pe_m > \alpha_1 h_f^{-15/7}$	$t_t^h > t_{g2}$ $Pe_m < \alpha_2 h_f^{-1/7}$	$t_t^h < t_{g3}$ $\nu < \alpha_3 Pe_m^2 h_f^{2/7}$	$B_1 G_2$ Unfeasible
$t_t = t_t^h$	$t_t^h < t_{b2}$ $Pe_m > \alpha_1 h_f^{-15/7}$	$t_t^h > t_{g3}$ $\nu > \alpha_3 Pe_m^2 h_f^{2/7}$	-	$B_1 G_3$ Unfeasible
		Transition in the second bending thermal phase $B2$		
$t_t^h < t_t < t_t^c$	$t_t^h > t_{b2}$ $Pe_m < \alpha_1 h_f^{-15/7}$	$t_t^c < t_{b3}$ $\nu < \alpha_4 Pe_m^{7/2} h_f^{-1/2}$	$t_t^c < t_{g2}$ $\nu > \alpha_5 Pe_m^{-7/2} h_f^{-1/2}$	$B_2 G_1$ Feasible
$t_t^h < t_t < t_t^c$	$t_t^h > t_{b2}$ $Pe_m < \alpha_1 h_f^{-15/7}$	$t_t^c < t_{b3}$ $\nu < \alpha_4 Pe_m^{7/2} h_f^{-1/2}$	$t_t^c < t_{g3}$ $\nu < \alpha_6 Pe_m^{14/3} h_f^{2/3}$	$B_2 G_2$ or $B_2 G_1$ Feasible
$t_t^h < t_t < t_t^c$	$t_t^h > t_{b2}$ $Pe_m < \alpha_1 h_f^{-15/7}$	$t_t^c < t_{b3}$ $\nu < \alpha_4 Pe_m^{7/2} h_f^{-1/2}$	$t_t^h > t_{g2}$ $Pe_m < \alpha_2 h_f^{-1/7}$	$B_2 G_2$ Feasible
$t_t^h < t_t < t_t^c$	$t_t^h > t_{b2}$ $Pe_m < \alpha_1 h_f^{-15/7}$	$t_t^c < t_{b3}$ $\nu < \alpha_4 Pe_m^{7/2} h_f^{-1/2}$	$t_t^h > t_{g3}$ $\nu > \alpha_3 Pe_m^2 h_f^{2/7}$	$B_2 G_3$ Unfeasible
		Transition in the third bending thermal phase $B3$		
$t_t = t_t^c$	$t_t^c > t_{b3}$ $\nu > \alpha_5 Pe_m^{-7/2} h_f^{-1/2}$	$t_t^c < t_{g2}$ $\nu > \alpha_5 Pe_m^{-7/2} h_f^{-1/2}$	-	$B_3 G_1$ Unfeasible
$t_t = t_t^c$	$t_t^c < t_{b2}$ $\nu > \alpha Pe_m^{7/2} h_f^{-1/2}$	$t_t^c > t_{g2}$ $\nu < \alpha_5 Pe_m^{-7/2} h_f^{-1/2}$	$t_t^c < t_{g3}$ $\nu < \alpha_6 Pe_m^{14/3} h_f^{2/3}$	$B_3 G_2$ Feasible
$t_t = t_t^c$	$t_t^c < t_{b2}$ $\nu > \alpha Pe_m^{7/2} h_f^{-1/2}$	$t_t^c > t_{g3}$ $\nu > \alpha_6 Pe_m^{14/3} h_f^{2/3}$	-	$B_3 G_3$ Feasible

Table B.1: Parameter space analysis. All conditions have to be respected for a scenario to be possible. For the model described in Chapter 3, the coefficients are: $\alpha_1 = 65$, $\alpha_2 = 650$, $\alpha_3 = 151$, $\alpha_4 = 8.3 \cdot 10^{-13}$, $\alpha_5 = 7.0 \cdot 10^9$, $\alpha_6 = 0.3$. For the more realistic model derived in Chapter 4, the coefficients are: $\alpha_1 = 65$, $\alpha_2 = 650$, $\alpha_3 = 0.6$, $\alpha_4 = 2.8 \cdot 10^{-7}$, $\alpha_5 = 7.0 \cdot 10^9$, $\alpha_6 = 1.2 \cdot 10^5$.

APPENDIX C

Effect of the prewetting film

To mitigate the problem at the contact line, we introduce a thin prewetting film, with thickness h_f such that $h(r, t) \rightarrow h_f$ as $r \rightarrow \infty$ (Section 2.1.3). In this appendix, we discuss the effect of changing the prewetting thickness h_f on some results presented in Chapter 3 and 4.

C.1 Scaling laws for the thickness and the radius

The scaling laws for the thickness $h_0(t)$ (3.54) as well as for the radius $R(t)$ (3.55) derived in Section 3.3 depends on the film thickness h_f . Accordingly, when rescaling the thickness by $h_f^{-1/11}$ and the radius by

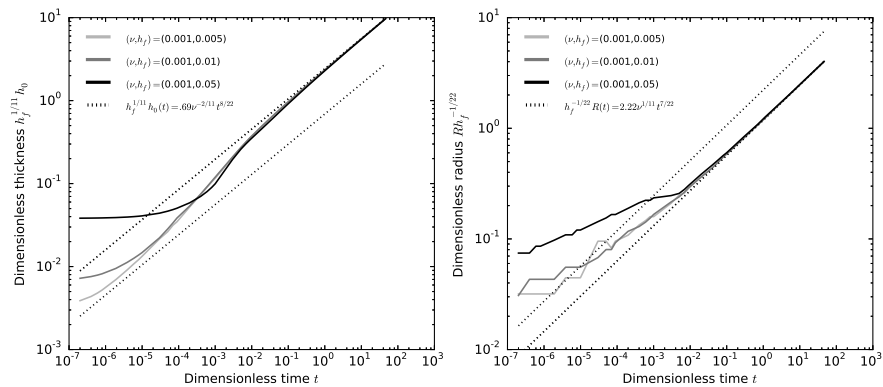


Figure C.1: Left: Dimensionless thickness at the center $h_0 h_f^{1/11}$ versus dimensionless time t for different sets (ν, h_f) indicated on the plot. Dashed-lines represent the scaling laws $h_0 h_f^{1/11} = 0.7\nu^{-2/11} t^{8/22}$ for $\nu = 1.0$ and 0.001 . Right: Dimensionless radius R versus dimensionless time t for the same sets (ν, h_f) . Dashed-lines represent the scaling laws $R h_f^{-1/22} = 2.2\nu^{1/11} t^{7/22}$ for $\nu = 1.0$ and 0.001 . Here, $\Omega = 10^5$ and $\eta(\theta) = \eta_1(\theta)$.

$h_f^{1/22}$, the different simulations collapse on the same curve (Figure C.1).

Similarly, when rescaling the extent of the cold fluid region $R(t) - R_c(t)$ by $h_f^{7/66}$, the different simulations also collapse on the same curve (Figure C.2). Similar results can be obtained for $R(t) - R_c(t)$ in the framework of the more realistic model described in Chapter 4. These scaling laws are thus able to account for the effect of the prewetting film thickness h_f which is, in general, rather weak.

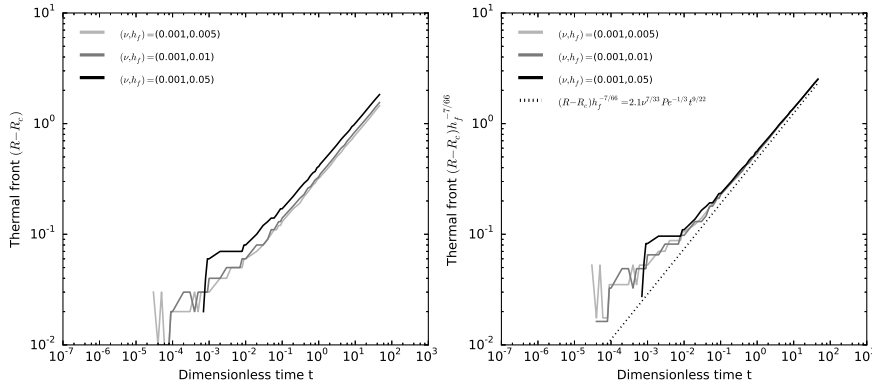


Figure C.2: Left: Extent of the cold fluid region $R(t) - R_c(t)$ versus dimensionless time for different combinations (ν, h_f) indicated on the plot. Right: Same plot but where we have rescaled the extent of the cold fluid region by $h_f^{7/66}$. Dashed-line: scaling law $(R(t) - R_c(t))h_f^{-7/66} = 2.1Pe^{-1/3}\nu^{7/33}t^{9/22}$.

C.2 Two stage growth in the second bending phase

In Chapter 4, for some simulations, the second phase of important thickening in the bending regime occurs in two stages: a first stage where the thickness drastically increases and a second stage where it continues increasing but much slower (Figure 4.4 and 4.5). To get some insights into this transition, we run some simulations for $\Omega = 1.0$ with a higher spatial resolution, i.e. $Dr = 0.005$ instead of $Dr = 0.01$ (Figure C.3).

The simulations show that this transition corresponds to the detachment of the thermal anomaly (Figure C.3). In particular, during the first stage, the thermal anomaly is still attached to the tip and the prewetting film, located beyond $r = R(t)$, is still cooling. In contrast, during the second stage, which is characterized by a decrease in the thickening rate, the prewetting film located beyond $r = R(t)$ is entirely cold, i.e.

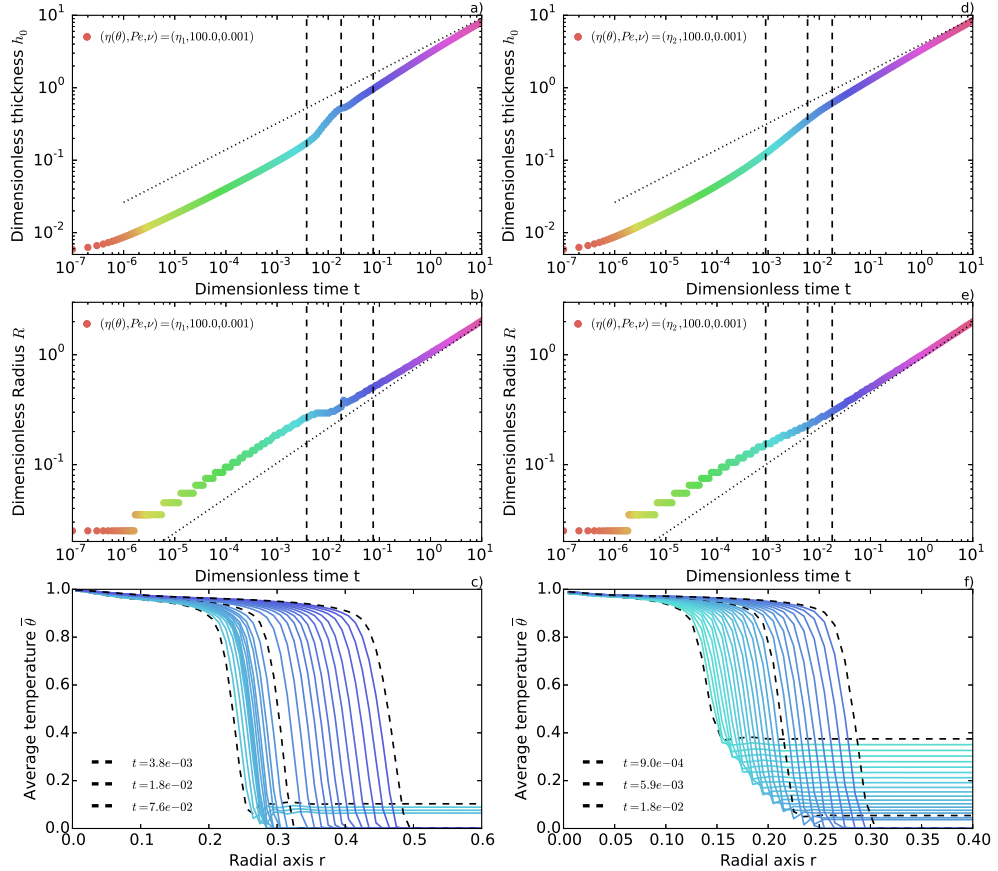


Figure C.3: Dimensionless thickness h_0 versus dimensionless time t for $Pe = 100.0$, $\nu = 0.001$, $\Omega = 1.0$ and the rheology $\eta_1(\theta)$. Colors refer to the time t . Dotted line: Scaling law $h_0 = 0.7h_f^{-1/11}\nu^{-2/11}t^{8/22}$. Vertical dashed-lines: initial, intermediate and final times of the temperature profiles plotted in c). b) Dimensionless radius R versus dimensionless time t for $Pe = 100.0$, $\nu = 0.001$ and the rheology $\eta_1(\theta)$. Colors refer to the time t . Dotted line: Scaling law $R = 2.2h_f^{1/22}\nu^{1/11}t^{7/22}$. Vertical dashed-lines: same than in a). c) Dimensionless average temperature over the flow thickness $\bar{\theta}$ versus radial axis r for times between $t = 3.8 \cdot 10^{-3}$ and $t = 7.6 \cdot 10^{-2}$. Dashed-line profiles: profiles at the three different times underlined in a) and b). Colors also refer to the time on the same scale than a) and b). d), e) and f), same plots than a), b) and c) but for the Arrhenius rheology η_2 .

$\bar{\theta} = 0$ for $r > R(t)$ and the thermal anomaly slowly gets away from the tip (Figure C.3). For instance, for $\eta_1(\theta)$, $\nu = 0.001$ and $Pe = 100.0$, the transitions between the two stages occurs at $t = 1.8 \cdot 10^{-2}$ and indeed coincide to the film becoming entirely cold (Figure C.3 a, b, c).

For the rheology $\eta_2(\theta)$, the transition is smoother because the viscosity increases on a wide range of temperature (Figure C.3 d, e, f). Even if this transition should be present for all the simulations, the smaller spatial resolution used in this Chapter 3 and 4 does not allow to resolve this transition for all the combinations of the dimensionless numbers.

C.3 Phase diagram

The phase diagram presented in section 4.5 and its application to the spreading of laccoliths depends on the chosen value for h_f . The meaning of the prewetting film thickness in the application to the spreading of laccolith is unclear. However, reasonable values for h_f are values with physical significance for this structural length scale at the tip of a laccolith and should range from a few centimeters to no less than 0.1 millimeter. Therefore, as the dependence with h_f is weak, a variation of 2 orders of magnitude does not change significantly the results (Figure C.4).

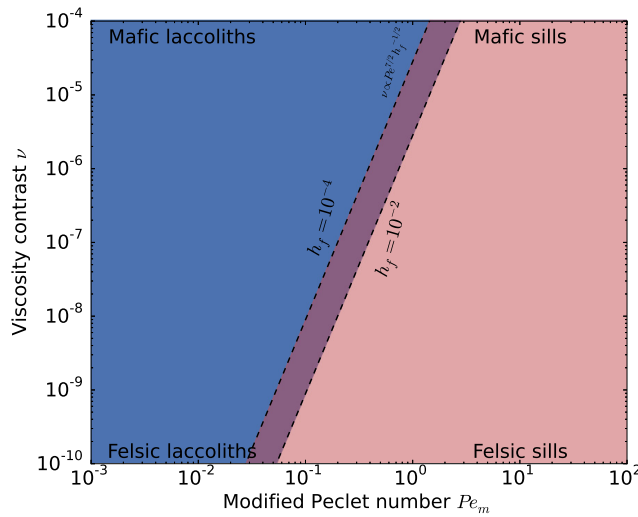


Figure C.4: Phase diagram for the evolution with bending and gravity for different combinations (ν, Pe_m) and different values for the film thickness $h_f = 10^{-2}$ and 10^{-4} .

The same result hold when we look at the relation between the thickness and the radius of the laccolith (4.49). Indeed, the best fit for the value of the viscosity contrast scales as $h_f^{-1/2}$, i.e. $\nu_{\text{best}} = h_f^{-1/2} 2.59 \cdot 10^{-10}$

and therefore, varying h_f by two orders of magnitudes change the viscosity contrast by one order of magnitude which is acceptable for our application.

APPENDIX D

Floor-fractured craters

D.1 Elastic stresses in the upper elastic layer

The stress conditions within the crater floor can be approximated using the small displacement theory. In an axisymmetric geometry, the small strain-displacement equations at the surface are:

$$\varepsilon_{rr} = \frac{\partial u_r}{\partial r} = -\frac{T_e(r)}{2} \frac{\partial^2 h}{\partial r^2} \quad (\text{D.1})$$

$$\varepsilon_{\theta\theta} = \frac{u_r}{r} = -\frac{T_e(r)}{2r} \frac{\partial h}{\partial r} \quad (\text{D.2})$$

Hence, the stress conditions at the surface are given by Hooke's laws for a material under plane stress:

$$\sigma_{rr} = -\frac{ET_e(r)}{2(1-\nu^2)} \left(\frac{\partial^2 h}{\partial r^2} + \frac{\nu}{r} \frac{\partial h}{\partial r} \right) \quad (\text{D.3})$$

$$\sigma_{\theta\theta} = -\frac{ET_e(r)}{2(1-\nu^2)} \left(\frac{1}{r} \frac{\partial h}{\partial r} + \nu \frac{\partial^2 h}{\partial r^2} \right) \quad (\text{D.4})$$

These equations are made dimensionless using the scaling of Section 3.5 where the pressure scale is $\rho_m g H$. Dimensionless radial and tangential stresses become:

$$\sigma_{rr} = -\Theta \Phi (1 + \Psi \xi(r)) \left(\frac{\partial^2 h}{\partial r^2} + \frac{\nu}{r} \frac{\partial h}{\partial r} \right) \quad (\text{D.5})$$

$$\sigma_{\theta\theta} = -\Theta \Phi (1 + \Psi \xi(r)) \left(\frac{1}{r} \frac{\partial h}{\partial r} + \nu \frac{\partial^2 h}{\partial r^2} \right) \quad (\text{D.6})$$

where $\xi(r)$ is given by (5.19) and Φ is a dimensionless number given by:

$$\Phi = \frac{6}{(1 - \nu^2)} \left(\frac{C}{T_e^0} \right)^2 \quad (\text{D.7})$$

The locations of the maximum stresses, where the fractures are the most likely to initiate, depend on the number Θ (Figure D.1 a). If the number Θ is such that $4\Lambda \gg C$, i.e. $\Theta > 10^{-3}$ the intrusion reaches the wall zone in an elastic regime and the maximum stresses are at the center. For $\Theta \sim 10^{-3}$, $4\Lambda \sim C$ and the transition to a gravity current regime occurs at the crater wall zone. In that case, the floor is still convex but the area of maximum stress is located within a crown at a given coordinate, intermediate between the center and the wall zone, i.e. $0 < r_{\sigma_{max}} < 1$ (Figure D.1 b). Radial and tangential stresses are of the same order of magnitude. For a large crater or a shallow intrusion, i.e. a small value of the number $\Theta < 10^{-3}$, the maximum stresses are concentrated within a crown adjacent to the wall zone upon the intrusion edge where the elastic deformation is important (Figure D.1 c). The radial stresses that develop at the surface are generally larger than the tangential stresses favoring a circular mode of fracturing.

D.2 Central peak

Central peaks induce an increase in the lithostatic pressure as well as an increase in the overlying layer elastic thickness directly above the intrusion center. Herein, we consider an extreme case where the central peak height is one third of the crater depth and its width is one fourth of the crater size by introducing an extra gaussian function into the elastic thickness expression:

$$T_e(r) = T_e^0(1 + \Psi(\xi(r)) + C_p(r))) \quad (\text{D.8})$$

with

$$C_p(r) = 50 \left(\frac{0.07}{4} \right)^2 \exp \left(-\frac{r^2}{2(\frac{0.07}{4})^2} \right) \quad (\text{D.9})$$

For a strengthless overlying layer and $\Theta = 0$ (Section 5.4.1 equation (5.27)), the central peak only adds an excess in lithostatic pressure at the center of the crater floor. In response, the intrusion preferentially develops around the central peak and then spreads until it reaches the crater wall (Figure D.2 a). At the crater wall, the lithostatic pressure increase induces the thickening of the intrusion. However, due to the

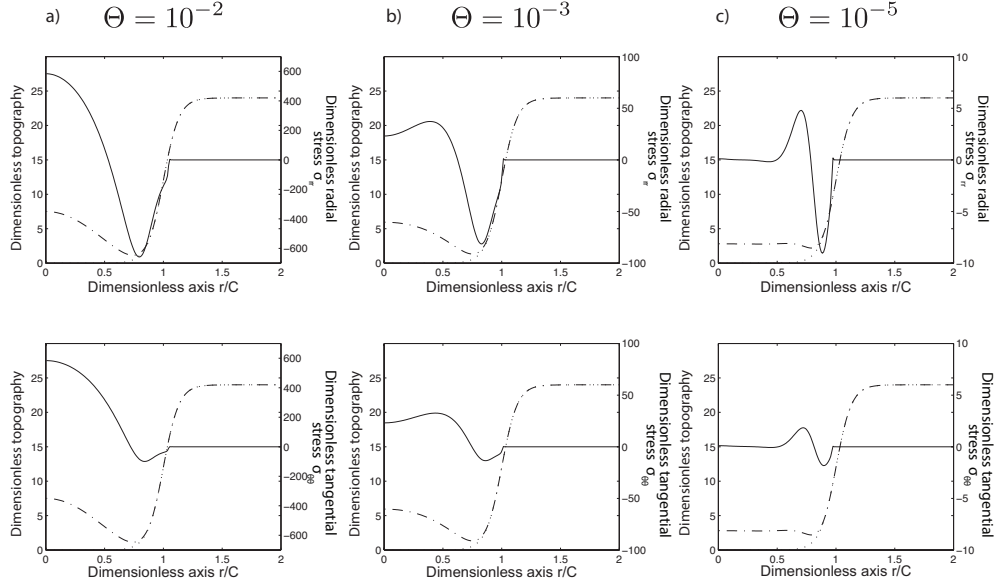


Figure D.1: Solid lines: Dimensionless radial stress σ_{rr} (top) and tangential stress $\sigma_{\theta\theta}$ (bottom) at the crater floor in the case of an intrusion spreading below an overlying elastic layer with a complex crater topography for $\Theta = 10^{-2}$ and $\Phi = 1100$ (left), $\Theta = 10^{-3}$ and $\Phi = 2500$ (center) and $\Theta = 10^{-5}$ and $\Phi = 4500$ (right) at $t = 2$. For all plots: the dotted lines represent the initial dimensionless topography $T_p(r)$ (5.26) and the dash-dotted lines represent the floor appearance $T_p(r) + h(r)$ at $t = 2$. Stress is considered positive in extension. We use $\gamma = 0.02$, $\Xi = 20$, $\zeta = 0.13$ and $\Psi = 1$.

excess of lithostatic pressure at the center, the center of the intrusion below the central peak does not thickens and the thickening only concerns an annulus located in between the central peak and the crater wall (Figure D.2 a). At the surface, the central peak height decreases until the thickening is important enough to compensate for the initial excess in lithostatic pressure. A balance between the two pressures gives the final height of the central peak, equal to the initial height times $(\rho_m - \rho_c)/\rho_m$ (Figure D.2 a). Next, the resulting central peak is just leveled up with the whole crater floor.

For an elastic overlying layer such that $\Theta = 10^{-5}$, the inner part of the intrusion adjacent to the central peak is bent by the weight of the central peak. As a consequence, during the thickening stage, a second circular moat, whose size is 4Λ , arises and borders the central peak. As previously, the central peak height decreases until the sum of the elastic and hydrostatic pressure compensate for the initial excess of lithostatic

pressure due to the central peak and is then leveled up during floor uplift.

Finally, in the case of a thick elastic overlying layer, i.e. a large value of Θ , the flexural wavelength is almost not affected by the presence of the central peak and the central peak is leveled up with the convex floor during crater floor uplift (Figure D.2 c).

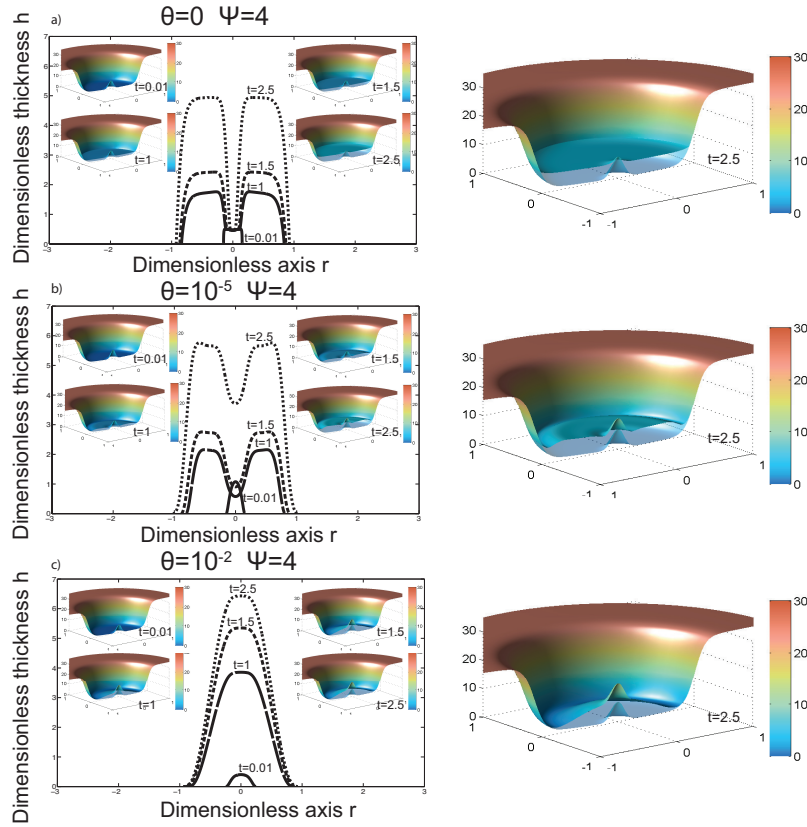


Figure D.2: **a)** Dimensionless intrusion profiles for different dimensionless times indicated on the plot for $\Psi = 4$ and for an intrusion spreading below a strengthless overlying layer with a complex crater topography and a central peak i.e. $\Theta = 0$ and $\zeta = 0.13$. For each time, a corresponding 3D graph, showing the dimensionless crater floor appearance given by $T_p(r) + h(r)$ where, here, $T_p(r) = \Xi\Omega(\xi(r) + C_p(r))$, is represented. For each plot, the initial topography given by $T_p(r) = \Xi\Omega(\xi(r) + C_p(r))$ is superimposed in low opacity. **b)** Same plot but for an overlying elastic layer such that $\Theta = 10^{-5}$. **c)** Same plot but for an elastic overlying layer such that $\Theta = 10^{-2}$. Here we use, $\gamma = 0.02$, $\Xi = 20$ and $\Psi = 4$.

APPENDIX E

Gravitationnal signature of lunar floor-fractured craters: Supplementary material

E.0.1 Synthetic gravity anomaly

The spherical harmonic coefficients associated with the intrusion thickness profile have the form

$$C_{lm} = \frac{4\pi\Delta\rho}{M} \frac{R_i^3}{2l+1} \sum_{n=1}^{n_{\max}} \frac{{}^nh_{lm}}{R_i^n n!} \frac{\prod_{j=1}^n (l+4-j)}{l+3} \quad (\text{E.1})$$

where ${}^nh_{lm}$ are the spherical harmonic coefficients of the expansion of the powers of the thickness profile $h_{topo}^n(\theta, \phi)$

$$h_{topo}^n(\theta, \phi) = \sum_{l=0}^{L_{\max}} \sum_{m=-l}^l {}^nh_{lm} Y_{lm}(\theta, \phi) \quad (\text{E.2})$$

These calculations were performed on grids that resolved spherical harmonics up to degree 1000, which corresponds to a grid spacing of 2.7 km. When calculating the spherical harmonic coefficients C_{lm} , n_{\max} was set equal to 9, which is more than sufficient given the small amplitudes of the magmatic intrusions considered here. Gravity anomalies are presented in mGal, which is 10^{-5} m s $^{-2}$ and calculated at a radius $r = R_0$ where R_0 is the mean lunar radius.

E.0.2 Effect of the downward continuation filter λ

We present the crustal gravity anomaly around two floor-fractured craters using different values for the downward continuation filter parameter λ . For the FFC Beals, that is 48 km in diameter, the amplitude of the gravity anomaly within the crater increases somewhat with increasing λ , due to the removing of regional negative trends, to reach a

maximum around $\lambda = 80$ (Figure E.1). For Taruntius, a floor-fractured crater that is a 56 km in diameter, models characterized by a $\lambda < 80$ do not remove enough of the positive regional trend to clearly delineate the central anomaly, while the models characterized by $\lambda > 80$ are too restrictive and would remove too much signal at the intrusion scale (Figure E.1).

Figure_E_Supp_1.pdf

Figure E.1: Top: Floor-fractured crater Beals, 48 km in diameter. Top left: topography (km) obtained from LOLA (64 ppd). Following plots: The crustal gravity anomaly using different values for the downward continuation filter parameter λ . The gravity anomaly within the crater becomes more apparent with increasing λ due to the removing of regional negative trends. Bottom: same plots but for the floor-fractured crater Taruntius, 56 km in diameter.

E.0.3 Definition of the gravity anomaly

Figure_E_Supp_2.pdf

Figure E.2: Definition of the gravity anomaly at a crater site. The gravity anomaly δ_g associated to a crater is equal to the mean value of the gravity anomaly measured interior to the crater rim (left) minus the mean gravity anomaly measured within an annulus surrounding the crater and extending from the outer flank of the rim to a circle of diameter $2D$.

E.0.4 Crater depth

The crater depth, d_c , is the difference in elevation between the crater rim and the crater floor. Following *Kalynn et al. (2013)*, we use the gridded topographic data within a circular region of radius D to derive the floor elevation and within an annulus bounded by $0.98D$ and $1.05D$ to derive the rim elevation. We use the diameter reported by *Head*

Table E.1: Gravity anomaly distribution characteristics for the two normal crater populations and the FFC population in the lunar in the highlands, maria and South Pole Aitken basin

	N	μ_{δ_g}	SEM $_{\delta_g}$	SD $_{\delta_g}$	t-test		KS
					t	p	D
Lunar highlands							
Unmod. Craters	4054	-0.71	0.12	7.44	3.24	0.00119	0.00
Unmod. Crat. FFC	584	-0.39	0.33	7.91	2.49	0.01284	0.04
FFC	80	2.03	1.07	9.57	0.00	1.00000	0.16
Lunar maria							
Unmod. Craters	306	1.51	0.68	11.85	1.08	0.27961	0.00
Unmod. Crat. FFC	70	1.94	1.32	11.01	0.81	0.41745	0.08
FFC	22	4.43	3.52	16.49	0.00	1.00000	0.17
Lunar SPA							
Unmod. Craters	603	-3.54	0.46	11.27	1.08	0.27939	0.00
Unmod. Crat. FFC	148	-3.86	0.94	11.49	1.14	0.25632	0.05
FFC	14	-0.25	2.52	9.42	0.00	1.00000	0.21

* N is the size of the population, μ_{δ_g} is the mean of the gravity anomalies (mGal), SEM $_{\delta_g}$ is the standard error of the mean (mGal), SD $_{\delta_g}$ is the standard deviation (mGal). t and p are the values of a Student's t-test that compares the gravity anomaly means of the different populations with the FFC gravity anomaly mean. D and p are the values of a two-sample Kolmogorov-Smirnov test that compared the gravity anomaly distribution of the different populations with the gravity anomaly distribution of the normal crater population. Unmod. Craters refers to the normal crater population and Unmod. Crat. FFC refers to the normal crater population that shares the spatial distribution of FFCs.

**Appendix E. Gravitationnal signature of lunar floor-fractured
224 craters: Supplementary material**

Table E.2: Topographic analyses for the normal crater populations and the FFC population in the highlands, maria and South Pole Aitken basin.

	N	μ_{depth}	σ_{depth}	t	p	A	B	$d = AD^B$
Lunar highlands								
FFC	80	1.87	0.94	0.00000	1.00000	0.70	0.33	
Unmod. Crat. FFC	584	1.93	1.07	-0.48457	0.62814	0.54	0.44	
Lunar maria								
FFC	22	1.16	0.59	0.00000	1.00000	0.18	0.62	
Unmod. Crat. FFC	70	1.14	0.73	0.07832	0.93775	0.05	0.93	
Lunar SPA basin								
FFC	14	1.88	0.81	0.00000	1.00000	0.05	0.93	
Unmod. Crat. FFC	148	2.09	1.10	-0.72867	0.46727	0.24	0.64	

* N is the size of the population, μ_{depth} is the mean of the population depth (km), σ_{depth} is the mean of the uncertainty in the depth estimation (km). t and p are the values of a Student's t-test that compared the mean depth of the normal crater population to the FFC mean depth. A and B are the coefficients of the power law relationship $d = AD^B$ and σ_{fit} is the dispersion around the power law best fit (km). Unmod. Crat. refers to the normal crater population that share the spatial distribution of FFCs.

et al. (2010) and *Jozwiak et al.* (2012) and assume these to be error-free. We produce histograms of elevations, binned in 50 m intervals, and examine the distributions. For the crater floor, the minimum elevation h_{\min} is affected by later crater deformation such as fractures, subsequent cratering or in some cases, wall slump and moats. For this reason, rather than considering the minimum h_{\min} and the mode elevation h_{mod} to characterize the crater floor depth as in *Kalynn et al.* (2013), we consider only the mode of the distribution h_{mod} and we take its value as the crater floor elevation h_{floor} . We assign to this value an uncertainty σ_{floor} equal to the width of the distribution mode. Concerning the rim elevation, we follow *Kalynn et al.* (2013) and take the rim elevation to be equal to the average of the modal h_{mode} elevation and the maximum h_{\max} elevation within the crater rim region. We assign an uncertainty to the rim elevation of $\sigma_{\text{rim}} = (h_{\text{mode}} - h_{\max})/2$ (*Kalynn et al.*, 2013). The crater depth, d_c , is the difference in elevation between the floor and the rim, to which we assign an uncertainty equal to $\sigma_d = (\sigma_{\text{floor}}^2 + \sigma_{\text{rim}}^2)^{1/2}$.

Table E.3: Derived FFC intrusion thickness (H_0) distribution characteristics in the highlands, maria and South Pole Aitken basin.

	N	μ_{H_0}	σ_{H_0}
Highlands	80.00	0.49	0.85
Maria	22.00	0.09	1.01
SPA	14.00	1.11	0.93

* N is the size of the population, μ_{H_0} is the mean of the population thickness at the center (km) and σ_{H_0} is the mean of the uncertainties in the thickness estimation (km).

Table E.4: Forward modeling for the density contrasts between the magmatic intrusions and the crust at the sites of floor-fractured craters in the highlands, maria and South Pole Aitken basin.

	N	Observed gravity		Synthetic gravity		Density contrast		t	t-test
		$\mu_{\delta_g^*}$	$SEM_{\delta_g^*}$	$\mu_{\delta_g^S}$	$SEM_{\delta_g^S}$	$\mu_{\Delta\rho}$	$SEM_{\Delta\rho}$		
Highlands	80	3.48	0.98	4.71e-03	2.19e-04	913	269	0.00000	1.1
Maria	22	2.48	2.93	4.68e-03	3.41e-04	484	669	0.69086	0.0
SPA	14	3.22	1.65	1.44e-02	1.99e-03	974	846	-0.08425	0.0

* N is the size of the population, $\mu_{\delta_g^*}$ is the mean of the corrected gravity anomalies, $SEM_{\delta_g^*}$ is the standard error of the mean of the corrected gravity anomalies, $\mu_{\delta_g^S}$ is the mean of the synthetic gravity anomalies obtained for a density contrast $\Delta\rho = 1 \text{ kg m}^{-3}$, $SEM_{\delta_g^S}$ is the standard error of the mean of the synthetic gravity anomalies, $\mu_{\Delta\rho}$ is the mean value of the density contrast between the magma and the crust $\mu_{\Delta\rho} = \sum_{i=0}^{i=N} \Delta\rho_i / N$, $SEM_{\Delta\rho}$ is the standard error of the mean density contrast. t and p are the values of a Student's t-test that compares the density contrast distribution of the different populations with the density contrast of the FFC population of the highlands.

Bibliography

- Anderson, E. M. (1951), The dynamics of faulting and dyke formation with applications to Britain. (Cited on page 7.)
- Andrews-Hanna, J. C., S. W. Asmar, J. W. Head, W. S. Kiefer, A. S. Konopliv, F. G. Lemoine, I. Matsuyama, E. Mazarico, P. J. McGovern, H. J. Melosh, G. A. Neumann, F. Nimmo, R. J. Phillips, D. E. Smith, S. C. Solomon, G. J. Taylor, M. A. Wieczorek, J. G. Williams, and M. T. Zuber (2013), Ancient igneous intrusions and early expansion of the Moon revealed by GRAIL gravity gradiometry, *Science*, 339(6120), 675–678. (Cited on page 159.)
- Baker, D. M. H., J. W. Head, C. I. Fassett, S. J. Kadish, D. E. Smith, M. T. Zuber, and G. A. Neumann (2011), The transition from complex crater to peak-ring basin on the Moon: New observations from the Lunar Orbiter Laser Altimeter (LOLA) instrument, *Icarus*, 214(2), 377–393. (Cited on page 125.)
- Balmforth, N. J., and R. V. Craster (2004), Dynamics of cooling viscoplastic domes, *J. Fluid Mech.* (Cited on pages 38, 45, 48, 49 and 53.)
- Bamberg, M., R. Jaumann, H. Asche, T. Kneissl, and G. G. Michael (2014), Floor-Fractured Craters on Mars – Observations and Origin, *Planetary and Space Science*, 98(C), 146–162. (Cited on page 189.)
- Barmin, A., O. Melnik, and R. Sparks (2002), Periodic behavior in lava dome eruptions, *Earth and Planetary Science Letters*, 199(1-2), 173–184. (Cited on page 32.)
- Bercovici, D. (1994), A theoretical model of cooling viscous gravity currents with temperature-dependent viscosity, *Geophys. Res. Lett.* (Cited on pages 38, 45, 46, 66 and 87.)
- Bercovici, D., and J. Lin (1996), A gravity current model of cooling mantle plume heads with temperature-dependent buoyancy and viscosity, *J. Geophys. Res.*, 101(B2), 3291–3309. (Cited on pages 38 and 45.)
- Bertozzi, A. L. (1998), The mathematics of moving contact lines in thin liquid films, pp. 1–9. (Cited on page 25.)

- Besserer, J., F. Nimmo, M. A. Wieczorek, R. C. Weber, W. S. Kiefer, P. J. McGovern, J. C. Andrews-Hanna, D. E. Smith, and M. T. Zuber (2014), GRAIL gravity constraints on the vertical and lateral density structure of the lunar crust, *Geophys. Res. Lett.*, *41*. (Cited on pages 159 and 170.)
- Blatt, H., R. J. Tracy, and B. Owens (2006), Petrology: igneous, sedimentary, and metamorphic. (Cited on page 87.)
- Bonaccorso, A. (2001), Mt Etna volcano: modelling of ground deformation patterns of recent eruptions and considerations on the associated precursors, *Journal of Volcanology and Geothermal Research*, *109*(1-3), 99–108. (Cited on page 187.)
- Bray, V. J., G. S. Collins, J. V. Morgan, and P. M. Schenk (2008), The effect of target properties on crater morphology: Comparison of central peak craters on the Moon and Ganymede, *Meteoritics*, *43*(12), 1979–1992. (Cited on page 127.)
- Bunger, A. P. (2008), A rigorous tool for evaluating the importance of viscous dissipation in sill formation: it's in the tip, *Geological Society, London, Special Publications*, *304*(1), 71–81. (Cited on page 185.)
- Bunger, A. P., and A. R. Cruden (2011), Modeling the growth of laccoliths and large mafic sills: Role of magma body forces, *J. Geophys. Res.*, *116*(B2), B02,203. (Cited on pages 22, 26, 29, 44, 121, 138, 151 and 185.)
- Bunger, A. P., and E. Detournay (2007), Scaling Relationships for Deep and Shallow Magma-Driven Intrusions, *AGU Fall Meeting Abstracts*, -1, 0369. (Cited on page 185.)
- Bunger, A. P., and D. Emmanuel (2005), Near-surface hydraulic fracture, *Engineering Fracture Mechanics*, *72*(16), 2468–2486. (Cited on page 36.)
- Bunger, A. P., E. Detournay, and R. G. Jeffrey (2005), Crack tip behavior in near-surface fluid-driven fracture experiments, *Comptes Rendus Mécanique*, *333*(4), 299–304. (Cited on page 185.)
- Büttner, R., B. Zimanowski, J. Blumm, and L. Hagemann (1998), Thermal conductivity of a volcanic rock material (olivine-melilitite) in the temperature range between 288 and 1470 K, *80*(3-4), 293–302. (Cited on page 85.)

- Cameron, A., and W. Benz (1991), The origin of the Moon and the single impact hypothesis IV, *Icarus*, *92*, 204–216. (Cited on page 13.)
- Cannavò, F., A. G. Camacho, P. J. González, M. Mattia, G. Puglisi, and J. Fernández (2015), Real Time Tracking of Magmatic Intrusions by means of Ground Deformation Modeling during Volcanic Crises, *Nature Publishing Group*, pp. 1–10. (Cited on page 187.)
- Canup, R. M. (2012), Forming a Moon with an Earth-like composition via a giant impact, *Science*, *338*, 1052–1055. (Cited on page 13.)
- Canup, R. M., and E. Asphaug (2001), Origin of the Moon in a giant impact near the end of the Earth's formation, *Nature*, *412*(6848), 708–712. (Cited on page 13.)
- Carslaw, H. S., and J. C. Jaeger (1959), Heat in solids. (Cited on page 84.)
- Castro, J. M., C. I. Schipper, S. P. Mueller, A. S. Militzer, A. Amigo, C. S. Parejas, and D. Jacob (2013), Storage and eruption of near-liquidus rhyolite magma at Cordón Caulle, Chile, *Bull Volcanol*, *75*(4), 1–17. (Cited on page 32.)
- Cayol, V., T. Catry, L. Michon, and M. Chaput (2014), Sheared sheet intrusions as mechanism for lateral flank displacement on basaltic volcanoes: Applications to Réunion Island volcanoes, *Journal of* (Cited on page 187.)
- Chadwick Jr., W. W., and J. H. Dieterich (1995), Mechanical modeling of circumferential and radial dike intrusion on Galapagos volcanoes, *Journal of Volcanology and Geothermal Research*, *66*(1-4), 37–52. (Cited on page 187.)
- Chevrel, M. O., T. Platz, E. Hauber, D. Baratoux, Y. Lavallée, and D. B. Dingwell (2013), Lava flow rheology: A comparison of morphological and petrological methods, *Earth and Planetary Science Letters*, *384*(C), 109–120. (Cited on page 32.)
- Clemens, J. D., and C. K. Mawer (1992), Granitic magma transport by fracture propagation, *Tectonophysics*, *204*(3-4), 339–360. (Cited on pages 6 and 7.)
- Corry, C. E. (1988), Laccoliths: mechanics of emplacement and growth. (Cited on pages 11, 18, 29, 30, 33 and 186.)

- Crisp, J., and S. Baloga (1990), A method for estimating eruption rates of planetary lava flows, *Icarus*, 85(2), 512–515. (Cited on pages 35 and 109.)
- Crisp, J. A. (1984), Rates of magma emplacement and volcanic output, *Journal of Volcanology and Geothermal Research*, 20(3-4), 177–211. (Cited on pages 9 and 120.)
- Cruden, A., and K. McCaffrey (2002), First international workshop on the Physical Geology of Subvolcanic Systems – Laccoliths, Sills, and Dykes, in *LASI 1*, pp. 8–11. (Cited on page 20.)
- Cruden, A., A. Bunger, and S. Morgan (2012), Emplacement dynamics of laccoliths, sills and dykes from dimensional scaling and mechanical models, in *LASI 1*. (Cited on pages 10, 11, 17, 19, 20, 30, 111 and 112.)
- Dahm, T. (2000), On the shape and velocity of fluid-filled fractures in the Earth, *Geophysical Journal International*, 142(1), 181–192. (Cited on page 8.)
- Das, S. B., I. Joughin, M. D. Behn, I. M. Howat, M. A. King, D. Lizarralde, and M. P. Bhatia (2008), Fracture Propagation to the Base of the Greenland Ice Sheet During Supraglacial Lake Drainage, *Science*, 320(5877), 778–781. (Cited on page 44.)
- Detournay, E., and A. Peirce (2014), On the moving boundary conditions for a hydraulic fracture, *INTERNATION JOURNAL OF ENGINEERING SCIENCE*, 84(C), 147–155. (Cited on page 185.)
- Diniega, S., S. E. Smrekar, S. Anderson, and E. R. Stofan (2013), The influence of temperature-dependent viscosity on lava flow dynamics, *J. Geophys. Res. Earth Surf.*, 118(3), 1516–1532. (Cited on pages 87, 104 and 109.)
- Dixon, J. M., and D. G. Simpson (1987), Centrifuge modelling of laccolith intrusion, 9(1), 87–103. (Cited on page 45.)
- Dombard, A. J., and J. J. Gillis (2001), Testing the viability of topographic relaxation as a mechanism for the formation of lunar floor-fractured craters, *J. Geophys. Res.*, 106(E11), 27,901–27,909. (Cited on pages 121, 148, 152 and 158.)
- Dyskin, A. V., L. N. Germanovich, and K. B. Ustinov (2000), Asymptotic analysis of crack interaction with free boundary, *International journal of solids . . .*, 37(6), 857–886. (Cited on page 36.)

- El-Baz, F. (1970), Lunar Igneous Intrusions, *Science*, 167(3914), 49–50. (Cited on page 120.)
- Elkins-Tanton, L. T., S. Burgess, and Q.-Z. Yin (2011), The lunar magma ocean: Reconciling the solidification process with lunar petrology and geochronology, *Earth and Planetary Science Letters*, 304(3-4), 326–336. (Cited on page 13.)
- Flitton, J. C., and J. R. King (2004), Moving-boundary and fixed-domain problems for a sixth-order thin-film equation, *European Journal of Applied Mathematics*, 15(06), 713–754. (Cited on pages 25, 26, 45 and 46.)
- Galushkin, Y. I. (1997), Thermal effects of igneous intrusions on maturity of organic matter: a possible mechanism of intrusion, *Organic Geochemistry*, 26(11-12), 645–658. (Cited on page 82.)
- Ganino, C., N. T. Arndt, M.-F. Zhou, F. Gaillard, and C. Chauvel (2008), Interaction of magma with sedimentary wall rock and magnetite ore genesis in the Panzhihua mafic intrusion, SW China, *Miner Deposita*, 43(6), 677–694. (Cited on page 82.)
- Garel, F., E. Kaminski, S. Tait, and A. Limare (2012), An experimental study of the surface thermal signature of hot subaerial isoviscous gravity currents: Implications for thermal monitoring of lava flows and domes, *J. Geophys. Res.*, 117(B2), B02,205. (Cited on page 61.)
- Garel, F., E. Kaminski, S. Tait, and A. Limare (2014), An analogue study of the influence of solidification on the advance and surface thermal signature of lava flows, *Earth and Planetary Science Letters*, 396(C), 46–55. (Cited on pages 38 and 45.)
- Garrick-Bethell, I., and M. T. Zuber (2009), Elliptical structure of the lunar South Pole-Aitken basin, *Icarus*, 204(2), 399–408. (Cited on page 171.)
- Gilbert, G. K. (1877), Report on the Geology of the Henry Mountains, Government Printing Office, Washington, DC. (Cited on pages 11 and 12.)
- Giordano, D., J. K. Russell, and D. B. Dingwell (2008), Viscosity of magmatic liquids: A model, *Earth and Planetary Science Letters*, 271(1-4), 123–134. (Cited on pages 32, 47 and 104.)

- Glazner, A. F., J. M. Bartley, D. S. Coleman, W. Gray, and R. Z. Taylor (2004), Are plutons assembled over millions of years by amalgamation from small magma chambers?, *GSA Today*, 14(4), 4–8. (Cited on pages 7, 9, 10 and 183.)
- Glotch, T. D., P. G. Lucey, J. L. Bandfield, B. T. Greenhagen, I. R. Thomas, R. C. Elphic, N. Bowles, M. B. Wyatt, C. C. Allen, K. D. Hanna, and D. A. Paige (2010), Highly Silicic Compositions on the Moon, *Science*, 329(5998), 1510–1513. (Cited on page 120.)
- Goodman, T. R. (1958), *The heat-balance integral and its application to problems involving a change of phase*, Trans. ASME. (Cited on page 48.)
- Gregg, T. K. P., and J. H. Fink (1996), Quantification of extraterrestrial lava flow effusion rates through laboratory simulations, *Journal of Geophysical Research*, 101(E7), 16,891–16,900. (Cited on page 110.)
- Habert, G., and M. De Saint-Blanquat (2004), Rate of construction of the Black Mesa bysmalith, Henry Mountains, Utah, *Geological Society*. (Cited on page 11.)
- Hall, J. L., S. C. Solomon, and J. W. Head (1981), Lunar floor-fractured craters: Evidence for viscous relaxation of crater topography, *J. Geophys. Res. Planets*, 86(B10), 9537–9552. (Cited on pages 121 and 158.)
- Han, S.-C., N. Schmerr, G. Neumann, and S. Holmes (2014), Global characteristics of porosity and density stratification within the lunar crust from GRAIL gravity and Lunar Orbiter Laser Altimeter topography data, *Geophys. Res. Lett.*, 41(6), 1882–1889. (Cited on page 13.)
- Harris, A., J. B. Murray, S. E. Aries, M. A. Davies, L. P. Flynn, M. J. Wooster, R. Wright, and D. A. Rothery (2000), Effusion rate trends at Etna and Krafla and their implications for eruptive mechanisms, 102(3-4), 237–269. (Cited on pages 32 and 107.)
- Head, J. W., and L. Wilson (1992), Lunar mare volcanism: Stratigraphy, eruption conditions, and the evolution of secondary crusts, *Geochimica et Cosmochimica Acta*, 56(6), 2155–2175. (Cited on pages 14, 120 and 153.)
- Head, J. W., S. L. Murchie, L. M. Prockter, M. S. Robinson, S. C. Solomon, R. G. Strom, C. R. Chapman, T. R. Watters, W. E. McClintock, D. T. Blewett, and J. J. Gillis-Davis (2008), Volcanism

- on Mercury: Evidence from the First MESSENGER Flyby, *Science*, 321(5885), 69–72. (Cited on page 121.)
- Head, J. W., C. I. Fassett, S. J. Kadish, D. E. Smith, M. T. Zuber, G. A. Neumann, and E. Mazarico (2010), Global distribution of large lunar craters: implications for resurfacing and impactor populations, *Science*, 329(5998), 1504–1507. (Cited on pages 169, 171, 175 and 220.)
- Hewitt, I. J., N. J. Balmforth, and J. R. De Bruyn (2014), Elastic-plated gravity currents, pp. 1–29. (Cited on pages 22, 25, 26, 33, 44, 45, 185 and 186.)
- Hiesinger, H. (2006), New Views of Lunar Geoscience: An Introduction and Overview, *Reviews in Mineralogy and Geochemistry*, 60(1), 1–81. (Cited on pages 120 and 125.)
- Horsman, E., B. Tikoff, and S. Morgan (2005), Emplacement-related fabric and multiple sheets in the Maiden Creek sill, Henry Mountains, Utah, USA, *Journal of Structural Geology*, 27(8), 1426–1444. (Cited on pages 11 and 19.)
- Horsman, E., S. Morgan, M. de Saint-Bланquat, G. Habert, A. Nugent, R. A. Hunter, and B. Tikoff (2009), Emplacement and assembly of shallow intrusions from multiple magma pulses, Henry Mountains, Utah, 100(1-2), 117–132. (Cited on pages 13 and 19.)
- Hort, M. (1997), Cooling and crystallization in sheet-like magma bodies revisited, *Journal of Volcanology and Geothermal Research*, 76(3-4), 297–317. (Cited on page 48.)
- Hosoi, A., and L. Mahadevan (2004), Peeling, Healing, and Bursting in a Lubricated Elastic Sheet, *Phys. Rev. Lett.*, 93(13), 137,802. (Cited on page 44.)
- Huang, Q., and M. A. Wieczorek (2012), Density and porosity of the lunar crust from gravity and topography, *J. Geophys. Res.*, 117(E5), E05,003. (Cited on page 13.)
- Huppert, H. E. (1982a), The propagation of two-dimensional and axisymmetric viscous gravity currents over a rigid horizontal surface, *J. Fluid Mech.*, 121(-1), 43–58. (Cited on pages 28, 45, 56, 129, 130, 131, 136, 138, 161 and 163.)
- Huppert, H. E. (1982b), Flow and instability of a viscous current down a slope, *Nature*. (Cited on page 51.)

- Jaeger, J. C. (1959), Temperatures outside a cooling intrusive sheet, *257*(1), 44–54. (Cited on pages 82 and 112.)
- Johnson, A. M., and D. D. Pollard (1973), Mechanics of growth of some laccolithic intrusions in the Henry mountains, Utah, I: field observations, Gilbert's model, physical properties and flow of the magma, *Tectonophysics*. (Cited on pages 11, 17, 18, 37 and 150.)
- Jolliff, B. L., L. R. Gaddis, G. Ryder, C. R. Neal, C. K. Shearer, R. C. Elphic, R. J. Johnson, P. J. Keller, R. L. Kerotev, D. J. Lawrence, P. G. Lucey, J. J. Papike, C. M. Pieters, P. D. Spudis, and L. A. Taylor (2000), New views of the Moon: Improved understanding through data integration, *Eos*, *81*(31), 349–360. (Cited on page 127.)
- Jozwiak, L. M., J. W. Head, M. T. Zuber, D. E. Smith, and G. A. Neumann (2012), Lunar floor-fractured craters: Classification, distribution, origin and implications for magmatism and shallow crustal structure, *J. Geophys. Res.*, *117*(E11), E11,005. (Cited on pages 18, 121, 122, 123, 124, 127, 148, 149, 150, 152, 158, 169, 171, 175 and 222.)
- Kalynn, J., C. L. Johnson, G. R. Osinski, and O. Barnouin (2013), Topographic characterization of lunar complex craters, *Geophys. Res. Lett.*, *40*(1), 38–42. (Cited on pages 125, 126, 127, 175, 176, 220 and 222.)
- Kavanagh, J. L., and R. S. J. Sparks (2011), Insights of dyke emplacement mechanics from detailed 3D dyke thickness datasets, *Journal of the Geological Society*, *168*(4), 965–978. (Cited on page 10.)
- Kavanagh, J. L., T. Menand, and R. S. J. Sparks (2006), An experimental investigation of sill formation and propagation in layered elastic media, *Earth and Planetary Science Letters*, *245*(3-4), 799–813. (Cited on pages 7, 8 and 19.)
- Kerr, A. D., and D. D. Pollard (1998), Toward more realistic formulations for the analysis of laccoliths, *Journal of Structural Geology*, *20*(12), 1783–1793. (Cited on page 18.)
- Kerr, R. C., and J. R. Lister (1995), Comment on “On the relationship between dike width and magma viscosity” by Yutaka Wada, *Journal of Geophysical Research: Solid . . .* (Cited on page 32.)
- Kiefer, W. S. (2013), Gravity constraints on the subsurface structure of the Marius Hills: The magmatic plumbing of the largest lunar volcanic

- dome complex, *J. Geophys. Res. Planets*, 118(4), 733–745. (Cited on page 178.)
- Kiefer, W. S., R. J. Macke, D. T. Britt, A. J. Irving, and G. J. Consolmagno (2012), The density and porosity of lunar rocks, *Geophys. Res. Lett.*, 39(7). (Cited on pages 14, 165 and 178.)
- Koch, F. G., A. M. Johnson, and D. D. Pollard (1981), Monoclinal bending of strata over laccolithic intrusions, *Tectonophysics*, 74(3-4), T21–T31. (Cited on pages 11, 18, 29 and 37.)
- Konopliv, A. S., R. S. Park, and D. N. Yuan (2014), High-resolution lunar gravity fields from the GRAIL Primary and Extended Missions, *Geophys. Res. Lett.*, 41, 1452–1458. (Cited on pages 159 and 167.)
- Krumbholz, M., C. F. Hieronymus, S. Burchardt, V. R. Troll, D. C. Tanner, and N. Friese (2014), Weibull-distributed dyke thickness reflects probabilistic character of host-rock strength, *Nature Communications*, 5, 1–7. (Cited on page 10.)
- Laneuville, M., M. A. Wieczorek, D. Breuer, and N. Tosi (2013), Asymmetric thermal evolution of the Moon, *J. Geophys. Res. Planets*, 118(7), 1435–1452. (Cited on page 121.)
- Lejeune, A. M., and P. Richet (1995), Rheology of crystal-bearing silicate melts: An experimental study at high viscosities, *Journal of Geophysical Research*, 100(B3), 4215–4229. (Cited on pages 38, 45, 47 and 104.)
- Lister, J. R., and R. C. Kerr (1991), Fluid-mechanical models of crack propagation and their application to magma transport in dykes, *Journal of Geophysical Research: Solid . . .*, 96(B6), 10,049–10,077. (Cited on pages 7, 17 and 36.)
- Lister, J. R., G. G. Peng, and J. A. Neufeld (2013), Viscous Control of Peeling an Elastic Sheet by Bending and Pulling, *Phys. Rev. Lett.*, 111(15), 154,501. (Cited on pages 22, 25, 26, 27, 28, 29, 32, 44, 45, 46, 55, 56, 62 and 74.)
- Maccaferri, F., M. Bonafede, and E. Rivalta (2011), A quantitative study of the mechanisms governing dike propagation, dike arrest and sill formation, *Journal of Volcanology and Geothermal Research*, 208(1–2), 39–50. (Cited on page 8.)

- Maccaferri, F., E. Rivalta, D. Keir, and V. Acocella (2014), Off-rift volcanism in rift zones determined by crustal unloading, *Nature Geosci.*, 7(4), 297–300. (Cited on pages 8 and 188.)
- Macedonio, G., F. Giudicepietro, L. D'Auria, and M. Martini (2014), Sill intrusion as a source mechanism of unrest at volcanic calderas, *J. Geophys. Res. Solid Earth*, 119(5), 3986–4000. (Cited on page 187.)
- Marsh, B. D. (1981), On the crystallinity, probability of occurrence, and rheology of lava and magma, *Contr. Mineral. and Petrol.*, 78(1), 85–98. (Cited on pages 47 and 104.)
- McCaffrey, K., and N. Petford (1997), Are granitic intrusions scale invariant?, *Journal of the Geological Society*, 154(1), 1–4. (Cited on pages 18, 19 and 33.)
- McKenzie, D. (1984), The Generation and Compaction of Partially Molten Rock, *Journal of Petrology*, 25(3), 713–765. (Cited on page 6.)
- McKenzie, D. (1985), The extraction of magma from the crust and mantle, *Earth and Planetary Science Letters*, 74(1), 81–91. (Cited on page 6.)
- Melosh, H. J. (1989), Impact cratering: A geologic process, 11, 253. (Cited on page 127.)
- Melosh, H. J., A. M. Freed, B. C. Johnson, D. M. Blair, J. C. Andrews-Hanna, G. A. Neumann, R. J. Phillips, D. E. Smith, S. C. Solomon, M. A. Wieczorek, and M. T. Zuber (2013), The origin of lunar mascon basins, *Science*, 340(6140), 1552–1555. (Cited on page 170.)
- Menand, T. (2011), Physical controls and depth of emplacement of igneous bodies: A review, *Tectonophysics*, 500(1-4), 11–19. (Cited on pages 7, 19 and 37.)
- Menand, T., K. A. Daniels, and B. P (2010), Dyke propagation and sill formation in a compressive tectonic environment, *J. Geophys. Res.*, 115(B08201). (Cited on page 8.)
- Michaut, C. (2011), Dynamics of magmatic intrusions in the upper crust: Theory and applications to laccoliths on Earth and the Moon, *J. Geophys. Res. Solid Earth*, 116(B05205). (Cited on pages 20, 21, 22, 25, 26, 27, 28, 33, 34, 35, 37, 38, 39, 44, 45, 51, 52, 55, 56, 102, 111, 121, 122, 130, 132, 137, 138, 146, 148, 151, 162, 163, 183, 185, 186 and 187.)

- Michaut, C., and D. Bercovici (2009), A model for the spreading and compaction of two-phase viscous gravity currents, *J. Fluid Mech.*, *630*, 299–329. (Cited on pages 25, 52, 129 and 136.)
- Michaut, C., and C. Jaupart (2006), Ultra-rapid formation of large volumes of evolved magma, *Earth and Planetary Science Letters*, *250*(1-2), 38–52. (Cited on page 48.)
- Michaut, C., and C. Jaupart (2011), Two models for the formation of magma reservoirs by small increments, *Tectonophysics*. (Cited on page 178.)
- Michaut, C., D. Baratoux, and C. Thorey (2013), Magmatic intrusions and deglaciation at mid-latitude in the northern plains of Mars, *Icarus*, *225*(1), 602–613. (Cited on pages 138 and 163.)
- Miller, R. B., and S. R. Paterson (1999), In defense of magmatic diapirs, *Journal of Structural Geology*, *21*(8-9), 1161–1173. (Cited on page 7.)
- Mizutani, H., T. Matsui, and H. Takeuchi (1972), Accretion process of the moon, *The Moon*, *4*(3-4), 476–489. (Cited on page 13.)
- Morgan, S., A. Stanik, E. Horsman, B. Tikoff, M. de Saint-Bланquat, and G. Habert (2008), Emplacement of multiple magma sheets and wall rock deformation: Trachyte Mesa intrusion, Henry Mountains, Utah, *Journal of Structural Geology*, *30*(4), 491–512. (Cited on pages 11, 19 and 37.)
- O’Keefe, J. D., and T. J. Ahrens (1999), Complex craters: Relationship of stratigraphy and rings to impact conditions, *J. Geophys. Res.*, *104*(11), 27,091–27,104. (Cited on page 125.)
- Patanè, D., G. Barberi, O. Cocina, P. De Gori, and C. Chiarabba (2006), Time-Resolved Seismic Tomography Detects Magma Intrusions at Mount Etna, *Science*, *313*(5788), 821–823. (Cited on page 187.)
- Patankar, S. (1980), Numerical heat transfer and fluid flow. (Cited on pages 198 and 203.)
- Pedersen, R., and F. Sigmundsson (2004), InSAR based sill model links spatially offset areas of deformation and seismicity for the 1994 unrest episode at Eyjafjallajökull volcano, Iceland, *Geophys. Res. Lett.*, *31*(14), L14,610. (Cited on page 187.)

- Petford, N., R. C. Kerr, and J. R. Lister (1993), Dike transport of granitoid magmas, *Geology*, 21(9), 845–848. (Cited on page 7.)
- Petford, N., A. R. Cruden, K. McCaffrey, and J. L. Vigneresse (2000), Granite magma formation, transport and emplacement in the Earth's crust, *Nature*, 408(6813), 669–673. (Cited on pages 10 and 183.)
- Pieri, D. C., and S. M. Baloga (1986), Eruption rate, area, and length relationships for some Hawaiian lava flows, *Journal of Volcanology and Geothermal Research*, 30(1-2), 29–45. (Cited on page 32.)
- Pike, R. J. (1974), Depth/diameter relations of fresh lunar craters: Revision from spacecraft data, *Geophys. Res. Lett.*, 1(7), 291–294. (Cited on pages 125, 169, 175 and 176.)
- Pike, R. J. (1976), Crater dimensions from apollo data and supplemental sources, *The Moon*, 15(3-4), 463–477. (Cited on page 128.)
- Pike, R. J. (1980), Formation of complex impact craters: Evidence from Mars and other planets, *Icarus*, 43(1), 1–19. (Cited on pages 125, 126, 127, 128, 169 and 175.)
- Pinel, V., and C. Jaupart (2000), The effect of edifice load on magma ascent beneath a volcano, ... *Transactions of the Royal* (Cited on page 8.)
- Pinel, V., and C. Jaupart (2004), Magma storage and horizontal dyke injection beneath a volcanic edifice, *Earth and Planetary Science Letters*, 221(1-4), 245–262. (Cited on page 8.)
- Pinkerton, H., and R. J. Stevenson (1992), Methods of determining the rheological properties of magmas at sub-liquidus temperatures, 53(1-4), 47–66. (Cited on page 104.)
- Platz, T., P. K. Byrne, M. Massironi, and H. Hiesinger (2015), Volcanism and tectonism across the inner solar system: an overview, *Geological Society, London, Special Publications*, 401(1), 1–56. (Cited on page 15.)
- Pollard, D. D., and A. M. Johnson (1973), Mechanics of growth of some laccolithic intrusions in the Henry Mountains, Utah, II: bending and failure of overburden layers and sill formation, *Tectonophysics*, 18(3-4), 311–354. (Cited on pages 18, 121 and 150.)

- Rivalta, E. (2010), Evidence that coupling to magma chambers controls the volume history and velocity of laterally propagating intrusions, *J. Geophys. Res.*, 115(B7), B07,203. (Cited on page 186.)
- Rivalta, E., M. Böttlinger, and T. Dahm (2005), Buoyancy-driven fracture ascent: Experiments in layered gelatine, *Journal of Volcanology and Geothermal Research*, 144(1-4), 273–285. (Cited on page 120.)
- Rocchi, S., D. S. Westerman, A. Dini, F. Innocenti, and S. Tonarini (2002), Two-stage growth of laccoliths at Elba Island, Italy, *Geology*, 30(11), 983–986. (Cited on pages 11, 19, 29, 30, 31, 103 and 107.)
- Rocchi, S., D. S. Westerman, A. Dini, and F. Farina (2010), Intrusive sheets and sheeted intrusions at Elba Island, Italy, *Geosphere*. (Cited on pages 12, 34 and 186.)
- Roni, E., D. S. Westerman, and A. Dini (2014), Feeding and growth of a dyke–laccolith system (Elba Island, Italy) from AMS and mineral fabric data, *Journal of the Geological Society*, 171, 413–424. (Cited on page 13.)
- Rubin, A. M. (1995), Propagation of magma-filled cracks, *Annual Review of Earth and Planetary Sciences*. (Cited on pages 7, 10 and 17.)
- Sato, H., K. Kurita, and D. Baratoux (2010), The formation of floor-fractured craters in Xanthe Terra, *Icarus*, 207(1), 248–264. (Cited on pages 121, 189 and 190.)
- Savitski, A. A., and E. Detournay (2002), Propagation of a penny-shaped fluid-driven fracture in an impermeable rock: asymptotic solutions, *International Journal of Solids and Structures*, 39, 6311–6337. (Cited on page 185.)
- Schultz, P. H. (1976a), Floor-fractured lunar craters, *The Moon*, 15(3-4), 241–273. (Cited on pages 15, 17, 38, 121, 122, 123, 124, 127, 148, 149, 150, 153, 154, 158, 159, 163, 164, 175, 177, 178 and 179.)
- Schultz, P. H. (1976b), Moon morphology: Interpretations based on Lunar Orbiter photography, *Austin, University of Texas Press, 1976. 641 p.*, -1. (Cited on page 125.)
- Schultz, P. H. (1977), Endogenic modification of impact craters on Mercury, *Physics of the Earth and Planetary Interiors*, 15(2-3), 202–219. (Cited on pages 190 and 191.)

- Schultz, P. H. (1978), Martian intrusions: Possible sites and implications, *Geophys. Res. Lett.* (Cited on page 121.)
- Schultz, P. H. (1988), Cratering on Mercury: A relook, *Mercury*, pp. 274–335. (Cited on page 125.)
- Schultz, P. H., and H. Glicken (1979), Impact crater and basin control of igneous processes on Mars, *J. Geophys. Res.*, 84(B14), 8033. (Cited on page 121.)
- Schultz, P. H., C. Koeberl, T. Bunch, J. Grant, and W. Collins (1994), Ground truth for oblique impact processes: New insight from the Rio Cuarto, Argentina, crater field, *Geology*, 22(10), 889–892. (Cited on page 127.)
- Schultz, R. A., R. Soliva, H. Fossen, C. H. Okubo, and D. M. Reeves (2008), Dependence of displacement–length scaling relations for fractures and deformation bands on the volumetric changes across them, *Journal of Structural Geology*, 30(11), 1405–1411. (Cited on page 10.)
- Senger, K., S. Planke, S. Polteau, and K. Ogata (2014), Sill emplacement and contact metamorphism in a siliciclastic reservoir on Svalbard, Arctic Norway. (Cited on pages 82, 108 and 112.)
- Shaw, H. R. (1972), Viscosities of magmatic silicate liquids; an empirical method of prediction, *Am J Sci*, 272(9), 870–893. (Cited on pages 32, 38, 45, 47 and 104.)
- Shearer, C. K. (2006), Thermal and Magmatic Evolution of the Moon, *Reviews in Mineralogy and Geochemistry*, 60(1), 365–518. (Cited on page 35.)
- Sillitoe, R. H., and J. F. H. Thompson (1998), Intrusion–Related Vein Gold Deposits: Types, Tectono-Magmatic Settings and Difficulties of Distinction from Orogenic Gold Deposits, *Resource Geology*, 48(4), 237–250. (Cited on pages 82 and 112.)
- Sjogren, W. L., P. M. Muller, and W. R. Wollenhaupt (1972), Apollo 15 gravity analysis from the S-band transponder experiment, *The Moon*, 4(3-4), 411–418. (Cited on page 159.)
- Sjogren, W. L., R. N. Wimberly, and W. R. Wollenhaupt (1974), Lunar gravity: Apollo 16, *The Moon*, 11(1-2), 35–40. (Cited on page 159.)

- Snoeijer, J. H., and B. Andreotti (2013), Moving Contact Lines: Scales, Regimes, and Dynamical Transitions, *Annu. Rev. Fluid Mech.*, *45*(1), 269–292. (Cited on page 25.)
- Stasiuk, M. V., C. Jaupart, R. Stephen, and J. Sparks (1993), Influence of cooling on lava-flow dynamics, *Geology*, *21*(4), 335–338. (Cited on page 32.)
- Taisne, B., and C. Jaupart (2009), Dike propagation through layered rocks, *Journal of Geophysical Research: Solid Earth*, (Cited on page 120.)
- Taisne, B., and S. Tait (2009), Eruption versus intrusion? Arrest of propagation of constant volume, buoyant, liquid-filled cracks in an elastic, brittle host, *J. Geophys. Res.*, *114*(B6), B06,202. (Cited on pages 7 and 159.)
- Taisne, B., S. Tait, and C. Jaupart (2011), Conditions for the arrest of a vertical propagating dyke, *Bull Volcanol*, *73*(2), 191–204. (Cited on page 7.)
- Thomson, B. J., E. B. Grosfils, D. B. J. Bussey, and P. D. Spudis (2009), A new technique for estimating the thickness of mare basalts in Imbrium Basin, *Geophys. Res. Lett.*, *36*(12), L12,201–5. (Cited on page 189.)
- Thorey, C., and C. Michaut (2014), A model for the dynamics of crater-centered intrusion: Application to lunar floor-fractured craters, *J. Geophys. Res.* (Cited on pages 45, 119, 158, 159, 161, 162, 163, 164, 165, 175 and 178.)
- Thorey, C., C. Michaut, and M. Wieczorek (2015), Gravitational signatures of lunar floor-fractured craters, *Earth and Planetary Science Letters*. (Cited on page 157.)
- Tsai, V. C., and J. R. Rice (2010), A model for turbulent hydraulic fracture and application to crack propagation at glacier beds, *J. Geophys. Res.*, *115*(F3), F03,007. (Cited on page 44.)
- Tuffen, H., M. R. James, J. M. Castro, and C. I. Schipper (2013), Exceptional mobility of an advancing rhyolitic obsidian flow at Cordón Caulle volcano in Chile, *Nature Communications*, *4*. (Cited on page 32.)

- Turcotte, D. L., and G. Schubert (1982), *Geodynamics: Applications of continuum physics to geological problems*, John Wiley, New York. (Cited on pages 23, 129 and 131.)
- Wada, Y. (1994), On the relationship between dike width and magma viscosity, *J. Geophys. Res.*, 99(B9), 17,743–17,755. (Cited on page 32.)
- Walker, G. P. L. (1989), Gravitational (density) controls on volcanism, magma chambers and intrusions, *Australian Journal of Earth Science*, 36(2), 149–165. (Cited on pages 7, 10, 120 and 159.)
- Watanabe, T., T. Masuyama, K. Nagaoka, and T. Tahara (2002), Analog experiments on magma-filled cracks: Competition between external stresses and internal pressure, *Earth Planet Sp.*, 54(12), e1247–e1261. (Cited on pages 7 and 8.)
- White, S. M., J. A. Crisp, and F. J. Spera (2006), Long-term volumetric eruption rates and magma budgets, *Geochem. Geophys. Geosyst.*, 7(3), Q03,010–21. (Cited on page 9.)
- Whittington, A. G., B. M. Hellwig, H. Behrens, B. Joachim, A. Stechern, and F. Vetere (2009), The viscosity of hydrous dacitic liquids: implications for the rheology of evolving silicic magmas, *Bull Volcanol.*, 71(2), 185–199. (Cited on page 32.)
- Wichman, R. W., and P. H. Schultz (1993), Floor-fractured crater models of the Sudbury Structure, Canada: Implications for initial crater size and crater modification, *Meteoritics*, 28(2), 222–231. (Cited on page 121.)
- Wichman, R. W., and P. H. Schultz (1995a), Floor-fractured impact craters on Venus: Implications for igneous crater modification and local magmatism, *J. Geophys. Res.*, 100(E2), 3233–3244. (Cited on pages 121, 158, 159, 190 and 191.)
- Wichman, R. W., and P. H. Schultz (1995b), Floor-fractured craters in Mare Smythii and west of Oceanus Procellarum: Implications of crater modification by viscous relaxation and igneous intrusion models, *J. Geophys. Res.*, 100(E10), 21,201–21,218. (Cited on page 121.)
- Wichman, R. W., and P. H. Schultz (1996), Crater-centered laccoliths on the Moon: Modeling intrusion depth and magmatic pressure at the crater Taruntius, *Icarus*, 122(1), 193–199. (Cited on pages 18, 121, 127 and 150.)

- Wieczorek, M. A., and R. J. Phillips (1998), Potential anomalies on a sphere: Applications to the thickness of the lunar crust, *J. Geophys. Res.*, 103(E1), 1715–1724. (Cited on pages 165 and 167.)
- Wieczorek, M. A., M. T. Zuber, and R. J. Phillips (2001), The role of magma buoyancy on the eruption of lunar basalts, *Earth and Planetary Science Letters*, 185(1-2), 71–83. (Cited on pages 14, 120 and 121.)
- Wieczorek, M. A., G. A. Neumann, F. Nimmo, W. S. Kiefer, G. J. Taylor, H. J. Melosh, R. J. Phillips, S. C. Solomon, J. C. Andrews-Hanna, S. W. Asmar, A. S. Konopliv, F. G. Lemoine, D. E. Smith, M. M. Watkins, J. G. Williams, and M. T. Zuber (2013), The crust of the Moon as seen by GRAIL, *Science*, 339(6120), 671–675. (Cited on pages 13, 120, 159, 167, 178 and 180.)
- Wilhelms, D. E., J. F. McCauley, and N. J. Trask (1987), The geologic history of the Moon, *U. S. Geological Survey Professional Paper*. (Cited on pages 120, 125 and 127.)
- Wilson, L., and J. W. Head III (1981), Ascent and eruption of basaltic magma on the Earth and Moon, *J. Geophys. Res.*, 86(B4), 2971–3001. (Cited on pages 120 and 121.)
- Wöhler, C., R. Lena, and J. Phillips (2007), Formation of lunar mare domes along crustal fractures: Rheologic conditions, dimensions of feeder dikes, and the role of magma evolution, *Icarus*, 189(2), 279–307. (Cited on pages 15 and 34.)
- Wöhler, C., R. Lena, and Geologic Lunar Research Group (2009), Lunar intrusive domes: Morphometric analysis and laccolith modelling, *Icarus*, 204(2), 381–398. (Cited on pages 18, 31, 34 and 35.)
- Zhou, M.-F., N. T. Arndt, J. Malpas, C. Y. Wang, and A. K. Kennedy (2008), Two magma series and associated ore deposit types in the Permian Emeishan large igneous province, SW China, *Lithos*, 103(3-4), 352–368. (Cited on page 82.)
- Zimbelman, J. R. (1998), Emplacement of long lava flows on planetary surfaces, *J. Geophys. Res. Solid Earth*. (Cited on pages 35 and 109.)
- Zuber, M. T., D. E. Smith, R. S. Zellar, G. A. Neumann, X. Sun, R. B. Katz, I. Kleyner, A. Matuszeski, J. F. McGarry, M. N. Ott, L. A.

Ramos-Izquierdo, D. D. Rowlands, M. H. Torrence, and T. W. Zagwodzki (2009), The lunar reconnaissance orbiter laser ranging Investigation, *Space Sci Rev*, 150(1-4), 63–80. (Cited on pages 34 and 175.)

Zuber, M. T., D. E. Smith, M. M. Watkins, S. W. Asmar, A. S. Konopliv, F. G. Lemoine, H. J. Melosh, G. A. Neumann, R. J. Phillips, S. C. Solomon, M. A. Wieczorek, J. G. Williams, S. J. Goossens, G. Kruizinga, E. Mazarico, R. S. Park, and D. N. Yuan (2013), Gravity field of the Moon from the gravity recovery and interior laboratory (GRAIL) mission, *Science*, 339(6120), 668–671. (Cited on page 159.)